Forschungszentrum Karlsruhe
in der Helmholtz-Gemeinschaft

Wissenschaftliche Berichte
FZKA 7098

Turbulent Thermal Mixing of a Heavy Liquid Metal Flow in a Target Window Geometry - The Heated Jet Experiment

M. Daubner, A. Batta, F. Fellmoser, C.-H. Lefhalm, R. Stieglitz

Institut für Kern- und Energietechnik
Programm Nukleare Sicherheitsforschung

September 2005

Forschungszentrum Karlsruhe

in der Helmholtz-Gemeinschaft

Wissenschaftliche Berichte

FZKA 7098

Turbulent thermal mixing of a heavy liquid metal flow in a target window geometry- The Heated Jet Experiment

Markus Daubner, Abdalla Batta, Frank Fellmoser, Cord-Henrich Lefhalm, Robert Stieglitz

Institut für Kern- und Energietechnik

Programm Nukleare Sicherheitsforschung

Forschungszentrum Karlsruhe GmbH, Karlsruhe

2005

Impressum der Print-Ausgabe:

Als Manuskript gedruckt

Forschungszentrum Karlsruhe GmbH
Postfach 3640, 76021 Karlsruhe

Mitglied der Hermann von Helmholtz-Gemeinschaft
Deutscher Forschungszentren (HGF)

ISSN 0947-8620

urn:nbn:de:0005-070986

Turbulente thermische Durchmischung einer flüssigen Schwermetallströmung in einer Fenster-Target-Geometrie - das „Heated Jet“-Experiment

Zusammenfassung

Das am Paul Scherrer Institut geplante MEGAPIE Experiment ist ein flüssigmetallgekühltes Spallationstarget, in dem eine eutektische Blei Wismut Legierung sowohl als Kühlmedium als auch als Neutronengenerator fungiert. Um eine ausreichende Kühlung des thermisch hochbelasteten Targets zu gewährleisten, wird die Strömung in angemessener Weise konditioniert. Hierbei wird die Hauptströmung in einem Zylinderspalt nach unten gepumpt und an einer U-Umlenkung, die sich in der Nähe des halbkugelförmigen Targets befindet, um 180° in ein Steigrohr umgelenkt. Damit am untersten Punkt des Strahlfensters keine unzulässig hohen Temperaturen auftreten, wird durch eine rechteckförmige Düse eine Jetströmung seitlich auf diese Region gerichtet.

Diese Strömungsgeometrie wurde im THEADES Kreislauf des KALLA Labors im Maßstab 1:1 aufgebaut. Ziel der Experimente ist der Nachweis der Kühlbarkeit der kugelförmigen Kalotte bei geeigneter Wahl des Durchflussverhältnisses in Haupt- und Jetkanal. Hierzu ist der untere Bereich des Fensters dicht mit Thermoelementen instrumentiert. Das Flüssigmetallexperiment wird durch ein ähnlich großes Wasserexperiment, in dem das Strömungsfeld untersucht wird, unterstützt und von einer dreidimensionalen numerischen Simulation begleitet.

Zur Ermittlung des optimalen Arbeitsbereiches des MEGAPIE Designs wurden unterschiedliche Durchflussverhältnisse, die nahezu den gesamten möglichen Arbeitsbereich umfassen ($7.5 \leq Q_{main}/Q_{jet} \leq 22.5$), vermessen und hinsichtlich der Stabilität der entstehenden Strömungsmuster untersucht. Das sich einstellende Strömungsmuster und die Turbulenzintensitätsverteilung hängt lediglich vom gewählten Durchflussverhältnis von Haupt- zu Jetstrom ab. Die Experimente zeigten für alle Durchflussverhältnisse (Q_{main}/Q_{jet}) ein zeitabhängiges instabiles Verhalten. Die Geometrie reagiert äußerst empfindlich auf Änderungen des Durchflussverhältnisses (Q_{main}/Q_{jet}), wobei im Rahmen dieser Untersuchungen drei unterschiedliche Strömungsmuster identifiziert werden konnten.

Zur sicheren, adäquaten Kühlung des MEGAPIE Designs kommen lediglich Durchflussverhältnisse Q_{main}/Q_{jet} in Frage, für die $Q_{main}/Q_{jet} \leq 12.5$ gilt. Nur bei dieser Konstellation ist der Jet in der Lage, den größten Teil des halbkugelförmigen unteren Teils des Targets zu erfassen. Obwohl die Strömung gerade bei diesen Durchflussverhältnissen einen höheren Grad an Instabilität aufweist, ist dies im Hinblick auf eventuelle Temperaturschwankungen im Strukturmaterial des MEGAPIE Targets unkritisch, da sich die Fluktuationen im wesentlichen in einem Frequenzbereich über 1Hz abspielen. Dabei erfolgt Durchmischung auf großen Skalen und ist am effektivsten. Bereits 105mm über dem Kugelboden zeigten sich nur noch kleine Temperaturunterschiede. Für diesen Betriebsmodus sind daher die kleinsten thermischen Spannungen zu erwarten.

Übersteigt das Durchflussverhältnis den Wert 12.5, entstehen komplizierte Strömungsmuster, die aus mehreren Teilströmen und Wirbeln bestehen. Im Hinblick auf das MEGAPIE Experiment sollte dieser Durchflussverhältnisbereich gemieden werden, weil sich insbesondere am thermisch höchstbelasteten Punkt des halbkugelförmigen Targets eine Zone mit reduzierter Geschwindigkeit ausbildet, die zu inakzeptabel hohen Temperaturen führen kann.

Die untersuchte Strömungsgeometrie weist eine erhebliche Empfindlichkeit bezüglich kleinster, auch weit stromauf befindlicher, Asymmetrien auf, sodass im Experiment keine symmetrische Strömung erzielt werden konnte. Ein direkter Vergleich der Simulation, in der Symmetrie angenommen wurde, mit dem Experiment, in dem sich immer eine unsymmetrische Temperaturverteilung einstellte, war nur begrenzt möglich.

Abstract

The MEGAPIE target to be installed at the Paul-Scherrer Institute in Switzerland is a prominent example of a window spallation target using liquid lead-bismuth both as coolant and neutron source. An adequate cooling of the target to maintain the temperatures in the structure within acceptable limits requires a conditioning of the flow. In MEGAPIE this is realized by a main flow transported downwards, u-turned at the proton beam facing the hemispherical shell into a cylindrical riser tube. In order to avoid a stagnation point close to the lowest part of the shell a jet flow is directed along the shell, which is superimposed on the main flow.

The heated jet experiment conducted in the THEADES loop of the KALLA laboratory is nearly 1:1 representation of the lower part of the MEGAPIE target and is aimed to study the cooling capability of the specific geometry in dependence on the flow rate ratio (Q_{main}/Q_{jet}) of main to jet flow. In this out-of pile experiment a heated jet is injected into a cold main flow at MEGAPIE relevant flow rate ratios. The resulting temperatures and their fluctuations are recorded in the densly instrumented lower shell region. The liquid metal experiment is accompanied by a water experiment in almost the same geometry to study the momentum field and a three-dimensional turbulent numerical fluid dynamic simulation (CFD).

Besides a detailed study of the envisaged nominal operation of the MEGAPIE target with Q_{main}/Q_{jet}=15 deviations from this mode are investigated in the range from $7.5 \leq Q_{main}/Q_{jet} \leq 22.5$ in order to give an estimate on the safe operational threshold of the MEGAPIE target.

The liquid metal experiment shows that, the flow pattern establishing in this specific design and the turbulence intensity distribution essentially depends on the flow rate ratio (Q_{main}/Q_{jet}) between main flow and bypass flow. All flow rate ratios investigated exhibit an unstable time dependent behavior. The MEGAPIE design is highly sensitive against changes of Q_{main}/Q_{jet}.

In the scope of this experimental study three completely different flow patterns were identified. A sufficient cooling of the MEGAPIE design is only ensured if $Q_{main}/Q_{jet} \leq 12.5$, because for this configuration the jet covers the whole lower shell. Although for $Q_{main}/Q_{jet} \leq 12.5$ the flow is more unstable compared to the other cases most of the fluctuations close to the centerline are in the high frequency range (>1Hz), so that they will not lead to severe temperature fluctuations in the lower shell material. For these conditions the thermal mixing occurs on large scales and is excellent. A major temperature equalization is found already in a distance of 105mm above the lowest part of the shell. Thus in this mode the smallest thermal stresses can be expected.

For flow rate ratios $Q_{main}/Q_{jet} > 12.5$ complex flow patterns consisting of several fluid streaks and vortices were identified. But, for an adequate cooling the MEGAPIE target such flow rate constellation should be avoided, since the material temperatures close to the bottom of the shell, where the highest heat load appears, may exceed the acceptable limit.

All conducted experiments showed a high sensitivity to asymmetries even far upstream. A direct comparison of the simulation, which assumed a symmetric flow, was due to the experimentally found asymmetry only partially possible.

Content

1 Introduction

Beam windows facing the proton beam of an accelerator have to withstand high surface heat fluxes of up to 140W/cm^2 and in case of miscellaneous beam focusing even up to 200W/cm^2. Although this is only a minor part (<10%) of total heat released by the proton beam within the window region it represents one of the most critical technical issues to be solved. In order to simplify the geometrical configuration for such spallation targets, heavy liquid metals serving both as coolant and as spallation source are considered in many concepts, see e.g. Yefimov et al. (1998), Salvatores et al. (1999), ADTF design team (2001), or Rimpault et al. (2003).

The thickness of the beam window material is usually small, because of the considerable heat release within the structure by the proton beam, which could lead to a possible exceeding of the maximum sustainable material temperatures. A prominent example of such a highly heat loaded beam window is the MEGAPIE beam window made of a 2.5mm thin T91 (9Cr-1MoVNb) martensitic steel shell, see Salvatores et al. (1999) and Knebel et al. (2001). The MEGAPIE spallation target is planned to be set into operation in the SINQ facility of the Paul Scherrer Institute (PSI) in Switzerland in 2005. A schematic graph of this eutectic lead bismuth ($Pb^{45}Bi^{55}$) cooled configuration is shown in figure 1.1.

Besides the material issue, an adequate heat transfer from the wall towards the cooling and neutron producing heavy liquid metal PbBi has to be ensured for all beam states appearing during beam-on operation in order to guarantee a reliable system. Thus, only the detailed knowledge of the convective-diffusive heat transport phenomena in turbulent heavy liquid metal flows enables an adequate design of such a beam window. Due to the low molecular Prandtl number of liquid metals of the order $O(10^{-1}\text{-}10^{-2})$ a non-similarity between the kinematic and thermal transfer processes appears, which is often not sufficiently treated in commercial computational fluid dynamic (CFD) codes, see e.g. Arien (2004). Therefore, numerically calculated temperature distributions may lead to design misconceptions. This problem is enforced in most technical applications, where the flows are thermally developing, so that the heat exchange through the thermal boundary layer plays a significant role.

The simulation of a 1:1 heat production scenario in a beam window like in MEGAPIE as depicted in figure 1.1a, is out of pile hardly feasible, because simultaneously three different heat transfer problems of a turbulent liquid metal flow occur in the immediate vicinity of the hemispherical shell as depicted in figure 1.1b. The individual energy transfer phenomena associated with any liquid metal cooled beam window configuration are:

a.) Turbulent heat transfer from a highly heat loaded surface (about 5-10% of the total heat generated by the proton beam).

b.) Cooling of the vicinity of a stagnation point on the shell. In MEGAPIE this is realized via a superimposed jet flow. Here, the mixing phenomenon of thermal energy in low Prandtl number fluids occurs.

c.) Internal heat generation (volumetric heating) by the spallation reaction.

Considering a turbulent flow with hydraulic Reynolds numbers Re of order 10^5 in the first two problems, the temperature is mainly behaving as a passive scalar and is thus via heating or cooling in a simulation experimentally accessible. The latter issue c.) is out of pile almost impracticable to deal with.

Hence, the solution strategy for the MEGAPIE window is to validate for the first two problems the numerical CFD tools by means of two benchmark experiments in the real 1:1 geometry. Under this premise flow rate configurations of main and bypass flow are investigated in a range likely to be attained in MEGAPIE.

Finally, if the heat transfer problem at the beam window and the mixing phenomenon is both experimentally and numerically solved, the impact of the volumetric heating on the temperature distribution may be computed numerically, see e.g. Smith at al. (2002). The heat transfer of the turbulent heavy liquid metal flow from a highly heat loaded surface is investigated within the context of the KILOPIE experiment, where the surface heat flux generated by the proton beam is simulated by *h*eat *e*mitting *t*emperature *s*ensing *s*urfaces so-called HETSS. A detailed description of this technique and the related experiment may be taken from Patorski et al. (2001).

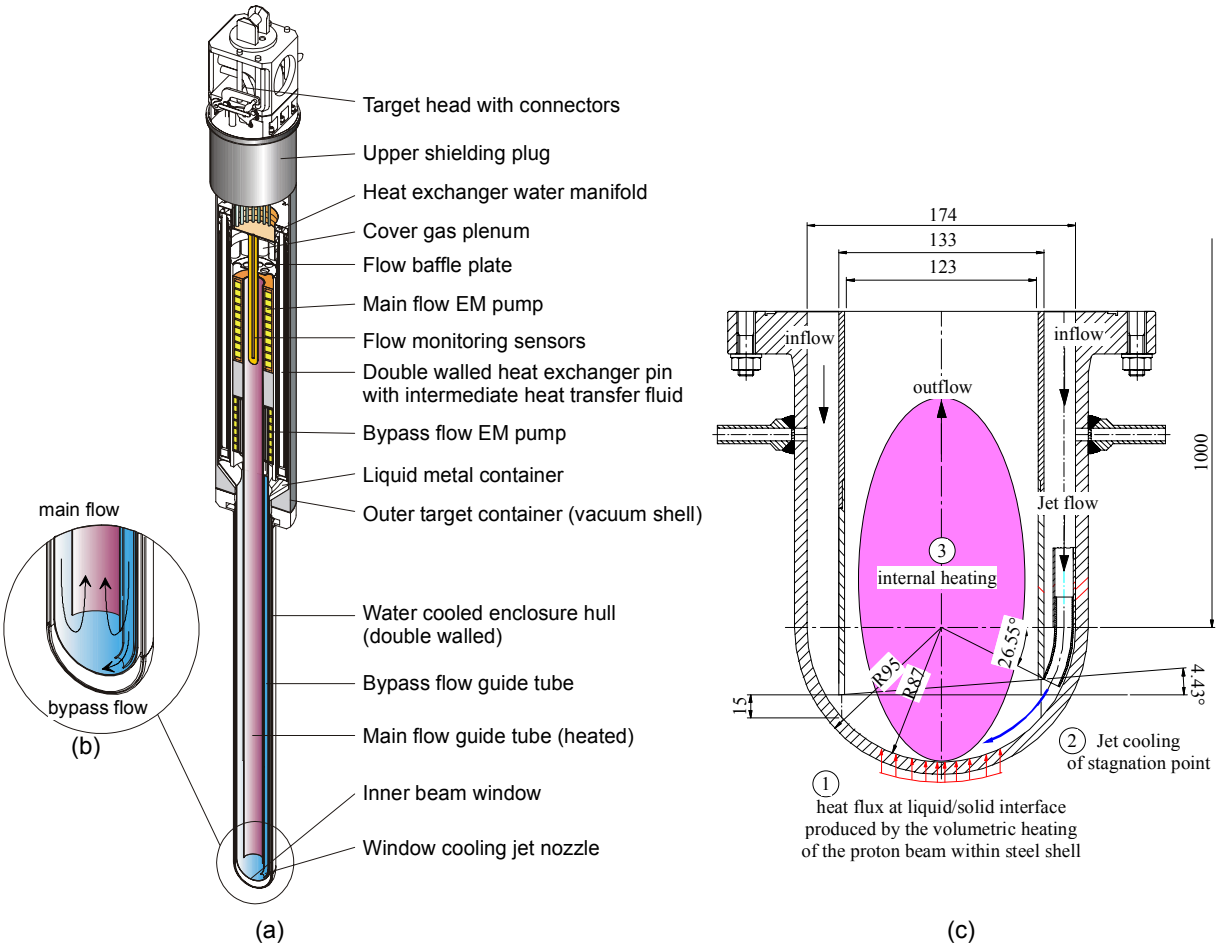

Figure 1.1: (a) Principle sketch of the PbBi operated MEGAPIE target. (b) Sketch of the lower target shell, in which a cross flow is induced via a jet exiting a bypass nozzle and fed by a pump. (c) Geometric dimensions of the lower target shell and zones of different heat transfer problems.

The objective of this report is first to elaborate the types of flow pattern which develops close to the hemispherical shell by the interaction of the main flow with the bypass flow at the nominal MEGAPIE flow rate ratio of main to bypass flow of 15:1 (later on called reference case). For this purpose a heated jet is injected into a colder main flow in a 1:1 experimental mock-up in such a way as to act also as an indicator for the flow pattern establishing by the interaction of both streams. The second goal is to investigate the thermal mixing of both streams at the nominal conditions in order to ensure that no thermal stresses and temperatures beyond acceptable limits appear in the structural material. Another purpose is to compare the experimental data with results from the numerical simulation on which the design is based on. Deviations from the nominal operation mode of the target as they may appear during the start-up/shut-down procedure or by regulations of the pump power may exhibit other flow patterns than the nominal operation mode. The influence of a variation of the flow rate variation as well as shifts of the temperature level on the flow pattern establishing and on the thermal mixing is investigated in the last step. This is of crucial importance since it determines the flow rate ratio threshold, in which the target can be reliably operated.

The report is organized as follows. First, the MEGAPIE target configuration is described. Herein, the flow paths, the mean temperatures, the flow velocities and the flow rates at the nominal operation point of the target are presented. The flow pattern establishing at the nominal operation point is qualitatively discussed in chapter 3 for a water experiment conducted in almost the same geometry. Within this context the physical phenomena appearing in merging flows in complex geometries are elaborated by means of plausibility arguments, vortex theory and similarity considerations. In section 4 the main features and assumptions of the numerical simulation of the liquid metal experiment are described and the flow field as well as the temperature distribution are presented. Then in paragraph 5 the thermal-hydraulic loop THEADES is described, in which the 1:1 experimental mock-up is embedded. This includes all instrumentation positions, the used coordinate system, the measurement matrix conducted and the relative errors of the individual instruments. The chapter 6 discusses the mean and temporal characteristics of the temperature field measured in the liquid metal experiment at the nominal operation point of the target. Based on a spatio-temporal analysis conclusions on the flow field can be drawn, which yields similar results as observed in the water experiment. The chapter is finished by a comparison of the numerical data with the experimental ones. Deviations from the nominal operation point (reference case), which are essentially described by another flow rate ratio of main to jet flow are investigated in paragraph 7. Finally, in chapter 8 from the results some final conclusions are drawn with respect to the operation threshold of the MEGAPIE beam window.

2 The MEGAPIE flow configuration

The Heated Jet experiment is closely related to the MEGAPIE experiment. A qualitative sketch of the fluid flow of the eutectic lead-bismuth eutectic alloy (LBE) flow through the MEGAPIE geometry is shown in figure 2.1. Besides the geometric dimensions given in millimeters typical temperatures and velocities are displayed.

The main flow is generated by an annular linear induction pump, which sucks cold fluid (T=230°C) from a pool below the PbBi-Oil heat exchanger and transports it via a manifold and a flow straightener through an annular gap. In this annular gap, called the 'downcomer', the fluid flows with a mean velocity of 0.33m/s downwards. Before leaving the gap the cross-section continuously decreases and hence the fluid is accelerated. Then it enters the beam window region. Within the beam window region the flow is turned by 180° into the riser tube where the spallation reaction takes place. In order to remove the stagnation point with its bad heat transfer capabilities from the center of the window as it may appear in an axis-symmetric configuration the riser tube is slanted. This ensures a defined flow singularity outside the highly heat loaded area and moreover introduces a swirl flow in the riser tube, which is desired for a homogeneous temperature distribution.

Although a recirculation is introduced in the mean flow by the slantation of the riser tube this measure is not sufficient to cool the immediate vicinity of the lower part of the beam window facing the proton beam, see Dury (2002). Therefore, a cross flow is superimposed on the main flow to ensure the cooling of the hemispherical window shell. The cross-flow is generated by a bypass or jet pump located in the upper target enclosure. This pump, also designed as an annular linear induction pump, transports fluid from the heat exchanger through the bypass duct to the nozzle. In order to ensure that along the hemispherical shell no stagnation point appears (which is accompanied by an excess of the temperature beyond material acceptable limits) the geometrical arrangement of the nozzle in the annular gap and the form of its orifice plays a decisive role. Here, numerous computational fluid dynamics (CFD) studies have been performed which are summarized by Tak and Cheng (2001), Smith (2002) and more recently by Roubin (2001, 2002, 2003). Although it turned out in the most recent calculations that a circular shaped nozzle leads to the best heat transfer in terms of the lowest beam window temperatures, a rectangular nozzle with an orifice area of 200mm^2 has been chosen, see Smith (2002). The nozzle orifice is arranged in such a way that the fluid exits the jet duct tangentially to the outer hemispherical shell.

Both, main flow and bypass flow merge in the riser and are guided upwards in direction of the instrumentation rod. From there the liquid flows to the upper target enclosure, where it is U-turned and directed back into the heat exchanger.

The projected temperatures and mass transfer rates envisaged at the nominal operation conditions for the MEGAPIE target at a power of 700kW are displayed in figure 2.1. However, deviations from this nominal conditions may appear because of the choice of different pumping powers in the main or in the bypass flow or a loss of one of the devices. Since the pumps are still in the fabrication and commissioning phase, mainly calculations are available at present. A detailed study of their capabilities is given in Dementjev et al. (2003)

and Stieglitz (2003). Both, main and bypass pumps have the capability to exceed the nominal operation point by a factor of 2 as depicted in figure 2.2.

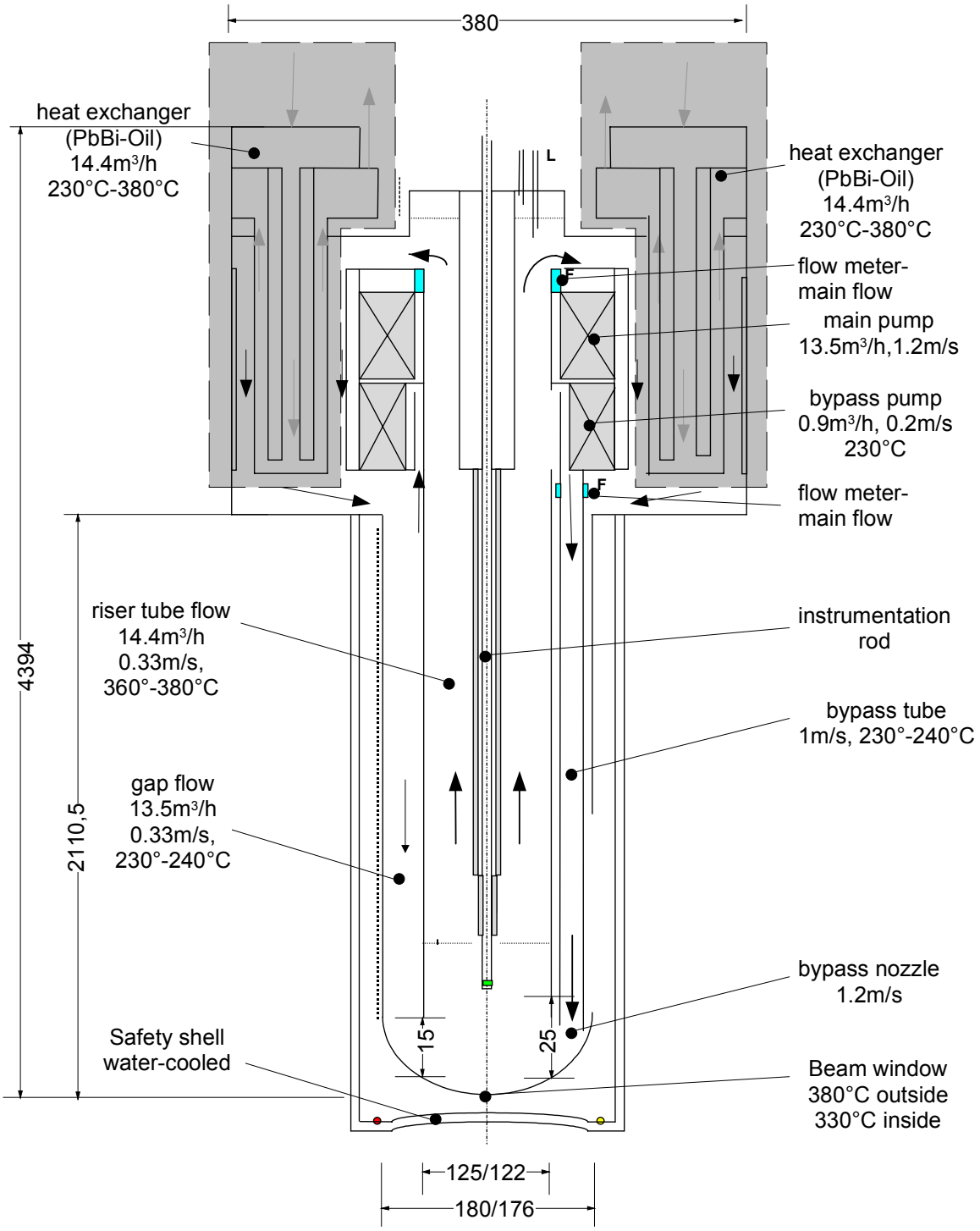

Figure 2.1: Schematic sketch of the flow paths in the MEGAPIE design and projected mass transfer and temperature distributions from Gröschel 2003. The geometrical dimensions are given in millimeters.

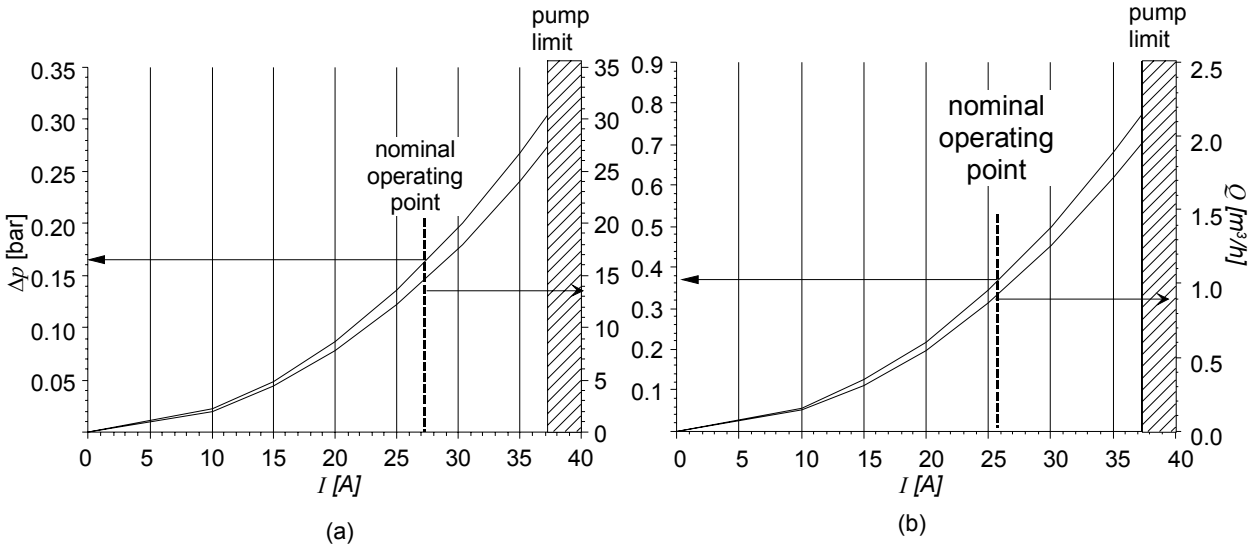

Figure 2.2: Attainable pressure head Δp [bars] and obtained flow rate Q[m^3/h] as a function of the supplied electric current I [A] for the main pump (a) and for the bypass pump (b) from Stieglitz (2003).

3 Analysis of the flow field in a water experiment

3.1 Experimental set-up of the water experiment

Due to the high density, corrosity, opaqueness and elevated operating temperatures commonly available flow visualization techniques can not be used in lead bismuth. Moreover, it is quite challenging in getting from a liquid metal experiment enough information to deduce the three-dimensional flow field which will develop in such a complicated geometry as the MEGAPIE target. To gain more detailed insight into the velocity field and its behavior we investigate a similar test section in a water loop and use the usual flow visualization and Laser-Doppler-Anemometry (LDA) techniques to gain qualitative and quantitative information on the flow field. Therefore, isothermal water experiments at nearly the same hydraulic Reynolds numbers and Froude numbers are performed in the HYTAS facility of the *KA*rlsruhe *L*ead *LA*boratory (KALLA). The similarity of the dimensionless parameters in both experiments ensure the transferability from the water to the lead bismuth results.

A sketch of the HYTAS loop system is displayed in figure 3.1. HYTAS is capable of circulating a maximum volumetric flow rate of 80m^3/h at a maximum pressure head of 0.4MPa with a maximal vertical test module length of 3.5m.

The MEGAPIE HYTAS test module is manufactured completely of plexiglass and all its geometrical dimensions are displayed in the figures 3.2 and 3.3, where all distances are given in millimeters. In figure 3.3 the detailed dimensions of the curvature of the nozzle which is also manufactured of plexiglass is illustrated.

Because the flow within the MEGAPIE geometry is extremely sensitive to smallest deviations from concentricity of the annular gap and to inhomogeneities arising from the inlet flow, at the top of the module a flow straigthener is installed, which has a length of 50mm and

consists of a glued set of tubes with an inner diameter of 3mm. The flow straightener is aimed to produce a homogeneous grid turbulence at the inlet flow of the annular gap. Also several distance spacers have been embedded in order to ensure concentricity. The dimensions and shape of the three spacer units may taken from figure 3.2a and 3.2b. In the absence of a flow straightener a swirl motion was found persisting throughout the whole mock-up. The same was detected in the experiment while omitting the spacers.

A more detailed description of the HYTAS facility, the used measurement techniques and the experimental series conducted for the MEGAPIE geometry may be taken from Knebel et al. (2002, 2003), Eiselt (2003) or Lefhalm et al. (2005). In the context of this report we restrict our discussion on the physical effects leading to the flow pattern appearing in the geometry at the nominal operation mode.

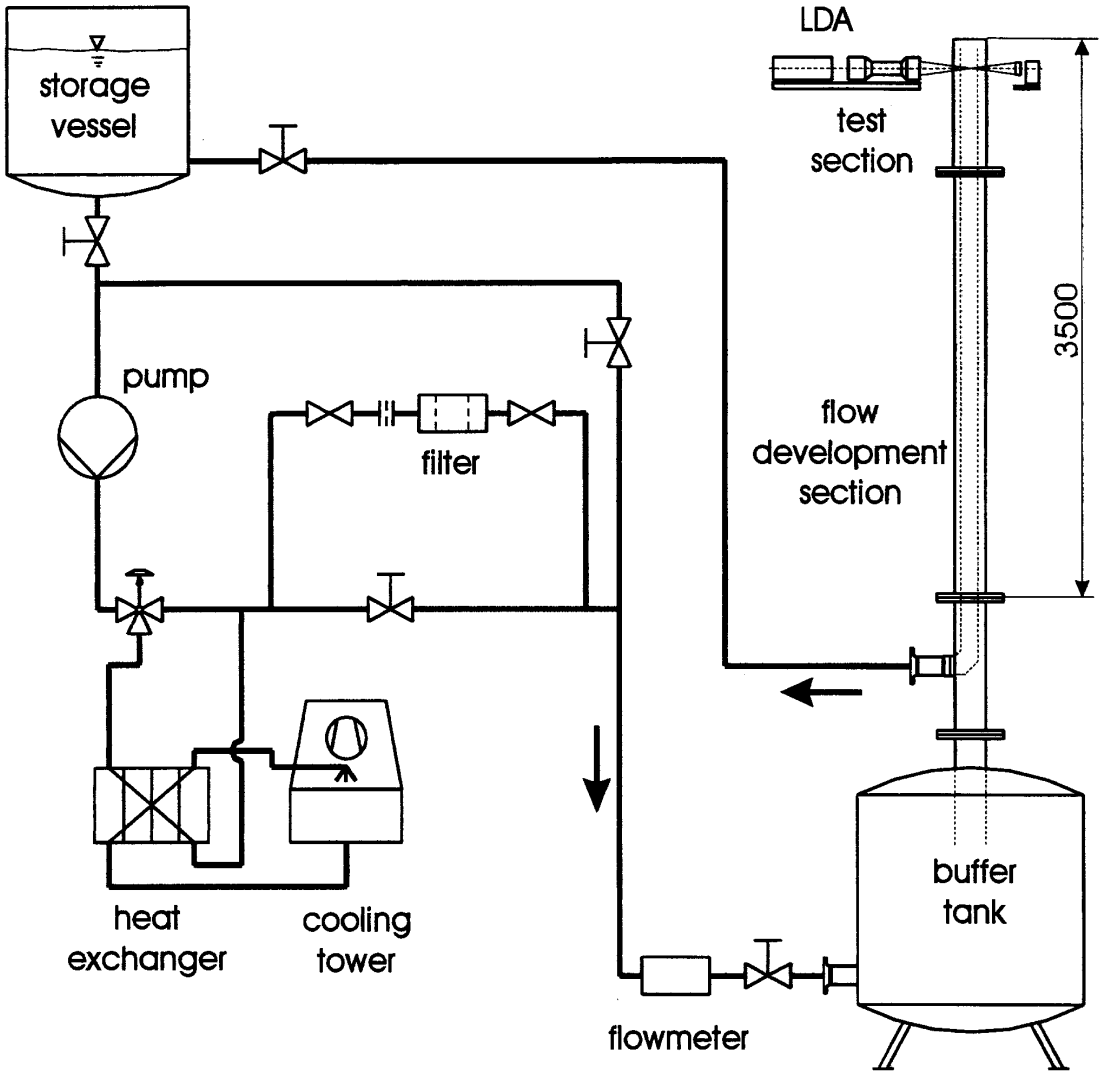

Figure 3.1: Sketch of the water test facility HYTAS aimed to investigate the isothermal momentum transfer of turbulent flow in target geometries.

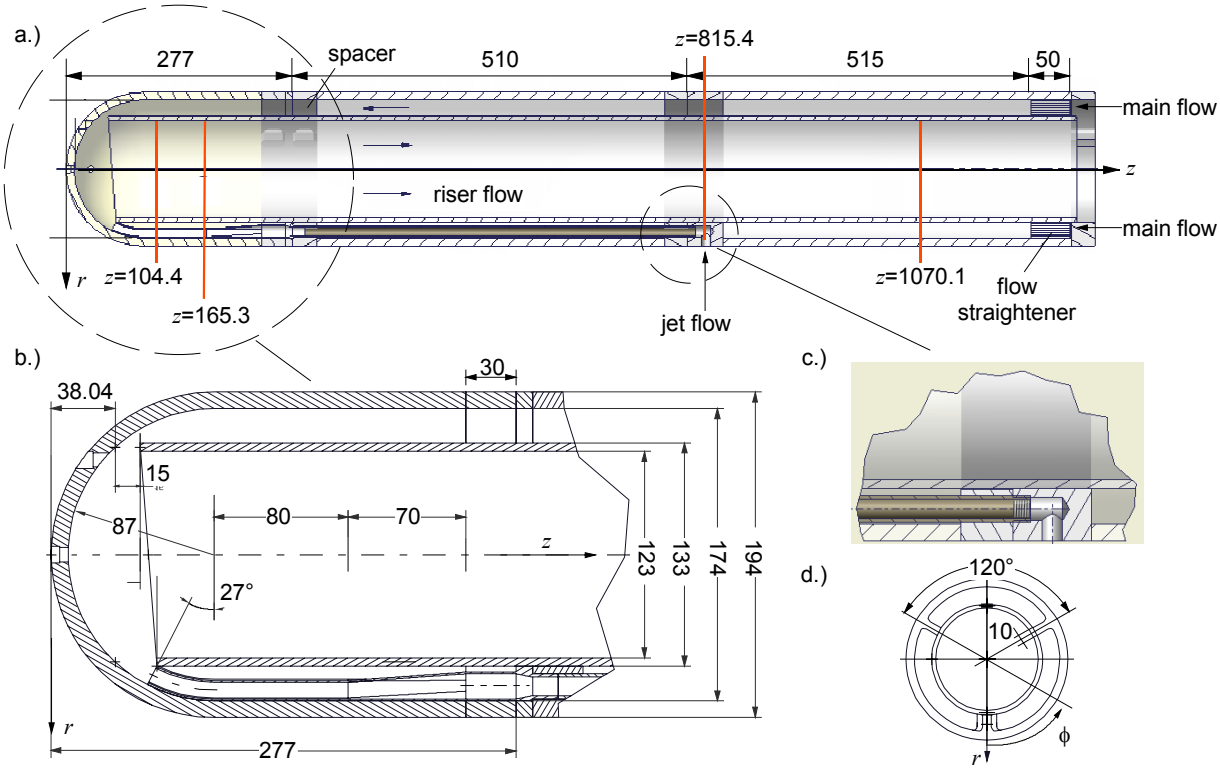

Figure 3.2: Geometry of the MEGAPIE-HYTAS water experiments and introduction of the coordinate system. a.) Length of the test section. b.) Detailed geometry close to the shell in the nozzle plane ϕ=0°-180°. c.) Inlet of the jet flow into the glass module. d.) Design and position of the spacers.

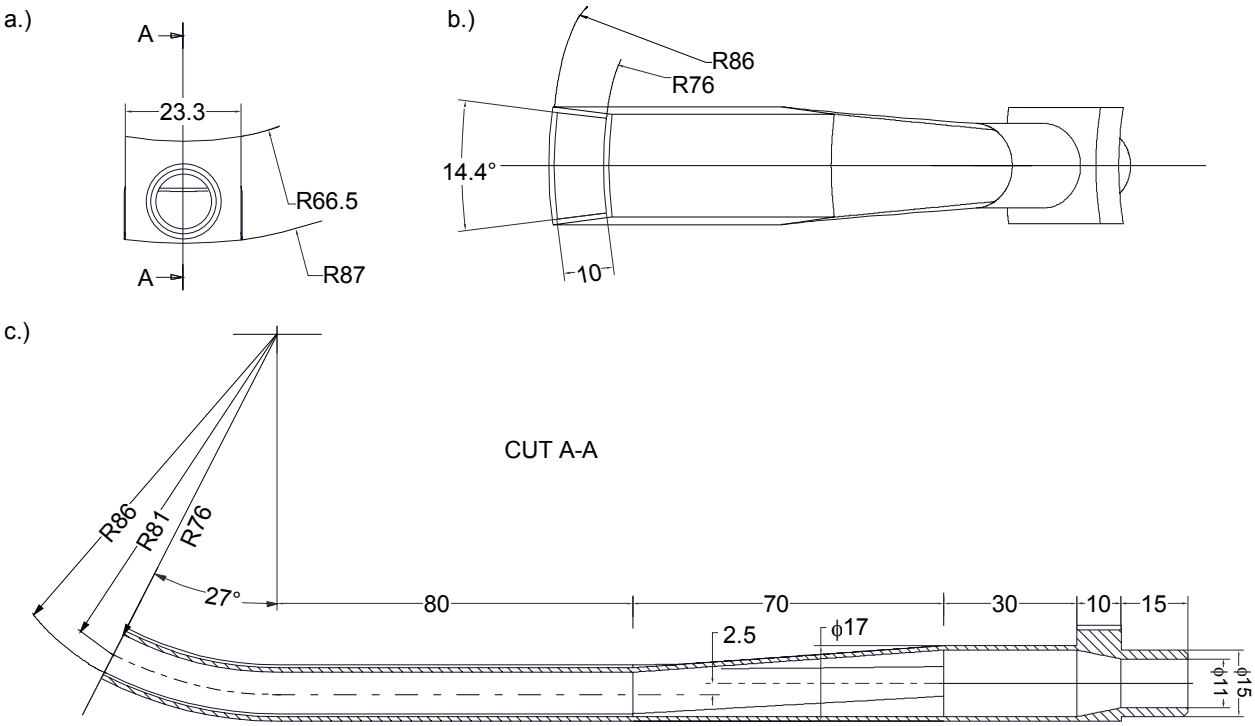

Figure 3.3: Details of the nozzle in the MEGAPIE HYTAS water experiment. a.) Front view of the nozzle. b.) Side view of the nozzle. c.) CUT A-A. All dimensions in mm.

3.2 Flow field without a jet flow

Let us consider in a first step investigate the flow in the MEGAPIE geometry without a bypass flow in two configurations. The first one is an axis-symmetric configuration with a planar riser tube end, see c.f. figure 3.4a, and the second one a configuration with a slanted riser tube as shown in figure 3.2a.

The flow pattern evolving in the axis-symmetric configuration at a hydraulic Reynolds number Re=5.4·10^4 is shown in the *L*aser-*L*ight-*S*heet-photographs (LLS) of the figures 3.4b (away from the beam window) and 3.4c close to the shell. The LLS-photography takes advantage of the light reflection of particles immersed in the fluid and transported with the flow. The illuminated regions exhibit then the streamlines of flow appearing in the geometry. Here the hydraulic Reynolds number of the gap is defined by

$$Re = \frac{\left(u_{main} \cdot s\right)}{\nu} \quad , \tag{3.1}$$

where u_{main} is the mean velocity in the gap, s the gap width and ν the kinematic viscosity.
Far away from the window in the annular gap the flow shows almost plane parallel streamlines indicating a fully developed inflow. In the upwards directed fluid flow of the riser tube, however, slightly inclined particle paths are observed. They may be due to an induced swirl flow by an non-perfect symmetrical set-up, see figure 3.4b. Another reason is that the upward flow in the riser tube is not fully developed only about six characteristic length after the u-turn at the lower end of the riser tube. The velocity fluctuations measured there are still about 20% and the velocity profile is still not developed, see Lefhalm et al. (2005).

The figure 3.4c illustrates the streamlines close to the shell. As the gap flow reaches the curved part of the shell it is accelerated because of the reduction of the cross-section. As the flow passes the lower edge of the riser tube the cross-section abruptly increases by 20%. This abrupt the cross-section increase at the lower end of the riser tube yields to a formation of a large scale toroidally shaped recirculation domain. The recirculation zone is characterized by a low mean velocity and it is attached to the inner side of the riser tube. Because of the simultaneous change of the flow direction at the edge of the riser tube, the recirculation area occupies most of the cross-sectional of the upwards directed flow. At the lower part of the shell the momentum of the main flow almost cancels out, and directly at z=r=0mm a stagnation point with zero velocity occurs. Adjacent to the stagnation point a region with reduced velocity is formed. Both the recirculation area in the riser tube and the reduced velocity close to the symmetry line at the bottom of the shell lead to an acceleration of the main flow in direction of the center axis of the pipe r=0mm, where a high velocity jet is formed. This jet flows upwards like in a chimney.

All measurements close to the shell exhibit a strongly time dependent flow. The velocity fluctuations observed up to a height z=200m reach values of order of the mean velocity in the riser tube.

In the MEGAPIE target as well as in the liquid metal experiment the riser tube is slanted with a minimum distance of the riser tube from the shell of 15mm at ϕ=180°). At ϕ=0°, where later the jet duct nozzle will be located, a maximal distance between shell and riser tube of 25mm exists.

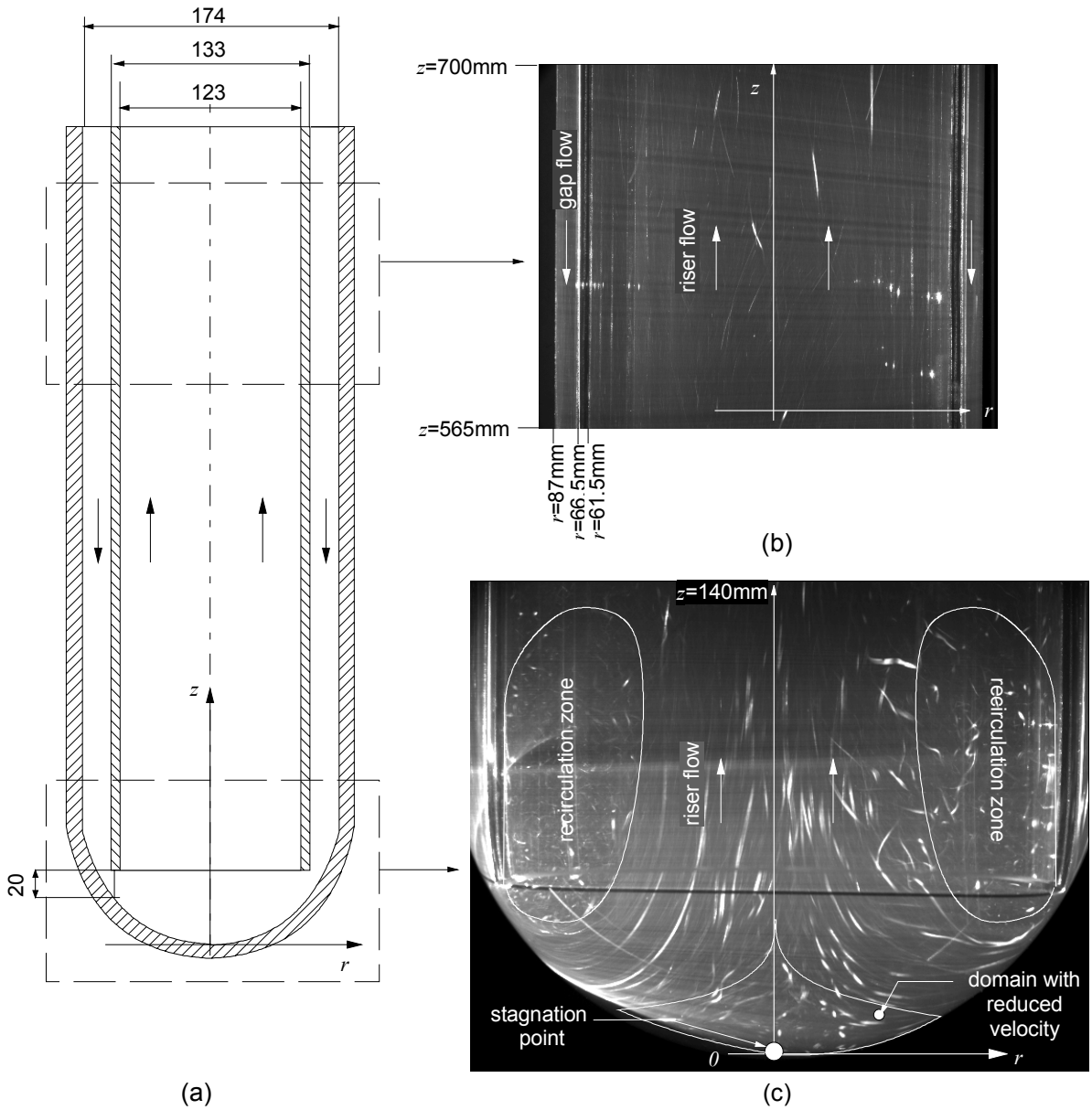

Figure 3.1: (a) Geometry of the MEGAPIE-HYTAS water experiment. (b) LLS-Photograph at the upper part of the beam window and (c) at the shell. In both graphs the Reynolds number is Re=5.4·10^4 and the illumination time is 196ms (from Eiselt 2003).

In the figure 3.5 the flow pattern establishing in the lower part of the shell at a hydraulic Reynolds number in the gap of Re=6·10^4 is shown in a LLS photograph. Overlayed to the light-sheet are the measured mean axial flow velocities (dark lines) at two discrete heights z=104.4mm and z=165.3mm on the line r-ϕ=180°. The distribution of the corresponding velocity fluctuations (RMS-values) on these lines are displayed brighter in the same graph. Both velocities and the fluctuations are normalized by the mean velocity in the individual domain, in order to get an insight on their magnitude.

The differences in the widths between the riser tube and the shell on the left and right hand side in figure 3.5 enforces differences in the related flow resistances. As a result the exit velocity and the corresponding mass flow rate from the gap is larger in the wider gap

than in the narrower gap. This means also that the momentum of the fluid coming from the wider gap is larger. As a consequence most of the rising fluid from the wider gap and redistributes towards the opposing inner wall of the riser tube. So, the flow separation at the lower inside of the riser tube is mainly formed on the side of the wide gap, but there it has a much larger extension than in the non-slanted case. On the side of the narrow gap only a small recirculation zone remains. In accordance with this asymmetry the stagnation point on the shell is displaced from its center position.

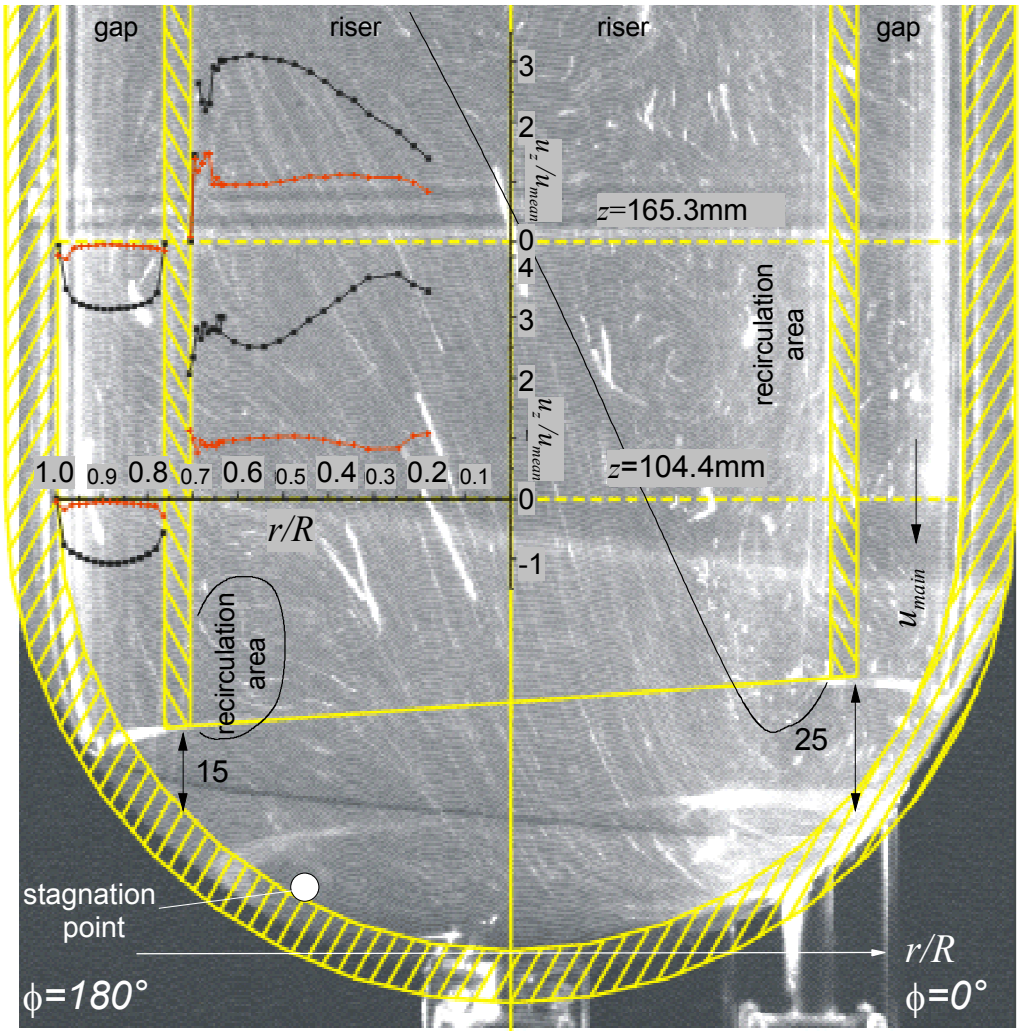

Figure 3.5: LLS-Photographs of the fluid flow in the MEGAPIE-HYTAS water experiment for a slanted riser tube. In both graphs the Reynolds number is Re=5.9·10^4 and the illumination time is 196ms. Overlayed to both graphs are measured normalized axial velocities (u_z/u_{mean}) and velocity fluctuations obtained using LDA at two discrete heights (z=104.4mm and z=165.3mm).

3.3 Flow field with a imposed jet flow

3.3.1 Similarity considerations for the mechanisms appearing with an imposed jet

Related to the jet flow let us first consider a case in which a jet flow is injected into the geometry while the main flow is at rest (u_{main}=0). If the jet is perfectly aligned with the hemispherical shell, it flows along the hemisphere. The dimensionless parameters describing the

problem are the jet Reynolds number Re_{jet} and the kinetic Froude number Fr_{kin}, which are defined as follows:

$$Re_{jet} = \frac{\left(u_{jet} \cdot d_h\right)}{\nu} \quad \text{and} \quad Fr_{kin} = \frac{\left(u_{jet}^2 - u_{main}^2\right)}{g \cdot d_{h,\,jet}} \quad , \tag{3.2}$$

with d_h the hydraulic diameter of the jet nozzle, u_{jet} the mean velocity of the jet, u_{main} the mean velocity of the main flow and g the gravity constant with g=9.81m/s^2. The hydraulic Reynolds number of both main and jet flow reaches in case of the MEGAPIE target values of the O(5·10^4-10^5) which corresponds to a highly turbulent flow. The other dimensionless number, the Froude number can be interpreted as force ratio of the inertial forces and the gravity forces. For the jet flow rates considered in MEGAPIE the kinetic Froude number reaches values of order O(1-10^1), which is not very large. For a parallel arrangement of jet and main flows at a Froude number of Fr_{kin}=20 the jet diameter grows linearly with the axial distance from its orifice and the axial velocity decreases rapidly as shown in the paper by Schneider (1985), by the experiments conducted by Ricoud and Spalding (1961) and later by articles of Zauner (1985) and Hussein et al. (1994). This is schematically illustrated in figure 3.6a. In a distance of 20 hydraulic diameters behind the nozzle exit the jet has transferred more than 80% of its momentum to the ambient flow. Due to the small difference of the Reynolds numbers of main and jet flow the shear rate between both main and jet flow is small and hence the turbulence production by this mechanism is insignificant. As a consequence the resulting vortices (with the vorticity ω), which rotate normal to the axial coordinate z, have a low intensity. The introduction of the jet flow into the geometry rather yields a change in the momentum field and generates another swirl in the riser tube, see Tak&Cheng (2001) or Roubin (2001-2003). Due to the conservation of vorticity (Helmholtz-vorticity theorem, see e.g. Lugt 1996) the swirl consists of a pair of counter-rotating vortices, which are sketched in figure 3.6b. An analysis of experimental results of the behavior of inertial jets at low Froude numbers shows that they are sensitive to their orientation see e.g. Ricoud and Spalding (1961). Thus, in a complex geometry as considered here, several flow patterns may evolve by varying the individual flow rates.

However, if the jet flow is not perfect tangentially aligned with the hemispherical shell and contains a wall normal component expressed by an angle α the jet can hit the hemispherically shaped wall and can, by its momentum, detach from it again. Such situations may occur due to the non-perfect nozzle shape or a differential elongation of the jet pipe versus the riser tube. Also a large main flow rate may cause by its momentum and pressure distribution a detachment of the jet after a short distance behind the nozzle. The potential streamline of such non perfect alignment is graphically sketched in figure 3.6c. The momentum transfer of the jet flow towards the ambient fluid remains at large axial coordinates z essentially similar to the case considered in figure 3.6a, if the main flow is at rest. Close to the lowest point of the shell, however, the detachment of the jet from the wall induces a secondary flow, for which the vorticity vector is of opposite sign of the upper one. This recirculation area is accompanied by rather small velocities and is therefore not acceptable for an adequate window cooling.

In a next step let us assume that the main flow is not at rest. We now superimpose the effects found in figure 3.5 with the considerations performed in figures 3.6a-3.6c. The flows evolving due to the interaction of the main flow with the jet flow are sketched schematically in figure 3.6d. Due to slanted riser tube the main flow still forms the recirculation area

(a) and a large portion of the fluid is distributed towards the opposing side of the riser tube in form of a large scale jet (c). The injection of the jet flow at ϕ=0° yields to a stronger momentum in opposite direction of the nozzle exit. Thus the recirculation area in the riser tube increases. The jet flow also leads to a further shift of the stagnation point from the center and it will almost disappear from the hemispherical part of the shell if the jet flow is tangentially aligned with the shell. If this is not the case and the jet has a wall normal component a vortex as denoted in figure 3.6c will appear. The momentum difference between main flow and jet flow induces counter-current rotating vortices (b), which are also found in the simulation by Roubin (2002). The vortices (b) will be transported by the main flow spirally upwards. Due to the interaction of the main flow with the jet flow close to the wall a horse-shoe vortex establishes, which yields to the formation of the vortex pair (d).

Of course, the described pattern is idealized and it assumes a symmetry in the r-z-ϕ=0°plane. If the geometry is slightly asymmetric an additional global swirl motion will be introduced, which is then superimposed to all other phenomena.

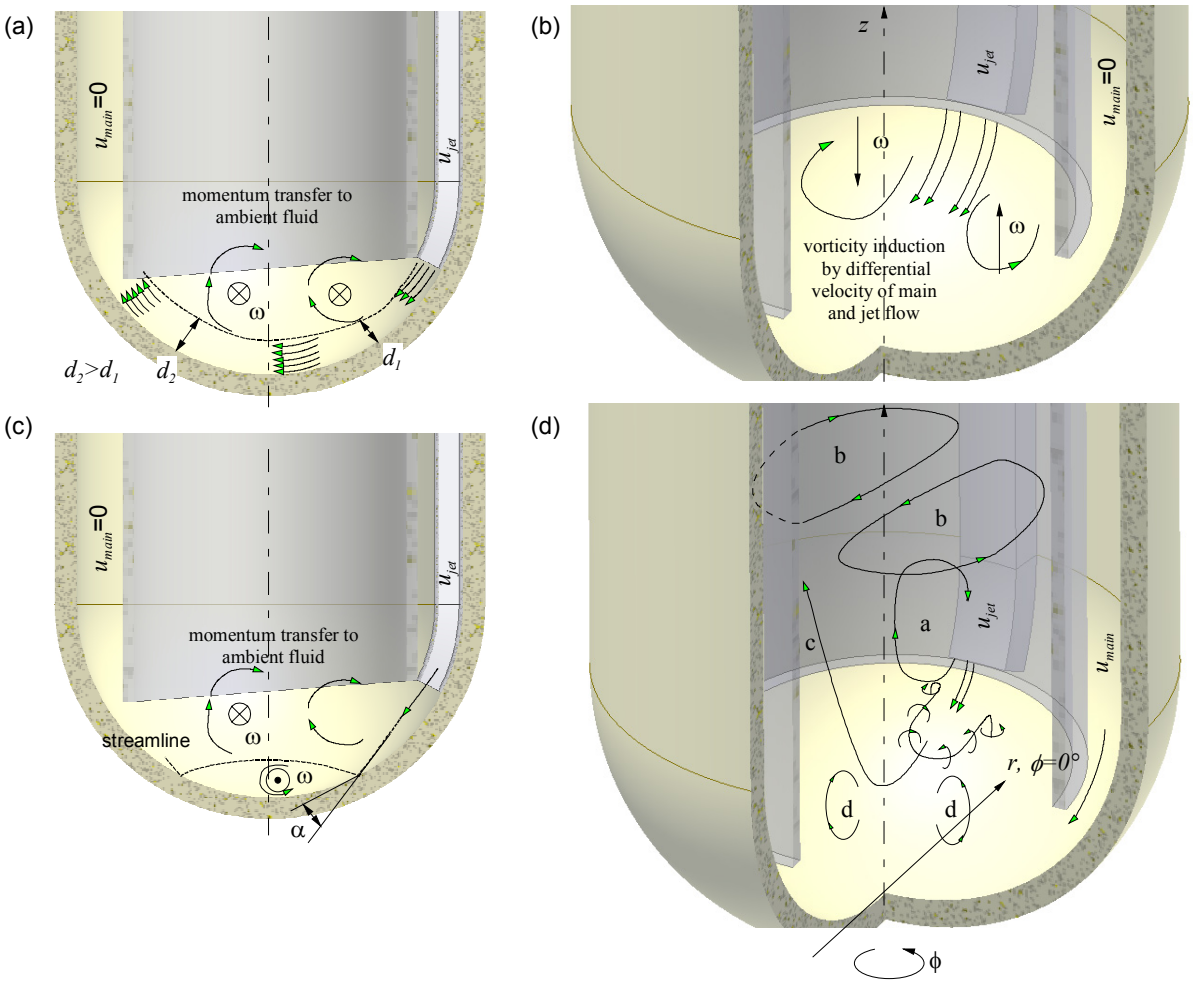

Figure 3.6: (a) –(c) main flow considered to be at rest. (a) Increase of jet thickness along the flow path and induction of secondary flow. (b) Vorticity generation in z-direction due to differential velocity. (c) Streamline of jet flow not aligned with the shell and additional vorticity induction. (d) Interaction of main and jet flow forming several flow paths.

3.3.2 Water experiment with an imposed jet

The water experiment with the slanted riser tube was repeated with the MEGAPIE-HYTAS mock-up with an additional jet flow. Due to the large possibilities of flow rate ratio combinations of main to jet flow we restrict our discussion on the nominal flow rate ratio combination of the MEGAPIE target, in which the flow rate of main to jet flow is 15:1.

The figures 3.7 show LLS-photographs of the flow pattern observed in the lower shell at several positions for this flow rate ratio in the plane ϕ=0°-180°. Here, again the illuminated regions exhibit the streamlines of flow.

As figure 3.7a shows again a large scale recirculation zone is formed in the riser tube for ϕ=0°. Because of the combined momentum of main and jet flow in this plane the recirculation area is larger than in the slanted riser tube case without bypass. Its radial extension grows in the lower part almost linearly with z. The combined momentum of jet and main flow also leads to a stronger deflection of the main part of the fluid flow towards the riser tube side opposite the nozzle exit. Here, an area with a high velocity jet is observed. At the boundary between the recirculation domain and high velocity region a set of counter-rotating vortices is visible, see figure 3.7b. The introduction of the jet extinguishes the small reciruclation area close to the inner side of the riser tube at ϕ=180° totally. Due to the jet flow the stagnation point is shifted further to the opposite side of the nozzle. It is approximately located at r=55mm, ϕ=180° (compared to r=42mm, ϕ=180° in the slanted case without bypass).

A closer view on the light-sheet shows a peculiar feature of this flow rate combination with respect to the MEGAPIE application. The streamline in figure 3.7d shows that the jet hits the wall close to the centerline at about $r\approx$20mm, ϕ=0° and then detaches from the wall. However, in this part of the window the highest surface heat flux appears and thus requires the best heat transfer characteristics. A part of the jet re-hits the hemispherical shell again for $r\approx$30mm, ϕ=180°.

The figure 3.7 illustrates the flow pattern further downstream in the riser tube. In contrast to the case without jet flow the intensity of the individual vortex structures at the same z-coordinated is stronger. Quantitative measurements performed using LDA and *u*ltra-sound *d*oppler *v*elocimetry (UDV) shows that both the intensity of the upwards directed high velocity jet and the fluctuation intensity is higher than in the configuration without jet, see Lefhalm et al. (2005).

The flow pattern establishing in the plane perpendicular to the nozzle for Q_{main}/Q_{jet}=15 at ϕ=90°-270° is illustrated in the figure 3.8. Close to the centerline the detachment of the jet flow is visible. Due to the interaction of the jet flow with main flow a secondary flow is induced, which is expressed by two counter-rotating vortices. These vortices are of the size of the riser radius. The flow pattern observed in this plane is more or less symmetric. Quantitative measurements confirmed this observation.

The nominal operation mode with a flow rate ratio of Q_{main}/Q_{jet}=15 exhibited for all Reynolds numbers investigated a strongly time dependent behavior in the lower shell and the fluctuation intensities recorded were of the order of the mean velocity. Compared to the case with-

out jet flow the configuration with jet flow revealed approximately the same turbulence level in the lower shell.

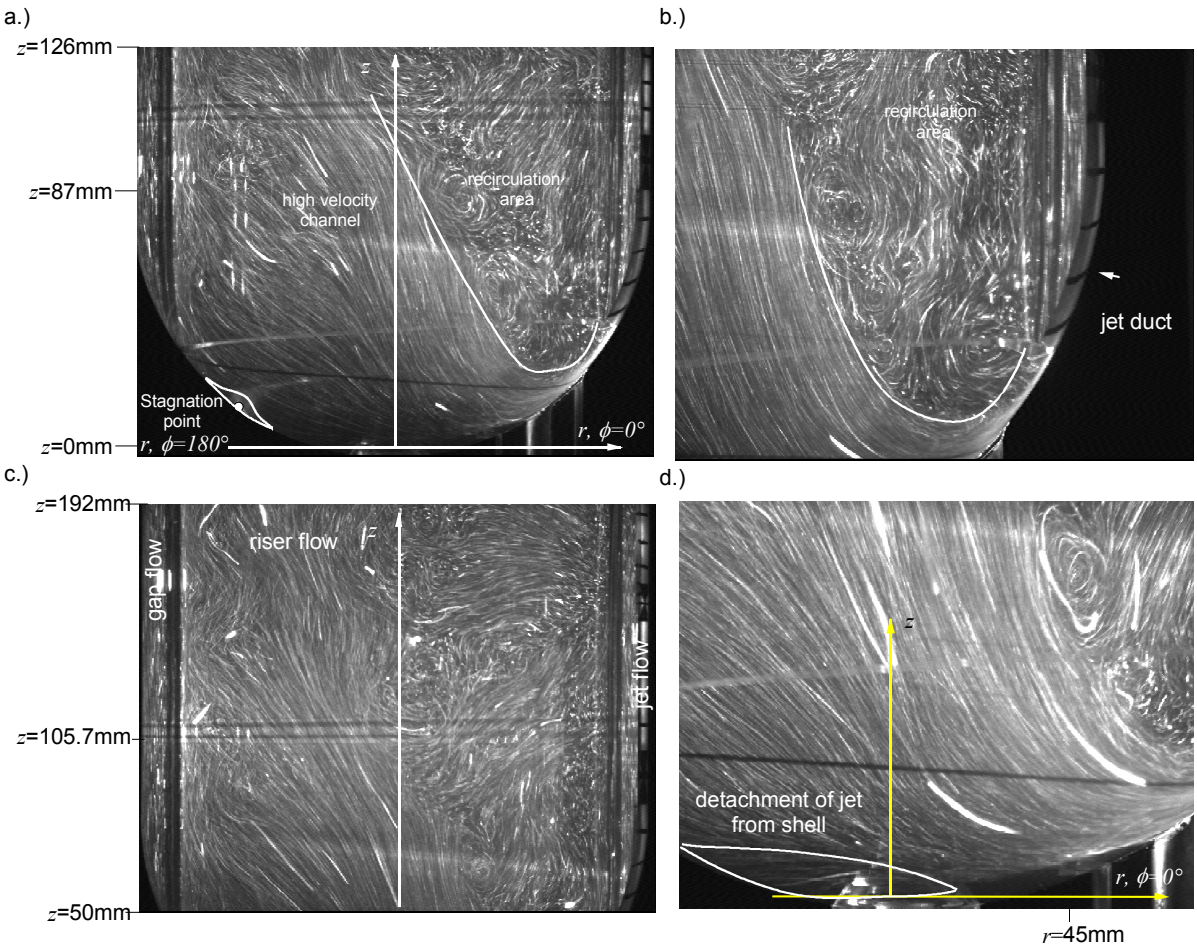

Figure 3.7: LLS-Photographs of the fluid flow in the MEGAPIE-HYTAS water experiment for a slanted riser tube with a jet flow Q_{main}/Q_{jet}=15 for ϕ=0°-180°. In all graphs the Reynolds number of the main flow in the gap is Re_{main}=5.9·10^4 and the illumination time is 196ms. a.) Lower shell with different flow regions; b.) close view on the jet flow exiting the nozzle and the adjacent riser flow; c.) flow pattern in gap and riser at higher z-coordinates and d.) close-up of the streamlines at the shells center.

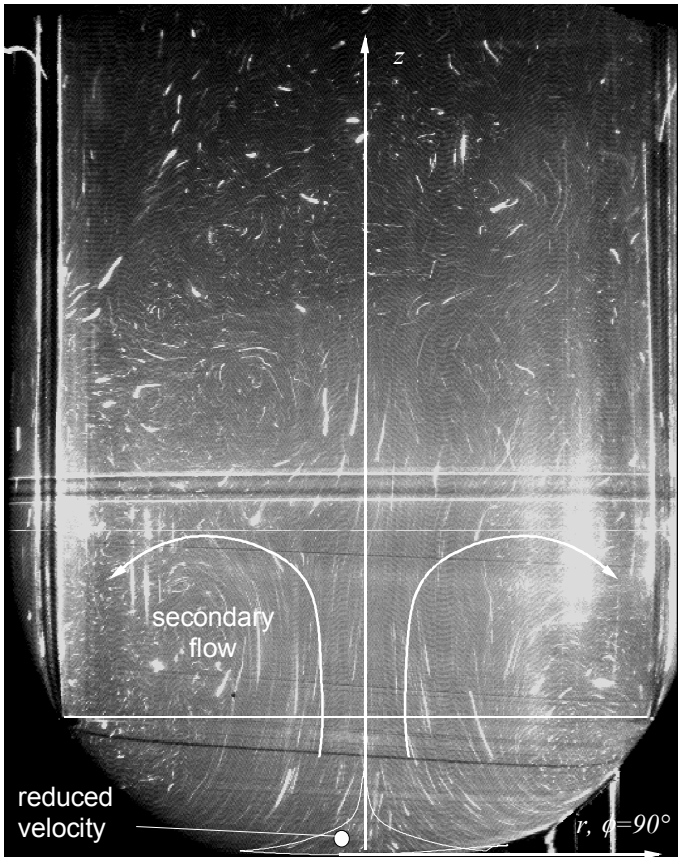

Figure 3.8: LLS-Photographs of the fluid flow in the MEGAPIE-HYTAS water experiment for a slanted riser tube with a jet flow Q_{main}/Q_{jet}=15 for ϕ=90°-270°. In all graphs the Reynolds number of the main flow in the gap is Re_{main}=5.9·10^4 and the illumination time is 196ms.

4 Experimental set-up of the PbBi experiment

4.1 The PbBi heated jet experiment in the KALLA THEADES loop

4.1.1 The THEADES loop

The Lead-Bismut loop THEADES (THErmalhydraulics and Ads DESign) is part of the KALLA laboratory at the Forschungszentrum Karlsruhe. It concentrates on thermalhydraulic single-effect investigations of ADS reactor like components which are of vital importance for the design work of a future ADS development and are funded in context of the EU-framework programs and national research programs. It serves also as an experimental platform for LBE experiments in the sense of an open user lab. The THEADES loop, in which the Heated Jet experiment is installed, is entirely fabricated of stainless steel (DIN 1.4571) and has been set into operation in November 2002. The main features of the THEADES loop are:

- temperature operating range 180- 400°C
- temperature stability ±0.1°K (at 195°C)
- maximum flow rate 47m³/h (at 5.9 bar)
- flow rate regulation ±0.1 m³/h

- max. pressure head 6.3bar
- max. installed electric power 2500 kW
- heat losses to ambient at 200°C 9 kW
- heat losses to ambient at 300°C 14.5 kW
- number of test sections 4
- inner diameter of connection piping 107mm
- max. test section length 3405mm
- oxygen control system (OCS) yes
- liquid metal inventory 4000litres (stored in sump tank)
- heavy liquid metal $Pb^{45}Bi^{55}$
- max. Reynolds number in the loop $9\ 10^5$
- Prandt number range 0.012-0.032

The pump and the loop characteristics of the THEADES loop are displayed in figure 4.1a. A three-dimensional flow scheme of the THEADES loop shows figure 4.1b. More detailed information about the KALLA laboratory and the THEADES loop may be taken from Knebel et al. (2002, 2003).

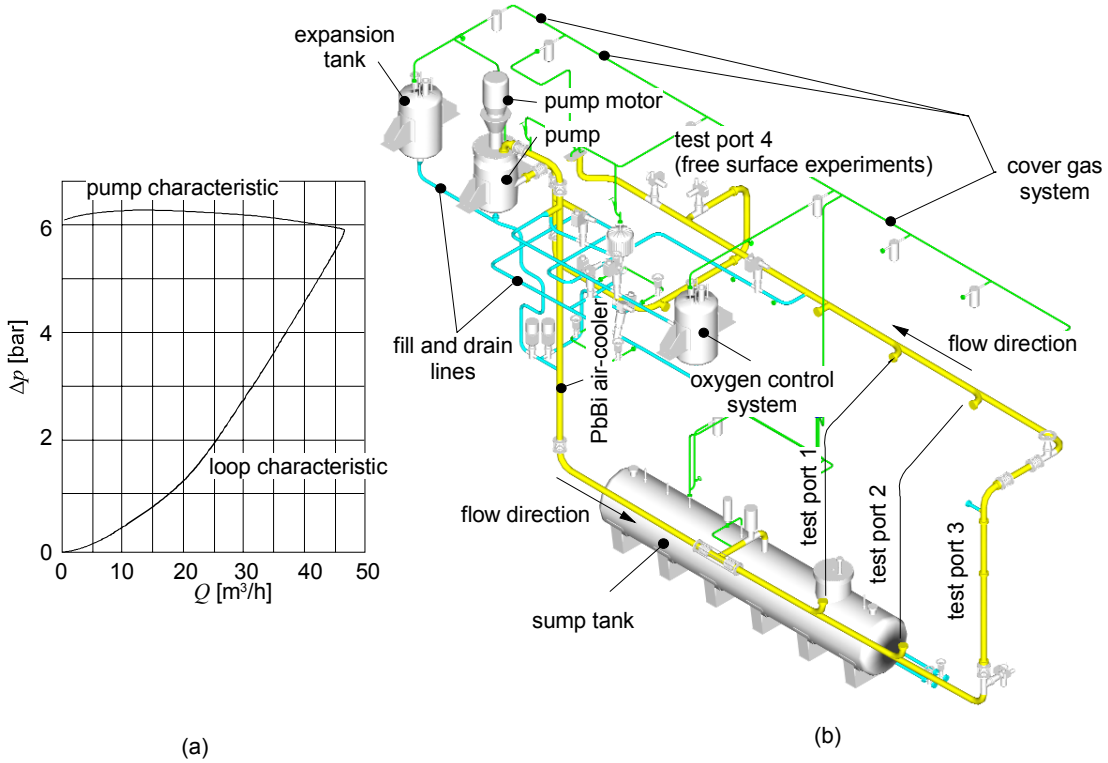

Figure 4.1: a.) Pump characteristics of the main pump in the THEADES loop. Here the flow rate Q [m^3/h] is shown as a function of the attained pressure head Δp [bar]. b.) Three-dimensional sketch of the flow scheme and the main components of the THEADES loop in KALLA.

4.1.2 The measurement devices at THEADES

The liquid metal experiment is embedded in the test ports 1, 2 and 3 of the THEADES loop. A detailed dimensional sketch of the location of the test module within the loop is de-

picted in figure 4.2. The main flow into the test module is guided via the test port 1. Centered over test port 2 the test module is located. The piping to test port 3 enters a electric heater, providing the heat source of the heated jet experiment. From there the jet flow is entering via the regulation valve V2.10 the bypass line into the test module.

Of crucial importance during the tests is the monitoring of the global flow parameters like the temperatures within the liquid and at the outside of the insulation as well as the pressures and the flow rates in the individual branches. This is necessary in order to get an assessment about the quality of the measurements. The figure 4.2 shows the location of the individual flow rate measurement devices used in the heated jet experiment. They are arranged in such a way that the flow rate in each of the branches can be detected using two physically different sensing methods to exclude systematic errors.

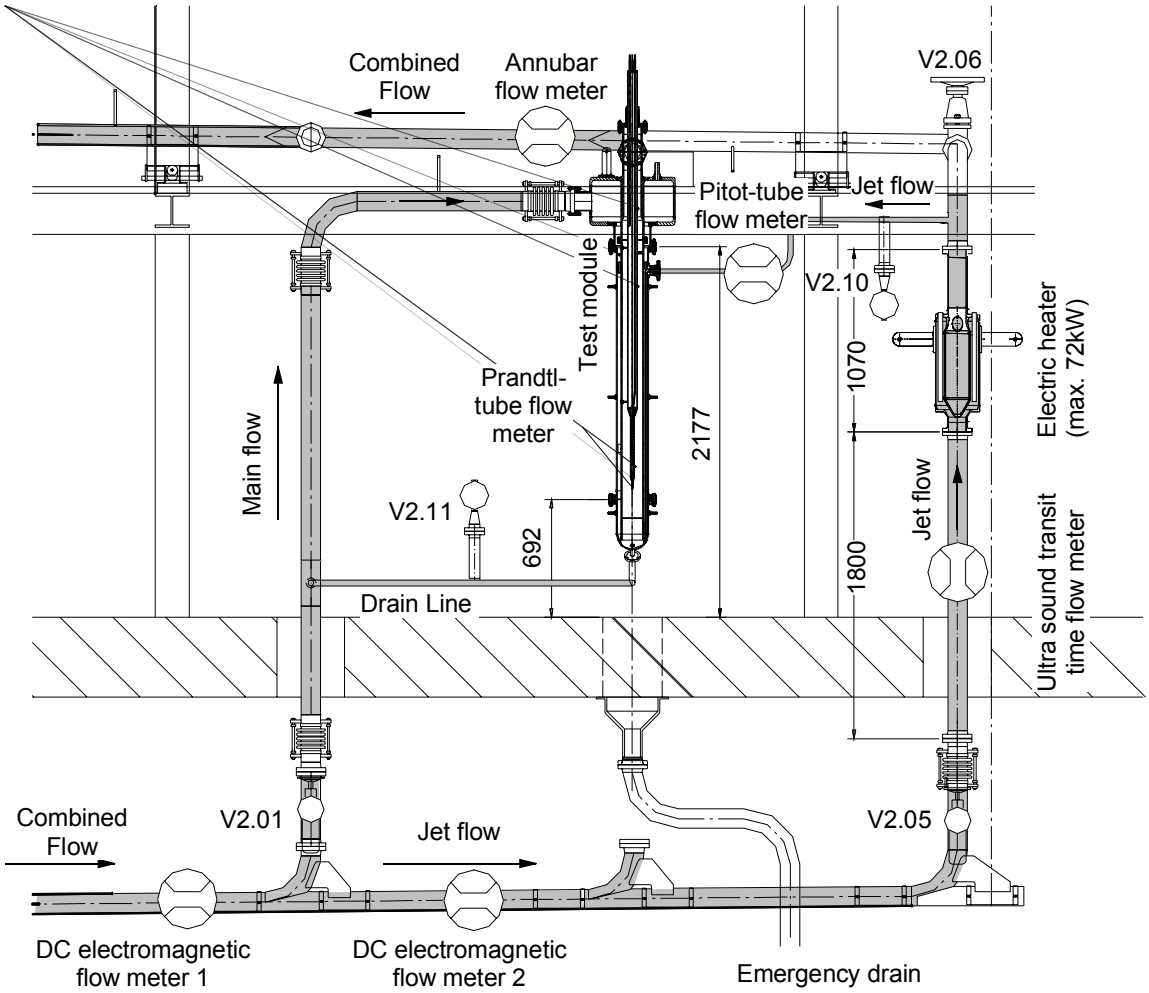

Figure 4.2: Detailed arrangement of the Heated Jet Experiment in the THEADES loop of KALLA and location of the measurement components.

The flow meters applied are:

- two DC electromagnetic flow meters (*DC-EM*),
- an ultra-sound transit time flow meter (*UTT*),
- an Annubar obstacle flow meter,
- a Pitot and a Prandtl tube.

All flow meters are calibrated against each other at different temperature levels from 220° to 370°C, so that errors due to temperature shifts or density changes can be corrected. Using this procedure the error of the DC –EM flow meters due to changes of the temperature and because of varying oxygen content could be reduced to less than ±1%.

The theory of DC electromagnetic flow measurement is described in detailed in the monographs of Shercliff (1962, 1987), however, for the application of this method in the lead bismuth eutectics (LBE) flows the obtained measurement signal depends additionally on the oxygen content of the fluid and on the electro-chemical wetting of the fluid with the steel duct, see e.g. Knebel et al. (2003) or Lefhalm (2005). Therefore, the oxygen content within the loop was kept at a constant value for the different temperature levels investigated. In order to resolve the wetting problem the temperature during a measuring day was kept constant in the feeding line and the flow meters were calibrated before starting the measurement and at the end of the same day.

The flow rate of the jet can be extremely small, so that three different methods are applied to determine it accurately. One is the ultrasonic transit-time method (UTT). In this method the transit-time of an ultrasonic wave travelling in form of a longitudinal wave through the medium is recorded. Upstream and downstream sensors are located at opposite sides of the pipe detecting the time difference between the two signals. The result is the mean flow velocity; a more detailed description may be taken from Lefhalm (2003) and Panametrics (2001). In figure 4.3 the operation principle is sketched. A longitudinal wave is emitted by the emitter E over the length L and detected at the sensor S. If both emitter and sensor are bi-functional (so that both of them can act as emitter ***and*** sensor) one can measure the time difference Δt between the upstream and downstream traveling time of the wave. From equation 4.1 the mean velocity u_0 can be calculated.

$$u_0 = \frac{c^2}{2L\cos\alpha}\Delta t, \tag{4.1}$$

where α is the inclination angle of the sound beam with respect to the flow.

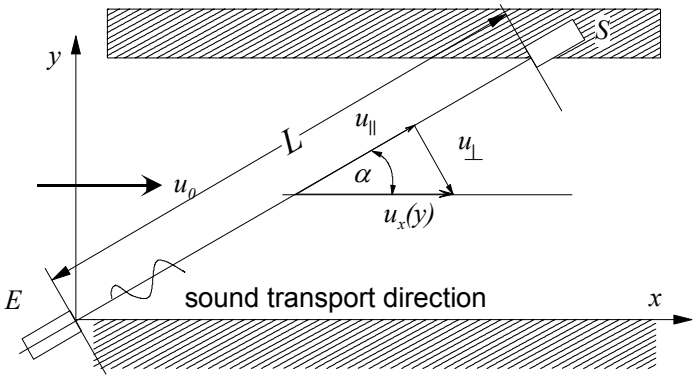

Figure 4.3: Operation principle of the ultra sound transit time flow meter (UTT) and the related signal path.

As an example for PbBi at 300°C the sound speed c is 1.6 10^3m/s. In order to detect mean velocities of 0.01m/s over a length of L=107.2mm (as the inner diameter of the pipe tubes of the THEADES loop) a time difference of Δt =6 10^{-10}s=0.6ns has to be resolved by the data

acquisition system (DAS). This time delay is about six times larger than the resolution time of the DAS. Thus, the flow rate resolution of the Ultra-Sound transit time flow meter (*UTT*) in the THEADES loop amounts to about ±0.054m^3/h for the jet flow. For the smallest jet flow rates investigated Q_{jet}=0.8m^3/h the error is then ±6.75% for the *UTT* method and it shrinks to ±3.29% for the largest jet flow rates.

The Pitot and Prandtl tubes used in the set-up rely on the measurement of pressures. By means of positioning the tube as depicted in figures 4.4a, b in the flow the total pressure p_0 can be measured by equation 4.2a. In case of using a Prandtl tube to determine the mean velocity it is essential to keep the liquid containing measurement pipes through the pressure gauge at constant and equal temperatures in order to avoid pressure corrections (see eq. 4.2b).

$$p_0 = p_1 + \rho_{meas}\, g\, h, \qquad p_{dyn} = \frac{\rho}{2} u_0^2 = \rho(T_1)\, g\, h \quad + \rho(T_2) g\, h \quad , \tag{4.2a,b}$$

where p_0 is the absolute outer pressure and ρ_{meas} the density of the fluid. Using Pitot tubes an absolute pressure transducer is connected at the end of the line so that p_1 is given for u=0. The dynamic pressure p_{dyn} can be calculated from the difference of the total pressure p_0 and the static pressure p_{stat} using a Prandtl tube. By measuring p_{dyn}=p_0-p_{stat} = $\rho_{meas}gh$. Finally, the local velocity *u(z)* can be calculated using equation 4.3:

$$u(z) = \sqrt{\frac{2 p_{dyn}}{\rho_{meas}}}, \tag{4.3}$$

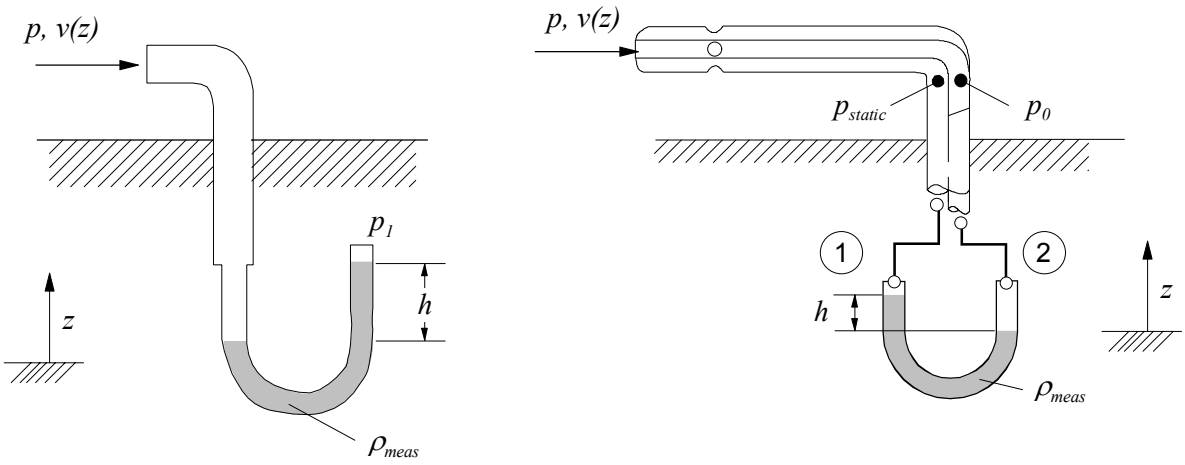

(a) (b)

Figure 4.4: Local flow velocity measurements using Pitot (a) and Prandtl tubes (b).

When using Pitot-tubes as flow rate measurement devices, at least two-sensors have to be located within the tube according to ISO3966-1977. Since the velocity profile varies as a function of dimensionless radius *r/D* the Pitot tubes have to be placed in such positions where this deviation is minimal. In figure 4.5a the dimensionless velocity is depicted as a function of the radius, see VDI (2001). It shows that at *r/D*=0.381 in a Reynolds number range *Re*=4·10^3-3.2·10^6 the deviation is less than 3%. Here, the hydraulic Reynolds number is formulated in the classical way with

$$Re = \frac{u_0 \cdot d}{\nu}, \tag{4.4}$$

where u_0 is the mean velocity, d the duct diameter and ν the kinematic viscosity in [m^2/s]. In the jet flow duct, owing an inner diameter of d=27.3mm, the flow rates during the experiment vary from 0.2m^3/h to 2m^3/h corresponding to Reynolds numbers from $1.6 \cdot 10^4$ to $1.6 \cdot 10^5$. In the considered Reynolds number range the systematic error shrinks down to ±0.95%. Another error source while using Pitot tube flow meters is that they require a developing length of at least 25 tube diameters downstream a 90° bend. For developing lengths of more than 35 characteristic diameters the systematic error is minimized to less than ±0.5%. The configuration of the Pitot-tubes in the heated jet experiment is depicted in figure 4.5b. In order to account for eventual asymmetries two bores are integrated in the Pitot tube which integrate the pressure at this position. The resolution of the Pitot flow rate measurement technique is given by the resolution of the used pressure gauges, a proper filling of the connected piping and a simultaneous temperature measurement to account for density changes. In case of the Pitot tube flow meter a differential pressure gauge from the company Rosemount (2003) is used which is based on a capacitive sensor using a transmission fluid.

The transducer is capable to resolve pressure differences with an accuracy of ±0.075% of the maximal span, which can be stepless adjusted via a remote control. During the experiments a span of 0-62mbar has been chosen, so that pressures of ±4.65Pascal can be resolved. Related to the duct dimensions the uncertainty of the flow rate measurement is at a mean temperature of T=360°C for the bypass flow ΔV=±0.03m^3/h. Summing up the systematic error of the Pitot technique and the resolution of the pressure gauges the total measuring error for the bypass system is at the lowest jet flow rate investigated (V=0.8m^3/h) ΔV=±0.037m^3/h and at the highest investigated (V=2m^3/h) ΔV=±0.059m^3/h, corresponding to an error of 4.6% and 2.95%.

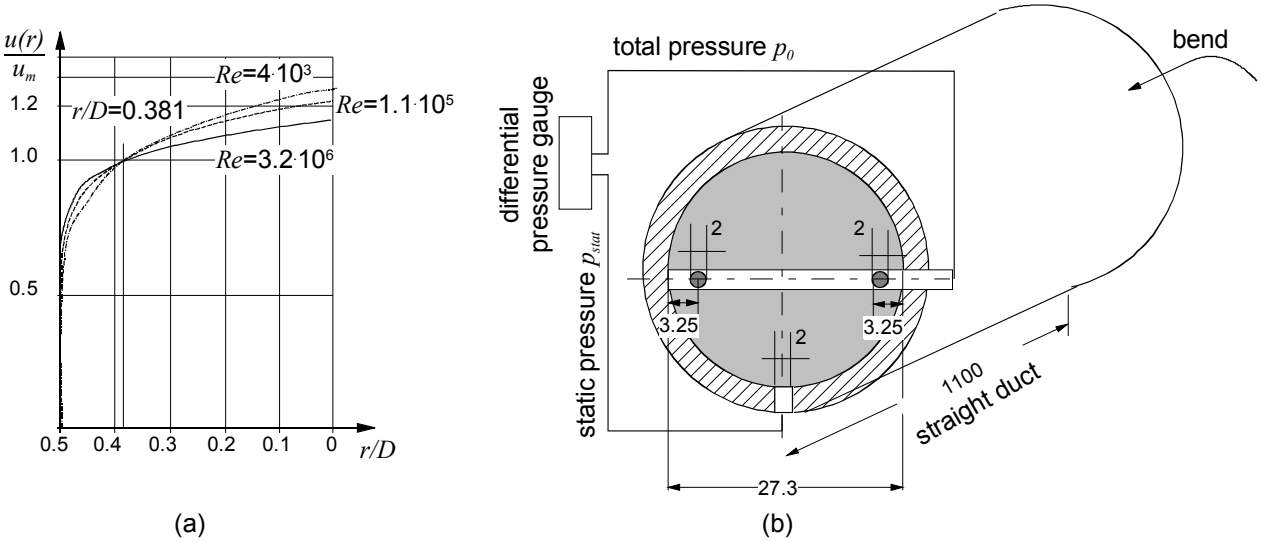

(a) (b)

Figure 4.5: (a) Local axial velocity normalized by the mean velocity as a function of the dimensionless radius r/D at different Reynolds numbers Re, see VDI (2001). (b) Schematic set-up of the Pitot-tube flow meter configuration in the channel providing the jet flow. The dimensions are given in millimeters.

In order to measure pressure losses at individual locations of the THEADES loop absolute pressure gauges from Kulite (2003) are used. These are piezoresistive silicon transducers, which are relatively small and can be screwed directly in any pressure tap of the pip-

ing. The measurement principle is based on a fast Wheatstone bridge in an integrated circuit. Due to their small dimensions they have a negligible inertia and hence allow a high frequency resolution of pressure fluctuations of the order of several hundred KHz. Because of the fabrication principle the maximal span is given and a calibration before each experimental run must be performed. Then, the pressure resolution is similar to that of the capacitive units.

The Prandtl –tube flow meter used for the measurement of the combined flow (jet and main flow) uses differential pressure gauges from Rosemount. Within the heated jet experiment the Kulite pressure transducers are able to resolve a local velocity with an accuracy of ±2.5mm/s corresponding to a flow rate of ΔV=±0.11m^3/h. The photograph in figure 4.6a shows the used Prandtl-tube, which is installed at the bottom of the instrumentation rod. The pressure tubes of both orifices of the sensor are arranged vertical and welded on the top to the instrumentation rod. The pressure measurement tubes guided to the sensors are shown in photograph 4.6b. There also the housing tubes of the thermocouples which are installed at the inner side of the riser tube and on the instrumentation rod are illustrated.

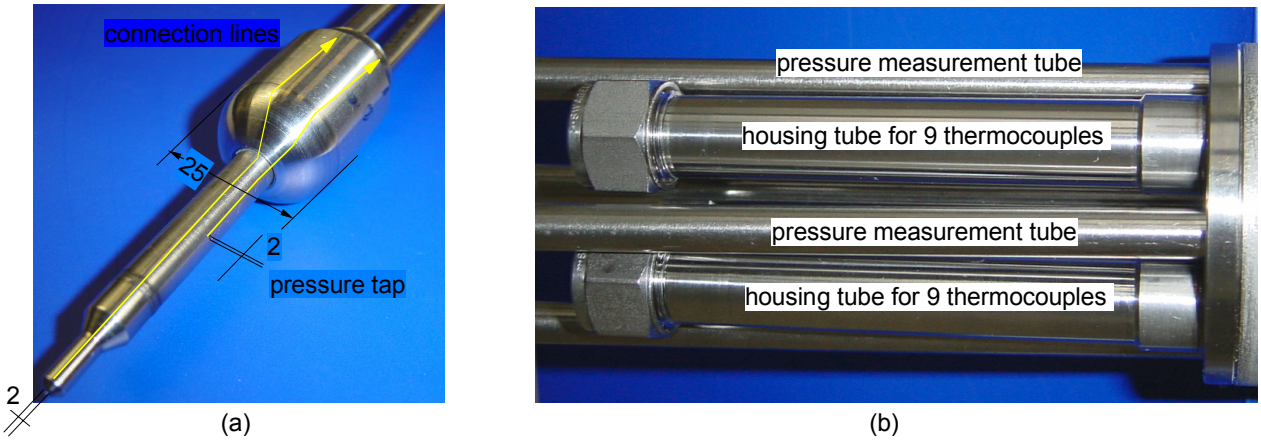

Figure 4.6: (a) Tip of the Prandtl-tube at the lower end of the instrumentation rod; dimensions in [mm]. (b) Connection tubes containing the thermocouples and pressure tubes of the Prandtl sensor which are located at the top of the instrumentation rod.

At the outlet of the experimental mock-up the combined flow is measured using an Annubar sensor which is based on a pressure difference measurement across an obstacle placed in the duct. Of course, using this measurement technology some constraints regarding the inlet conditions exist. The flow facing the cylindrical obstacle has to be fully developed in the sense that no lateral pressure gradients appear and the axial derivatives in flow direction are zero. This leads for turbulent flows immediately to a required developing length of at least 30 hydraulic diameters upstream in the pipe. A technical feasible solution to overcome this long developing length, which is for the Annubar sensor (a tube with 60 mm inner diameter) about 1.8m, is the reduction of the diameter and the installation of a flow straightener, which equalizes the flow. The pressure difference measurement method of the Annubar sensor takes advantage of the fact that the pressure loss of the flow around an arbitrary symmetric obstacle expressed in terms of a c_W value is at Reynolds numbers of $Re \geq 5\ 10^3$ independ-

ent of the Reynolds number. The mean velocity u_0 and hence the flow rate can be calculated using equation 2.5.

$$u_0 = \sqrt{\frac{2\,\Delta p}{\rho\, c_W}} \quad . \tag{4.5}$$

The ideal c_W values may be taken from Beitz and Küttner (1986) or other standard handbooks. In reality, however, the device has to be calibrated. The independence of the c_W values from the Reynolds number holds up to Re~5 10^5. In order to measure small velocities and to calibrate both techniques against each pressure transducers resolving smallest pressure differences are required. Here, the used pressure transducers are capable in resolving an absolute pressure of 12.5 Pascal. Thus, the minimal velocity to be resolved by the pressure difference method is a mean velocity of v_0=0.05m/s corresponding to maximum error of the flow rate of ΔV=±0.55m^3/h. The used Annubar sensor, the flow straigthener and the pressure connection are displayed in the photographs 4.7a-c. All pressure measurement based flow meters (Pitot, Prandtl and Annubar sensors) require a completely filled pressure line in order to avoid long response times or misreadings. Thus, all pressure lines own a closeable valve (see figure 4.8) with which each of the lines can be purged separately. The purge procedure is performed opening one valve, through which the fluid flows to the O_2-control container of the THEADES loop. If a closed liquid metal jet is observed through a glass window, a proper filling can be assumed.

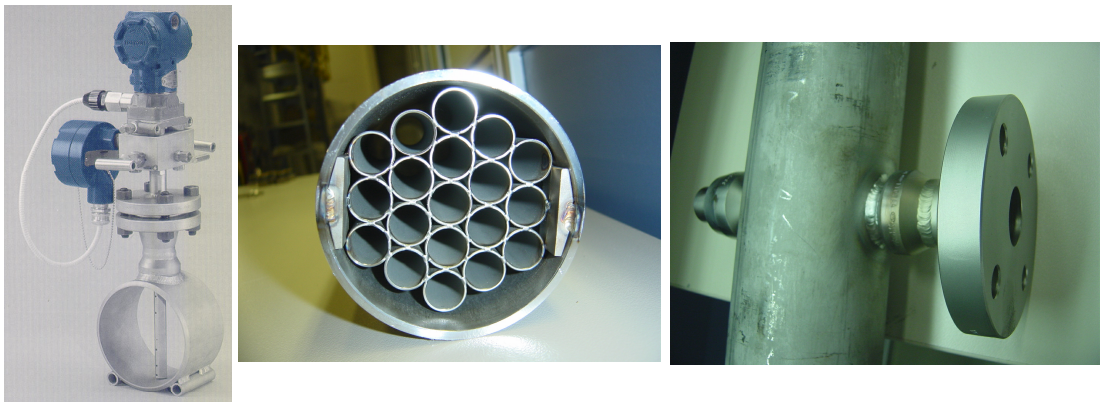

(a) (b) (c)

Figure 4.7: (a) Annubar flow meter as it is used in the heated jet experiment. (b) Flow straightener installed upstream the flow meter. (c) Flange for insertion of cylinder and pressure taps.

In order to generate a temperature difference between the jet flow and the main flow a electrical heated unit consisting of six electrical resistance heaters is installed in the piping of simulating the jet flow. These resistance heaters allow a maximum heating power of 72kW. However, only about one half this power can be used in order to keep in the range of inertial jets.

The heat input is measured via the electric current and the potential drop over each of the six heater rods. This is necessary to perform a heat balance. In order keep the temperature fluctuations of the jet inlet temperature as small as possible the heaters are stepless regulated so that the temperature fluctuations in the jet flow inlet before entering the module oscillate only by ±0.22°C.

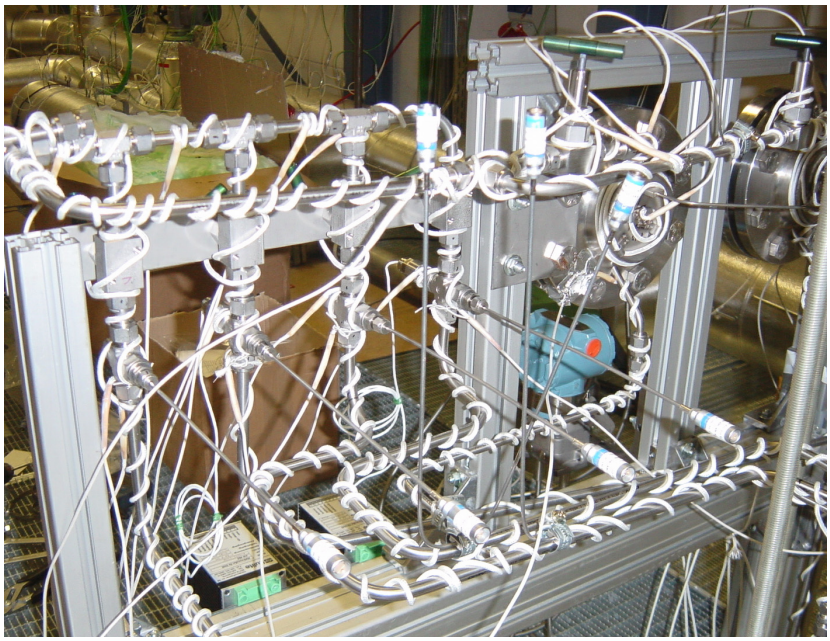

Figure 4.8: Photograph of the pressure measurement lines and purge lines of the Pitot, Prandtl and Annubar flow meters in the Heated Jet experiment before thermal insulation.

4.2 The experimental geometry and its instrumentation

The geometrical set-up of the heated jet experiment is illustrated in figure 4.9a. It corresponds geometrically almost 1:1 to the lower part of the MEGAPIE beam window (except for the outer thickness of the lower shell). The entire module is fabricated of stainless steel (DIN 1.4571). The exact dimensions may be taken from the figures 4.9-4.13. In order to present coherent results a right handed r-z-ϕ coordinate system is introduced. The origin of this coordinate system is the lowest point of the hemispherical shell at the fluid solid interface. The photographs 4.9b-e show major components of the heated jet experiment during fabrication and before the final assembly. The italic numbers in the graphs correspond to sensor positions. The list of sensors embedded in the experimental mock-up in the is entirely described in the sensor list which is given in Appendix A.

The main flow is entering the module in the upper collector and is guided via steel vanes into a flow straightener, which is made of 22 tubes with an inner diameter of 16mm and length of 80 mm in order to ensure a hydrodynamically fully developed turbulent flow in the annular gap. The flow straigthener ends at a height of z =1625mm. The centerline of the rectangular shaped jet duct enters the annular main flow gap of the module at z=1683mm. The gap adapted geometry of the jet pipe has rectangular edges, is made of 1.5mm thick steel sheets, and has an inner cross-section of 60x12mm. The gaps between the riser tube and the outer housing are equidistant.

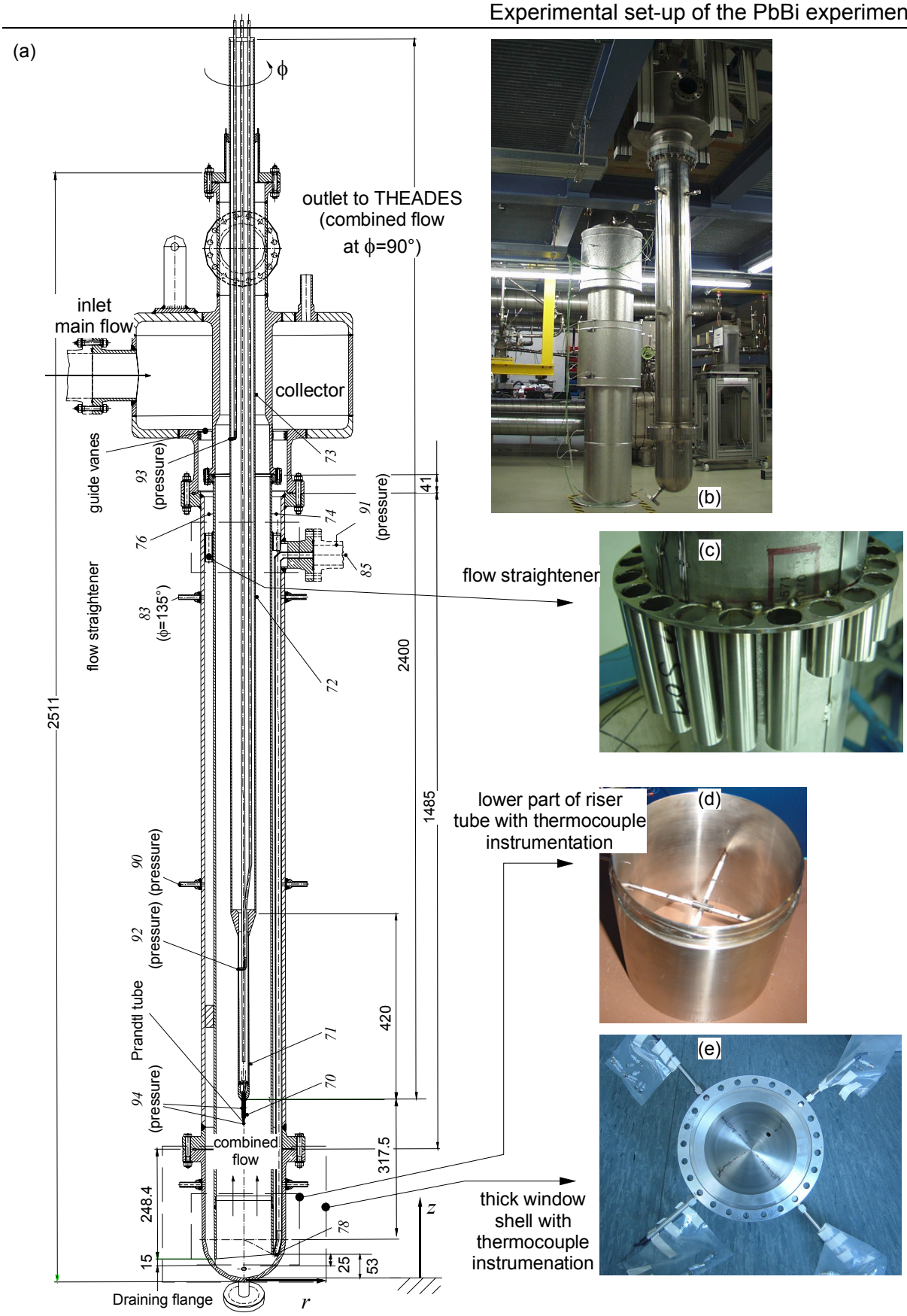

Figure 4.9: (a) Geometrical set-up of the heated jet experiment module and introduction of the coordinate system. The dimensions are in mm and the italic numbers indicate measurement positions. (b) Photograph of the module. (c) Flow straigthener. (d) Lower part of the riser tube. (e) Instrumented lower shell.

At z=107mm the nozzle with the inner cross sectional area of 20x10mm is welded to the jet duct as shown in figure 4.10a. The centerline of the orifice was located at z=51mm before the start of the experiment. The tube of the nozzle contacted the slanted riser tube (see figure 4.10a) at the position of maximal slantation. However, the post test analysis after the experimental campaign showed that due to a relaxation of the weld seams the nozzle position has moved in positive z-direction. This stress relaxation yielded to a change of the axial position z from z =53.7mm to z =55.7mm (in total to Δz =2mm at room temperature (T=25°C). Also the radial position of the nozzle exit changed. The nozzle wall was no more in contact with the riser tube. The distance between both was Δz =+0.65mm, so that the nozzle exit position was at r=67.15mm instead of r=66.5mm. The geometrical set-up of the nozzle with respect to the riser tube after the experiment is shown in figure 4.10b. The post-test examination of the geometry showed that the riser tube was still concentric in the outer housing (deviation less than 0.3% ≅ ±0.534mm). However, the relaxation of the jet duct did not lead to a distortion or inclination of the nozzle, so that the geometry was still mirror-symmetric with respect to the nozzle plane r-z at ϕ=0°.

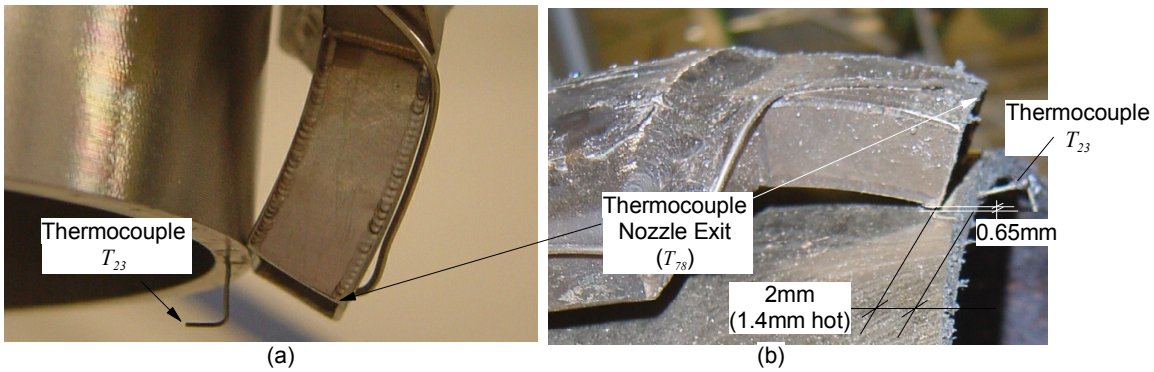

Figure 4.10: (a) Position of the Heated Jet nozzle before the experiment and (b) after the post test analysis.

During the experiments a constant inlet temperature of the jet flow into the jet duct of $T_{in,jet}$=360°C was ensured with an accuracy of ±0.1°C. For the main flow a temperature of $T_{in,main}$=300°C was established. As the jet flow enters the jet duct it heats up the jet wall and transfers heat (energy) via the duct walls to the gap flow as schematically shown in figure 4.11. Thus, the main and the jet flow act as a co-current heat exchanger. Due to the higher temperature of the jet flow the jet duct expands relatively to the riser tube according to the thermal expansion of steel. This relative elongation can be calculated taking the mean temperature of the top of the jet duct $T_{jet,top}=(T_{in,jet}-T_{in,main})/2$ and the mean temperature at the bottom of the jet duct via $T_{jet,bottom}=(T_{78}-T_4)/2$. Additionally, the mean temperature of the riser tube T_{riser} has to be calculated from the gray marked regions in figure 4.11 by averaging. Applying this procedure the relative elongation Δl of the riser tube is for the nominal flow rate case (Q_{main}=18m^3/h and Q_{jet}=1.2m^3/h)

$$\Delta l = \alpha \cdot l_0 \cdot \left[\left(\frac{T_{jet,top} + T_{jet,bottom}}{2} \right) - T_{riser} \right] = 0.64mm \quad , \tag{4.6}$$

where α is the thermal expansion coefficient of stainless steel ($1.7 \cdot 10^{-5} K^{-1}$ at T=330°C), l_0 the length of the jet tube at room temperature (l_0 =1586mm) and $T_{jet,top}$=330°C, $T_{jet,bottom}$=320°C and T_{riser}=302°C. This is in close agreement with the observation.

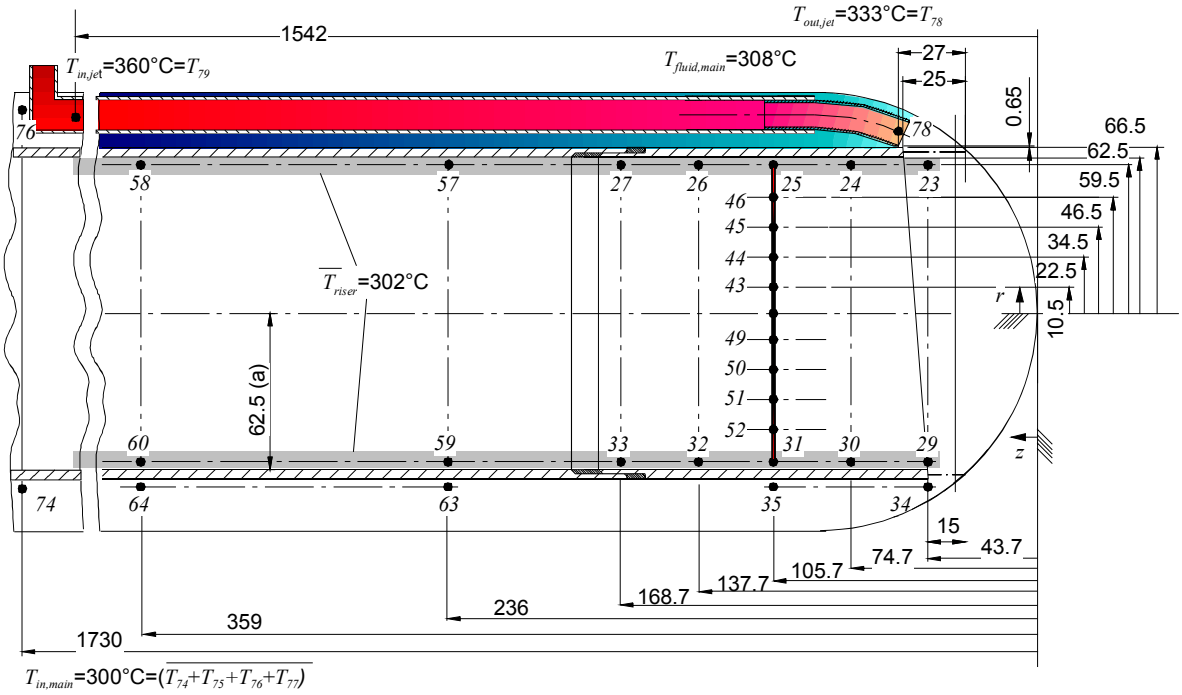

Figure 4.11: The italic numbers denote the thermocouples integrated in the riser tube and located close or in the jet tube in the nozzle plane (r-z, ϕ=0°-180°). Dimensions are in mm.

Within the riser tube 44 thermocouples are embedded. Their location is schematically illustrated in figure 4.12a, the detailed location may be taken from the appendix A. In the lower shell 18 thermocouples (T_i) are embedded in a distance of 3mm apart from the wall as shown in figure 4.12b.

The merging main and jet flows are directed upwards into the slanted riser tube. Within the riser tube also several thermocouples are integrated close to the fluid-wall interface (the exact locations may be taken from figure 4.12b and 4.13). Additionally, a crosswise arrangement of thermocouple consisting of 10 thermocouples in the nozzle plane (ϕ=0°-180°) and 7 thermocouples transverse to it (ϕ=90°-270°) is installed in a height of z=105.7mm. The photograph 4.9d shows the set-up of the thermocouple cross.

Further downstream this arrangement the flow is facing an instrumentation rod in a height z=349mm. This instrumentation rod has the identical outer shape as the one of MEGAPIE but here a Prandtl tube is installed. This sensor measures the time mean velocity at this position. At z=404.5mm the instrumentation rod is spherically shaped to an outer diameter of 25mm and at z=824mm the rod diameter again increases conically over an axial distance of 50mm to reach its final outer diameter of 57mm. The figure 4.13 shows the geometrical set-up of the lower part of the instrumentation rod and the shell up to height of z=500mm.

The fluid exits the module at z=2340mm and ϕ=90° towards the THEADES loop.

The entire test section is thermally insulated via a 160mm thick layer of rock wool with a specific heat conductivity of λ=0.043W/(mK). By measuring the temperature at the outside of the thermal insulation the heat losses can be calculated, see appendix B. As a reference case for the experiment a heating power 30.1kW has been chosen. This yields a jet constant

jet flow temperature of $T_{in,jet}=T_{79}$=360°C. For this reference case flow rates in the downcomer of Q_{main}=18m^3/h and in the jet duct of Q_{jet}=1.2m^3/h have been set. The average inlet temperature of the main flow was adjusted to $T_{in,main}=(T_{74}+T_{75}+T_{76}+T_{77})/4$=300°C. For the reference case the temperature difference between the outer side of the insulation ($T_{insulation}$=32.2°C, almost constant throughout the surface) and the ambient environment showed a nearly constant value of ΔT=12.2°C.

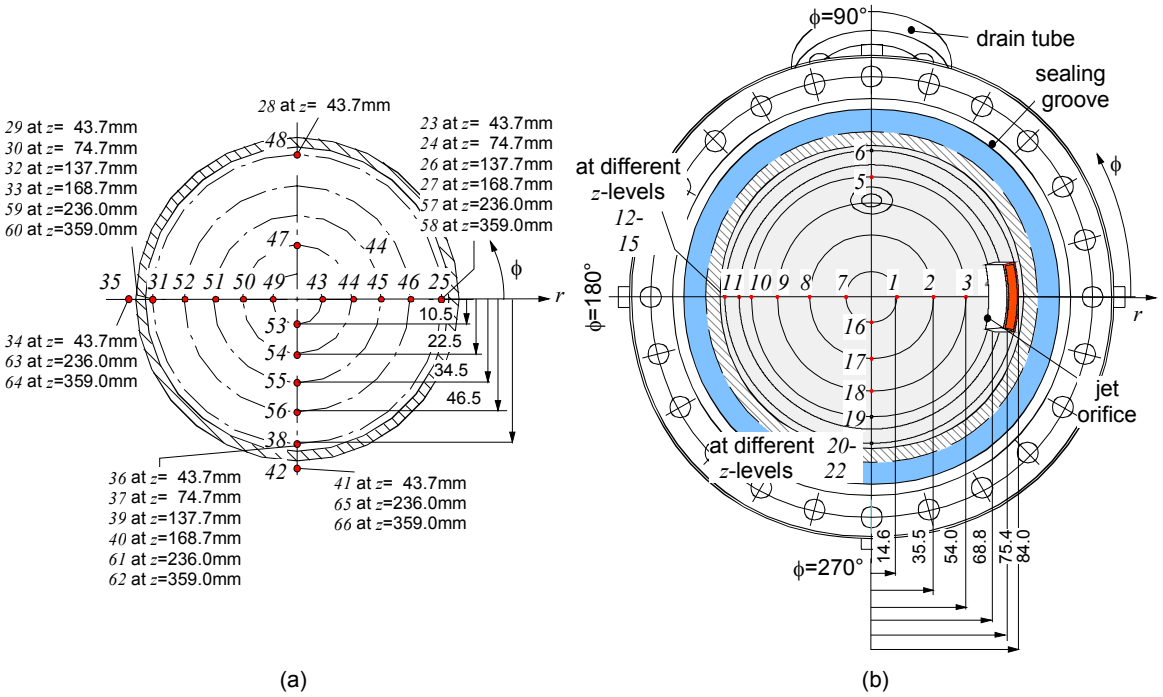

Figure 4.12: (a) Dimensional drawing of the thermocouple positions in the riser tube in the plane z=105.7. (b) Thermocouple positions (italic) embedded in the lower shell of the heated jet experiment.

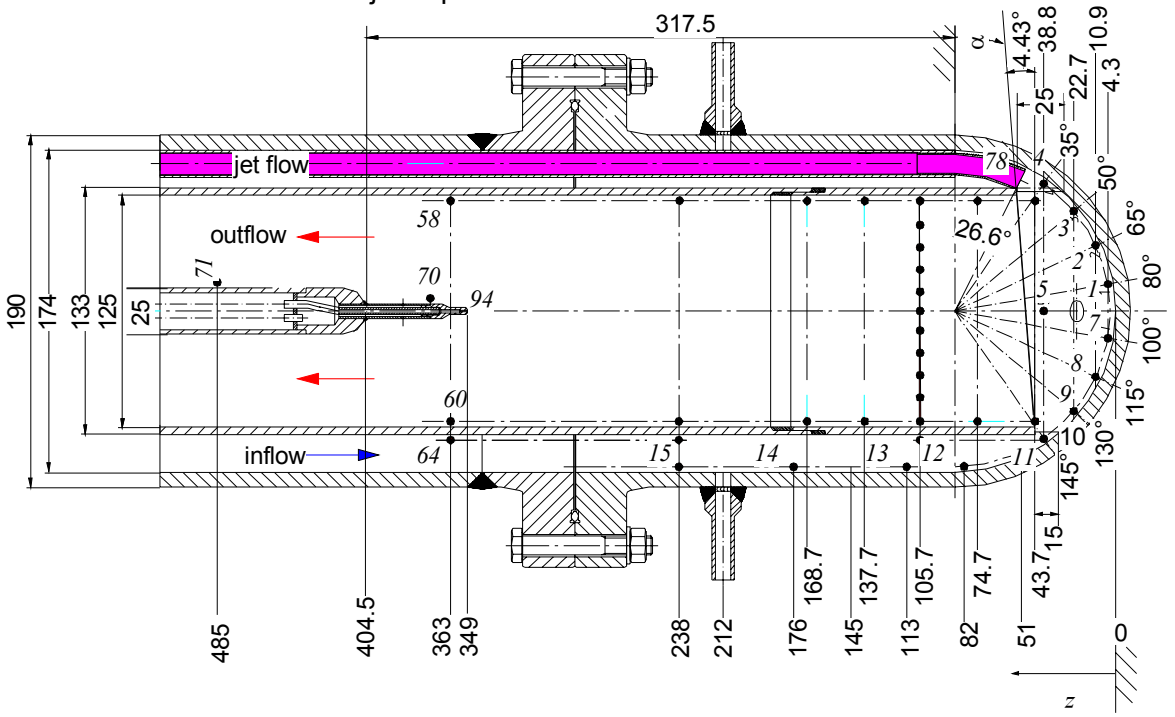

Figure 4.13: Measurement positions (italic) in the lower shell and the instrumentation rod in the nozzle plane (ϕ=0°). Dimensions are in mm

4.3 Measurement matrix

The matrix of the experiments conducted is shown in figure 4.14. In all series constant inlet temperatures of the jet flow of T_{79}=360°C (and in another campaign T_{79}=345°C) and of the main flow of T_{main}=300°C were chosen. The tentative operational range for the MEGAPIE target is given by the capabilities of the main pump and the jet pump. The envisaged nominal operation point of the target has a main flow rate of Q_{main}=13.5m^3/h and a jet flow rate of Q_{jet}=0.9m^3/h, which corresponds to is a flow rate ratio of Q_{main}/Q_{jet}=15. This point is marked by a black circle in figure 4.14.

Since the water experiments demonstrated, that the flow rate ratio is mainly determining the occurring flow pattern the same flow rate ratio Q_{main}/Q_{jet}=15 was chosen as a reference in the liquid metal experiment. In order to minimize the measurement errors the flow rates were increased to Q_{main} =18m^3/h and Q_{jet}=1.2m^3/h. This reference point is denoted as a black square in figure 4.14.

Within the first variation the jet flow was kept constant at Q_{jet}=1.2m^3/h while the main flow was varied from Q_{main}=9m^3/h to 24m^3/h simulating in the lowest case a power loss of the main pump.

A similar strategy was used for the second variation, in which the main flow was set to a constant value Q_{main}=18m^3/h and the jet flow varied from Q_{jet}=0.8m^3/h to 1.62m^3/h.

In a third series for the nominal conditions (Q_{main}=18m^3/h and Q_{jet}=1.2m^3/h) the inlet temperatures of the jet flow were been varied.

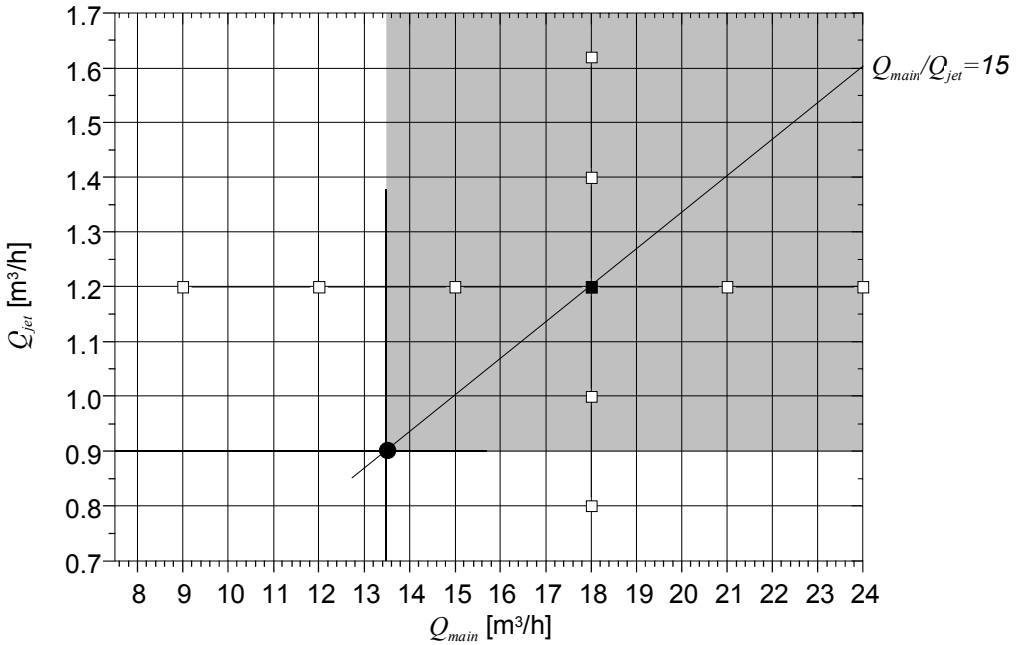

Figure 4.14: Experimental matrix of the heated jet experiments (• nominal MEGAPIE operation point, ! nominal operation point heated jet experiment).

4.4 Definition of the statistical functions used for the analysis of the PbBi experiment

For the characterization of the time dependent signals the following definitions are used. The root mean square value (RMS) of a sample time history record is given by:

$$RMS[x(t)] = \left[\lim_{t_{end}\to\infty} \frac{1}{t_{end}} \int_{t=0}^{t=t_{end}} \left(x^2(t) - \bar{x}^2 \right) dt \right]^{\frac{1}{2}}, \tag{4.7}$$

where $x(t)$ is the temporal signal and $\bar{x}$ the time averaged mean value, which is defined by

$$\bar{x} = \lim_{t_{end}\to\infty} \frac{1}{t_{end}} \int_{t=0}^{t=t_{end}} x(t)\, dt. \tag{4.8}$$

The autocorrelation function $R_x(\tau)$ providing a tool for detecting periodic deterministic data, which might be masked in a random background, is defined in the following way:

$$R_x(\tau) = \lim_{t_{end}\to\infty} \frac{1}{t_{end}} \int_{t=0}^{t=t_{end}} x(t) \cdot x(t+\tau)\, dt. \tag{4.9}$$

Here, $R_x(\tau)$ is always a real valued even function with a maximum at τ=0. A check of the correct calculation of the autocorrelation $R_x(\tau)$ can be easily performed, because the following relations hold for sufficiently long measuring times t [0, t_{end}]:

$$\bar{x} = \sqrt{R_x(\tau = t_{end})} \quad \text{and} \quad RMS[x(t)] = \sqrt{R_x(\tau = 0)} \quad . \tag{4.10}$$

The power spectral density PSD of random data describes the frequency composition of time dependent data in terms of the spectral density of its mean square value. In case of an acquisition with a high frequency resolution Δf the PSD of a time dependent signal $x(t)$ is defined by

$$PSD[x(t)] = \lim_{\Delta f\to 0} \frac{1}{\Delta f} \left[\lim_{t_{end}\to\infty} \frac{1}{t_{end}} \int_{t=0}^{t=t_{end}} x^2(t, f, \Delta f)\, dt \right]. \tag{4.11}$$

The cross-correlation CC_{xy} of two temporal signals $x(t)$ and $y(t)$ is calculated by,

$$CC_{xy} = \lim_{t_{end}\to\infty} \frac{1}{t_{end}} \int_{t=0}^{t=t_{end}} x(t) \cdot y(t+\tau)\, dt \, . \tag{4.12}$$

Two useful relations give upper bounds for the absolute value of CC_{xy}, which are,

$$\left| CC_{xy}(\tau) \right|^2 \le R_x(\tau = 0) \cdot R_y(\tau = 0) \quad \text{and} \quad CC_{xy}(\tau) \le \frac{1}{2} \left[R_x(\tau = 0) + R_y(\tau = 0) \right]. \tag{4.13}$$

A normalization of the cross-correlation with the products of the autocorrelation values of the signals $x(t)$ and $y(t)$ at τ=0 yields the cross-correlation coefficient $CCC[X(t),Y(t)]$. If $CCC[X(t),Y(t)]$=0 both signals are uncorrelated. The peaks in the plot CC_{xy} versus τ indicate the existence for a correlation at a discrete time displacement. The cross- correlation delivers information about:

- the time delays. The displacement time corresponds to the time required for the signal to pass through the system, if $x(t)$ is interpreted as an input and $y(t)$ as an output of the system.
- the determination of transmission paths. Transmission paths through a closed system are associated with different delay times, which can be identified by the peaks in the cross-correlogram for each of the path contributing to the signal output.
- the detection and recovery of signals in noise. The $CCC[X(t),Y(t)]$ provides a greater signal-to-noise ratio than the autocorrelation.

The cross spectral density permits the measurement of time delays as a function of the frequency, which is not available directly from the cross-correlation. The time delay through a system at any frequency f is given by t=$\Theta(f)/(2\pi f)$, where Θ is the phase angle. For the pre-

sent analysis the given definitions are sufficient, more detailed information may be taken from Bendat & Piersol (1971) or Wolf (1999).

5 Numerical simulation of the PbBi experiment

5.1 Features of the numerical simulation

The heated jet experiment Was been simulated using the commercially available computational fluid dynamics code CFX in version 5.6, see Vieser et al. (2002).

In order to represent the geometry adequately a structured grid consisting of $1.2 \cdot 10^6$ mesh cells was generated. The grid depicted in figure 5.1a has been chosen in such a manner to get a high resolution in terms of low y^+-values near the walls. Here, the dimensionless distance from the wall y^+ is defined as:

$$y^+ = \frac{\Delta y \cdot u_\tau}{\nu} \quad \text{where} \quad u_\tau = \sqrt{\frac{\tau_\omega}{\rho}} \quad . \tag{5.1}$$

u_τ is the friction velocity, Δy is the wall normal distance from the wall, τ_ω the wall shear stress and ρ und ν the specific material density and kinematic viscosity. The y^+-values are calculated depending on the numerical solution for the velocity field. However, the achieved near wall y^+-resolution, which is shown in figure 5.1b, still shows considerable values especially opposite the nozzle where y^+ is of order $O(10^2)$. Despite the cell number used is quite large and at the edge of our computational equipment the mesh should be further refined to get more accurate results.

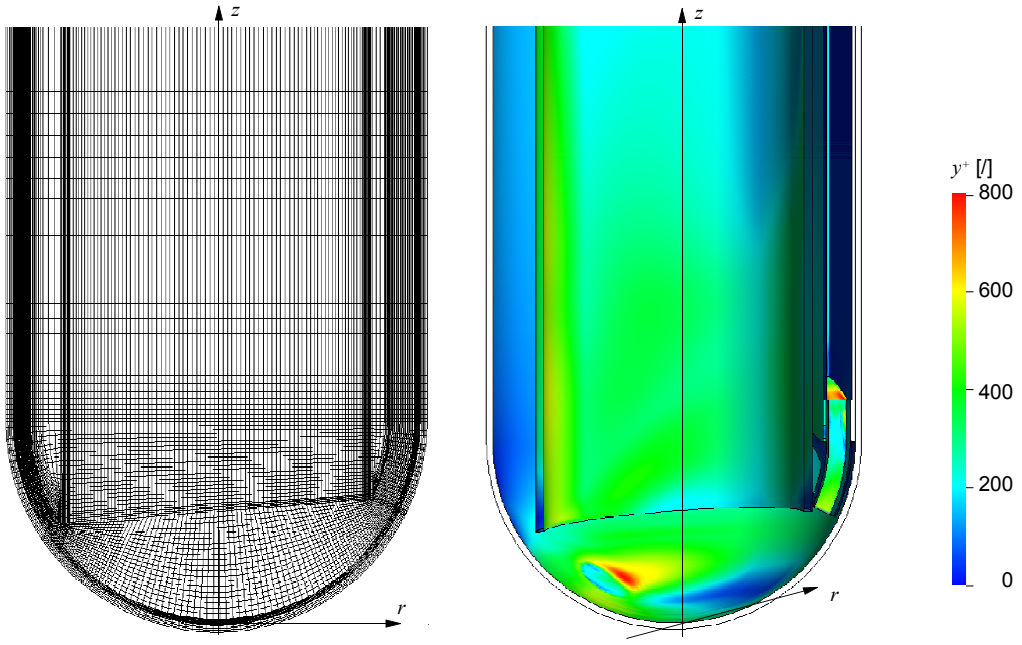

(a) (b)

Figure 5.1: (a) Mesh generated in the commercial CFD code CFX 5.6 in the plane r-z-ϕ=0°-180° to simulate the heated jet experiments. (b) Distribution of the y^+-values obtained in the CFD simulation in the wall nearest mesh cells.

The heated jet experiment is modeled geometrically at the inlet side in a 1:1 scale up to a height of z=1680mm. This includes both, the annular gap of the main flow and the jet chan-

nel. Here, also the heat losses of the heated jet flow towards the adjacently flowing colder main flow via the jet tube made of stainless steel have been considered. Additionally, the energy transfer from the hotter riser flow to the colder inflow in the gap has also been taken into account. The simulation does not account for the instrumentation rod in order to limit the computation time due to the complex grid generation close to the instrumentation rod.

A significant feature of the jet inlet configuration has been omitted. In the experiment the jet flow enters the module perpendicular to the main flow and is guided via a sharp edged 90° bend to flow parallel to the main inlet flow. Because this feature of the experimental configuration requires a significant effort in generating a refined mesh, in order to resolve the flow pattern there, the simulation assumes a parallel inflow of gap flow and jet flow.

As kinematic inlet conditions for both main and jet flow in the height z=1680mm a hydrodynamically fully developed turbulent flow was been assumed. Regarding the turbulence quantities at the inlet the default values have been set, which correspond to homogeneous grid turbulence. At the outlet of the simulated constant average static pressure boundary conditions were used.

Since the heat losses to the ambient were found to be very small in the experiment, adiabatic conditions at the outer walls were applied. Due to the relatively large Reynolds numbers based on the hydraulic diameter (Re>10^5) at the reference operating conditions buoyancy plays no significant role. Nevertheless, the temperature dependence of the thermo-physical data of the fluid were taken into account. The specific thermo-physical molecular quantities for the eutectic PbBi have been taken from Imbeni et al. (1999). A list of the thermo-physical data from 150°C to 400°C is given in Appendix C.

Within the simulation of the turbulent PbBi flow the *shear stress turbulence* model (SST) was used. The SST model combines the advantages of the k-ε model with the ones of the k-ω-model and takes advantage of the fact that for using in the near wall region the k-ω-model an analytical solution for the viscous sublayer is known for small y^+ values, see e.g. Wilcox (1986). The matching of the k-ω-model close to all walls to the k-ε model in the rest of the fluid domain is performed by means of blending functions. The detailed description of the model and the procedure may be taken from the CFX5.6 user manual (Vieser et al. 2002). The temperature wall function is modeled using the formulation proposed by Kader (1981).

Regarding the advection terms in the turbulent simulation a second order differencing scheme has been used.

5.2 Summary of the simulation parameter set

- Thermally conducting stainless steel wall with a constant heat conductivity of λ=14.7W/(mK).
- Variable density of the fluid using the thermal-physical data from Imbeni et al. (1999).
- Second order advection scheme.
- Simulation of the full geometrical height of the experimental set-up up to z=1680mm.
- Fully developed flow for the mean quantities and grid turbulence for the turbulence at the inlet of the main flow in the gap and at the inlet of the jet duct.
- At outlet constant pressure conditions were set (default).

- Default values for the constants of the SST turbulence models were used.
- Symmetry conditions in the plane ϕ=0°. Calculation of half of the domain.
- Adiabatic heat flux conditions to the ambient.
- Shear stress turbulence model (SST) for the whole flow domain.
- Constant turbulent Prandtl number Pr_t=0.9 (assumption of the Reynolds analogy).
- Disregard of the sharp 90°-bend of the jet inlet into the test module.
- Omission of modeling the instrumentation rod.

5.3 Results of the numerical simulation

For the nominal operation point of the experiment with a main flow rate of Q_{main}=18m^3/h and jet flow rate of Q_{jet}=1.2m^3/h several numerical simulations were performed. The details of the parameter variations may be taken from Batta et al. (2004). The temperature levels at the inlet at z=1680mm correspond to the experiment with T_{in}=300°C for the main flow and $T_{in,jet}$=360°C for the jet. In this context we refer to the simulation results considered to be the most adequate one.

For all calculations performed a steady solution was obtained for the reference case. In the figures 5.2a, b the calculated velocity vectors in the r-z-plane (ϕ=0°-180° and ϕ=90°) are shown for this parameter set. The main flow features are briefly described below.

The main flow in the annular gap far from the window is fully developed in the r-z-plane, which is expressed by a flat flow velocity profile except for the domain of the jet channel. There, the mean velocity in the gap is about 20% lower due to the higher wall friction.

As the main flow approaches the window region the cross section is continuously decreasing and thus the main flow is accelerated. This is marked by the number zero in figure 5.2b. The discontinous cross-sectional expansion at the U-turn of the downwards oriented main flow in the gap into the upwards directed riser flow causes a flow separation, which is expressed by the formation of a recirculation area (1) at the bottom end of the riser tube, see figure 5.2b. This recirculation zone occupies most of the cross sectional area close to the window. It confines a high velocity chimney developing around the axis of the geometry. The calculated velocities are reaching 2.5 times higher values there compared to the mean velocity u_0 (2).

In the lower part of the shell a second recirculation domain (3) establishes with extremely low velocities. The plane ϕ=90° is hardly affected by the jet flow arising from the 20x10mm nozzle. It corresponds nearly to the flow pattern found in the water simulation experiment without any bypass jet, see Knebel et al. (2003) or Eiselt (2003).

In the plane ϕ=0°-180° the jet flow is superimposed to the main flow, as shown in figure 5.2a. The introduction of a cross flow by means of a high velocity jet changes the momentum transfer in the plane ϕ=0°-180° significantly. As the jet exits the nozzle it accelerates by its momentum an additional portion of the fluid towards the opposite side of the riser tube (5, figure 5.2a). Most parts of the fluid motion transported towards ϕ=180° originate from the slanted riser tube, see c.f. figure 3.7a. A part of the jet flow also impinges the lower hemispherical shell in the region (6). Nevertheless, close to the centerline in the lower part of the shell at r=z=0 the fluid velocity remains still small. The momentum exchange between main

flow and jet flow leads to the fact that the jet is not covering the whole shell in the nozzle plane (ϕ=0°), as figure 5.2a shows. The interaction of main and jet flow and the geometrical set-up yields in the calculation velocities of less than 0.5m/s in the nozzle plane for 12mm<r<55mm (ϕ=0°). The strong main flow creates because of the slanted riser tube a third recirculation area (4) in the nozzle –plane (ϕ=0°). This recirculation domain occupies a significant part of the riser tube. However, the jet flow, aimed to ensure high fluid velocities close to r=z=0 where the highest heat fluxes appear in the MEGAPIE application, does not fulfill this task in the current geometrical configuration. In a global view the computed velocity distribution agrees qualitatively quite well with the Laser-Light Sheet (LLS) photographs of the water experiment shown in figure 3.7.

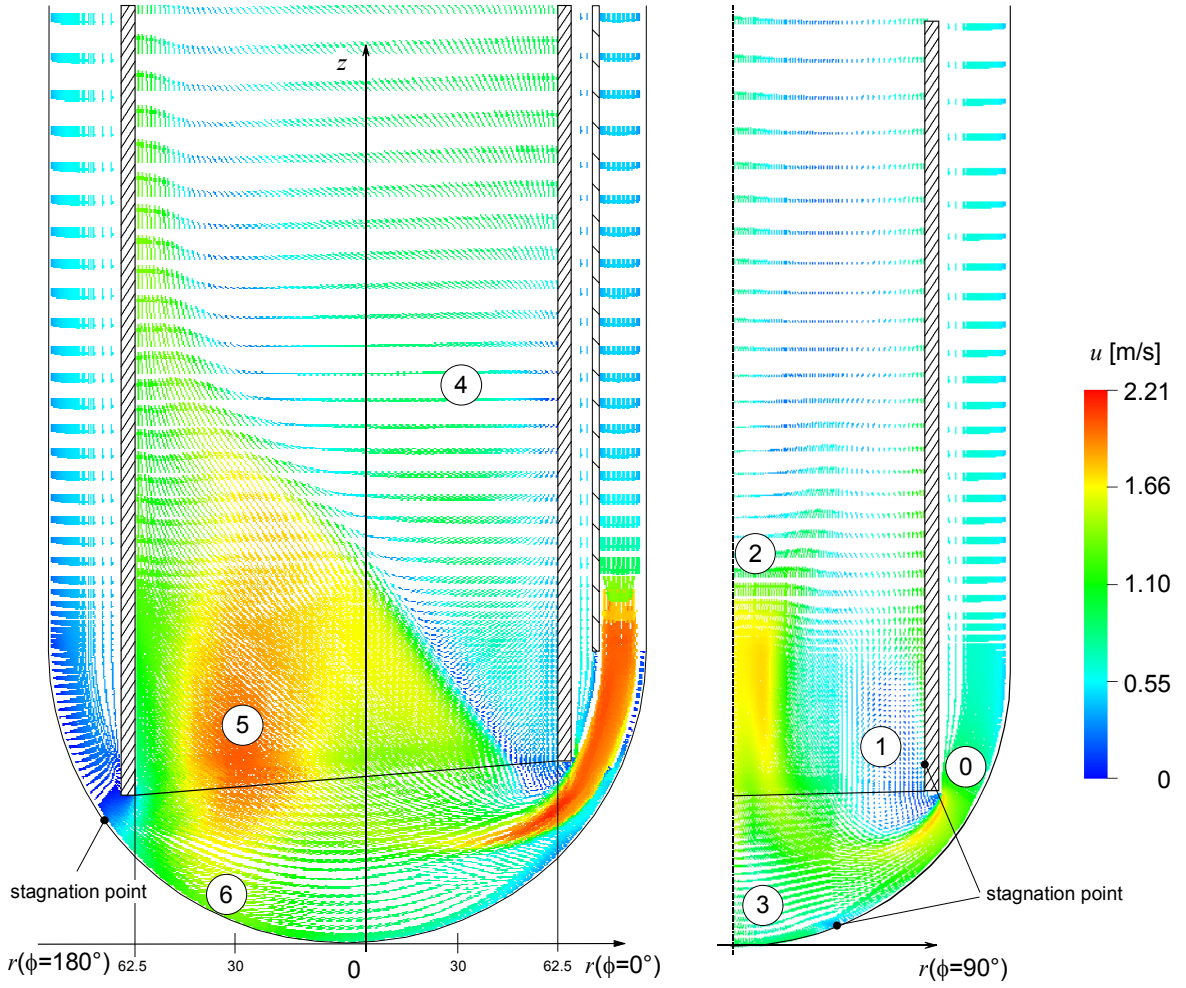

Figure 5.2: Calculated velocity vectors (using SST) for Q_{main}=18m^3/h and Q_{jet}=1.2m^3/h in the (a) r-z-plane(ϕ=0°-180°) and (b) r-z-plane(ϕ=90°). The corresponding dimensional velocity scale is depicted on the right side.

The computed streamlines of imaginary flow particles exiting the nozzle in the plane ϕ=0°-180° are shown for the nominal case in figure 5.3. The graph illustrates that the majority of the particles do not approach the window shell closely in the sector ϕ=0°. Even for radii r<12mm in the sector ϕ=180° hardly any particle reaches the shell. As a consequence enhanced heat transfer caused by the jet can not be expected there. Only a minor part of the

fluid particles reaches the shell in a region 35.5mm<r<68.8mm at ϕ=180° opposite the nozzle exit. There they lead to a change in the velocity distribution.

However, in the MEGAPIE application the proton beam releasing the heat flux by internal heating of the structure material is focused in the plane ϕ=0°-180° to a radius of 25mm around the axis of the shell. The Gaussian shaped power distribution of the beam with its maximum at r=0mm requires a well heat transfer. Therefore, from the calculation it may be concluded that the jet duct geometry and its nozzle exit position does not represent an optimal design for the MEGAPIE target in the thermal-hydraulic sense. Most of the fluid particles leaving the jet duct lead to a momentum change in the plane ϕ=0°-180°. This is expressed by high flow velocities close to the riser tube opposite the jet nozzle in the sector ϕ=180° between 56mm<r<87mm.

The velocity difference between the main flow turning into the riser tube and the jet leads to an induction of a swirl flow, which was also found by Tak et al. (2001) and Roubin (2003). This swirl is flowing helically upwards. Because of the assumed symmetry two vortices are generated, one in the volume 0<ϕ<180° and a second one in the region 180°<ϕ<360°.

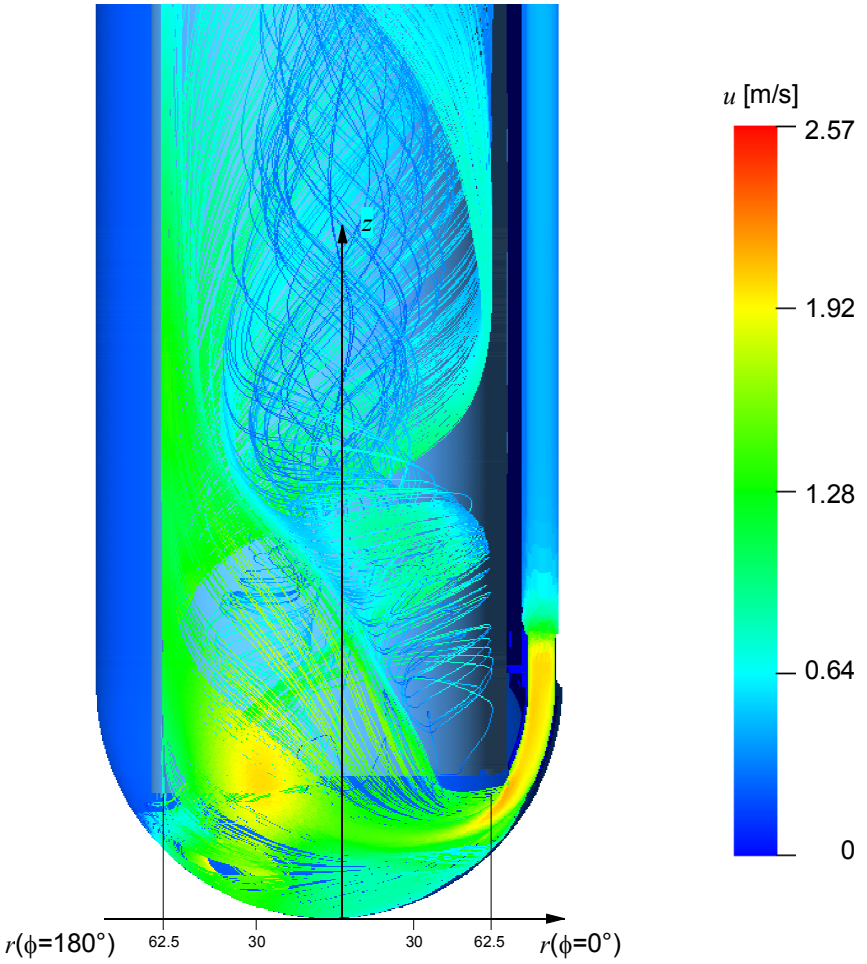

Figure 5.3: Calculated streamlines of imaginary fluid particles exiting the jet duct nozzle in the plane ϕ=0° for Q_{main}=18m^3/h and Q_{jet}=1.2m^3/h.

Since the heat transfer in the heated jet is mainly governed by the momentum exchange, the corresponding temperature field should exhibit a similar pattern. If buoyancy effects can be neglected the temperature is acting as a passive scalar, which is transported

by the velocity field. As shown in §3.3.3 the heated jet behaves in the investigated parameter range as an inertial jet, which allows to conclude from the temperature field on the velocity field.

Because of the low Prandtl number Pr of the eutectic alloy PbBi the thermal boundary layers are significantly larger than the viscous ones. Their thickness δ_{th} scales with $Pe^{-1/2}$ whereas the thickness of the viscous boundary layer ($\delta_{viscous}$) scales as $Re^{-1/2}$. Here the Prandtl number Pr, the Peclet number Pe and the Reynolds number Re are defined as

$$\begin{aligned} Pr &= \frac{\nu \cdot \rho \cdot c_p}{\lambda} \quad = 0.0219 \text{ at } T = 300°\text{C} \quad , \\ Pe &= \frac{u_0 \cdot d_h}{\kappa} \qquad \text{with } \kappa = \frac{\lambda}{\rho \cdot c_p} \quad , \\ Re &= \frac{u_0 \cdot d_h}{\nu} \qquad \text{and } Pe = Pr \cdot Re \quad ; \end{aligned} \tag{5.2}$$

where ν is the kinematic viscosity, ρ the specific density, c_p the specific heat capacity, λ the heat conductivity of the liquid. u_0 is the mean velocity of the considered domain and d_h its hydraulic diameter given by $4 \cdot A/C$ with A the cross-sectional area and C its circumferential length. The relatively good thermal conductivity expressed by the low Prandtl number leads to a fast temperature equalization, which is required in the MEGAPIE design to obtain low thermal stresses induced by differential elongation of the riser tube.

For a later on consistent representation of the results, we introduce the term temperature difference or temperature elevation (rise) as the difference between the local temperature value T_i and the mean inlet temperature of the main flow T_{in}. The subscript i indicates the individual measurement position.

The computed distribution of temperature difference for the nominal flow condition in the nozzle plane (ϕ=0°-180°) and perpendicular to it (ϕ=90°) is illustrated in the figures 5.4a,b.
In figure 5.4a the heat loss of the jet flow towards the main flow via the jet duct is easily seen. The simulation gives a temperature decrease of about 9.6K per meter of the jet channel and directly at the jet nozzle exit at the position of the thermocouple T_{78} the simulation shows a local value of ΔT=45°K.
As the jet leaves the nozzle orifice, the thermocouple (T_4) located closest to the nozzle exit, experiences only a minor temperature increase. The reason is that because of the nozzle shape and its orientation most of the thermal energy is transported by the momentum of the jet towards the central region of the hemispherical shell. The impact of the jet on the increase of the temperature in the lower part of the shell close to r=z=0 is small (T_3, T_4). As the fluid proceeds towards the centerline in the plane ϕ=0°-180° the temperature difference gradually increases from T_4 to T_1, where it reaches a local maximum. From there the temperature difference monotonically decreases and at the position of thermocouple T_{11} the temperature has almost reached the one of the main flow. As the velocity field in figure 5.2 has shown the jet is not strong enough to enter the opposite side of the annular gap tube. Thus, hardly any temperature rise is visible, which is confirmed by the computed temperatures. The jet flow transports hardly any thermal energy through the large scale recirculation area of the riser in the sector ϕ=0°. Further downstream in the riser tube the jet flow hits the wall opposite the jet nozzle for z>100mm in form of two fingers, see fig 4.4a. As the flow is transported beyond

values of z>363mm scarcely any temperature differences within fluid are found in the numerical simulation.

In the plane perpendicular to the jet duct (ϕ=90°-270°) the largest spreading of the temperature difference is obtained directly at the shell, where it covers a domain of 25mm next to the axis. However, further downstream the temperature distribution is rapidly equalized, which is caused by the intensive turbulent energy exchange of the fast upwards flowing jet with the adjacent fluid domains. Here, only a small chimney with elevated temperatures of the radius of about 7.5mm around the axis is observed as the figure 5.4b displays. This rather local effect could mean for the MEGAPIE design that in case of miscellaneous beam positions local overheating is likely to occur. For z>200mm in the sector ϕ=90° hardly any temperature increase is found in the simulation.

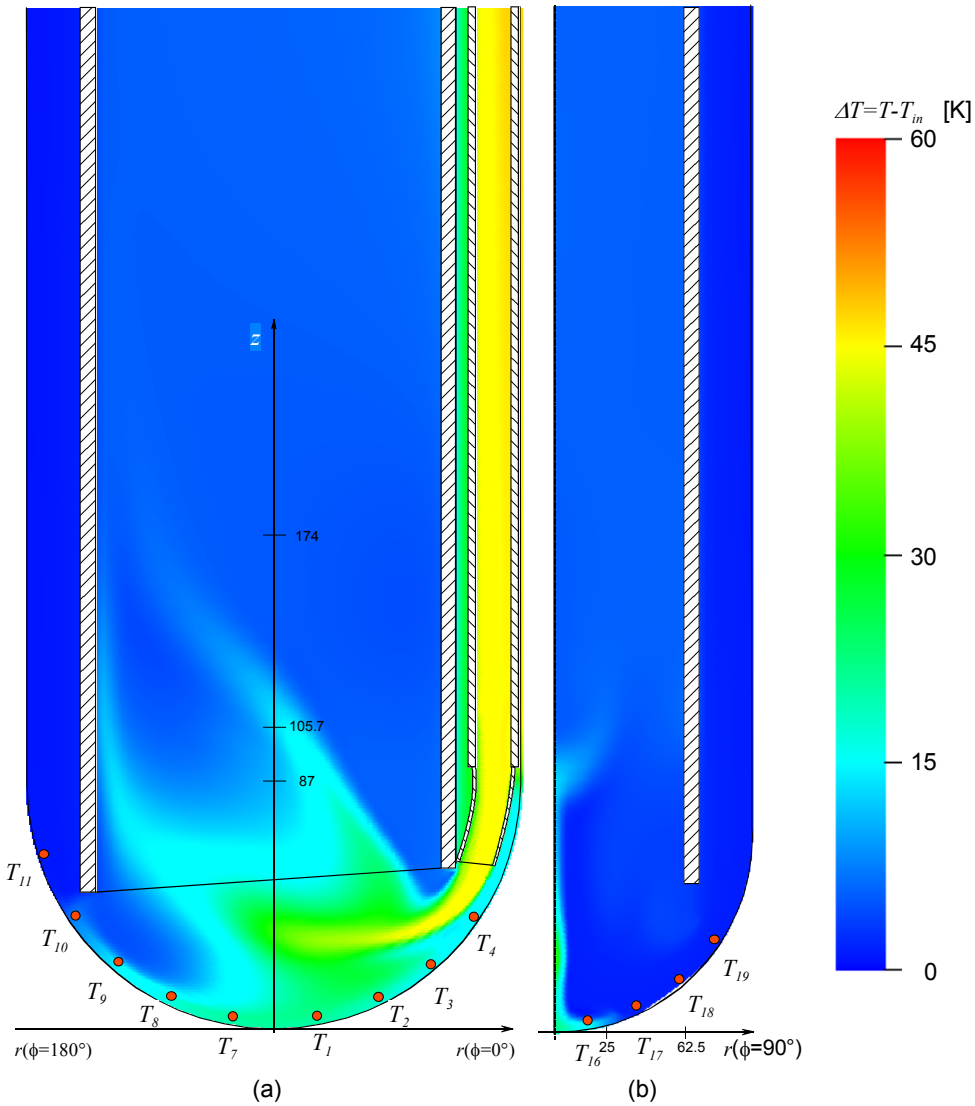

Figure 5.4: Calculated temperature difference contours using the SST-model and a constant turbulent Prandtl number Pr_t=0.9 for Q_{main}=18m^3/h and Q_{jet}=1.2m^3/h in the (a) r-z-plane(ϕ=0°-180°) and (b) r-z-sector (ϕ=90°). The circles indicate the measurement positions. The dimensional temperature difference scale in Kelvin [K] is given on the right side.

6 Analysis of the temperature field in the PbBi experiment for the nominal operation mode

The experimental results discussed in this paragraph refer all to the defined reference case with a main flow rate of Q_{main}=18m^3/h and a jet flow rate of Q_{jet}=1.2m^3/h at an inlet temperature T_{in}=300°C of the main flow and $T_{in,jet}$=360°C for the jet. All temperature differences shown in this chapter use the inlet temperature of the main flow T_{in} as a reference, except it is otherwise stated.

The presentation follows the flow path of the jet flow from the gap to the nozzle into the riser tube geometrically.

The mean values presented here were obtained in experimental runs with a record length of 600s, for which constant in- and outlet temperatures, pressures and flow rates had been set-up. The measurement series were repeated on several days. As a criterion for the acquisition start a relative change of the mean temperatures at the lower shell (16 thermocouples) and the rake (10 thermocouples at z=105.7mm) of less than 0.2°C per minute was set. The repeatability proof of the measured mean temperatures as well as for the temperature fluctuations is shown in detail in appendix D.

6.1 Measured mean temperature distribution at nominal conditions

The jet flow enters the experimental mock-up in the nominal operation mode with a temperature T_{79}=360.0°C. As the jet flow exits the nozzle at T_{78} (z=46.3mm, r=70.6mm, ϕ=0°) a temperature of T_{78}=333.94°C is measured. Thus, in the nominal operation mode more than 40% of the whole thermal power of the heated jet is transferred to the main flow in the gap and the adjacent steel structure before leaving the nozzle. Several reasons lead to this quite significant energy loss.

The first one is that the main flow is hitting the sharp edged jet duct like an impinging jet. A literature review shows, that impinging jets reveal Nusselt numbers of the order O(10^3) and more in Reynolds number range investigated here, see e.g. Lowery & Vachon (1975), Donaldson et al. (1971) and Oh et. al (1998). In the Oh et al. (1998) experiment conducted in air (Prandtl Pr=0.7) the measured surface heat flux was $3.15 \cdot 10^6$W/m^2 at a Reynolds number which corresponds to the one considered here. Assuming a similar heat transfer rate as this experiment for our configuration the main flow acting as impinging jet would remove a thermal power of 2582W from the hot jet duct flow. This corresponds to a temperature decrease of the bulk jet temperature of ΔT=5.2K. Because the thermal energy of the jet flow is transferred to the main flow in the annulus, the main flow temperature level increases. A thermal power of 2582W corresponds to a mean bulk temperature increase of the main flow in the downcomer of ΔT=0.32K.

A second aspect is that the insertion of the jet duct decreases the cross-sectional area of the downcomer gap by 27% which leads to a sidewise redistribution of the main flow, to an increased turbulence intensity and to an increase of its main velocity. All these issues associated with the jet duct inlet cause an enhanced heat transfer from the heated jet towards the main flow.

Another issue for the quite significant thermal energy loss of the jet is the heat conduction in the quite thick structural material of the outer main flow tube. A measure for the

amount of heat transferred from the jet duct towards the fluid and the surrounding structure is given by the Biot number, which can be defined as

$$Bi = \frac{\lambda_{Steel} \cdot d_{gap}}{\lambda_{PbBi} \cdot t_W} \quad ; \tag{6.1}$$

where d_{gap} is 1mm of liquid layer between jet duct and outer wall, λ_i the thermal conductivities of the steel and the liquid and t_w the thickness of the outer steel wall. The Biot number Bi accounting for the ratio of the thermal conductivity of the wall compared to that of the fluid yields values smaller than unity. In our case Bi is i.e. 0.16 in the region of the jet duct. In this particular domain thermal energy is transported rather in the wall than the fluid. But, a quantification of these losses is difficult.

One relatively small contribution to the energy loss arises from the heat losses to the environment. The appendix B shows that the heat losses to the ambient amounts to 216W in total, which is less than 0.7% of the total energy level of the jet.

Both, heat conduction in the structure and convective heat transfer in the fluid lead to an elevation of the temperature level in axial direction and also circumferentially. At a height z=892mm the thermocouples T_{80}, T_{82} (r=76.5mm in mid of gap), which are located at an angle ϕ=±45°, already show a temperature of 302.4°C, which documents the lateral increase of the main flow temperature with decreasing z compared to the inflow temperature. Figure 6.1 illustrates the lateral temperature rise. As the downcomer flow proceeds downstream the temperature rise covers already an angle of ϕ=±90° in the plane z=363mm. At the end of the downcomer in a height z=113mm the heat transfer process from the jet to the outer wall and from there to the main flow in the gap has reached the opposite side. There, the thermocouple T_{13} (r=84mm close to the wall, ϕ=180°) shows a temperature of 300.22°C:

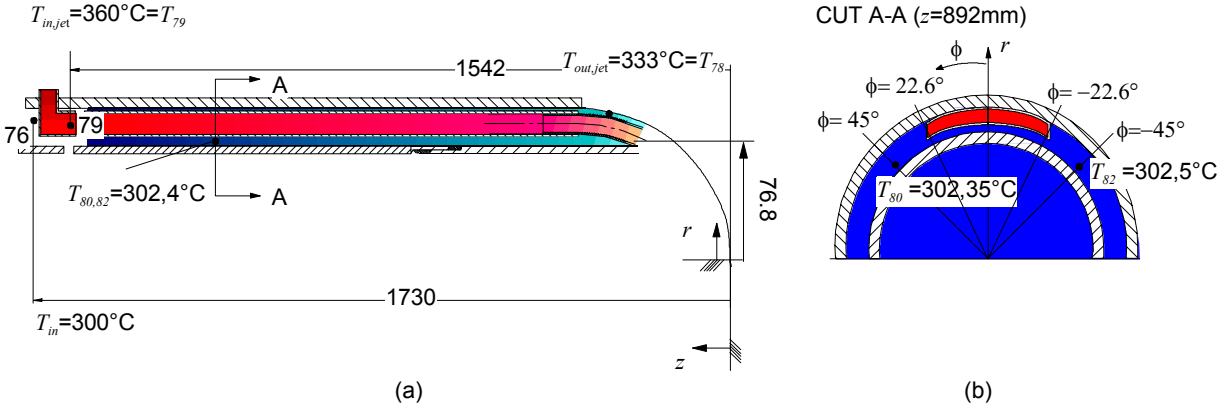

Figure 6.1: Measured temperatures of the main flow in the center of the annular gap at different heigths for the nominal conditions Q_{main}=18m^3/h, Q_{jet}=1.2m^3/h, T_{in}=300°C and $T_{in,jet}$=360°C.

The figure 6.2 shows the measured mean temperature rise ΔT_i=(T_i-T_{in}) close to the shell at a radius of r=84mm as a function of the geometry adapted coordinate s at the reference conditions in the plane ϕ=0°-180° and ϕ=90°-270°. From right to left the first point at s=225.76mm shows the jet outlet temperature measured by the thermocouple T_{78}. (r=70.6mm), which is the only thermocouple not on the line with r=84mm.

In the plane of the jet (ϕ=0°-180°) the thermocouple closest to the nozzle (T_4) is not directly facing the jet stream, which is reflected by a temperature significantly lower than the nozzle exit temperature. Its neighboring element (T_3) is hit by the jet and thus there the highest temperature rise is measured. From this point the temperature difference monotonously de-

creases down to s=117.3mm, which is far beyond the symmetry line (, located at s=136.66mm). From there again the temperature difference gradually increases down to s=73.3mm, which denotes a second temperature peak in the jet plane. The peak temperature measured at T_9 is still higher than the adiabatic mixing temperature rise ΔT_{ad} of ΔT_{ad}=3.79°C. This temperature elevation indicates that a part of the jet is reflected at the shell, detaches from it and re-hits again close to the thermocouple T_9. This is partially in agreement with the velocity field calculations presented in chapter 5, which predicts a reduced velocity in this region (, see figure 5.2, region 6). For values of s<51.3mm the measured temperature differences correspond to the inlet temperature of the main flow T_{in} and hence the temperature elevation is almost zero (T_{10}=T_{11}= T_{12}). Thus, for this flow rate combination the jet does not penetrate into the annular gap at the opposite side.

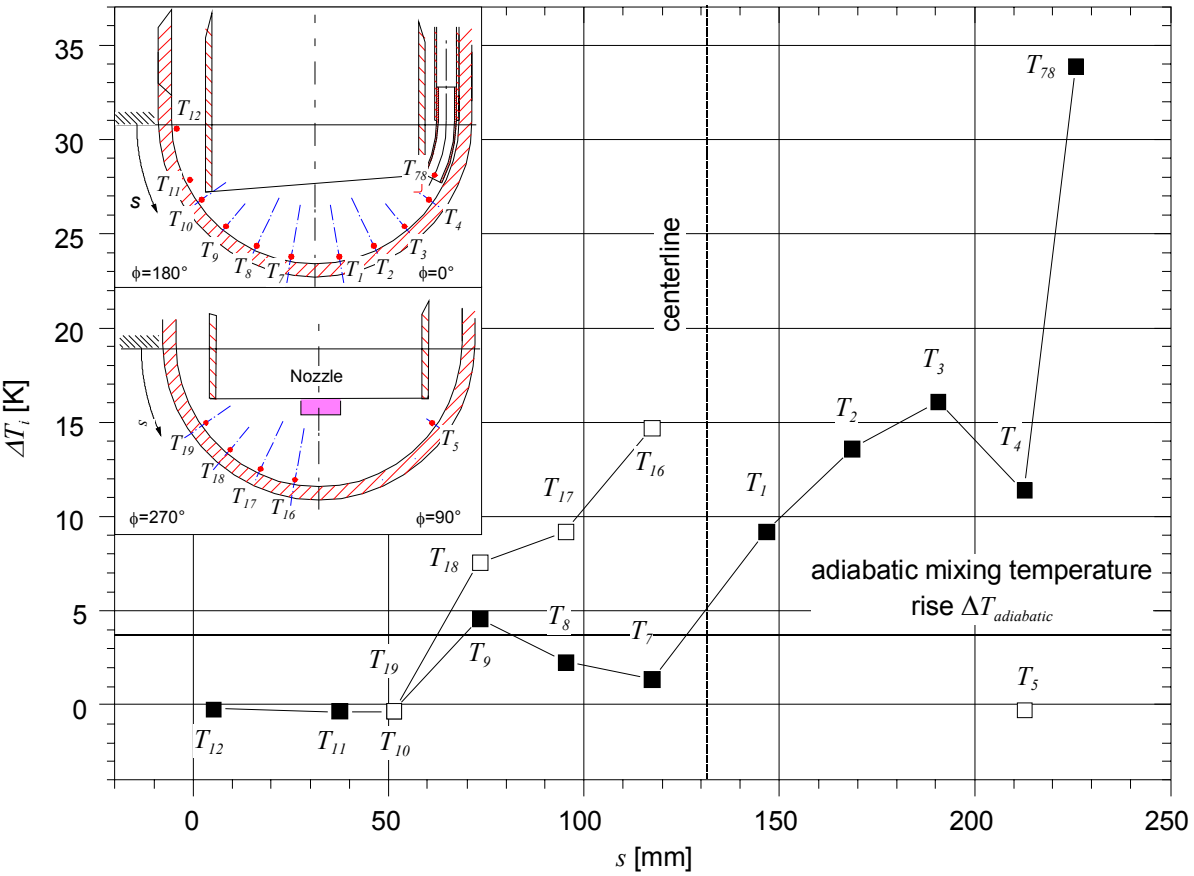

Figure 6.2: Measured distribution of temperature rise as a function of the geometry adapted coordinate s in the plane ϕ=0°-180° (■) and ϕ=90°-270° (□) for the nominal conditions Q_{main}=18m^3/h, Q_{jet}=1.2m^3/h, T_{in}=300°C and $T_{in,jet}$=360°C.

In the plane ϕ=90°-270° transverse to the jet the temperature rise distribution exhibits a qualitatively different shape, as depicted in figure 6.2. For values of s up to 51.3mm the temperature readings in both planes coincide indicating that the flow there is not affected by the jet and thus heat transfer plays a negligible role there. However, from there the temperature rapidly increases and reaches a maximum at the thermocouple T_{16} (s=117.3mm, r=14.6mm, z=4.3mm, ϕ=270°), where a temperature elevation of ΔT=14.68°C is recorded. This values is more than 10 times larger than that of the thermocouple T_7 in the jet plane with the same r-z-coordinates. This peak level of the temperature is nearly the same magnitude as the one of the thermocouple (T_3) directly facing the jet. Unfortunately, no additional ther-

mocouples were located between s=117.3mm and s=212.6mm, which could have given additional information about a symmetrical temperature reading in the sector ϕ=90° and ϕ=270°. However, as stated in chapter 4 an asymmetry of the geometry was not detected before and after the experimental runs.

A reasonable explanation for the evolution of a hot area close to the shell in the sector ϕ=270° is the assumption that the jet is reflected on the hemispherical shell and the main streak is transported towards ϕ=180°. Generally, the interaction of main and jet flow yields to the generation of a horseshoe like vortex pattern. If the jet is reflected at the wall, the induced vortices of the horseshoe transport thermal energy in the region below the reflected streak and thus the temperature increases. The figure 6.3 illustrates this process schematically.
Some evidence for this argumentation show the figures 7.2 and 7.22, in which either the jet flow rate is kept constant and Q_{main} varies (chapter 7.1) or the main flow rate Q_{main} is kept constant and Q_{jet} varies (chapter 7.2). If the jet flow rate keeps constant and the main flow is reduced the temperatures close to the centerline increase, because the momentum field close to the centerline keeps almost the same, while thermal energy transfer towards the main flow is decreased due to its lower velocity (see figure 7.2). If the main flow is kept constant and the jet flow rate is increased continuously the intensity of the generated secondary vortex should grow and hence the temperatures close to the centerline, which is shown in figure 7.12.

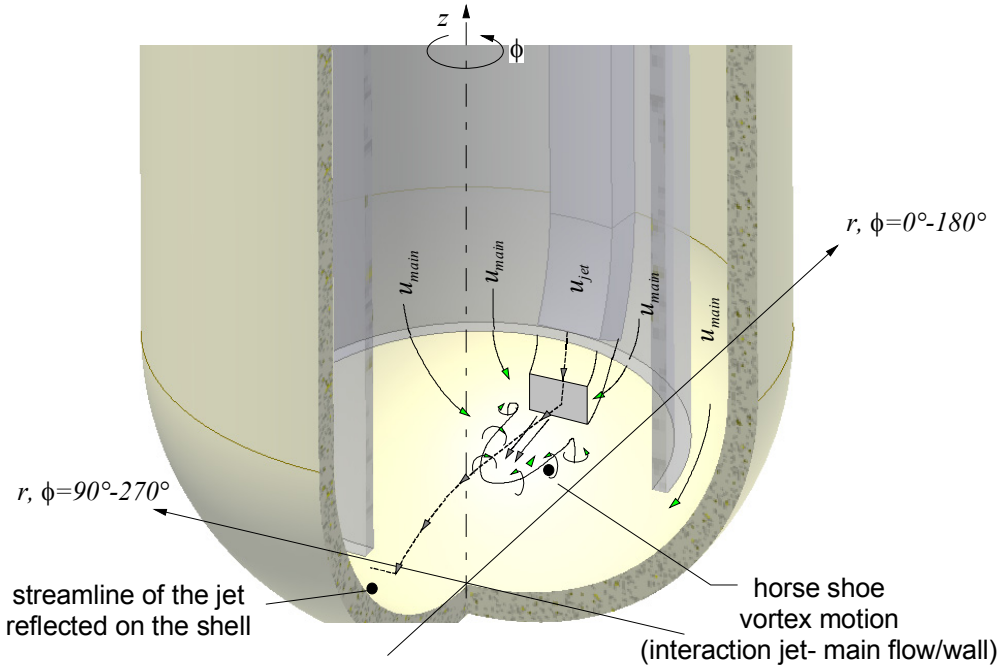

Figure 6.3: Generation of a horseshoe like vortex pattern for a hot jet reflected at the hemispherical shell, which transports thermal energy transverse to the nozzle plane by the induced secondary flow.

From the immediate vicinity of the shell the flow turns into the riser tube. In figure 6.4 the temperature distribution close to the wall at a radius of r=59.5mm is shown as a function of the axial coordinate z on three different lines with ϕ=const.
The temperature measurements near the wall adjacent to the line (ϕ=0°) show a temperature increase just after the flow turns around at z=43.7mm with a temperature increase of ΔT=6.58°C at the thermocouple T_{23}. The next measurement position on this line exhibits a significantly higher temperature (T_{24}). Beyond this line the temperature difference significantly

drops and between 137.7mm<z<238mm the temperature stays almost constant. It is close to the adiabatic mixing temperature. The qualitative shape of the distribution of the temperature rise for z<137.7mm suggests a recirculation area between 25mm<z<137.7mm, which may be generated in the way that one part of the jet detaches from the main streak at the bottom end of the riser tube and forms a vortex. At z=363mm the temperature increases again considerably. This can be explained by a helical upwards directed fluid motion, which transports thermal energy through this region. The helical vortex motion is also predicted by the simulation as shown in figure 5.3. One the line ϕ=180° the temperature difference increases nearly monotonically up to z=363mm. But, even at z=363mm it does not reach the adiabatic mixing temperature, as figure 6.4 shows. A generally similar behavior exhibits the distribution along the line ϕ=90°. It is remarkable here that the temperature close to the bottom of the riser tube is distinctly higher (by 1.9K at z=43.7mm) than in the plane ϕ=180°. A reasonable explanation for this higher temperature in the transverse plane is the interaction of the jet flow with the main flow generating a vortical motion as indicated in figure 6.3. Further downstream, with growing values of z, the temperature increases and reaches almost the value of the adiabatic mixing temperature for z=363mm.

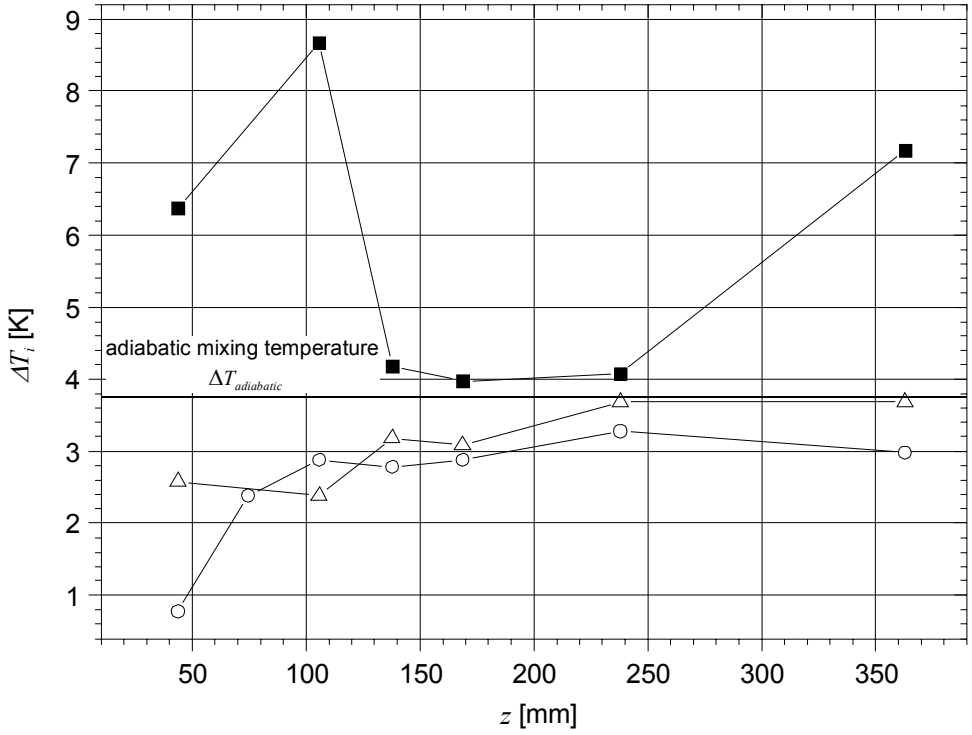

Figure 6.4: Measured distribution of the temperature difference along the inner side of the riser tube wall as a function of the axial length z at r=59.5mm on the line ϕ=0° (■), ϕ=180° (o) and ϕ=90°(Δ) for the nominal conditions Q_{main}=18m^3/h, Q_{jet}=1.2m^3/h, T_{in}=300°C and $T_{in,jet}$=360°C.

The graph 6.5 illustrates the radial temperature distribution within the riser tube on the lines ϕ=0°-180° and ϕ=90°-270° in a constant height of z=105.7mm. Within the graph the downwards oriented main flow in the annular gap is marked in gray.

The temperature of the main flow in the gap shows both for ϕ=180° and ϕ=270° a temperature increase of ΔT=0.35K (T_{35} at r=69.5mm, ϕ=180° opposite the nozzle) and ΔT=0.48K (T_{42} at r=69.5mm, ϕ=270°) compared to the inlet temperature of the main flow. This is partially caused by the heat transfer processes described before. But, additionally another heat trans-

fer process is active, which is responsible for the temperature increase in the annular gap. The countercurrent arrangement of gap and riser flow acts like a countercurrent heat exchanger transporting thermal energy from the riser tube into the annular main flow. Assuming only heat conduction between the two closest thermocouples (which represents a drastic underestimation of the heat transfer rate, because both are far outside the thermal boundary layers and thus convection plays a significant role,) a heat flux of $q''=2\cdot10^3 Wm^{-2}$ for ϕ=180° and $q''=2.8\cdot10^3 Wm^{-2}$ for ϕ=90° can be assessed.

Following the temperature rise profile on the line ϕ=180° towards the center the level soon reaches the adiabatic mixing temperature and it keeps this value up to r=10.5mm. From there it increases to a peak temperature 1.2K above the adiabatic mixing value (T_{44} at r=22.5mm, ϕ=0°) indicating a jet or vortex motion. Further on it falls back to the mixing temperature (T_{46} at r=46.5mm, ϕ=0°). From r=46.5mm towards the riser tube a steep temperature rise is recorded which is caused by conductive and convective interaction of the heated jet duct, the structure material and the counter-current flow arrangement of gap and riser flow.

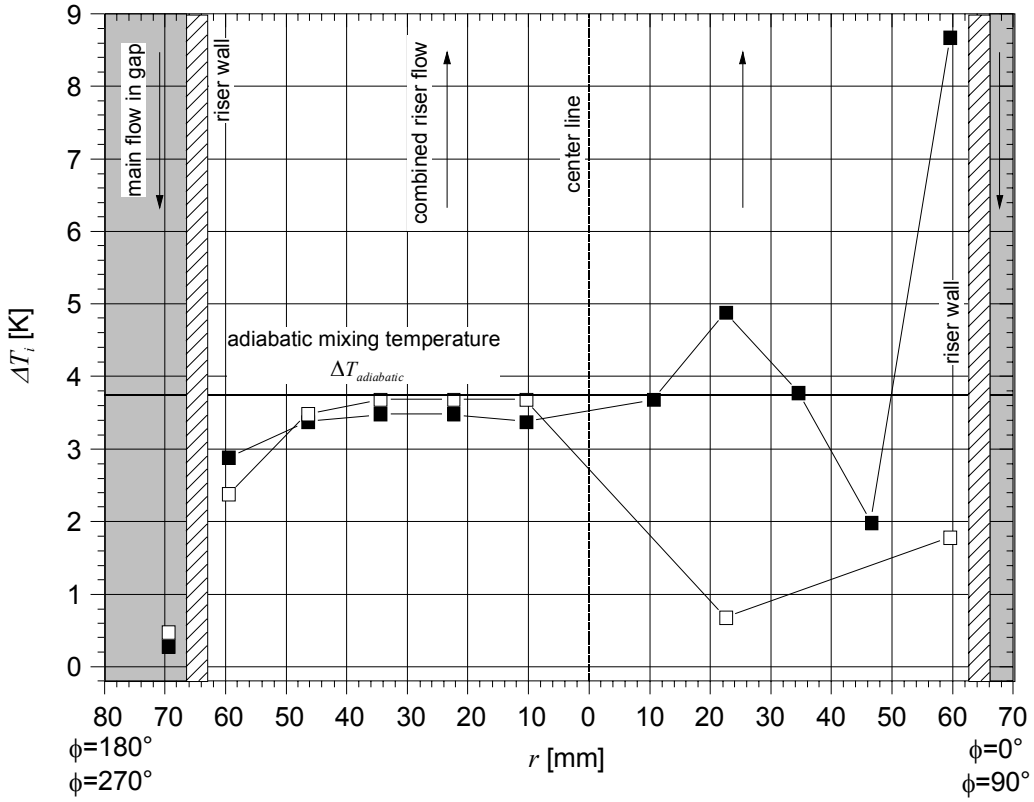

Figure 6.5: Measured distribution of the temperature difference in the height z=105.7mm as a function of the radius r for the lines ϕ=0° (■) and ϕ=90° (□) and for the nominal conditions Q_{main}=18m³/h, Q_{jet}=1.2m³/h, T_{in}=300°C and $T_{in,jet}$=360°C.

The temperature distribution on the line ϕ=270° exhibits a similar shape like on the line ϕ=180° for 10.5mm<r<69.5mm. Here also the temperature monotonically increases towards the duct center and reaches there almost the level of the adiabatic mixing temperature. However, for on the line ϕ=90° at r=22.5mm a depression of the temperature is found in contrast to the line ϕ=0°. This is observed for T_{47} (r=22.5mm, ϕ=90°) and the temperature recorded there is about 3K less than the adiabatic mixing temperature. One explanation for this behavior is that a part of the stream of the relatively cold main flow is transported through this re-

gion. Another explanation for this behavior could be that a global vortex exists within the riser tube. However, close to the riser tube on the line ϕ=90° the temperature increases to values higher than that of the main flow in the annular gap.

More serious is the shape of the temperature distribution in the line ϕ=90°-270°. It is far of being symmetric with respect to r=0mm, which was a major ingredient for the numerical simulation.

The nominal operation mode with the defined flow rate ratio of Q_{main}/Q_{jet}=15 has been established in several tests coming either from smaller flow rate ratios or from larger one. These test were aimed to check, if the evolving temperature distribution depends on the history of the flow rate adjustment. Nevertheless, all these test resulted in the same non-symmetric temperature distribution in the riser tube. More details can be found in appendix D. Thus, the flow field establishing at the nominal flow rate ratio is independent of history effects of the THEADES loop. From these measurements we conclude, that the flow field developing in this geometrical set-up is highly sensitive to marginal deviations from symmetry, which may be caused by asymmetry of the inflow or by the geometry. This experimental observation is supported by the water tests performed in almost the same set-up in HYTAS, where a similar sensitivity was observed, see Knebel et al. (2003), Eiselt (2003) and Stieglitz et al. (2005).

6.2 Analysis of the flow field based on temporal temperature data

6.2.1 Influence of a temperature difference between main and jet flow on the flow pattern.

All conducted water experiments demonstrated that the flow in the MEGAPIE configuration is highly turbulent and that the normalized turbulence intensities close to the window reaches order of one values. Thus, in the liquid metal experiment where a heated jet is injected into the colder main flow the temperature fluctuations can act as indicator for the velocity field. However, this is only then justified if the turbulent fluctuations are mainly determined by the momentum exchange than buoyancy effects.

If a hotter fluid is injected into a colder fluid domain an additional non-dimensional parameter appears arising from the different temperatures of the jet compared to the main flow. It is the densimetric Froude number Fr_{dens}, which additionally includes buoyancy effects due to density differences at the individual temperature levels of jet and main flow. The densimetric Froude number is defined as

$$Fr_{dens} = \frac{\rho_{main}\left(u_{jet}^2 - u_{main}^2\right)}{g \cdot \left(\rho_{main} - \rho_{jet}\right) \cdot d_{h,jet}}; \qquad (3.3)$$

In co-arranged vertical flow large densimetric Foude numbers (Fr_{dens} >(5.10^2) indicate a flow regime dominated by the momentum exchange, see e.g. Knebel et al. (1998) or Ruffin et al. (1994). There, buoyancy effects play a negligible role. Hence these jet are called inertial jet and the temperature fluctuations can be used as a tracer for the velocity field. This is of major importance, since it was impossible to measure directly the velocity in the liquid metal experiment. Especially the chapter 5.3, where cross-correlations are performed, uses the inertial character of the jet flow as a major assumption.

The densimetric Froude number calculated for a flow rate ratio of Q_{main}/Q_{jet}=15 with an inlet temperature of the main flow of T_{in}=300°C and an exit temperature at the nozzle of T_{jet}=334°C is about Fr_{dens}~O(10^3- 10^4), which is in the inertial range of co-arranged jets. For a vertical arranged heated jet and a surrounding colder main flow the centerline velocity u_{CL} of an inertial jet decays according to

$$\frac{\left(u_{CL}-u_{nozzle,exit}\right)}{\left(u_{nozzle,exit}-u_{main}\right)}=4.1\cdot\left(\frac{x}{d_{h,jet}}+2.84\right)^{-1}, \tag{3.4}$$

where x is the distance behind the nozzle, see c.f. Chen & Rhodi (1975, 1980), Ogino et al. (1980) or Ruffin et al. (1994). Transferring this relation to the jet velocity in the considered geometry, the momentum impact of the heated jet on the center of the hemispherical shell is of nearly the same magnitude as that of the main flow. Hence, a strong influence of the heated jet on the temperature distribution can not be expected there.

Moreover, using the temporal behavior of the temperature readings to conclude on the velocity between discrete positions, especially in the immediate vicinity of the shell region allows to compare the experimental data of the water experiments with the liquid metal series and thus ensures, to draw a coherent picture on the flow features to be expected in the MEGAPIE target.

6.2.2 Flow field reconstruction by means of the temporal temperature data

Of crucial importance for the operational performance of a target is the temporal stability of the flow pattern, once a specific flow rate combination has been set. Large fluctuations can cause local excesses of the sustainable material temperatures, which may lead to differential elongations (accompanied by high material stresses or elastic deformations) or even in the worst case yield to a failure of the whole system. A temporal analysis of such a time-dependent flow characteristics is inevitable from the technical point of view.

A second aspect of much more importance is the fact that in the investigated flow rate ratio parameter region of Q_{main}/Q_{jet} the heated jet behaves like an inertial jet. This allows to conclude from the time dependent temperature readings on the local velocities at discrete measurement points. Moreover, by the calculating normalized cross-correlations between discrete points flow patterns establishing in the investigated geometry can be extracted. This methodology enables to compare the results of the water experiment with the ones obtained in the liquid metal experiment.

The methodology to detect flow patterns requires steady inlet conditions. The long-term-investigations performed for the nominal operation mode Q_{main}/Q_{jet}=15 were repeated four times at different days. The deviations between the individual tests were in the range of the resolution accuracy of the individual sensors. Each run lasted 600 seconds and was thus significantly longer than any of the time scales of the flow instabilities, which may occur in the experimental mock-up. The long duration was aimed to ensure that no artificial disturbances which may arise from the THEADES loop like pump-oscillations, auxiliary heaters etc., influences the temporal data within the experimental mock-up. The recording frequency of the thermocouples was chosen to f=128Hz, being at least two times higher than their temporal resolution of 40Hz, see Krebs et al. (1983) or Bremhorst et al. (1992). An acquisition frequency significantly higher than the sensor response time is necessary to avoid an aliasing

effect. The temporal resolution of the thermocouple is given by its dimensions and according to its maximal resolution of 40Hz only time differences of τ=0.025s between two signals can be captured.

But, there exists also a spatial resolution limit between two discrete positions, which mainly depends on the properties of the fluid. The transport velocity of a temperature fluctuation in a homogeneous fluid is given by the wave velocity u_W, which can be defined in the unsteady case by

$$u_W = \sqrt{2 \cdot \frac{\lambda}{\rho \cdot c_p} \cdot \omega} \quad , \tag{6.2}$$

where λ is the heat conductivity, ρ the specific density, c_p the specific heat capacity and ω the vorticity ($\omega \sim u/r$). In order to resolve the spatial extension of a vortex structure by temperature fluctuations the ratio of the temperature propagation velocity to the vortex velocity must by significantly smaller than unity (u_w/u_{main}<0.1). This immediately yields that thermal areas of less than 5mm in diameter are not resolvable.

The figures 6.6 show the time series of the temperature recordings of the jet inlet temperatures $T_{in,jet}$ (T_{79}) and that of the main flow in the annular gap T_{in} (T_{74}) with two temporal increments. While the inlet conditions of the main flow is completely free of any surges exhibiting a RMS value of 0.06K, the jet inlet temperature shows an oscillation frequency of 120 seconds and an amplitude of 0.48K (peak to peak). This effect is caused by the inertia of the power control of the jet heater. Nevertheless, the RMS value of the temperature fluctuation is 0.21K at the jet flow inlet, which corresponds to a total fluctuation intensity of 0.58% at the jet duct inlet. This order of magnitude is acceptable for a spatial-temporal analysis. A cross-correlation of both inlet signals shows no distinct time shift. The normalized peak cross-correlation coefficient $CCC[T_i, T_j]$ between both inlet temperatures is less than 10^{-2}. A similar cross-correlogram was performed for the pressures jet flow inlet p_{91} and the pressure at the main flow inlet p_{90}. The normalized peak cross-correlation coefficient $CCC[p_{90}, p_{91}]$ also exhibited values of 10^{-2}. Both checks are necessary to ensure that no loop specific time scales enters the analysis of the time-dependent behavior of the flow in the considered problem. They would be superimposed as noise to the correlations of interest. The same procedure was conducted for the flow rate, but also here the found normalized $CCC[Q_{jet}, Q_{main}]$ does not exceed 10^{-2} values. Based on the experimental boundary conditions a sensible spatial-temporal analysis can be performed.

Although, both inlet conditions in the gap and the jet are close to that of a perfectly stationary turbulent flow ($\partial/\partial t$=0) the flow pattern evolving in the lower shell and the riser tube are highly time dependent. In order to illustrate the temporal character of the flow along the hemisphere a time history of the isotherms in the nozzle plane (ϕ=0°) along the geometry adapted coordinate s is shown in figure 6.7.

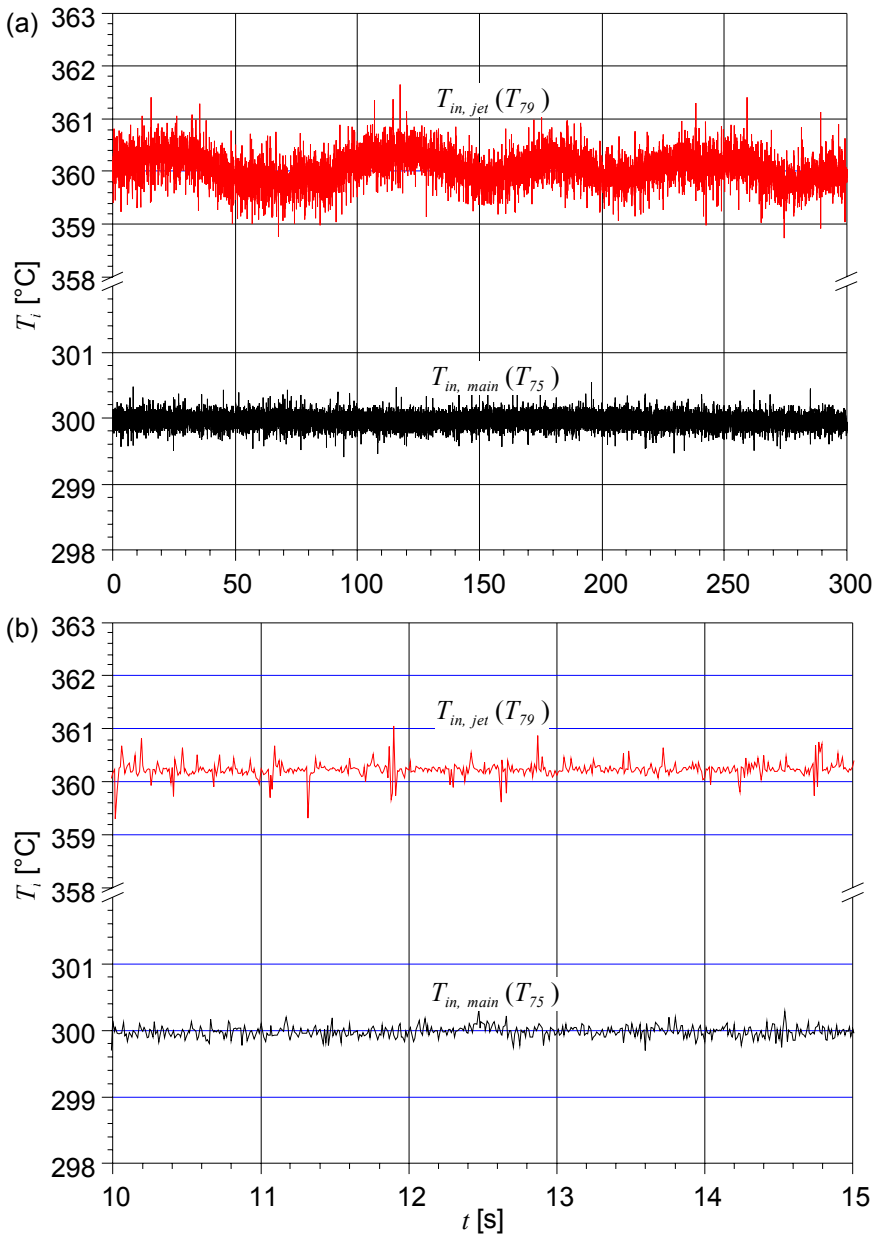

Figure 6.6: Measured time series of the main inlet temperature T_{in} (T_{74}) and the jet inlet temperature $T_{in,jet}$ (T_{79}) for the reference conditions Q_{main}=18m^3/h, Q_{jet}=1.2m^3/h, T_{in}=300°C and $T_{in,jet}$=360°C.

The figure 6.7 illustrates, that as the jet exits the nozzle it impinges the wall close to the thermocouple T_3. The thermocouple T_4 only experiences a minor temperature rise. The time series at the thermocouples T_3, T_2 and T_1 exhibits an intermittent pattern of temperature elevations. Close to the nozzle exit tangents of the isotherms can be conceived as velocity directions. The time history illustrates that the jet velocity changes its direction with time. An indication that the jet impinges onto the shell and than it detaches from it, can also be taken from this graph. There, the jet affects the temperatures at the shell between T_3 and T_1, for T_7 and T_8 which is marked by the darker regions the jet detaches from the shell. Then a part of the jet reaches again the shell at T_9, which is expressed by the brighter color. This reattachment of the jet onto the shell is also rather irregular. Finally, at the elements T_{10}, T_{11} and T_{12} no temperature elevation is observed at any time, indicating that the jet does not enter this region.

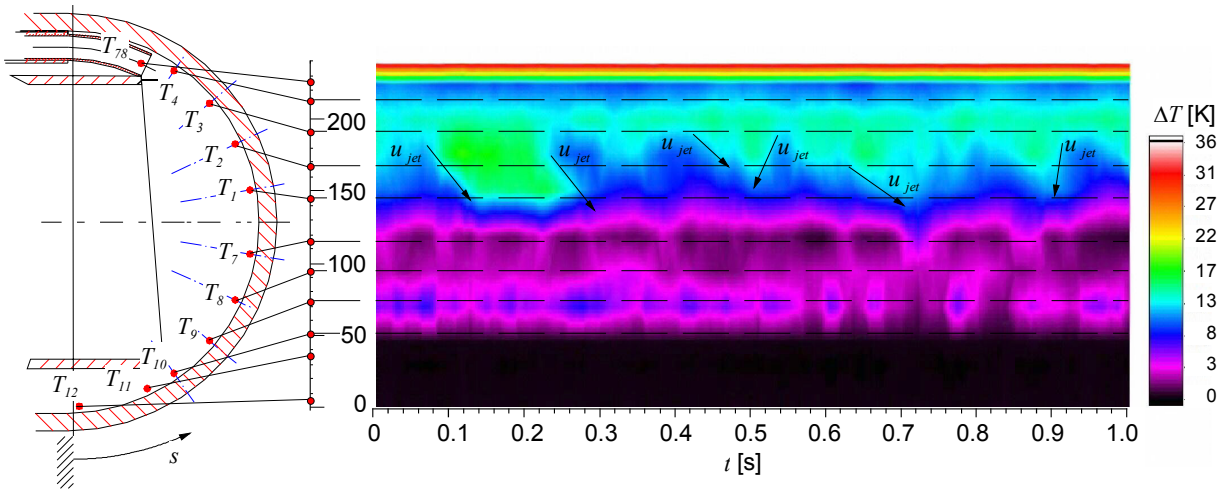

Figure 6.7: Measured isotherms along the lower shell in the nozzle plane (ϕ=0°-180°) as a function of the time t in [s] for the nominal conditions with Q_{main}=18m^3/h, Q_{jet}=1.2m^3/h; T_{in}=300°C and $T_{in,jet}$=360°C.

An indication for the fact that the jet impinges the lower shell, detaches from it and then part of it reattaches the shell is obtained from the calculation of the normalized cross-correlation coefficient $CCC[T_9, T_{78}]$ between the temperatures at T_9 on the shell and the nozzle exit temperature T_{78}. The $CCC[T_9, T_{78}]$ between both shows two relative maxima as depicted in the figure 6.8. These maxima define two delay times. The largest maximum is attributed to the main velocity in the annular gap at τ=0.282s. Because, assuming using the mean velocity in the gap to govern the transport of heat gives a peak at τ=0.291s. The second a smaller peak at τ=0.101s corresponds to the nozzle exit velocity. Using this value and the correlation length Δs one gets $\Delta s/v_{jet}$=τ=0.0912s. From this observation two advection time scales may be inferred in the considered geometry. The absolute value of $CCC[T_9, T_{78}]$ is by far larger than the one between T_{78} and the neighboring position T_8. Here the $CCC[T_8, T_{78}]$ reaches a maximum value of 0.04 only.

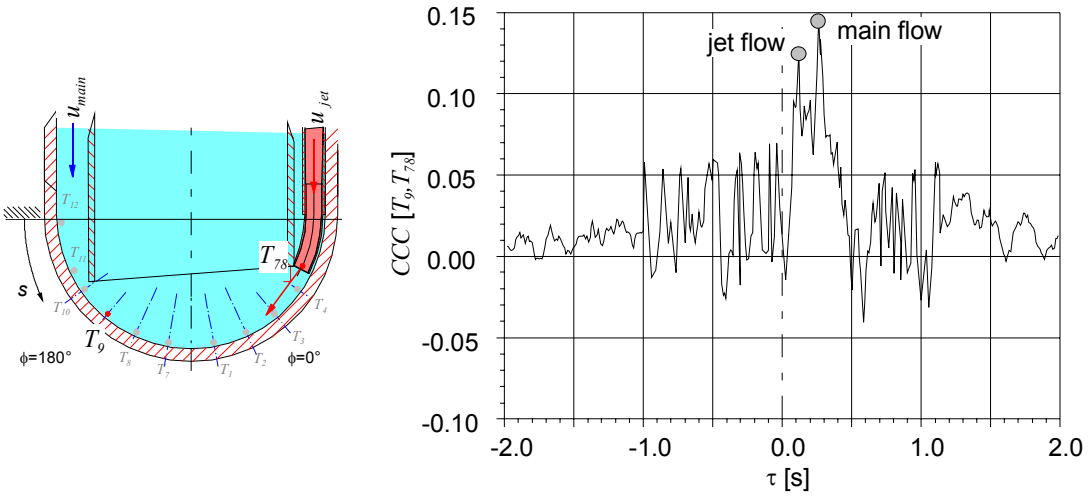

Figure 6.8: Calculated $CCC[T_9, T_{78}]$ between T_9 and $T_{in,jet}$ (T_{78}) as a function of the time delay τ for the nominal conditions with Q_{main}=18m^3/h, Q_{jet}=1.2m^3/h, T_{in}=300°C and $T_{in,jet}$=360°C.

Quite strong fluctuations appear also in the plane perpendicular to the nozzle close to the shell. However, they are more irregular and exhibit stronger fluctuations than in the nozzle plane. Figure 6.9 displays the measured isotherms as a function of time for the nominal conditions. The time scale on the abscissa is 10 times larger than in figure 6.7. The figure 6.9 shows that a random sequence of hot and cold fluid parcels is impinged onto the shell. Here the measured temperatures close to the centerline are lower than those further apart from it. Especially the variations observed at T_{18} close to the riser tube are significantly larger than those close to the centerline at T_{16}. This indicates an impact of the jet on the whole shell.

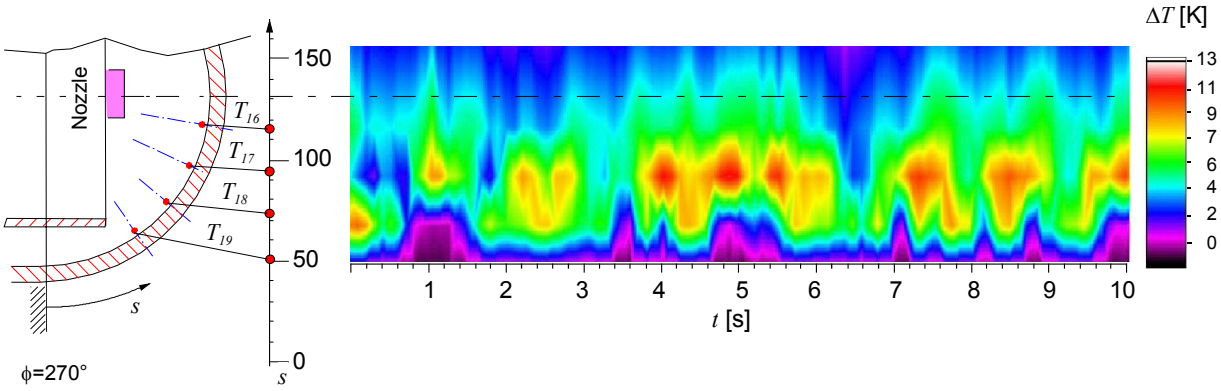

Figure 6.9: Measured isotherms along the lower shell in the plane normal to the nozzle and the sector ϕ=270° as a function of the time t for the nominal conditions with Q_{main}=18m^3/h, Q_{jet}=1.2m^3/h, T_{in}=300°C and $T_{in,jet}$=360°C.

Finally, a calculation of the cross-correlation coefficients $CCC[T_2, T_{16}]$ between T_2 and T_{16} demonstrates that the jets disintegrates into several streams as it hits the lower shell between the positions T_3 and T_1. The figure 6.10 shows the $CCC[T_2, T_{16}]$ as a function of the time delay τ. The graph shows two extrema, which correspond almost to the mean nozzle exit velocity u_{jet} and that of the main velocity in the downcomer u_{main}, indicating a transport of heat and momentum between both positions. The time delay found for both peaks is smaller than the time scale for molecular heat conduction. The sign of both peaks is opposite, because the transport velocity of the main flow is in the opposite direction to that of the jet flow.

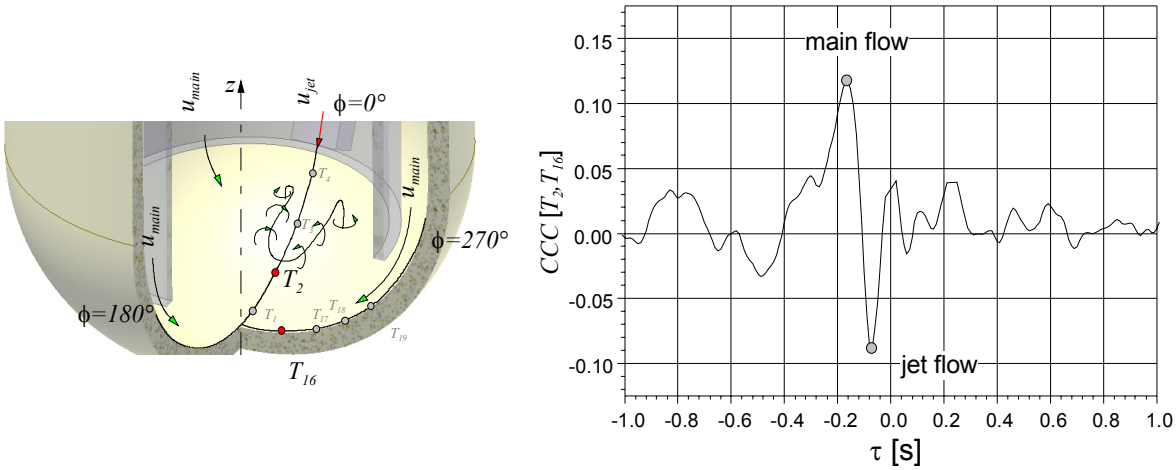

Figure 6.10: Calculated $CCC[T_2, T_{16}]$ between T_2 (sector ϕ=0°) and T_{16} (sector ϕ=270°) as a function of the time delay τ for the nominal conditions with Q_{main}=18m^3/h, Q_{jet}=1.2m^3/h, T_{in}=300°C and $T_{in,jet}$=360°C.

The CCC between the nozzle plane and the one perpendicular to it rapidly decreases, and finally it reaches a value of 0.04 between the positions T_2 and T_{19},. This is not considered as correlated. The hot temperature parcels arising from the jet are transported sidewise along f=270° with the main velocity of the downcomer flow u_{main}. This can be concluded from the $CCC[T_{17}, T_{18}]$ of the two shell positions T_{17} and T_{18}, which exhibits a peak at τ=0.069s corresponding to a mean velocity of 0.58m/s (almost the value of the main flow in the gap u_{main}). This is illustrated in figure 6.11.

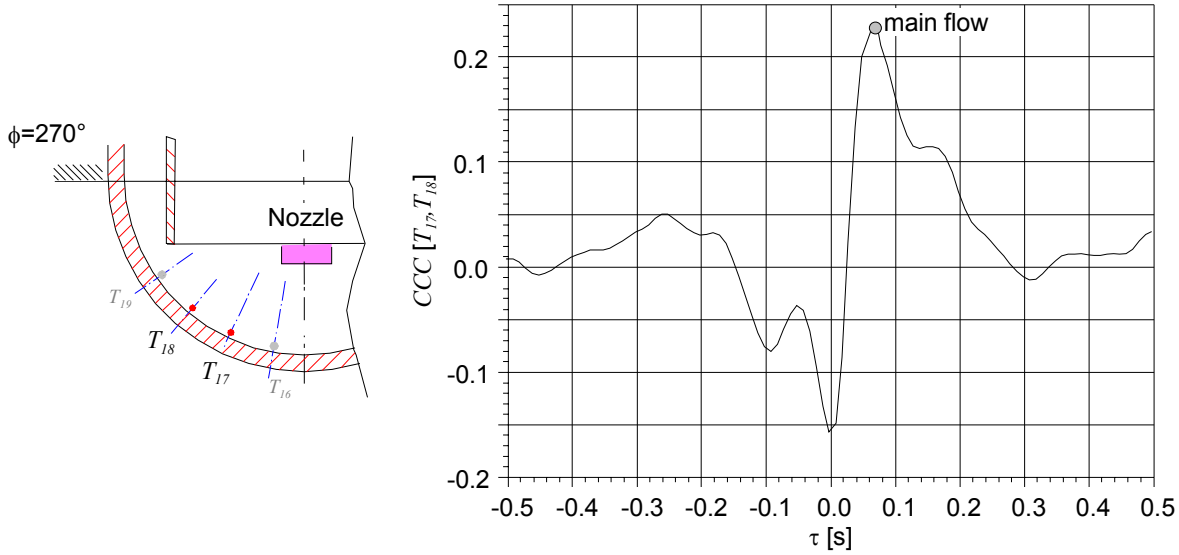

Figure 6.11: Calculated $CCC[T_{17}, T_{18}]$ between T_{17} and T_{18} (sector ϕ=270°; perpendicular to the nozzle) as a function of the time delay τ for the nominal conditions Q_{main}=18m^3/h, Q_{jet}=1.2m^3/h, T_{in}=300°C and $T_{in,jet}$=360°C..

The fluctuation intensity is given by the root mean square values (RMS). In the figures 6.12a and 6.12b the RMS-values of the temperature differences in the nozzle plane and normal to it are shown along the geometry adapted coordinate s. In graph 6.12b the RMS-values are normalized by the adiabatic mixing temperature in order to get an impression of the magnitude of the fluctuation intensity.

In the nozzle plane the peak fluctuations are located at positions, where the jet impinges the hemispherical wall of the shell at T_2(s=168.6mm), T_1(s=146.6mm) and T_9(s=73.9mm). The double peak nature of the RMS-profile corresponds to that of the mean temperatures, see figure 6.2. The normalized fluctuation level is at these locations about 40-50% of the adiabatic mixing temperature. Close to the centerline the fluctuation intensity is considerably lower, which indicates a more stable flow domain.

In the plane perpendicular to the nozzle the temperature fluctuations are even larger than in the nozzle plane. Here, the maximum RMS-value reaches 2.5K at T_{17}(s=130.5mm, ϕ=270°), which is caused by the interaction of the jet and the main flow.

In both planes the RMS-values significantly decrease towards the annular gap to values less than 0.2°K , which corresponds to relative intensities of less than 10%.

Except for the region, where the jet detaches from the wall the fluctuation intensities are reach an order of magnitude, which would be desirable for the MEGAPIE operation. At T_7 and T_8, however, the in the MEGAPIE target the structure at the shell still faces the proton beam, both the low measured turbulence intensities as well as the detachment of the jet could lead to temperatures, which are beyond acceptable limits.

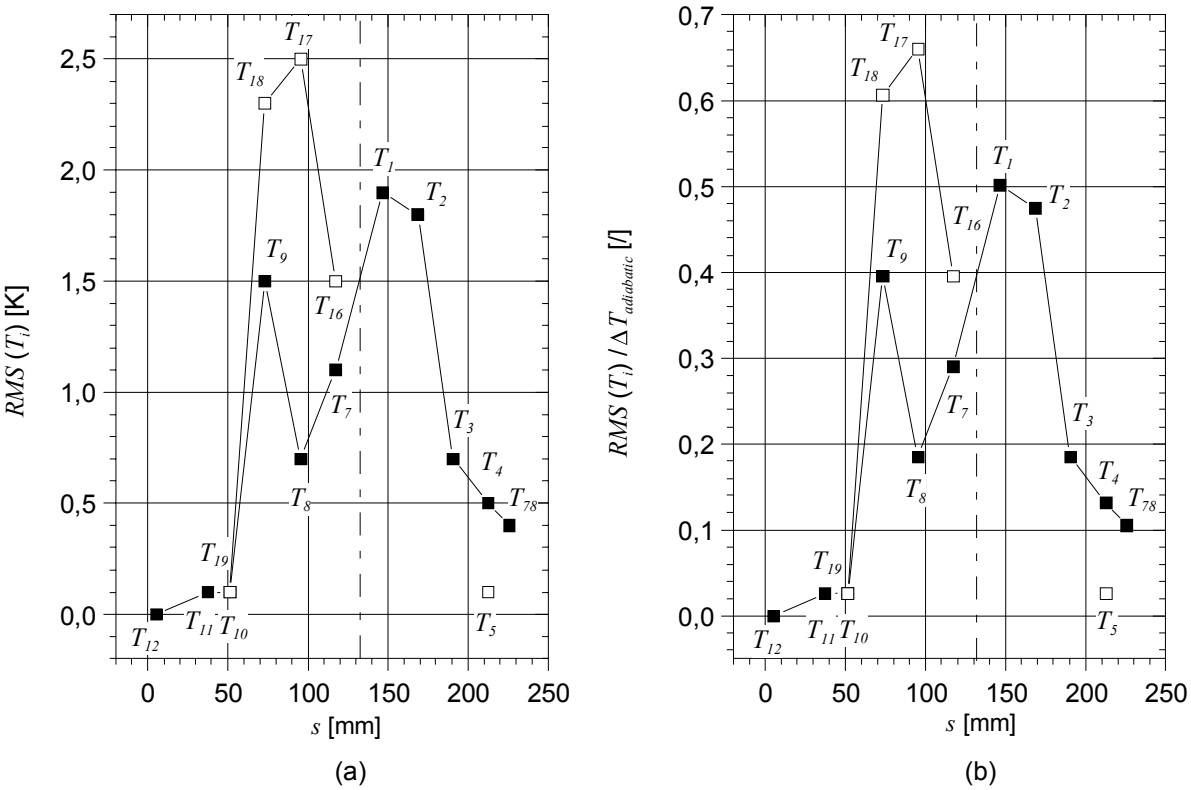

(a) (b)

Figure 6.12: (a) Temperature fluctuation distribution (*RMS*-values) as a function of the geometry adapted coordinate s for ϕ=0° (■) and ϕ=90° (□) and for the nominal conditions with Q_{main}=18m^3/h, Q_{jet}=1.2m^3/h, T_{in}=300°C and $T_{in,jet}$=360°C. (b) same as (a) normalized with the adiabatic mixing temperature $\Delta T_{adiabatic}$.

The temperature fluctuations recorded close to the inner side of the riser wall on the lines ϕ=0°,90° and180° are considerably smaller than those measured near the shell. Only the T_{23} (r=59.5mm, z=43.7mm) on the line ϕ=0°, which is placed free in the flow, shows a higher fluctuation level. The figure 6.13 shows the normalized temperature fluctuations as a function of the axial coordinate z on all three riser wall near lines.

On the line ϕ=0° the *RMS* values of the temperature fluctuations monotonically decreases with ascending z. But, on the line ϕ=180° the *RMS* values increase up to the thermocouple T_{30} (z=74.7mm). As the axial coordinate rises further the fluctuation level continuously drops. On the line ϕ=90° the *RMS* values exhibit an irregular distribution at a low level.

The temporal behavior of the temperature fluctuations close to the wall is displayed in the figures 6.14a-c as a function of the axial coordinate z and the time t on all lines ϕ =0°, ϕ =180° and ϕ =270°. Although the calculated isotherms are interpolated due to the non-equidistant arrangement of the thermocouples characteristic features of the flow can nevertheless be observed. The time records for all elements of the graphs 6.14 are shown in the graphs 6.15a-c in a larger temporal resolution.

The free thermocouple T_{23} (z=43.7mm) close to the riser tube and adjacent to the jet duct at experiences a temperature elevation. The next peak is located at T_{25} (z=105.7mm). Between both peaks the temperature drops to smaller values. This double peak structure is relatively stable, especially at T_{25} the fluctuations are small. This is an indication that the flow is mainly transported transverse to this thermocouple.

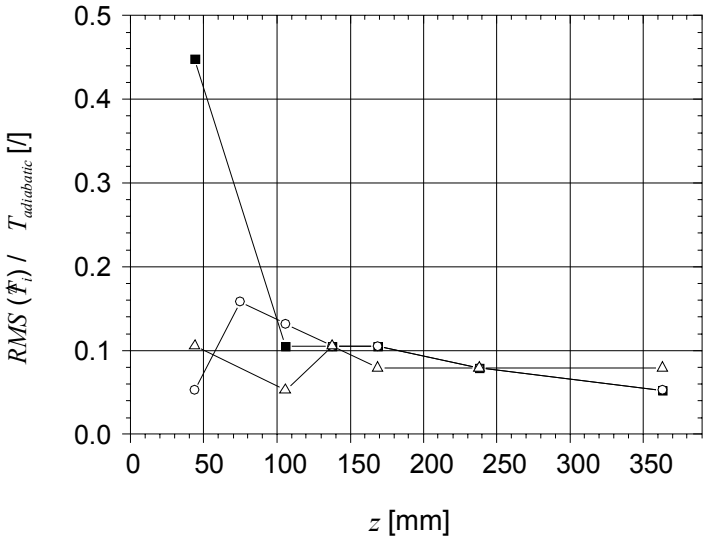

Figure 6.13: Normalized RMS-values of the temperature fluctuations as a function of the axial length z on the lines ϕ=0° (■), ϕ=180° (o) and ϕ=90°(Δ) at r=59.5mm close to the riser tube wall for the nominal conditions.

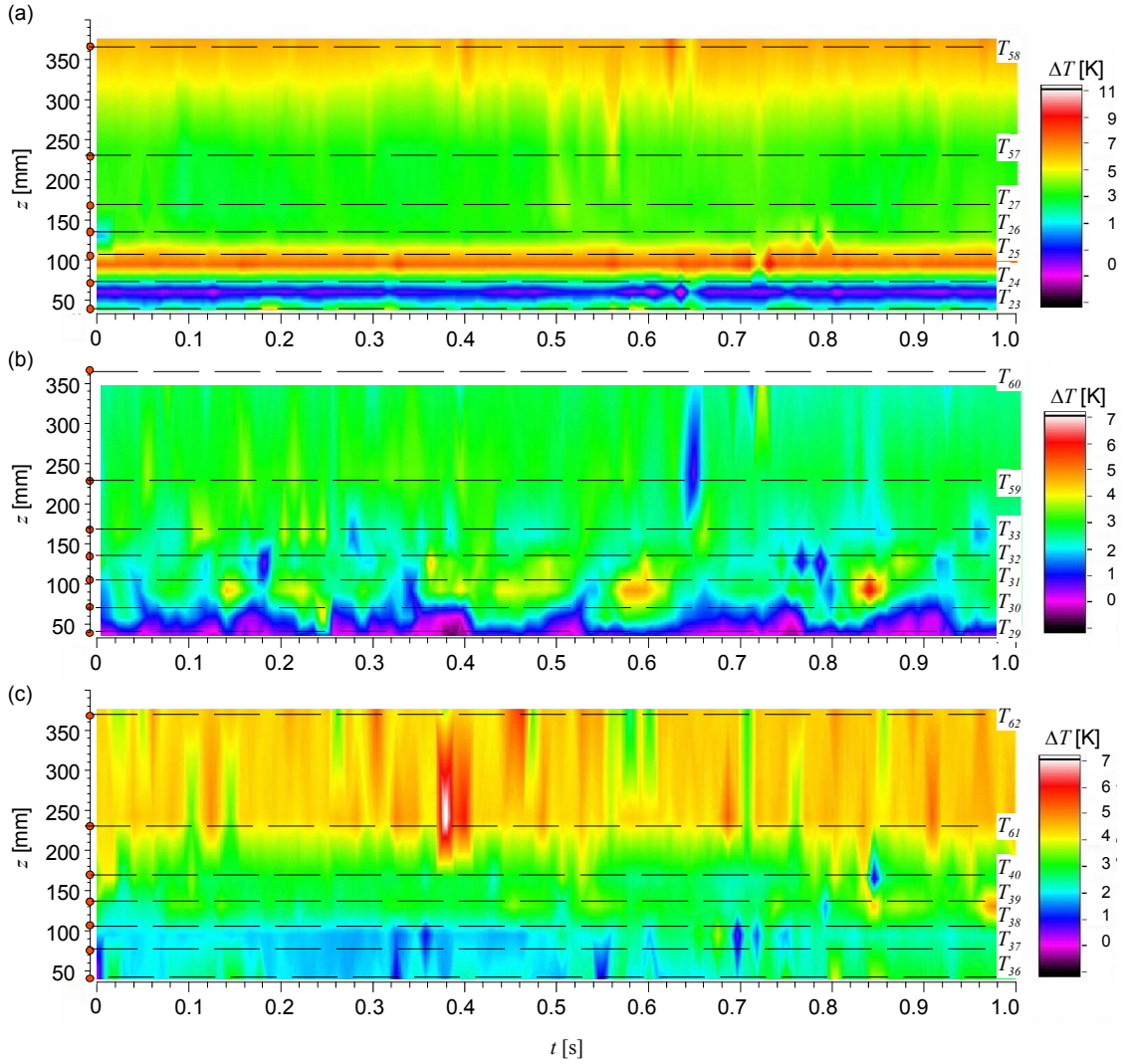

Figure 6.14: Measured isotherms along the inner side of the riser tube at r=59.5mm as a function of the time for the nominal conditions with Q_{main}=18m^3/h, Q_{jet}=1.2m^3/h, T_{in}=300°C and $T_{in,jet}$=360°C. The circles denote the measurement locations. (a) ϕ=0°, (b) ϕ=180° and (c) ϕ=270°.

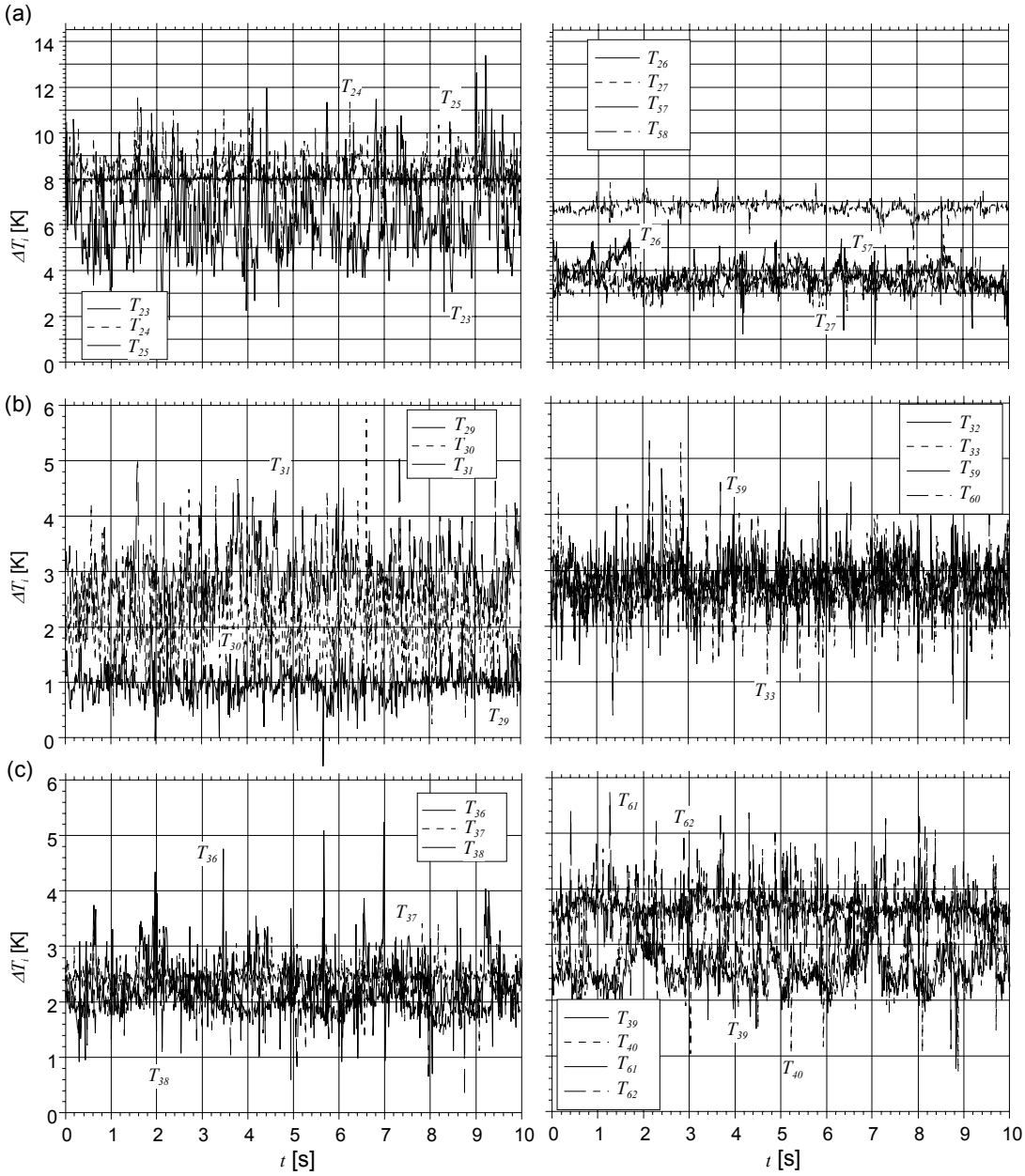

Figure 6.15: Measured time history of the thermocouples T_i located along the inner side of the riser tube at r=59.5mm as a function of the time for the nominal conditions with Q_{main}=18m^3/h, Q_{jet}=1.2m^3/h, T_{in}=300°C and $T_{in,jet}$=360°C. Thermocouples at ϕ=0° (a), ϕ=180° (b) and ϕ=270°(c).

The $CCC[T_{24}, T_{27}]$ between the thermocouples T_{24} and T_{27} on the riser tube at ϕ=0°, which is shown in figure 6.16a, yields a peak value of almost 0.11 at a time shift of τ=0.105s. This is associated with a transport velocity of 0.885m/s. The velocity is about half of the mean nozzle exit velocity. The temporal structure of the temperature distribution and the CCC values indicate, that a part of the jet separates at the lower end of the riser tube and forms a closed vortex, which is continuously produced. All the fluctuations appearing in this vortex are transported downstream in positive z-direction with the main velocity of the riser flow. This inferred from the fact that the $CCC[T_{26}, T_{58}]$ between the elements T_{26} (z=137.7mm) and T_{58} (z=363mm) shows a peak at τ=0.5s which corresponds to a velocity 0.44m/s, which is almost the same as the one of the combined main and jet flow (u=0.4346m/s). This normalized cross-correlation $CCC[T_{26}, T_{58}]$ is depicted in figure 6.16b.

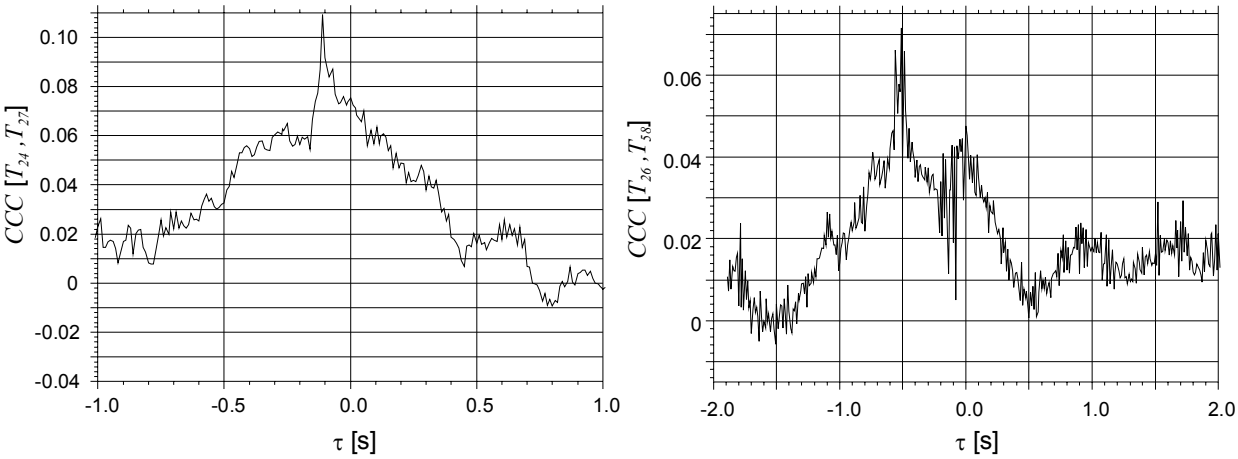

Figure 6.16: Calculated $CCC[T_{24}, T_{27}]$ (a) and $CCC[T_{26}, T_{58}]$ (b) on the line ϕ=0° as a function of the time delay τ for the nominal conditions with Q_{main}=18m^3/h, Q_{jet}=1.2m^3/h.

The temperature in the riser tube on the line ϕ=0° shows an increase at T_{58} (z=363mm). It is suggested that this elevation is caused by a helical upwards motion in the riser tube. A series of normalized cross-correlations indicate a slowly counter-clockwise rotating vortex along the inner wall of the riser tube. Based on the calculated delay time τ a vorticity ω of 1Hz can be calculated. This corresponds to a rotation velocity of 0.052m/s. The figure 6.17 shows the series of normalized cross-correlations $CCC[T_i, T_j]$ along this flow path. The calculated peak values decrease with increasing length of the correlation distance due to the mixing of the thermal energy downstream. This spiral upward motion may be the explanation for the detected asymmetry of the temperatures in the riser tube shown in figure 6.5. It is unclear where this motion comes from.

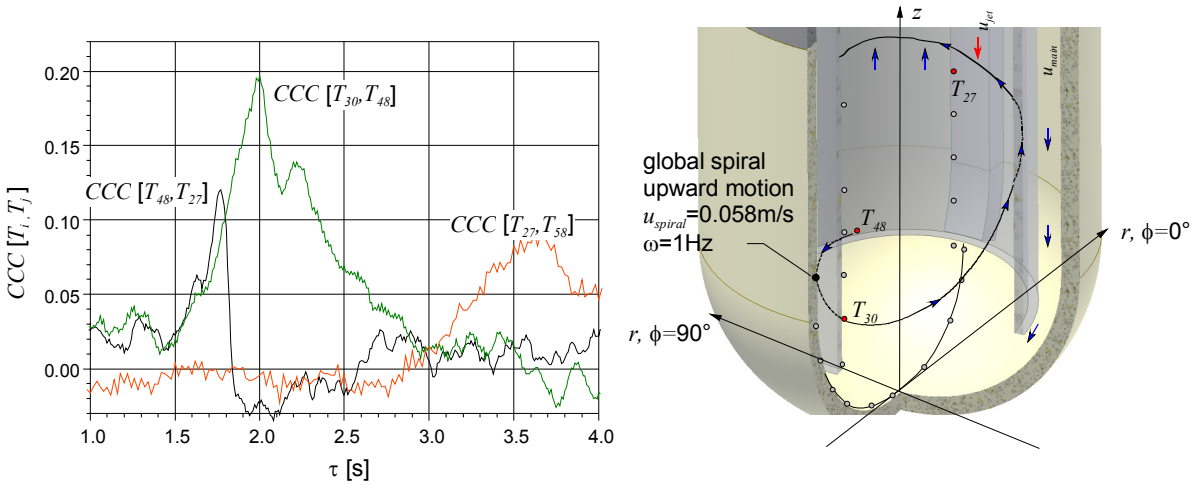

Figure 6.17: Calculated $CCC[T_i, T_j]$ at the inner side of the riser tube (r=59.5mm) as a function of the time delay τ from T_{30} (z=74.7m, ϕ=180°) to T_{48} (z=105.7m, ϕ=90°) then to T_{27} (z=168.7m, ϕ=0°) and finally up to T_{58} (z=363m, ϕ=180°) for the nominal conditions with Q_{main}=18m^3/h, Q_{jet}=1.2m^3/h.

As demonstrated by figure 6.14b the jet hardly reaches the opposite side of the riser tube. Only in the range between z=74.7mm and z=105.7mm a rather irregular arrival of temperature parcels is observed. Downstream the temperature rapidly equalizes and reaches nearly the adiabatic mixing temperature. Here, sometimes irregularly cold parcels appear. In the plane perpendicular to the nozzle at ϕ=270° the temperature is relatively low for small axial z-values. But, as the flow proceeds downstream the temperature rapidly increases. Here, a pattern caused by bypassing of hot temperature parcels is observed.

Finally, an analysis of the lateral flow distribution is conducted in order to determine the vortex structures in the transverse plane. The figures 6.18 shows the temporal evolution of the temperature in the plane ϕ=0°-180° and the one perpendicular to it ϕ=90°-270° as a function of the radius r at a constant height of z=105.7mm. The corresponding time records of selected thermocouples are shown in figure 6.19 with a different temporal resolution.

In figure 6.19a the temperature distribution in the plane ϕ=0°-180°is displayed. It shows quite large temperatures close to neighboring jet duct. The temperature T_{25} nearest to the wall is almost free of fluctuations. Adjacent to it intermittently cold parcels are traveling downstream. Next to these packs of higher temperature travel downstream. The hot and cold packages are appearing in the nozzle plane staggered and shifted to each other. For r>20mm in the sector ϕ=180° the fluctuation intensity decreases and nearly stays constant. Nevertheless, the temperature fluctuations in the riser tube are at the height z=105.7mm at least by a factor of two higher than in the downwards oriented main flow in the annular gap.

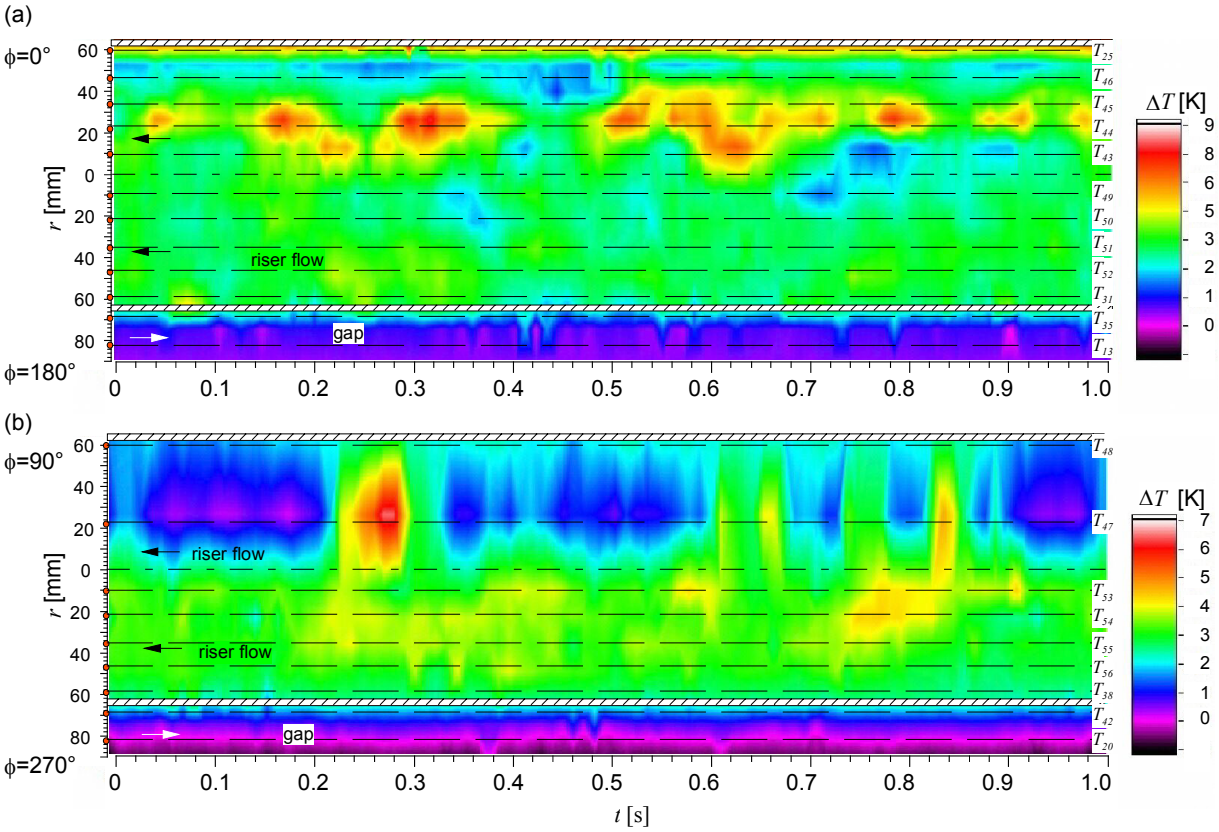

Figure 6.18: Measured isotherms in a height of z=105.7mm as a function of t in seconds for the nominal with Q_{main}=18m^3/h, Q_{jet}=1.2m^3/h. (a) ϕ=0°, (b) ϕ=90°.

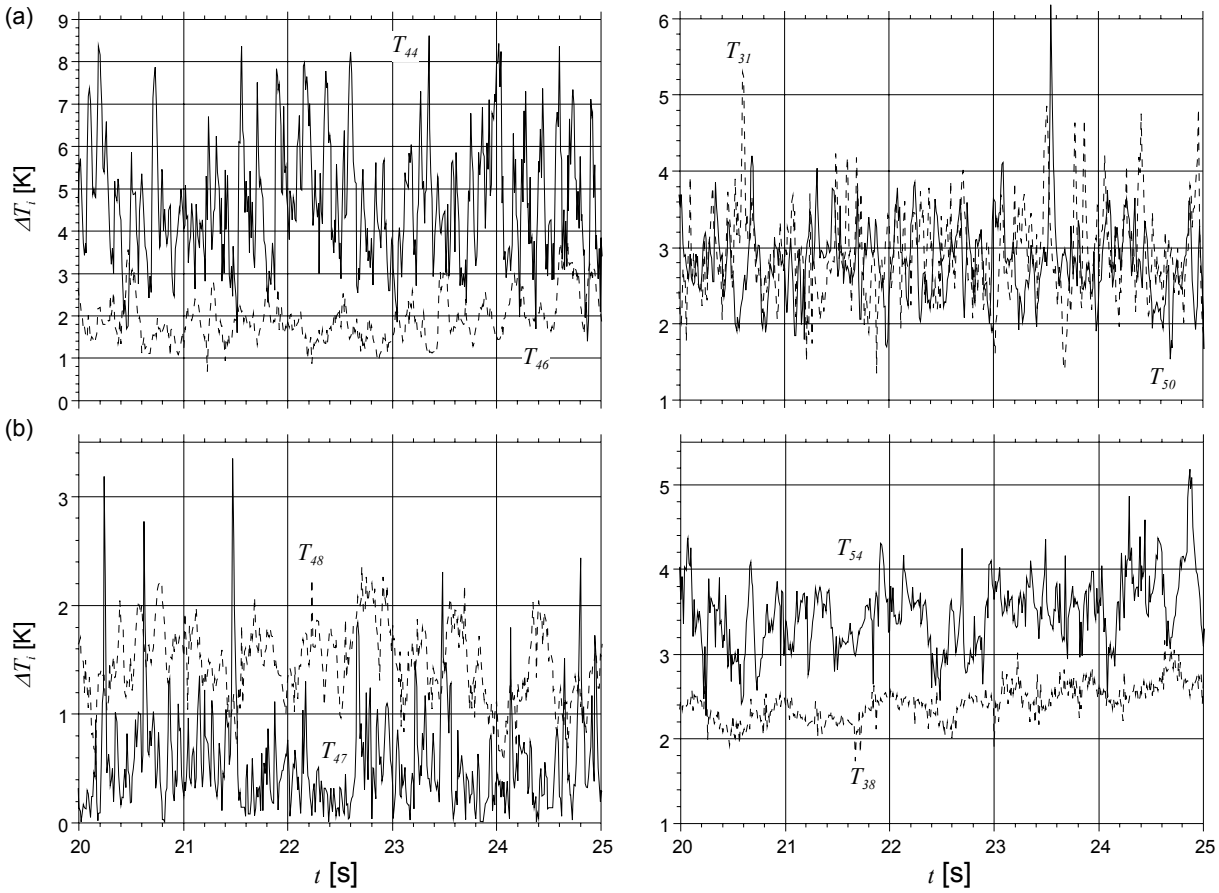

Figure 6.19: Measured time history of selected thermocouples T_i in a height of z=105.7mm for the nominal conditions. Thermocouples on the rake at ϕ=0°-180° (a), ϕ=90°-270° (b).

In the plane perpendicular to the nozzle the temperature pattern is far from being symmetrical as the numerical simulation assumes. In the sector ϕ=90°, temporarily irregular cold and hot temperature parcels are passing through the cross. The temperature difference between these packages reaches values of more than 7K. However, in the opposite sector ϕ=270° the fluctuations are significantly smaller and the maximum peak to peak difference detected is only about 3.2K.

The conjectured reason for this asymmetry is a non-symmetrical detachment of the jet at the lower rim of the riser tube. This experimental finding conforms with the global counter-clockwise helical upward motion indicated in figure 6.17. The origin of this asymmetrical behavior is likely a geometrical asymmetry, which is caused by different thermal expansions of the riser tube during the experiment, because the post-test analysis for isothermal conditions exhibited a geometric set-up. Water experiments conducted in the same geometry have shown a high sensitivity of the flow to weak asymmetries of the geometry and the induction of a swirl flow even for marginal geometrical deviations (asymmetries less than 0.5mm), see Knebel et al (2003) or Eiselt (2003).

The RMS-values of the temperature fluctuations measured in the cross in the plane z=105.7mm support data obtained by the time series. The values which are normalized with the adiabatic mixing temperature, are shown in figure 6.20. On both lines for ϕ=0°-180° and for ϕ=90°-270° the peak value of fluctuation is obtained at r=22.5mm and the RMS values

decrease monotonically towards the outer walls. The RMS values in the nozzle plane are considerably higher than normal to it and reach peak values of 32% of the adiabatic mixing temperature.

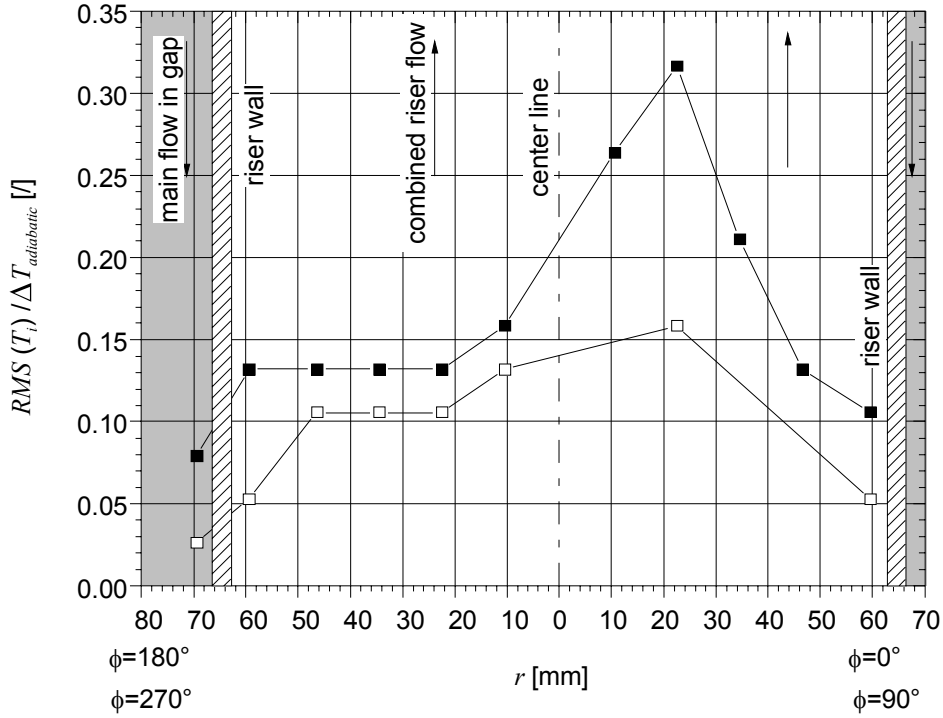

Figure 6.20: Normalized temperature fluctuations in the plane z=105.7mm as a function of the radius r for ϕ=0°-180° (■) and ϕ=90°-270° (□) and the nominal conditions with Q_{main}=18m^3/h, Q_{jet}=1.2m^3/h.

An information about the kind of turbulence appearing in the investigated geometry can be obtained by calculating the power spectral density PSD of the temperature fluctuations at a distinct position. In low Prandtl number fluid flows, which are governed by an isotropic turbulence field, at first an inertia dominated convection domain appears. In this domain the fluid is transported and deformed faster by the flow than the temperature decays diffusively, see Batchelor (1959). Consequently, the energy spectrum (PSD) of the temperature fluctuations decreases by $k^{-5/3}$, where k is the wave number (or frequency k=2π·f). It is followed for higher frequencies by the conduction regime, in which turbulent temperature fluctuations are damped mainly by molecular heat conduction. In this domain the PSD of the temperature fluctuations descends much faster in a power law proportional to $k^{-17/3}$. The transport behavior of a passive scalar like the temperature in a non-isotropic essentially two-dimensional turbulent flow, e.g. in swirl flows or magnetohydrodynamic flows is significantly different. There, the PSD exhibits in the inertia-convective domain a decay of k^{-1}, while in the inertia-conductive range it obeys a k^{-7} power law, see Lesieur and Herring (1985) or Burr (1998).

In figure 6.21 the PSD of the temperature fluctuations at the thermocouple T_{49}, which is located close to the center of the rake at r=-10.5mm (z=105.7mm) is shown as a function of the frequency f. The graph shows that the inertia-convective range with the slope f~–5/3 is fairly well approached by the experimental data: In the inertial-conductive range a decay proportional to f~–5.1 is found. This is larger than predicted for the conductive range and it is significantly larger than for flows dominated by two-dimensional turbulence. This shows that although a weak vortical upward motion is present the turbulence field behaves rather isotropically.

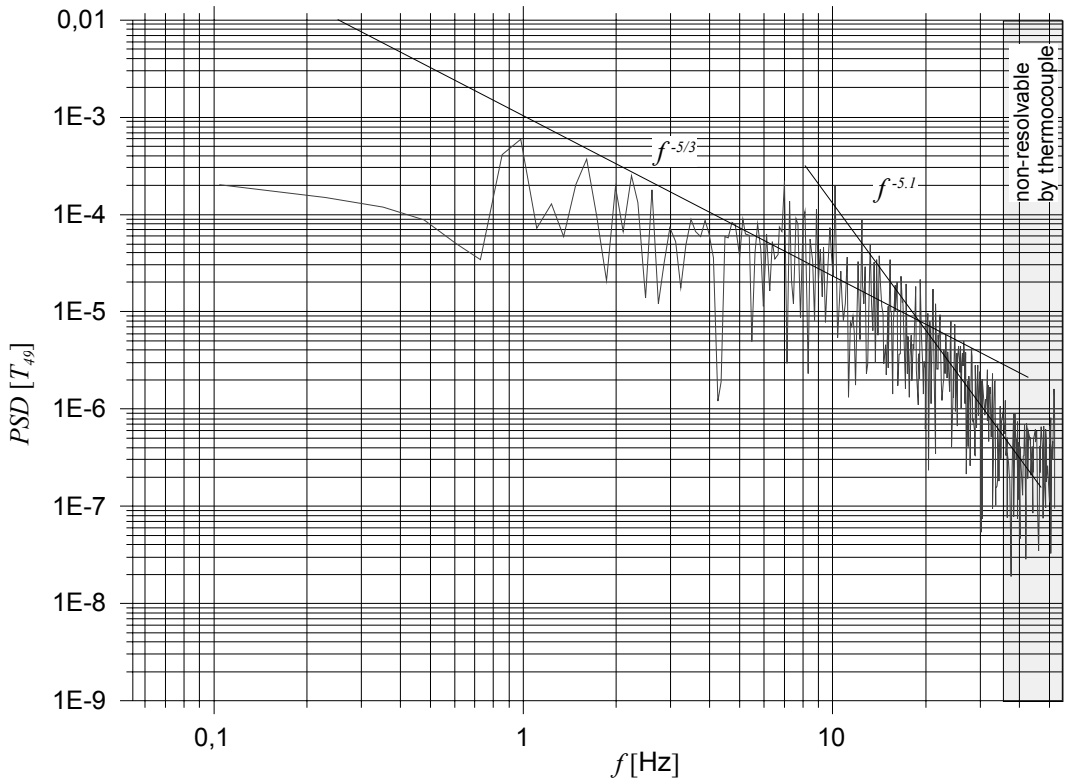

Figure 6.21: PSD of the temperature fluctuations at T_{49} in the plane z=105.7mm as a function of the frequency f for the nominal conditions with Q_{main}=18m^3/h, Q_{jet}=1.2m^3/h.

The numerical simulation predicts due to the differential velocities of main and jet glow the induction of a vortex in each of the halves of symmetrically assumed geometry according to the sketch shown in figure 3.6a. This vortex pair is counter-rotating and is transported spirally upwards by the combined riser flow. Also in the liquid metal experiment this vortex pair can be detected by means of cross-correlations.
In the plane ϕ=0°-180° the signals should exhibit an uncorrelated behavior, which is shown in the figure 6.22b. Bur, in the plane ϕ=90°-270°, significant correlations between T_{38} and T_{53} as well as T_{47} and T_{48} can be identified as depicted in figure 6.22c. This shows the existence of a vortex pair. The results displayed in figure 6.22c suggest a vortex in each of the sectors $0°<\phi<180°$ and $180°<\phi<360°$. The vortex has dimension of the duct diameter and is rotating with a circumferential velocity of u_ϕ=0.38m/s. This vortex pair is counter-rotating, because the $CCC[T_{48}, T_{38}]$ yields a negative sign at a positive time shift τ, which is illustrated in figure 6.22d.

From the spatio-temporal analysis we may now postulate a flow pattern which is schematically shown in figure 6.23. The characteristic velocities determined at discrete positions are real values. The figure illustrates the flow pattern in the lower shell. It consists of several vortices and streaks, which are superimposed. This super-position arising both from the geometrical set-up and the interaction of the main flow with the jet yields to this complex multi-streak and multi vortex pattern. Thus, any change of the flow rate ratio between the main flow and the jet flow will lead to a different composition of the pattern, especially in the lower part of the hemispherical shell.

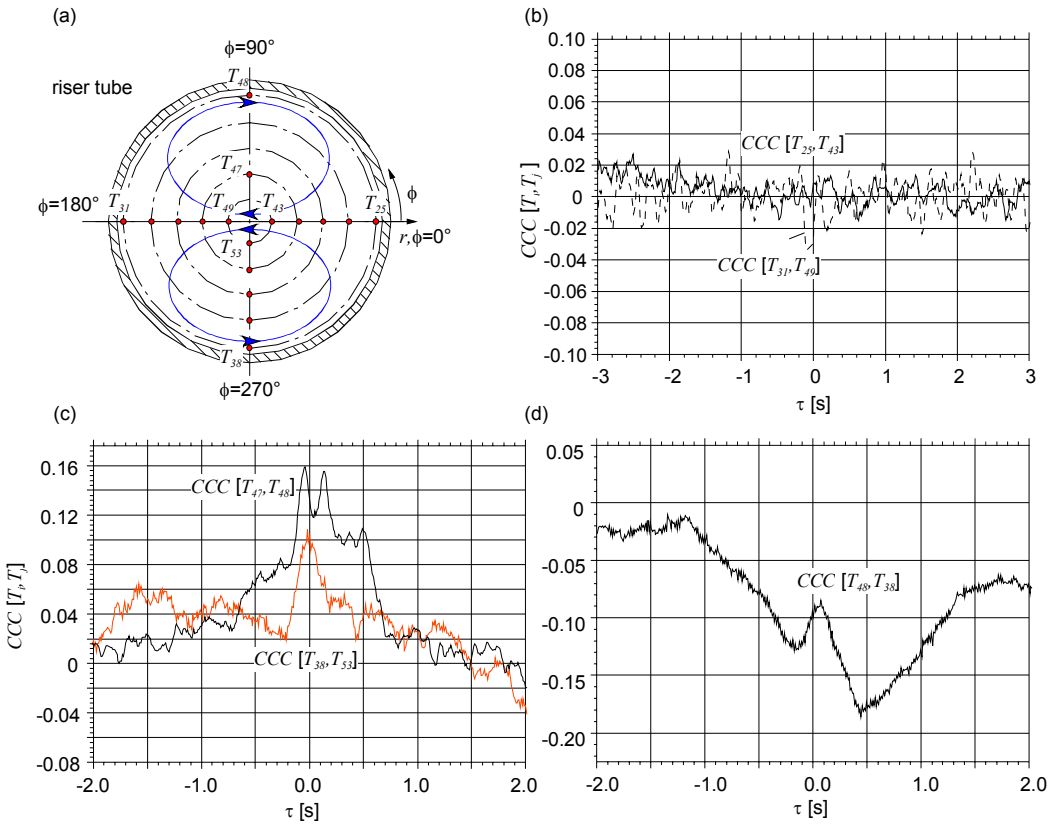

Figure 6.22: (a) Sketch of the thermocouple positions T_i in the riser tube at z=105.7mm. (b) Calculated cross-correlations $CCC[T_{31}, T_{49}]$ and $CCC[T_{25}, T_{43}]$ in the nozzle plane ϕ=0°-180° as a function of the time delay τ. (c) $CCC[T_{38}, T_{53}]$ and $CCC[T_{47}, T_{48}]$ in the plane ϕ=90°-270°. (d) $CCC[T_{48}, T_{38}]$. All calculated correlations are performed for the nominal conditions with Q_{main}=18m³/h, Q_{jet}=1.2m³/h.

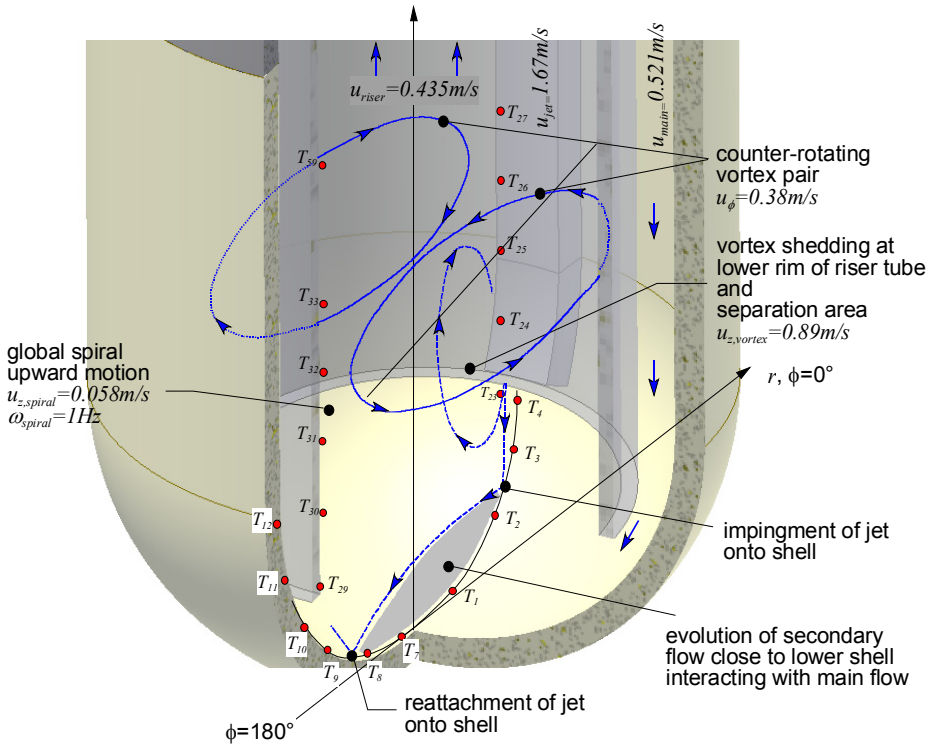

Figure 6.23: Conjectured flow pattern and vortices with their characteristic velocities deduced from the temporal analysis for the nominal conditions.

6.3 Comparison with the numerical simulation

In this context we compare the numerically obtained results with the experimental ones. Within the scope of the numerical simulation several parameters have been tested like mesh size, advections schemes, different turbulence models, effect of the thermal boundary conditions as well as buoyancy effects, for more details see e.g. Batta el. (2004). In this subchapter we compare the experimental data with the numerical ones based on the model assumptions which have been explained in section §5.

Since the local quantities acquired in the experiment are all local temperature readings (except for the local velocity at the instrumentation rod and some pressure values), we restrict our discussion to the comparison of local temperature data. Due to the lack of experimental data for the local velocity, the computed velocity data are used in some cases to explain the phenomena observed. Before entering the discussion, we would like to recall that in the numerical representation of the problem two simplifications of the geometrical arrangement have been made, which affect the obtained data significantly.

The first crucial simplification is related to the inlet of the jet duct into the mock-up at z=1683mm. Within the experimental set-up this is realized as a sharp edged 90° bend introduced from outside into the fluid confining shell, whereas in the simulation a plane parallel inflow is considered. The experimental configuration corresponds to the impinging jet problem associated with a high heat transfer ratio and a significant sideways displacement of the main flow, as explained in section §6.1. As the discussion in this paragraph showed the disregard of the experimental set-up leads only for the impinging jet problem to an underestimation of the jet bulk temperature of about ΔT=5.2K. However, to account for a proper modeling of the inlet a fine resolution of the mesh would be required in this region, which requests more than the currently available computing resources.

The second simplification in the simulation is the disregard of the instrumentation rod. In the experimental set-up the cross-sectional reduction of the riser tube due to the instrumentation rod amounts in to 4%, which increases the mean velocity within the riser by the same value. The impact of this effect on the counter-current heat exchanger of gap flow to riser flow is approximately of the same order.

Finally, the third reduction of the numerical simulation is the assumption of a symmetry of the flow with respect to the plane ϕ=0°-180°. As the experimental data of the mean temperatures in the riser tube as well as the spatio-temporal analysis revealed is the flow far of being symmetric in the riser tube. It is unclear, where the asymmetry arises from but especially this experimental finding makes the direct comparison of the experimental data with the numerical ones problematic.

Finally, before entering the comparison of simulation and experiment a few additional statements to the treatment of the thermal energy transfer in low Prandtl number fluids should be made. Related to the design of heavy liquid metal adapted components adequate turbulence models are required to predict the temperature field in the cooling fluid. The standard models, which are used in commercial codes, are not suitable for the simulation of convective heat transfer in heavy liquid metals several reasons. These models use most a turbulent Prandtl number to describe the turbulent heat transport and hence assume the Reynolds analogy between the convective transport of momentum and heat. This assumption is not valid for liquid metals because the momentum field is mainly turbulence dominated and has only thin viscous wall layers, whereas the temperature field is less turbulence dominated and

has thick wall layers governed by molecular conduction. The problematic use of the Reynolds analogy in liquid metal flows is discussed strongly as shown recently in european activities like ASCHLIM (2003) or other recent papers by Grötzbach et al. (2004). Improved turbulent heat transfer modelling for liquid metals requires more sophisticated methods. Additional transport equations have to be used which characterize the statistics of the temperature fluctuations which have a completely different time scale then the velocity fluctuations. In Carteciano (1996) the TMBF turbulence model is described which consists of a combination of a low–Reynolds number k-ε model and a second order 5–equation heat flux model. Certain model extensions for liquid metal flows were developed and implemented in the TMBF based on the analysis of data from direct numerical turbulence simulations, see Carteciano et al. (1999).

The figures 6.24a, and 6.24b show the measured and calculated temperatures on the lower shell as a function of the geometry adapted coordinate s in the plane ϕ=0°-180° (fig. 6.24a) and the plane ϕ=90°-270° (fig. 6.24b). Additionally, the measured (■) and the computed (O) nozzle exit temperatures are shown in figure 6.24a, which are located at s=225.76mm on a slightly different radius (r=70.6mm).

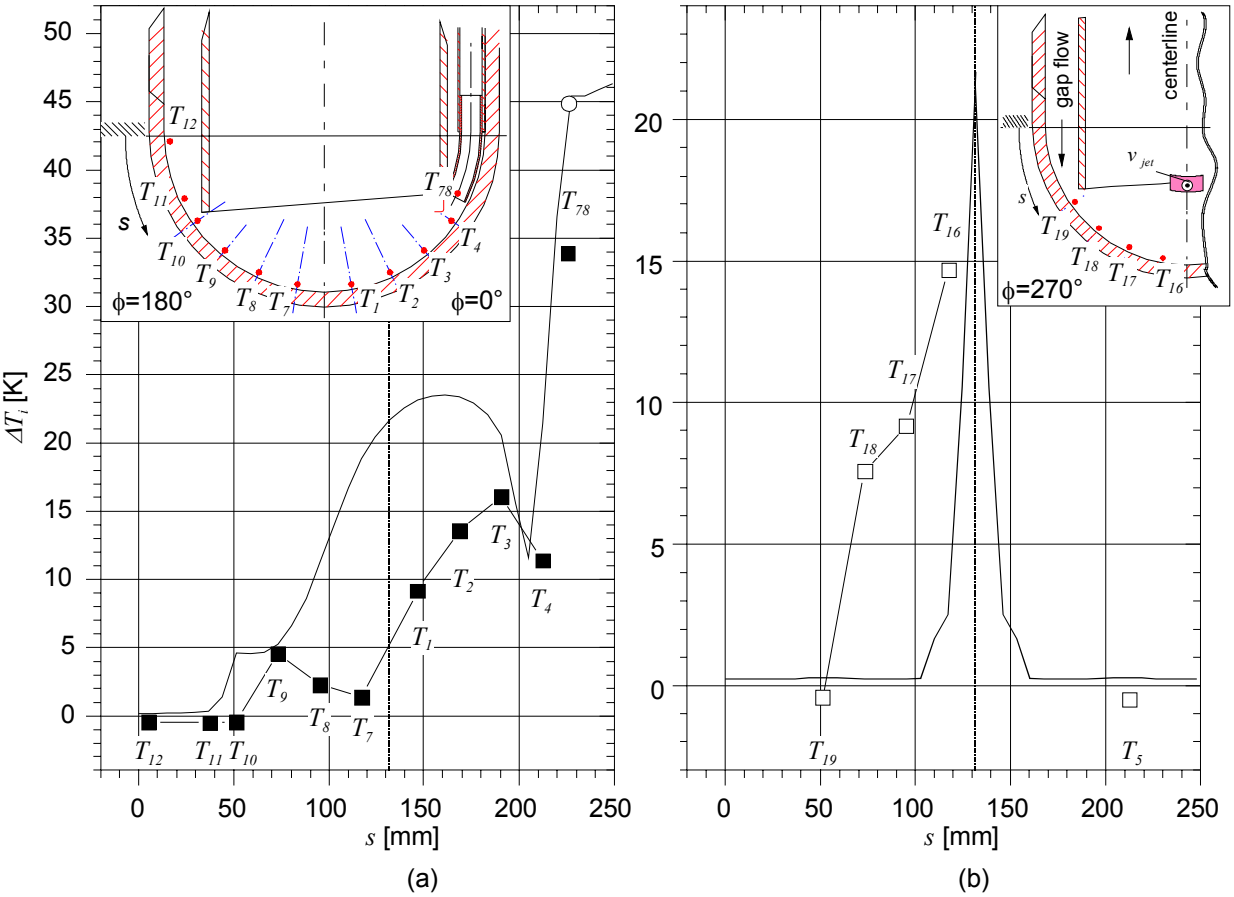

Figure 6.24: Measured (■) and calculated (-) temperature differences on the lower shell as a function of the geometry adapted coordinate s (r=84mm) for the reference conditions Q_{main}=18m³/h, Q_{jet}=1.2m³/h, T_{in}=300°C and $T_{in,jet}$=360°C. (a) plane ϕ=0° and (b) plane ϕ=90°. The open circle in figure 6.24a denotes the calculated nozzle exit temperature.

In the nozzle- plane (ϕ=0°-180°) the simulation shows a qualitatively similar distribution as the experiment. But, significant differences exist with regards to the absolute values of the temperature rise. The calculated temperature are by far higher than the numerical ones, which is attributed mainly to the improper modeling of the jet duct inlet. But, also the deficits of the turbulence models, which uses for the heat transfer a constant turbulent Prandtl number approach, leads to an underestimation of the temperature as the jet and main flow travel in the gap downstream. This was shown e.g. in the experiments conducted by Lefhalm et al. (2003, 2004) or Burr (1998). Although the deficits of such model assumptions in fluids with low molecular Prandtl number are known since the late forties and fifties, see Martinelli (1947) or Kirillov et al. (1959), currently no advanced models are available in the commercial code packages that could handle this issue adequately.

Downstream the nozzle exit the temperature distribution both in simulation and experiment behave qualitatively similar, characterized by a rapid drop directly after the nozzle exit (T_4) and an elevation to a peak value. Beyond this peak the temperature rapidly decreases caused by the jet approaching the wall of the hemispherical shell. When the centerline of the duct is reached at s=131mm, significant differences between simulation and experiment arise. While the numerical simulation suggests a monotonous decrease of the temperature on the whole lower shell down to s=40mm (close to T_{10}) the experiment exhibits a double peak structure suggesting a different velocity field in the plane ϕ=0°-180°. In the experiment the effect of the jet flow on the temperature distribution ends already at s=73.3mm (T_9) and does not cover the whole shell. In contrast to the simulation the jet does not enter the annular gap of the main flow opposite the nozzle.

In the plane ϕ=90°-270° the comparison of the numerical and experimental data shows severe differences. While the numerical simulation predicts only a small region, confined to a distance of $\pm$25mm around the risers centerline, which is affected by the heated jet, the experiment exhibits a broad spreading of the temperature elevation. A direct comparison with the first thermocouple next to the centerline (T_{16} at s=117.3mm) shows a discrepancy of 12.1K between measured value ΔT=14.68K and computed value ΔT =2.51K. In the experiment a considerable temperature rise is even found at the shell close to the riser wall at the thermocouple T_{18} (s=73.3mm, r=54mm, z=22.7mm). Here, a value of ΔT_{18}=7.6K is recorded which is one fourth of the maximum peak temperature difference in the whole lower shell. Especially the considerable discrepancy at T_{18} illustrates, that significant differences between the numerically calculated and the experimentally identified momentum field exist, which are mainly arising from the asymmetry of the flow.

In the figures 6.25 the calculated and the measured temperature rise is shown as a function of the radius r at a height of z=105.7mm for the planes ϕ=0°-180° (fig. 6.25a) and ϕ=90°-270° (fig. 6.25b). The main flow in the annular gap is marked in gray.
The radial temperature distribution of the numerical simulation exhibits in the nozzle plane a completely different behavior compared to the one observed in the experiment, see figure 6.25a. Within the simulation two temperature rise peaks appear, one close to the wall at ϕ=180°, r=62.5mm and a second even higher one at r=6.2mm in the sector ϕ=0°. Both appear in form of thermal stripes with strong radial temperature gradients. Their origin is the detaching of the jet at the lower edge of the riser tube and the transport of the thermal energy towards the sector ϕ=180°. The computation suggests a significant thermal energy transport across the whole riser in this direction, which is able to reach the opposite side resulting there in a temperature rise. The experiment, however, does not show a temperature increase

of similar magnitude. It rather shows a smooth temperature increase up to r>10.5mm in the sector ϕ=180°, where almost the adiabatic mixing temperature is obtained. Close to the wall at r=59.5mm and ϕ=180° the temperature rise drops to values of 3K. Only for r>10.5mm in the sector ϕ=0° two peaks appear one at r=22.5mm (T_{44}) and a second one close to the wall at r=59.5mm (T_{25}). While the first one is caused by a global vortex motion, the latter is attributed to a convective transport of small high temperature packages traveling along the riser wall (see discussion in chapter 6.3).
In the plane ϕ=90°-270° the disagreement between numerical simulation and experiment is smaller in absolute values. But, here also the predicted and observed profiles differ qualitatively. While the experimental data show for in the sector ϕ=270° mm a smooth growth of the temperature from the wall towards the riser centerline and reach almost the adiabatic mixing temperature, the simulation shows significantly smaller temperatures except for the immediate vicinity of the centerline. In the centerline domain for radii r<16mm a temperature rise of 8K is computed corresponding to a radial heat flux q''=5500Wm^{-2} ($q''=\lambda\ \Delta T/\Delta r$). Additionally, in the range of the transition from the bulk of the riser tube towards the high temperature rise domain in the center the temperature has minima at r=19.5mm. Thus the computational results suggest that the heat transfer in this plane is governed more by molecular conduction than by convective processes.
In both graphs of figure 6.25 the temperature gradients of the simulation are considerably larger than for the experimental observations. The formation of large gradients, however, suggest a weak interaction of the main flow with the jet flow. In contrast to the numerical simulation the experimental data exhibit only small gradients, except for the wall adjacent to the jet duct, which shows that the turbulent mixing process is finished at this height to a large extend.
The most severe observation in graph 6.25 is that the radial temperature distribution in the plane ϕ=90-270° is not symmetric. This cannot be reproduced by the calculations which assumed symmetry. Thus the flow field numerically calculated differs very much from the experimental one. Consequently a further comparison of the numerical and experimental data yields no additional information in the graphs 6.26 and 6.27 are shown for completeness.

Figure 6.26 compares the measured and computed temperature distributions close to the riser wall at a radius of r=59.5mm and the sector ϕ=0° for increasing axial coordinate values of z.

The figure 6.27 compares experimental and numerical temperature distributions on the lines r=59.5mm in the sector ϕ=90° (a) and the sector ϕ=180° (b).

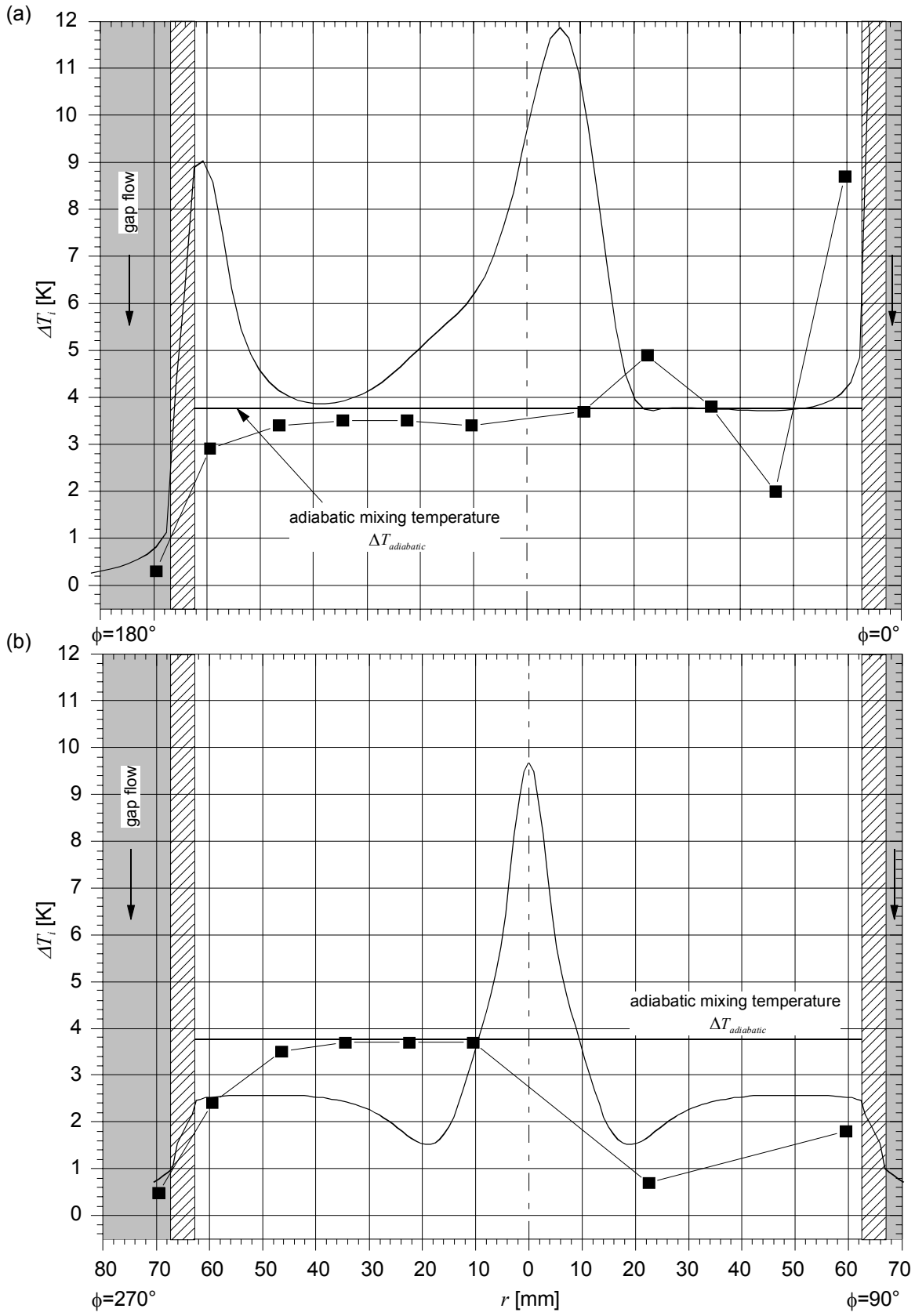

Figure 6.25: Comparison of the computed (—) and measured (■) temperature distribution as a function of the radius r at a height of z=105.7mm and the nominal conditions Q_{main}=18m^3/h, Q_{jet}=1.2m^3/h, T_{in}=300°C and $T_{in,jet}$=360°C. (a) ϕ=0°-180°and (b) ϕ=90°-270°.

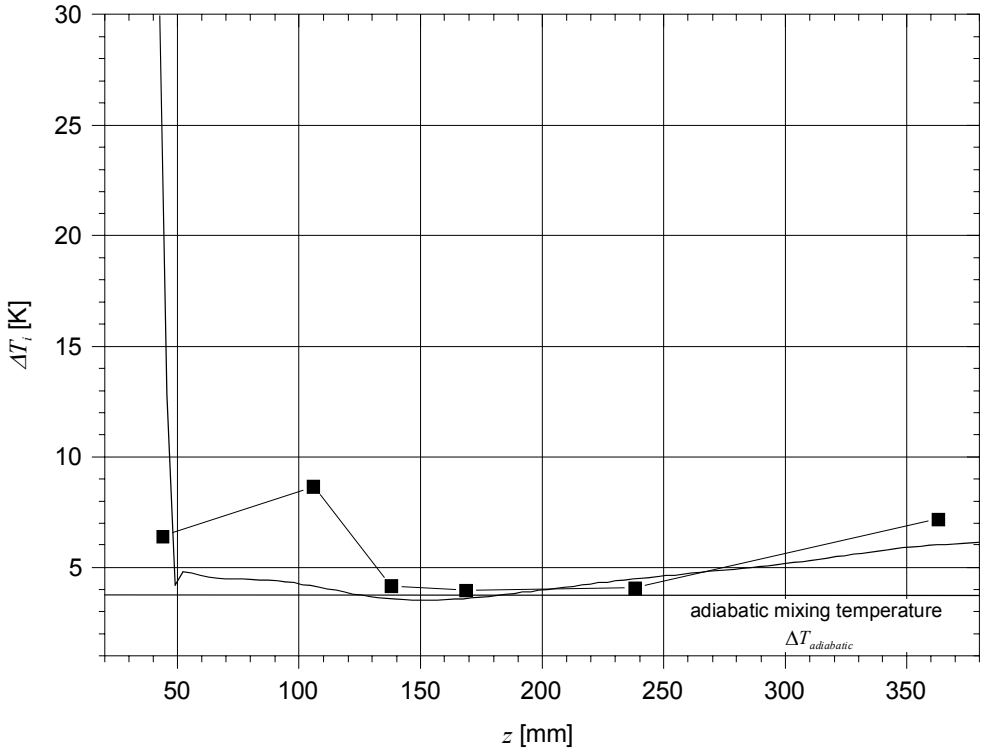

Figure 6.26: Comparison of the computed (—) and measured (■) temperature rise distributions at r=59.5mm as a function of the axial length z in the sector ϕ=0° for the nominal conditions with Q_{main}/ Q_{jet}=15, T_{in}=300°C and $T_{in,jet}$=360°C.

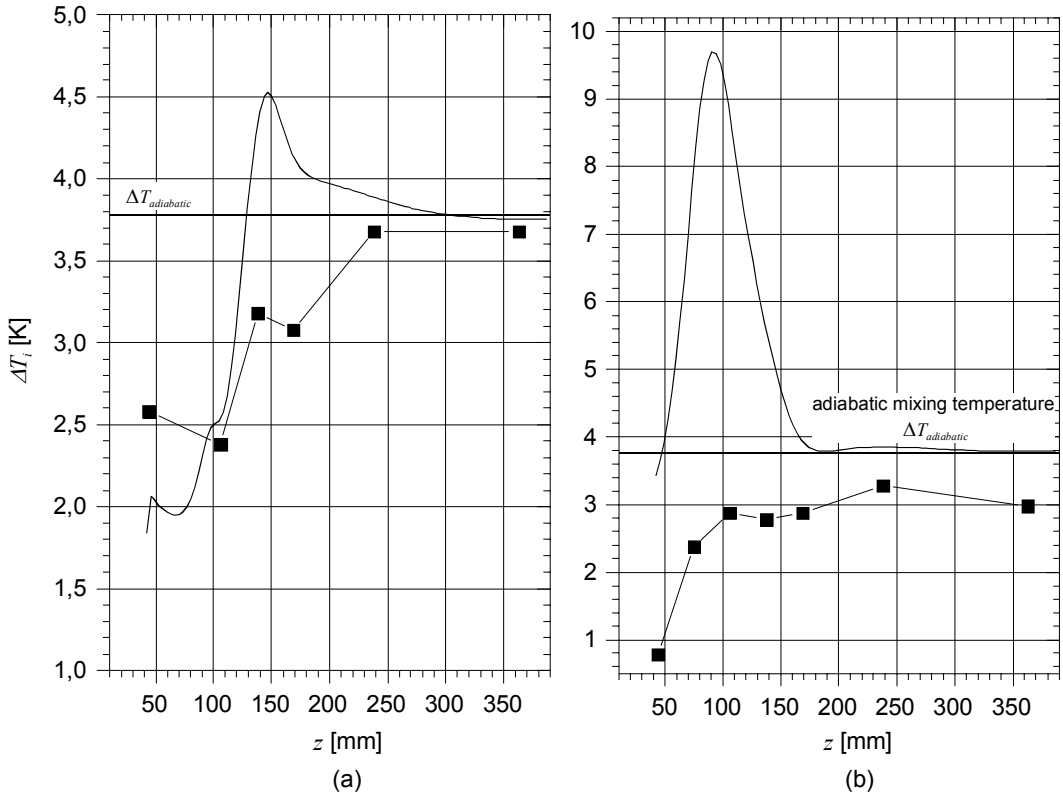

Figure 6.27: Comparison of the computed (—) and measured (■) temperature distributions at r=59.5mm as a function of the axial length z and the nominal conditions with Q_{main}=18m^3/h, Q_{jet}=1.2m^3/h, T_{in}=300°C and $T_{in,jet}$=360°C. (a) sector ϕ=90°and (b) sector ϕ=180°.

6.4 Summary of the nominal operation mode with Q_{main}/Q_{jet}=15

Most of the experimental effort was spent on the investigation of the nominal mode with a flow rate ration of Q_{main}/Q_{jet}=15, because this mode is envisaged to be the operational mode of the MEGAPIE target. In summary the analysis of this flow rate ratio shows, that

a.) the flow in the lower target shell is highly time dependent, although at both inlet flows (main flow and jet flow) an insignificant fluctuation level was measured. The thermocouples on the shell in the nozzle plane (ϕ=0°-180°) show temperature fluctuations of up to 50% of the adiabatic mixing temperature. The RMS values are highest close to the shells centerline. On the centerline in the plane perpendicular to the nozzle (ϕ=90°-270°) the RMS values of the temperature fluctuations exhibit even higher values.

b.) An analysis of the time records, the spatio-temporal time series and the $CCC[T_i,T_j]$ in the nozzle plane ϕ=0°-180°, shows that the jet impinges on the shell before reaching the centerline and detaches from it. The jet splits off in several streams and one of the streams reattaches the shell on the other side of the centerline. The calculation of the cross-correlations between several discrete positions in the nozzle plane shows that in this process, both main and jet flow, take actively part in, because both characteristic velocities are indirectly sensed.

c.) By conducting a series of $CCC[T_i,T_j]$ calculations several time scales, which are not attributed to turbulence were discovered. They show that in the riser tube a global helically upwards directed vortex exists. This vortex is responsible for the non-symmetry of the mean temperature profiles in the plane ϕ=90°-270°. Superimposed to this global helical motion two other vortex structures are identified. The first one is a separation vortex, in which a part of the jet flow separates at the lower edge of the riser tube and is transported by the main flow downstream. The second one are two counter-rotating vortices, which rotate in the planes z=constant (vorticity vector in $\pm z$-direction) and are separated by the plane ϕ=0°-180°.

d.) As the flow proceeds downstream in the riser the temperature fluctuations decrease. In a height of z=105.7mm the mean RMS values are about 15-20% of the adiabatic mixing temperature. Close to the walls even 10% and less are obtained. Also the differences in the RMS distribution between the nozzle plane (ϕ=0°-180°) and transverse to it (ϕ=90°-270°) decrease.

e.) The power spectral density of the temperature records gives an indication for an isotropic turbulence structure in the lower shell. Most of the thermal energy fluctuations are located in a frequency spectrum larger than 1Hz, which does not yield in the adjacent structural material to critical temperature oscillations causing fatigue effects.

f.) The comparison of the experimental and numerical data show, that any disregard of the specific inlet conditions of the jet flow (90°-bend) into the geometry even far upstream affects the temperature level calculated in the whole domain.

g.) The numerical simulation shows that the jet and the corresponding temperature rise covers the whole shell in the plane (ϕ=0°-180°), which could not be verified by the experimental data. Also in the plane perpendicular to the nozzle (ϕ=90°-270°) the nu-

merical simulation shows a strongly confined jet traveling along the shell, while the experimental data exhibits a significant radial temperature spreading attributed to both an interaction of the jet with the shell and an interaction of jet flow with the main flow.

h.) Due to the experimentally detected asymmetry of the flow in the riser tube and in contrast the assumed symmetry in the calculation a detailed study of the validity of the turbulent heat transport models used in the simulation can not be drawn.

i.) The experiment shows a well mixing of the thermal energy in the riser tube already in a small distance away from the shell, which is expressed by small temperature gradients.

Although the well thermal mixing behavior in the riser tube is desired in the MEGAPIE application in order to keep the thermal stresses and the differential elongation within acceptable limits the flow rate ratio Q_{main}/Q_{jet}=15 is likely not the best operation mode for the target. The experimental data, both of the liquid metal and the water tests, showed that for this flow rate ratio the jet does not cool the lower bottom of the shell at the centerline effectively, where the highest temperature due to the proton beam will appear. The jet rather hits the wall before reaching the lower bottom of the shell and splits off in several streams. Also the flow is highly time-dependent the

The liquid metal experiment and also the water test exhibited that the geometry is highly sensitive to marginal geometrical deviations, which causes a flow asymmetry. Even smallest asymmetries in the set-up yield in both experimental series to an asymmetric flow in the target geometry so that also in MEGAPIE such a scenario can likely be expected.

7 Analysis of the temperature field in the PbBi experiment for other flow rate ratios

Start-up and shut- down procedures or other operational purposes may lead to different flow rate ratio than the envisaged nominal case with Q_{main}/Q_{jet}=15. Also the previous analysis showed that the nominal flow rate ratio is likely not the best operation mode for an effective cooling of the lower target shell. The aim of this chapter is search for a flow rate ratio in which the jet covers the whole lower shell in both directions, in order to ensure a sufficient cooling of the window and thus a safe operation of MEGAPIE. Another objective is to investigate the turbulent mixing in the geometry, the temporal behavior and the stability of the flow for each of the flow rate ratios set-up during the liquid metal experiments. As the water experiments have shown, see e.g. Stieglitz et al. (2005) the flow rate ratio between main and bypass flow determines the establishing flow pattern in the lower shell for Reynolds numbers Re>2.10^4.

In order to allow a comparison the experimental results for the different flow rate ratios, the temperature readings are normalized with the adiabatic mixing temperature $T_{adiabatic}$, which can be calculated performing a thermal energy balance between the individual inlet flows and the outlet flow. The resulting calculated adiabatic temperatures account also for the heat losses of the test module to the ambient environment. In order to determine the heat

losses in the considered geometry the temperatures at the outside of the thermal insulation are continuously monitored at four axial positions. The heat losses itself are calculated analytically and are about 184W in the cylindrical part, which is below 1% of the total thermal energy input. A more detailed description is given in Appendix B

7.1 Variation of the main flow

In this chapter the main flow is varied from Q_{main}=9m^3/h up to Q_{main}=24m^3/h in six steps, while the jet flow Q_{jet} is kept constant at 1.2m^3/h. Also the inlet temperatures of main and jet flow were set to constant values with T_{in} =300°C for the main flow and $T_{in,jet}$=360°C for the flow.

The corresponding quantities of this flow rate variation like the mean velocities in the gap and riser tube, the adiabatic mixing temperatures as well as the kinetic and densimetric Froude numbers are listed in table 7.1. The nominal operation mode with Q_{main}/Q_{jet}=15 is highlighted. As table 7.1 shows the densimetric Froude number is in all case significantly larger than unity in the investigated parameter range and hence in all cases the jet behaves as an inertial jet.

Q_{main} [m^3/h]	$u_{mean,gap}$ [m/s]	$u_{mean,riser}$ [m/s]	Q_{main} / Q_{Jet} [/]	$T_{adiabatic}$-T_{in} [K]	Fr_{kin} [/]	Fr_{dens} [/]
9	0.260	0.231	7.5	7.06	20.71	2576
12	0.346	0.299	10.0	5.47	20.30	2525
15	0.433	0.367	12.5	4.48	19.79	2461
18	0.520	0.437	15.0	3.79	19.20	2388
21	0.606	0.503	17.5	3.24	18.40	2289
24	0.693	0.570	20.0	2.86	17.42	2165

Table 7.1: Mean velocities in the annular gap and riser flow in [m/s], adiabatic mixing temperature rises in [K], kinetic and densimetric Froude numbers for varying main flow in the heated jet experiment for a constant jet flow rate of Q_{jet}=1.2m^3/h and T_{in}=300°C and $T_{in,jet}$=360°C.

7.1.1 Mean temperature distribution for the main flow variation

In the figures 7.1 and 7.2 the measured mean temperature differences ΔT along the lower shell are shown as a function of the geometry adapted coordinate s for six different volumetric flow rates of the annular gap flow in both planes ϕ=0°-180° and ϕ=90°-270°. Like in the previous chapter all temperature differences shown here use the inlet temperature of the main flow T_{in} as a reference, except if it is otherwise stated.

First, the temperature distribution in the nozzle plane (ϕ=0°-180°) is discussed. With increasing main flow the nozzle exit temperatures decreases monotonically. Responsible for this is the enhanced convective heat transport from the jet duct towards the adjacent main flow. As the flow exits the nozzle the thermocouple T_4 experiences only a minor part of the heated jet for all investigated flow configurations. This is expressed by a local minimum of

the temperature there. Beyond this position, however, the temperature distributions significantly differ from each other. For the lowest main flow rate Q_{main}=9m^3/h the temperature continuously increases from T_4 over T_3, T_2 to T_1. With decreasing s from T_1 the temperature successively decreases down to T_{12}. But, even at the position T_{12} (r=84mm, z=82mm,ϕ=180°), which is far in the annular gap, a significant temperature rise of ΔT=5.3K is found. This temperature distribution shows that the jet covers the whole fluid-solid interface along the lower shell and it even enters upwards into the annular gap and displaces there a part of the main flow.

As the flow rate of the main flow is increased the position of the temperature peak at the lower shell moves from T_1 (for Q_{main}=9m^3/h) to T_2 (Q_{main}=12 and 15m^3/h) to T_3 (Q_{main}=18,21 and 24m^3/h). Also the shape of the temperature distribution changes. For Q_{main}=12m^3/h the temperature increases continuously up to T_2 and then monotonically drops up to T_{12}. But, in contrast to the previously discussed case a significant temperature gradient close to the centerline appears indicating a flow separation there. Nevertheless, the jet flow is still capable to penetrate into the annular gap of the downcomer as the temperature difference of 3.8K at T_{11} shows.

A similar behavior of the interaction of main flow with the jet flow is observed for Q_{main}=15m^3/h, because both cases exhibit a similar temperature distribution. The only difference found between both cases is, that for Q_{main}=15m^3/h the momentum of the jet in the nozzle plane is not strong enough to enter the annular gap of the downcomer. The temperature distribution pattern qualitatively alters its shape as the main flow is increased further. For the nominal case and for Q_{main}=21 and 24m^3/h a double peak structure of the temperature is found along the lower shell. While the location of the first temperature peak remains at the position T_3 the second temperature peak is shifted from T_9 (Q_{main}=18m^3/h, nominal case) to T_8 (Q_{main}=21 and 24m^3/h). In all of these three cases the temperature close the centerline is low. The strong main flow bounds the jet to hit the shell close to T_3 as in the reference case and hence the highest temperature is recorded there. But, in contrast to the reference case an increasing main flow rate yields to the fact that the momentum of detached jet is hardly sufficient to reattach the shell beyond the centerline. For Q_{main}=21m^3/h a second peak at T_8 can be identified. But at the highest main flow rate the temperature difference almost disappeared.

The complexity of the interaction of the main flow with the jet flow is illustrated by the temperature distribution in the plane normal to the nozzle ϕ=90°-270°, which is shown in figure 7.2.

For the lowest main flow rate Q_{main}=9m^3/h the jet flow is rather confined to the centerline and spreads in radial direction. The temperature drops from T_{16} to T_{17}, T_{18} to T_{19}, indicating a mixed conductive convective heat transport governed by the jet flow. In case of main flow rates of Q_{main}=12 or 15m^3/h a double peak of the temperature is observed with the first maximum close to the centerline at T_{16} and a second one at T_{18}. The double peak disappears as the main flow rate is increased further to Q_{main}=18m^3/h where again a continuous decay of the temperature from T_{16} to T_{19} is observed. However, as the main flow grows to values of Q_{main}=21 and 24m^3/h the temperature at T_{16} drops considerably. At the discrete measurement positions temperature peaks are located at T_{17} (Q_{main}=21m^3/h) and even further away from the center at T_{18} for Q_{main}=24m^3/h. Adjacent to this temperature peaks the temperature monotonically drops on both sides.

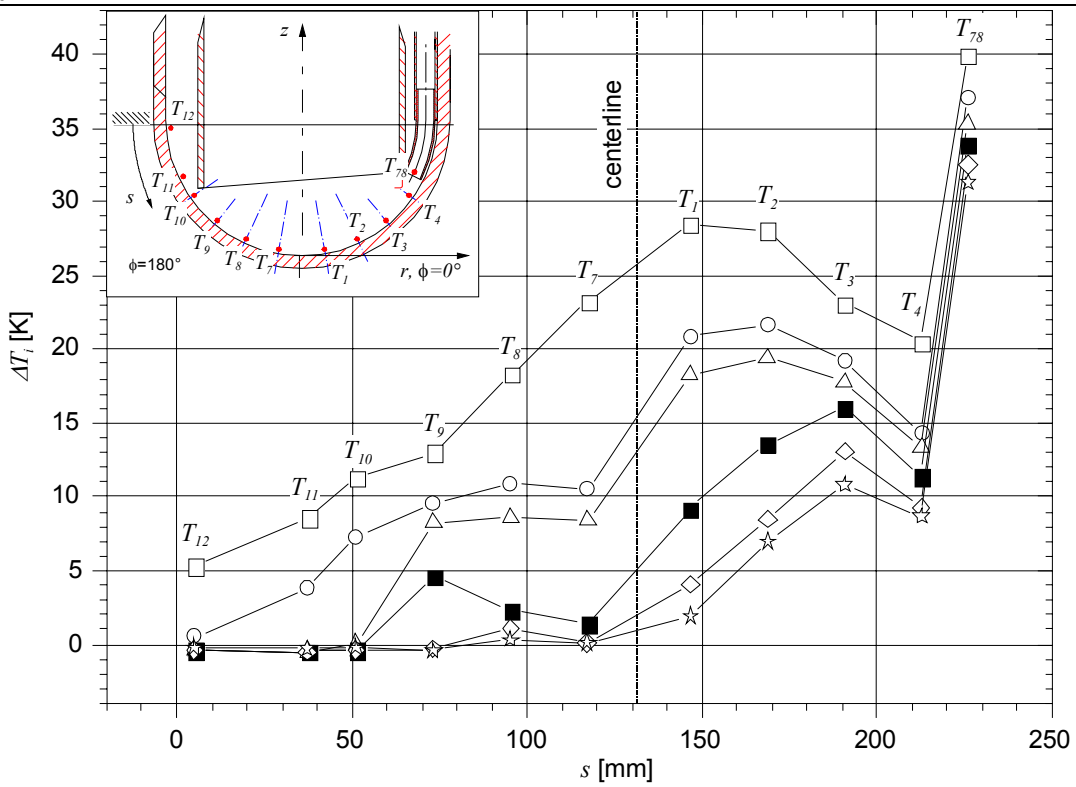

Figure 7.1: Measured temperature distribution as a function of the geometry adapted coordinate s in the plane ϕ=0°-180° for different main flow rates Q_{main} and constant jet flow rate Q_{jet}=1.2m^3/h; T_{in}=300°C and $T_{in,jet}$=360°C. (□) Q_{main}=9m^3/h, (O) Q_{main}=12m^3/h, (Δ) Q_{main}=15m^3/h, (■) Q_{main}=18m^3/h, (◊) Q_{main}=21m^3/h and (ζ) Q_{main}=24m^3/h.

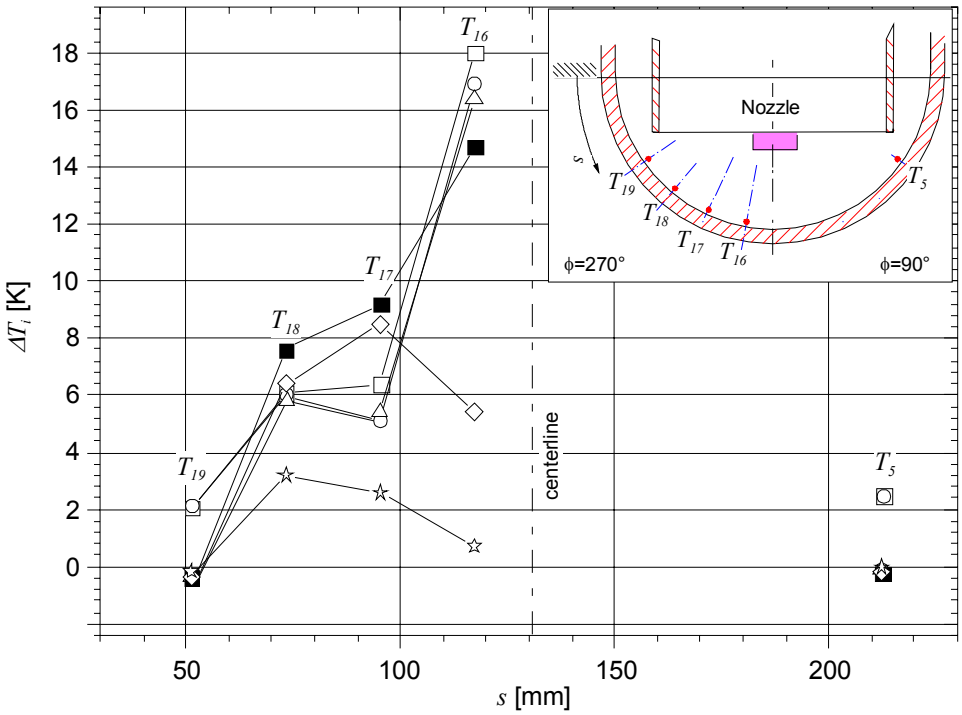

Figure 7.2: Measured temperature distribution as a function of the geometry adapted coordinate s in the plane ϕ=90°-270° for different main flow rates Q_{main} and the conditions Q_{jet}=1.2m^3/h, T_{in}=300°C and $T_{in,jet}$=360°C. (□) Q_{main}=9m^3/h, (O) Q_{main}=12m^3/h, (Δ) Q_{main}=15m^3/h, (■) Q_{main}=18m^3/h, (◊) Q_{main}=21m^3/h and (ζ) Q_{main}=24m^3/h.

The sequence of figures 7.3 qualitatively tries to explain the reasons for the temperature distribution measured in the plane ϕ=90°-270°.
For low main flow rates (Q_{main}=9m^3/h) the jets cross-section widens along its flow path and covers almost the whole shell. This leads to a temperature peak on the centerline. Adjacent to the peak the temperature drops monotonically in both radial directions.
With increasing main flow the jet impinges on the shell and detaches from it. Below the jet a secondary flow establishes, which transports heat from the jet towards the shell. The widening of the jet is less expressed and due to the interaction of the main flow with the jet a second vortex is generated transporting heat to T_{18}.
A further increase of the main flow (to Q_{main}=18m^3/h) leads to stronger confinement of the jet and the jet looses more momentum and thermal energy before it reaches the plane ϕ=90°-270°. Additionally, the stronger interaction of main and jet flow leads to an intensified secondary flow leading in a first step to a broadening of the temperature distribution.
Finally, at the highest main flow rates the jet hardly is able to cross the plane ϕ=90°-270°. The interaction of main and jet flow happened already before this plane is reached. The large scale vortex motion resulting from the interaction of jet and main flow transports thermal energy in the transverse direction.

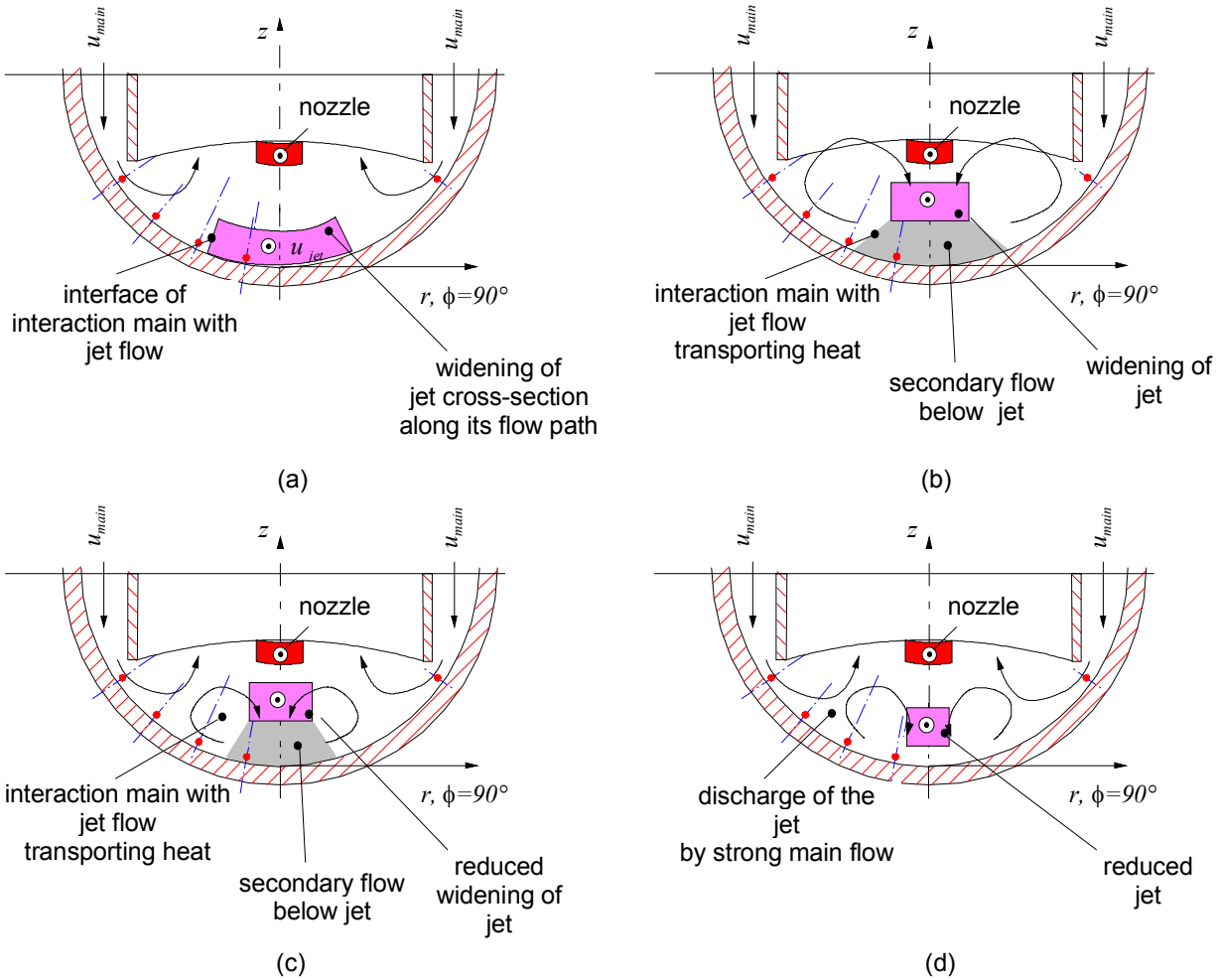

Figure 7.3: Schematic illustration of the interaction of the main flow with the jet flow in the plane ϕ=90°-270° close to the lower shell. (a) Q_{main}=9m^3/h; (b) Q_{main}=12 and 15m^3/h; (c) Q_{main}=18m^3/h; (d) Q_{main}=21 and 24m^3/h

The graphs 7.4a-c show the temperature evolution near the inner side of the riser tube (r=59.5mm) as a function of the axial coordinate z for the different main flow rates on the lines ϕ=0° (7.4a), ϕ=180° (7.4b) and ϕ=270° (7.4c). In order to compare the results and to exhibit differences in the flow patterns between the individual cases the graphs 7.4d-f show the same results but the data are normalized with ($T_{adiabatic}$-T_{in}).

In the sector ϕ=0° and for low z-values the temperature rise most sensitive to the individual flow rate ratios. Here for the highest main flow rate of Q_{main}=24m^3/h the highest temperature elevation is measured. However, the second highest temperature is not found for Q_{main}=21m^3/h; it is detected for the case Q_{main}=12m^3/h. This illustrates the complex interaction of main flow and jet flow close to the immediate vicinity of the sharp edged riser tube. At this flow discontinuity smallest changes lead to significantly different local flow configurations.

Beyond z>105.7mm for all main flow rates the temperature drops continuously up to the position z=238mm, where it almost reaches the adiabatic mixing temperature for all flow rate ratios investigated.

On the opposite side of the nozzle at ϕ=180° the situation is different for axial values z<238mm. In case of main flows of Q_{main}=9 and 12m^3/h the jet is able to reach the inner side of the riser tube opposite the nozzle exit. This is expressed by a considerable temperature rise for z=43.7mm. Beyond this position temperature drops continuously up to the position z=137.7mm (for Q_{main}=9m^3/h) and z=168.7mm (for Q_{main}=12 and 15m^3/h). Then it grows downstream due to the mixing again and reaches for the position z=238mm a value almost close to the adiabatic mixing temperature. However, for main flow rates equal or exceeding 18m^3/h hardly any temperature increase is on the inner side of the riser tube opposite the nozzle (at ϕ=180°). In these cases the lowest temperatures are recorded at the lower edge of the riser tube (at z=43.7mm), indicating that the jet does not reach this position. Beyond this position the temperature grows with z, while the temperature rise for Q_{main}=18m^3/h at the same z-coordinate is faster than that for Q_{main}=24m^3/h. The reason for the more rapid increase of the temperature at the reference case compared to Q_{main}=21m^3/h and Q_{main}=24m^3/h could be that a larger portion of the jet is able to cross the ducts centerline at r=0mm (plane ϕ=90°-270°). This enables a more efficient mixing of thermal energy of the remaining hot jet with the main flow. Downstream of z=238mm also the temperatures for the high main flow rates have reached almost the value of the adiabatic mixing temperature.

Finally the line ϕ=270° is analyzed. Here, at the two lowest main flow rates (Q_{main}=9 and 12m^3/h) a significant temperature peak is recorded at z=43.7mm. For low main flow rates the velocity difference between main and jet flow is most expressed and hence the vortex formation related to the differential velocity is strongest. This yields to counter-rotating vortices transferring heat in transverse direction. After z=43.7mm for both of the low main flow rates the temperature drops considerably up to the position z=105.7mm. This behavior suggests, that the vortex pair in the lower shell keeps stable at its position in the lower shell. Superimposed to this structure is the U-turn of the main flow into the riser tube forming a stable secondary flow. Downstream beyond the position z=105.7mm the temperature rises monotonically for both of the lower main flow rates and it reaches almost the adiabatic mixing temperature at z=363mm.

For Q_{main}=15m^3/h the interaction of main and jet flow leads to a peak temperature at the position z=137.7mm. Downstream this peak the temperature drops to reach at z=363mm the value of the adiabatic mixing temperature. The behavior for Q_{main}=15m^3/h differs completely from that at the higher and the lower main flow rates and marks a transition between different flow structures.

The temperature distribution of the main flow rates Q_{main}=21 and 24m^3/h correspond in non-dimensional values qualitatively and quantitatively to that of the nominal case (Q_{main}/Q_{Jet}=15 and Q_{main}=18m^3/h) and exhibits no new features.

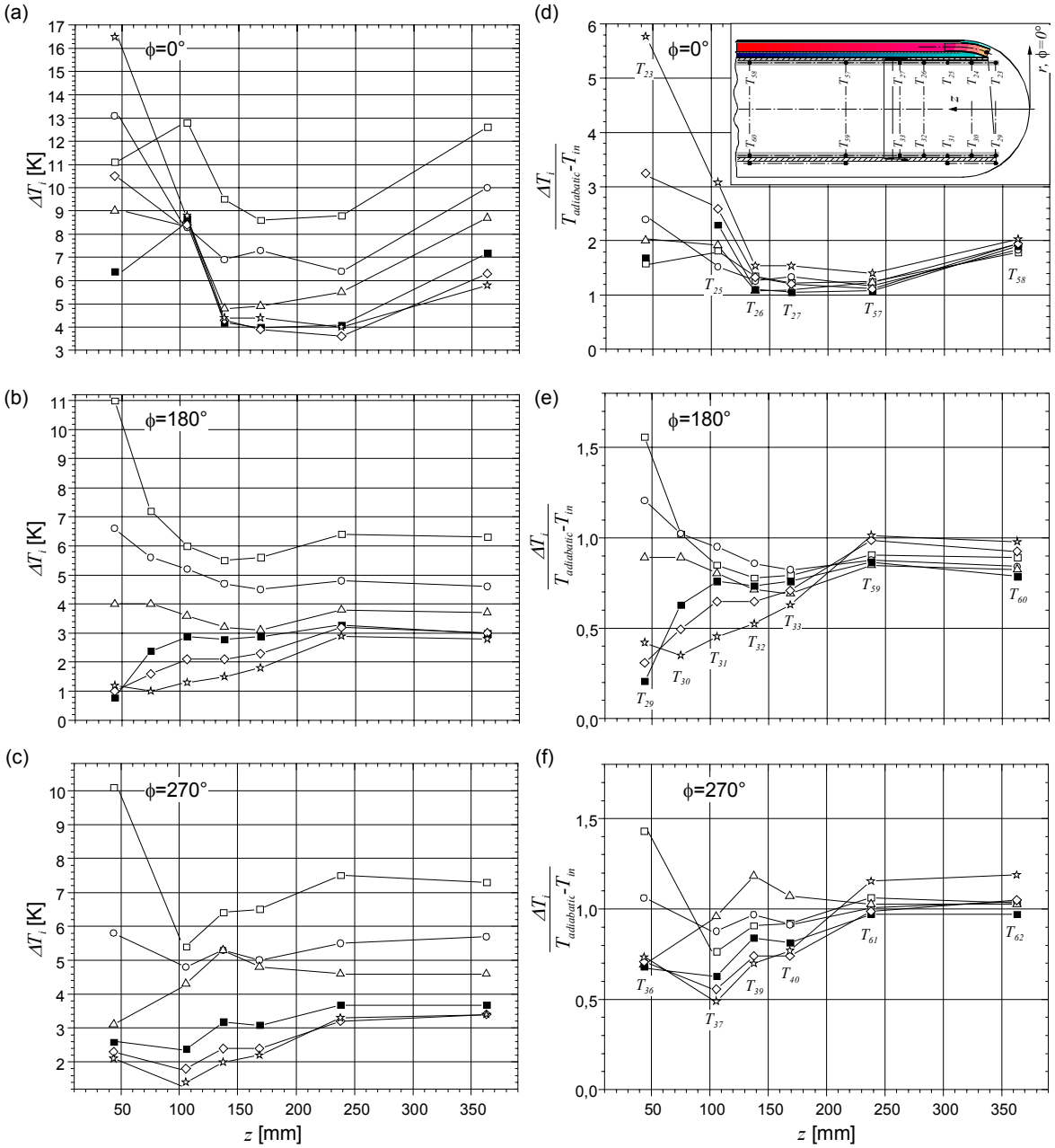

Figure 7.4: Measured dimensional and non-dimensional temperature distribution as a function of the axial length z at r=59.5mm for different main flow rates Q_{main} and the conditions Q_{jet}=1.2m^3/h, T_{in}=300°C and $T_{in,jet}$=360°C. (a) and (d) ϕ=0°, (b) and (e) ϕ=180° and (c) and (f) ϕ=270°. (□) Q_{main}=9m^3/h, (O) Q_{main}=12m^3/h, (Δ) Q_{main}=15m^3/h, (■) Q_{main}=18m^3/h, (◊) Q_{main}=21m^3/h and (ζ) Q_{main}=24m^3/h.

The figures 7.5a-c show the location of the sensing elements and the temperature distribution as a function of the radius r for different main flow rates in the nozzle plane ϕ=0°-180°. Figure 7.4c, in which the temperature is normalized with ($T_{adiabatic}$-T_{in}), illustrates that the temperature mixing at the height z=105.7mm behaves similarly for all main flow rates in the range 9m^3/h≤Q_{main}≤18m^3/h. The distribution is characterized by a weak temperature increase

from the riser tube in the sector ϕ=180° towards the duct centerline. It reaches a local maximum in the middle between the wall and the centerline, which is of order of the adiabatic mixing temperature. Then it drops to a local minimum at the two positions close to the centerline. For r=22.5mm in the sector ϕ=0° a second peak is observed, which is more pronounced for the higher main flow rates than for the smaller ones. With increasing radial coordinate the temperature strongly falls and reaches a minimum at r=46.5mm in the sector ϕ=0°. The local minimum is more pronounced for the higher main flow rates compared to smaller ones. From this local minimum the temperature exhibits in all cases a steep increase towards the riser tube wall at r=59.5mm, where for all main flow rates 9m^3/h≤Q_{main}≤24m^3/h the maximum temperature in the nozzle plane is recorded.
Except for the latter described temperature peak near the wall adjacent to the jet duct the main flow rates Q_{main}≥21m^3/h exhibit a different temperature distribution compared to the lower ones. For Q_{main}=21m^3/h the temperature increases from the riser tube wall in the sector ϕ=180° up to the riser centerline, where it shows a first peak. This is followed by a weak temperature drop and another temperature increase to a second peak of similar magnitude. For r>22.5mm the behavior corresponds to the other cases. The double peak structure of the temperature suggests that for this flow rate ratio two vortices are located in this plane. The first one originates from the flow separation at the lower rim of the riser tube and is located in the domain r>0mm. The second one is attributed to the interaction of the main flow with the jet flow in the lower part of the shell, where the main flow lifts off a part of the jet and generates this vortex, which contains parcels of higher temperature.
Finally, a further increase of the main flow rate to Q_{main}=24m^3/h generates again a different temperature distribution in the nozzle plane. Although there is a small local maximum in the sector ϕ=180° (exactly at r=46.5mm), hardly any significant temperature elevations are observed there. In the direction of the jet duct towards the sector ϕ=0° a steep temperature increase is measured, which reaches a peak value twice as high as the adiabatic mixing temperature at r=22.5mm. The formation of this peak illustrates that the momentum of the main flow at the highest main flow rate is so strong in the nozzle plane that the jet is hardly able to cross the riser tubes centerline. The impact of the hot jet on the temperature distribution is mainly confined to the sector ϕ=0°.

The figures 7.5d-f illustrate the measuring locations and temperature distributions in the plane normal to the nozzle in a height z=105.7mm. Here, again in figure 7.5f the temperature rise is normalized with ($T_{adiabatic}$-T_{in}).
Generally, for all flow rate ratios investigated the temperature distribution is asymmetric with respect to r=0mm as figure 7.5e, f illustrate.
Again, the main flow rates in the range 9m^3/h≤Q_{main}≤18m^3/h behave qualitatively similar. For these flow rate ratios (7.5≤Q_{main}/Q_{jet}≤15) cases the temperature increases in the sector ϕ=270° from the riser tube wall towards the ducts centerline. There, nearly the adiabatic mixing temperature is attained. With increasing r in the sector ϕ=270° the temperature drops to a local minimum and then increases towards the riser tube wall at r=59.5mm. Also here, the increase is stronger for the higher flow rates than for the smaller ones. The flow rate ratio Q_{main}/Q_{jet}=17.5 (Q_{main}=21m^3/h) marks the transition of the flow patterns, because here a local temperature maximum is obtained close to the centerline of the riser tube. Adjacent to this peak the temperature drops rapidly in the sector ϕ=90°, see figure 7.5f. For r>0mm in the sector ϕ=90° the temperature distribution behaves like that for the smaller flow rates. The temperature peak near the centerline is an indication that for this flow rate combination the

jet is not split into several streams as for smaller mass flow rates. Due to the large momentum of the main flow the range of the influence of the jet is limited to the nozzle plane ϕ=0°-180°. This argument is supported by the fact that a further increase of the flow rate ratio to Q_{main}/Q_{jet}=20 (Q_{main}=24m^3/h) yields only one temperature maximum, which is recorded on the close to the centerline of the riser tube. Next to this peak the temperature significantly drops in both sectors ϕ=90° and ϕ=270°. For this flow rate ratio the hot jet is mainly confined to the nozzle plane.

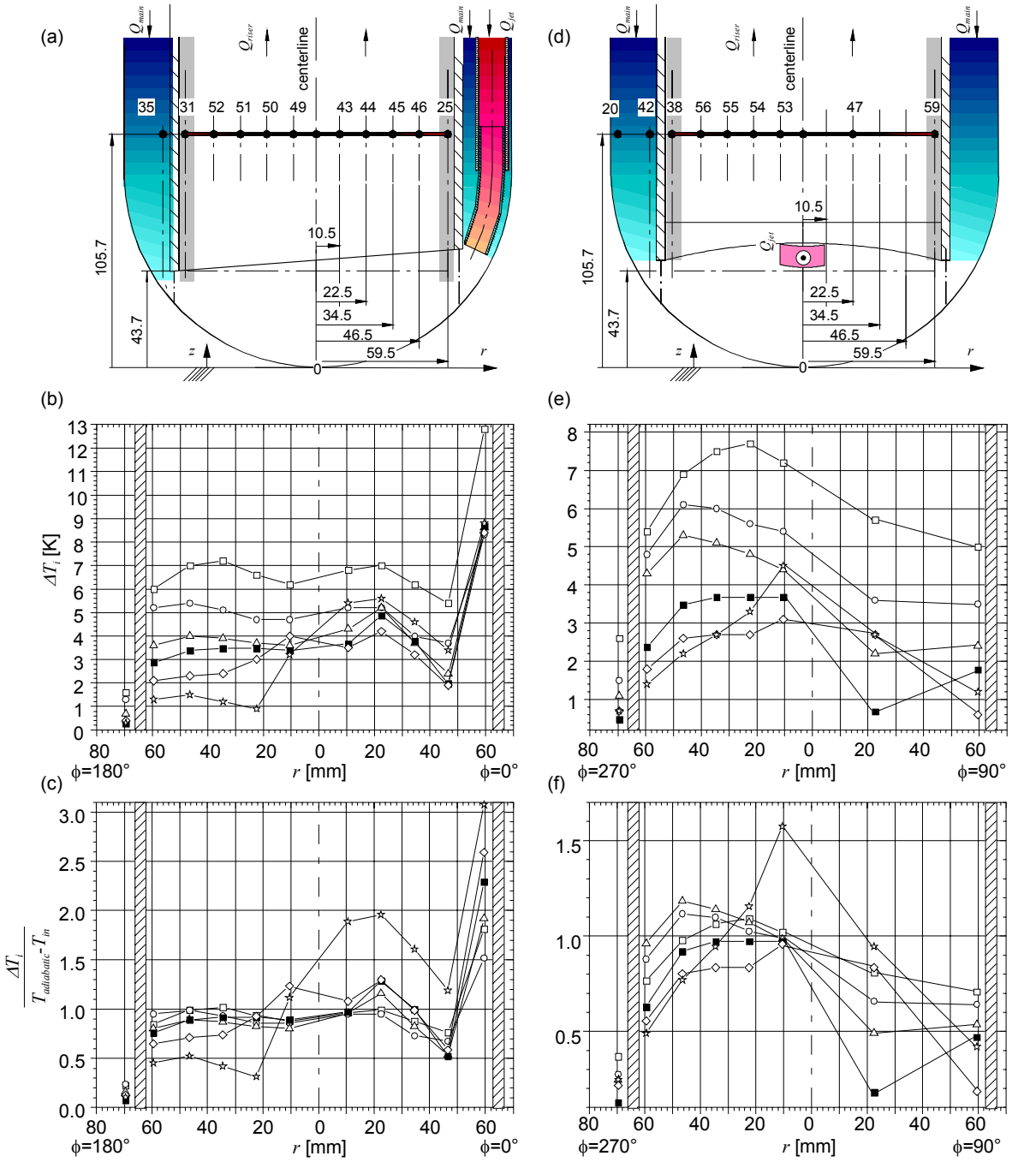

Figure 7.5: Measurement locations in the nozzle plane ϕ=0°-180° (a)-(c) and normal to it ϕ=90°-270° (d). Measured dimensional and non-dimensional temperature distribution as a function of the radius r at a height z=105.7mm and Q_{jet}=1.2m^3/h, T_{in}=300°C, $T_{in,jet}$=360°C. (□) Q_{main}=9m^3/h, (O) Q_{main}=12m^3/h, (Δ) Q_{main}=15m^3/h, (■) Q_{main}=18m^3/h, (◊) Q_{main}=21m^3/h and (ζ) Q_{main}=24m^3/h.

7.1.2 Influence of the main flow variation on the turbulent temperature fluctuations

Since the flow is highly turbulent even for the smallest main flow rates at Reynolds numbers of O(10^5) and, moreover, several geometry discontinuities like sharp edges, U-turns and also free shear layers and the jet impingement on the wall occur, fluctuations are to be expected. The Reynolds numbers appearing in the annular gap, the nozzle exit and the riser tube are given in table 7.2. Here also the temperature dependence of the thermophysical fluid properties in the different regions is taken into account.

Q_{main} [m^3/h]	Q_{main}/Q_{jet} [/]	$Re_{mean,gap}$ [/]	Re_{riser} [/]	Re_{jet} [/]
9	7.5	50.306	167.222	137.132
12	10.0	67.074	215.443	136.402
15	12.5	83.843	263.889	135.946
18	15.0	100.611	312.266	135.592
21	17.5	117.380	360.639	135.229
24	20.0	134.148	409.065	134.927

Table 7.2: Calculated temperature dependent Reynolds numbers in the flow rate ratios investigated in the heated jet experiment. Boundary conditions: Q_{jet}=1.2m^3/h, T_{in}=300°C, $T_{in,jet}$=360°C. Nominal case with Q_{main}/Q_{jet}=15 is highlighted.

The figures 7.6a, b show the RMS values of the temperature in the nozzle plane as a function of the geometry adapted coordinate s for different flow main flow rates in a dimensional and a non-dimensional form.

For the lowest main flow rate investigated Q_{main}=9m^3/h (Q_{main}/Q_{jet}=7.5) the jet flows along the contour of the hemispherical shell, as already shown in figure 7.1, and also the RMS values for s>131.9mm are below 10% of the adiabatic mixing temperature. This indicates that the jet remains unchanged before reaching the symmetry line and the shear between main flow and jet does not lead to a significant turbulence production close to the fluid-solid interface. As the flow proceeds across the centerline the RMS values rapidly increase by a factor of 4, which is caused by the interaction of the main flow with the jet. Finally, as the jet enters the annular gap of the main flow, it is decelerated by the momentum of the main flow. This process is highly unsteady and leads to a mixing of the thermal energy on large scales. Sometime the jet is even strong enough to reach the thermocouple T_{12} for Q_{main}/Q_{jet}=7.5.

For flow rate ratios in the range $10 \leq Q_{main}/Q_{jet} \leq 12.5$ the RMS value close to the nozzle exit is still small with $RMS(T_i)/\Delta T_{adiabatic}$<0.1. However, it rapidly increases as the jet flow proceeds towards the centerline. There, the jet meets the main flow and is pushed partly away from the shell. This process occurs irregularly on large scales and shows for T_7 and T_8 temperature fluctuations of more than 3-4K. The remaining part of the jet proceeds along the shell and the fluctuation level decays from T_8 to T_{10}. Finally, sometimes the jet is able to enter the annular gap. This causes in the case of Q_{main}/Q_{jet}=10 a second peak of the fluctuation intensity. At the position T_{12} for the flow rate ratio Q_{main}/Q_{jet}=10 temperature fluctuations are

still observed, while for Q_{main}/Q_{jet}=12.5 the normalized RMS-value is less than 0.1K corresponding to the fluctuation intensity of the undisturbed main flow in the gap.
For flow rate ratios in the range of 15≤ Q_{main}/Q_{jet}≤20 a double peak profile of the RMS- values of the temperature fluctuations is observed. The local extrema are located next to the positions, where the jet impinges onto the wall. There the highest gradients in the temperature field occur. The first maximum appears directly at the nozzle exit, where the jet hits the hemispherical shell. As the flow rate ratio is increased this maximum is shifted towards the nozzle exit, e.g. for Q_{main}/Q_{jet}=15 the maximum value is at T_1 (s=146.6mm), moves for Q_{main}/Q_{jet}=17.5 to T_2 (s=168.6mm) and finally for Q_{main}/Q_{jet}=20 it is located at T_3 (s=190.6mm). The second local maximum is observed, where the jet reattaches the wall beyond the centerline. Here again a similar behavior of the shift of the RMS-peak towards the nozzle exit is with increasing main flow rates is observed. It is positioned for Q_{main}=18m^3/h at T_9 (s=73.3mm) and moves to T_8 (s=95.3mm for Q_{main}=21m^3/h) and is finally located at T_7 (s=1175.3mm for Q_{main}=24m^3/h). The reason for this shift towards the nozzle is the increasing momentum of the main flow, which reduces the impact of the jet flow on the whole flow field and especially on the shells temperature. An increasing main flow confines the jet to a domain adjacent to the nozzle in the sector ϕ=0°. The peaks of the dimensionless temperature fluctuations drop for increasing flow rate ratios. For Q_{main}/Q_{jet}=15 the peak shows a maximum of 0.5, which is reduced to 0.38 for Q_{main}/Q_{jet}=17.5 and finally 0.32 for Q_{main}/Q_{jet}=20. This is caused by two effects: The first attributed to a reduced shear production rate, because the velocity difference between main and jet flow drops with increasing main flow rate. The reduced shear productions yields less strong secondary flows which are potentially unstable, because they can interact with the cold main flow. The second effect is that the jet flow gets more confined for growing main flow rates.

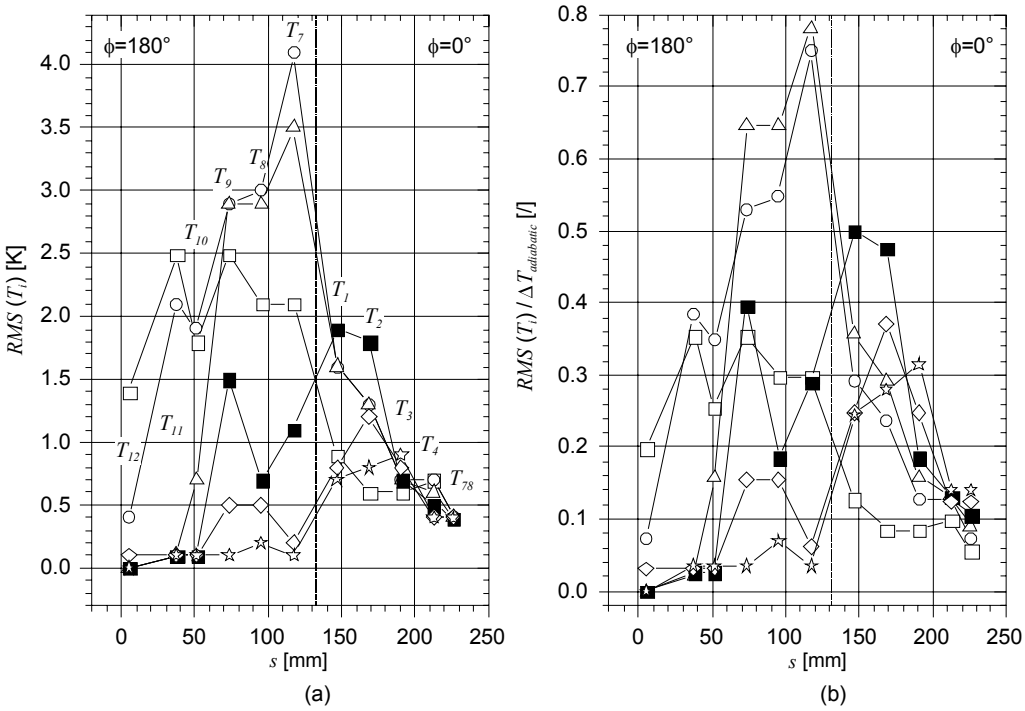

Figure 7.6: Measured dimensional (a) and non-dimensional (b) temperature fluctuation distribution (RMS-values) as a function of the geometry adapted coordinate s in the plane ϕ=0°-180° for different main flow rates Q_{main}. (□) Q_{main}=9m^3/h, (O) Q_{main}=12m^3/h, (Δ) Q_{main}=15m^3/h, (■) Q_{main}=18m^3/h, (◊) Q_{main}=21m^3/h and (ζ) Q_{main}=24m^3/h.

The non-normalized and normalized intensity of the temperature fluctuation in the plane perpendicular to the nozzle for the line ϕ=90-270° is shown as a function of the geometry adapted coordinate s along the lower shell in the figures 7.7a, b.
In the range of $7.5 \leq Q_{main}/Q_{jet} \leq 10$ the jet almost covers the lower part of the shell at the centerline, as sketched in figure 7.3. As the non-dimensionalized figure 7.7b exhibits the mean fluctuation level for these main flow rates is relatively large. Even close to the annular gap temperature fluctuations of 25-30% are recorded indicating a highly time dependent interaction of main and jet flow. Nevertheless, the fluctuation intensities close to the centerline (T_{16} and T_{17}) and near the annular gap (T_{19}) are smaller than the RMS-value measured in the mid of the shell at T_{18}. There, fluctuation intensities are 10% larger than at the other positions. The relatively large RMS-values in the nozzle plane (ϕ=0°) beyond the centerline and the high fluctuation intensities recorded for the sector ϕ=270° suggests an unsteady flow pattern in the whole lower shell, which is characterized by a locally intermittent interaction of main and jet flow.
As the flow rate ratio increases the jet becomes more and more confined and hence bound to the nozzle plane ϕ=0°-180°. Thus the scaled fluctuation intensity close to the centerline decreases from 0.45 for Q_{main}/Q_{jet}=12.5 to 0.4 for Q_{main}/Q_{jet}=15. For these flow rates the peak fluctuations appear in the middle between the centerline and the riser tube.
Again the flow rate ratio Q_{main}/Q_{jet}=17.5 represents a transition to another flow pattern. Here the highest fluctuation intensity is measured close to the centerline with a value of 0.7. As the mean temperature profile in figure 7.1 shows the jet is to a large extend decelerated by the momentum of the main flow close to the centerline in the nozzle plane. The deceleration of the jet pushes the remaining jet streak towards the side in the 90°-270° direction, which yields there to an increase close to the centerline, see figure 7.2. Because this not a steady, but an intermittent process, the fluctuation intensity at is position T_{16} close to the centerline is considerably large. The fluctuation intensity continuously decreases from the centerline towards the annular gap.
For the highest flow rate ratio Q_{main}/Q_{jet}=20 (Q_{main}=24m^3/h) the jet is almost fully decelerated by the main flow before reaching the centerline, because the mean temperatures measured in the nozzle plane and transverse to it show only a temperature difference of less than 1K close to the centerline. While the non-dimensional RMS-value of the temperature fluctuations in the nozzle plane (T_7) shows a nearly steady behavior with 0.04, the adjacent thermocouple T_{16} in the sector ϕ=270° close to the centerline exhibits a value of 0.26 (6 times larger). This indicates an unstable displacement of the jet towards the plane ϕ=90°-270°, which is additionally supported by the increase of the fluctuation intensity towards T_{16}.
For flow rate ratios of from $12.5 \leq Q_{main}/Q_{jet} \leq 20$ the momentum of the main flow is strong enough, that no secondary flow arising from the interaction of main and jet flow are able to reach the thermocouple T_{19} and hence the fluctuation intensity there is close to zero.

In the figures 7.8a-f the RMS-values of the temperature close to the inner walls of the riser tube (at the radius r=59.5mm) are illustrated as a function of the axial coordinate z at three angular positions (ϕ=0°, ϕ=180°, ϕ=270). While in the graphs 7.8a-c the dimensional values are shown, the figures 7.8d-f show the results in a non-dimensional way.

In the nozzle adjacent line in the sector ϕ=0° the thermocouple T_{23} (z=43.7mm), which has no direct wall contact, senses the highest temperature fluctuations, because there high shear rates occur due to the U-turn of the velocity and the collision of jet and main flow. Downstream this position the fluctuations rapidly decrease for all main flow rates investi-

gated. At the positions 137.7mm<z<168.7mm a second significantly smaller peak of the RMS-values appears, which is attributed to the reattachment of the separated flow originally produced at the lower edge of the riser tube. This second peak increases with increasing flow rate ratio, because a larger portion of the jet flow is conserved to the sector next ϕ=0° than for lower flow rate ratios. Additionally, the location of the second peak moves downstream for increasing main flow rates. For Q_{main}/Q_{jet}=7.5 it is at T_{26} (z=137.7mm), while for Q_{main}/Q_{jet}=20 it is located at T_{27} (z=168.7mm). This shift is caused by the higher mean flow rates.

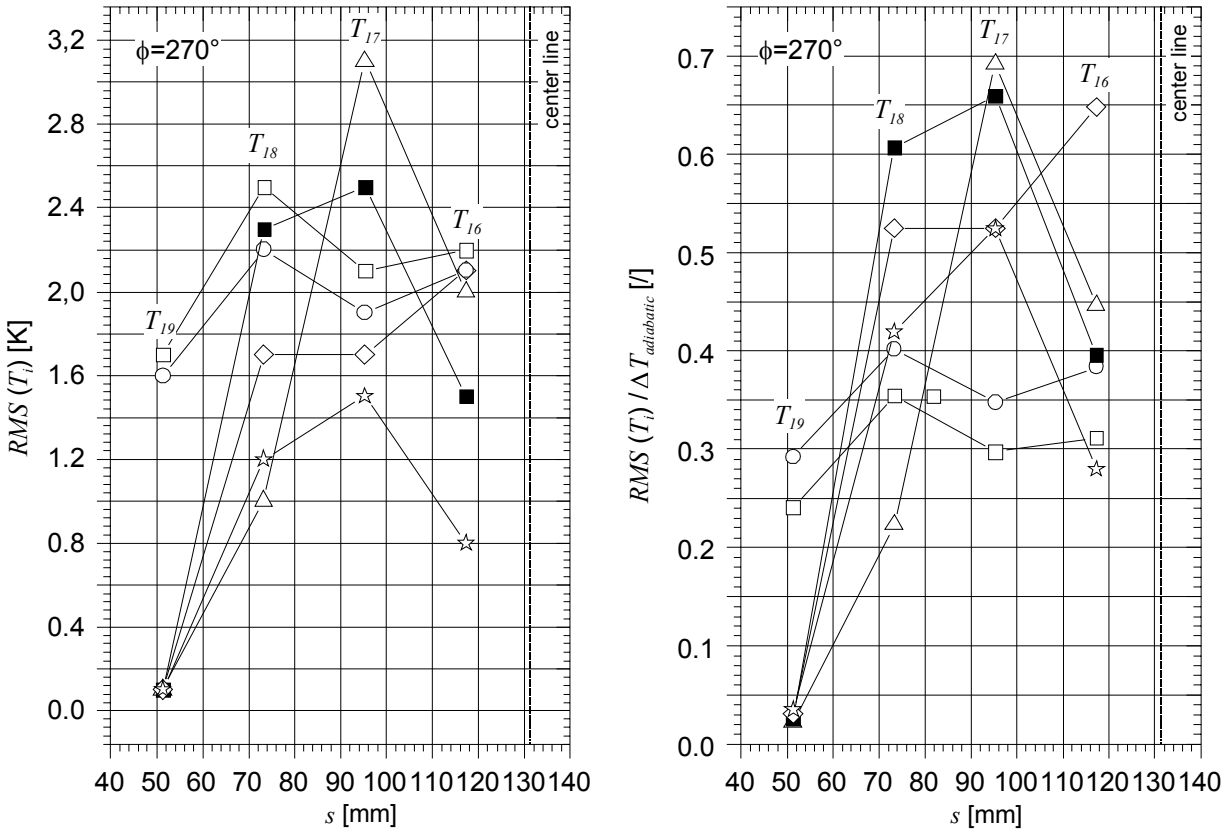

Figure 7.7: Measured dimensional (a) and non-dimensional (b) temperature fluctuation intensity distribution (RMS-values) as a function of the geometry adapted coordinate s in the sector ϕ=270° at r=0mm for different main flow rates Q_{main} and Q_{jet}=1.2m^3/h, T_{in}=300°C and $T_{in,jet}$=360°C. (□) Q_{main}=9m^3/h, (O) Q_{main}=12m^3/h, (Δ) Q_{main}=15m^3/h, (■) Q_{main}=18m^3/h, (◊) Q_{main}=21m^3/h and (ζ) Q_{main}=24m^3/h.

Close to the riser tube side opposite the nozzle in the sector ϕ=180° (fig 7.7b,e), the analysis of the fluctuations is more difficult.

For the small flow rate ratios (7.5≤Q_{main}/Q_{jet}≤10) the jet is capable to penetrate into the annular gap and mixing there with the main flow. The position of maximum fluctuations is for this flow configuration shifted to the lower shell and to the annular gap.

For a flow rate ratio Q_{main}/Q_{jet}=12.5 the jet mixes with the main flow in the vicinity of the lower edge of the riser tube. There strong gradients of the velocity field occur, which cause also rather high temperature oscillations.

A time history of the temperature for a 10min record of the readings at T_{29} is shown in two temporal resolutions in figure 7.9. The peak to peak difference of the temperature re-

cords are 3.2K, which is of order of the rise of the adiabatic mixing temperature. A calculation of the $PSD(T_{29})$ at T_{29} showed a broadband spectrum of the temperature fluctuations and contains no preferred frequency. At the highest main flow rates the jet is not able to reach the riser tube at ϕ=180° and thus the fluctuation intensities recorded there are close to zero. In case of flow rate ratios $Q_{main}/Q_{jet}\leq$12.5 the fluctuation intensity decreases continuously for z>105.7mm. In case of $Q_{main}/Q_{jet}\geq$15 a local weak maximum is observed, which originates from the turbulent mixing of parts of the jet with the main flow. This peak value is shifted downstream with increasing flow rate ratio due to the larger mean velocity and ,additionally, it decreases for high flow ratios, because at those conditions a diminishing portion of the jet is able to cross the risers centerline causing at the opposite side in the sector ϕ=180°.
On the line r=59.5mm at ϕ=270° the situation is much more complex. At low flow rate ratios $Q_{main}/Q_{jet}\leq$10 the jet does not only travel along the shell it also spreads continuously in ϕ=90°-270° direction, as the measurements in figure 7.2 and the sketch 7.3 illustrate. Thus the fluctuation intensities measured close to the shell near the riser tube are attributed mainly to the immediate interaction of the jet and the main flow.

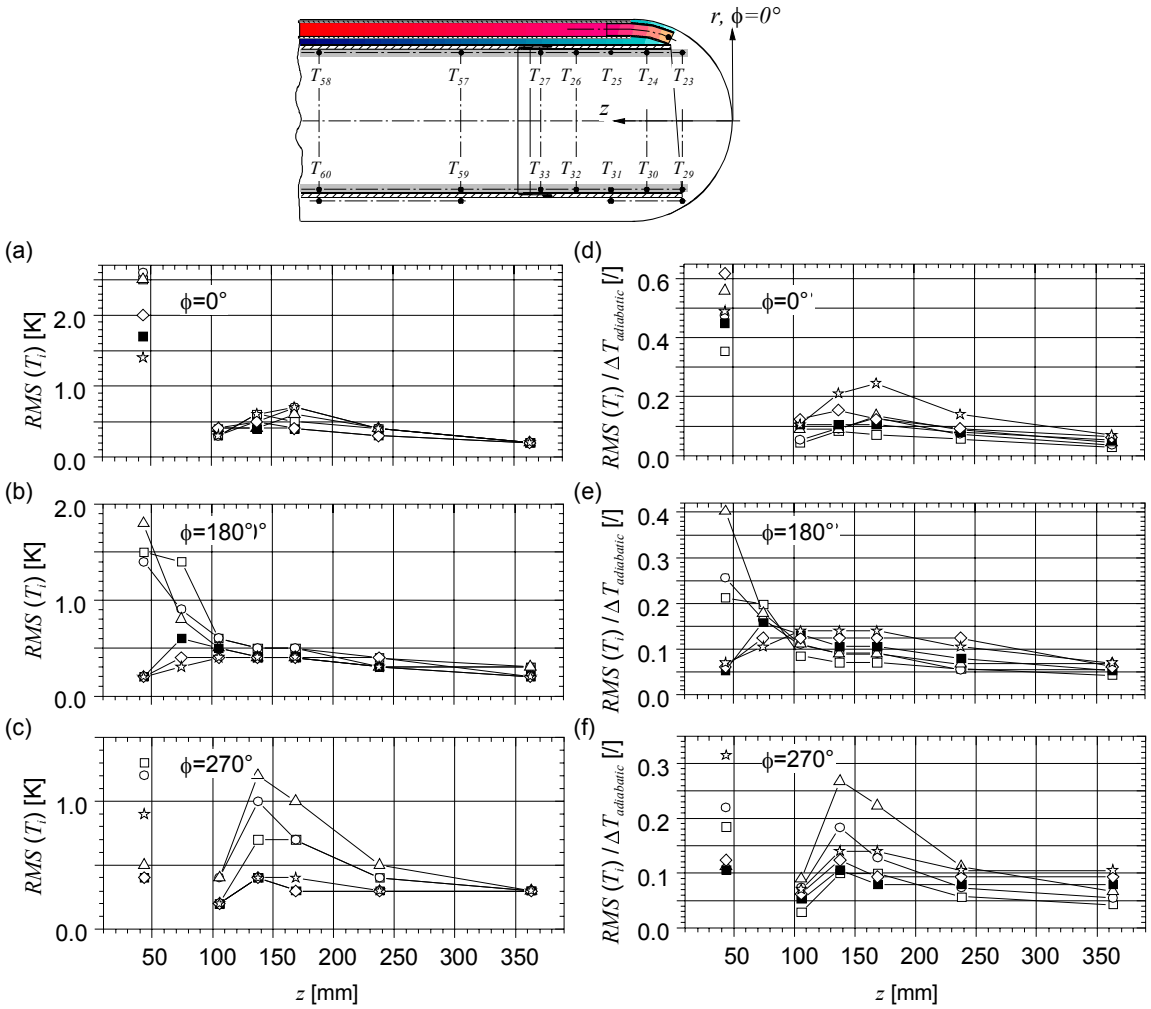

Figure 7.8: Measured dimensional (a-c) and non-dimensional (d-f) temperature fluctuation intensity distribution (*RMS*-values) as a function of the axial coordinate z on the lines ϕ=0°(a, d), ϕ=180°(b, e) and ϕ=270°(c, f) at r=59.5mm for different main flow rates Q_{main} and Q_{jet}=1.2m^3/h, T_{in}=300°C and $T_{in,jet}$=360°C. (□) Q_{main}=9m^3/h, (O) Q_{main}=12m^3/h, (Δ) Q_{main}=15m^3/h, (■) Q_{main}=18m^3/h, (◊) Q_{main}=21m^3/h and (ζ) Q_{main}=24m^3/h.

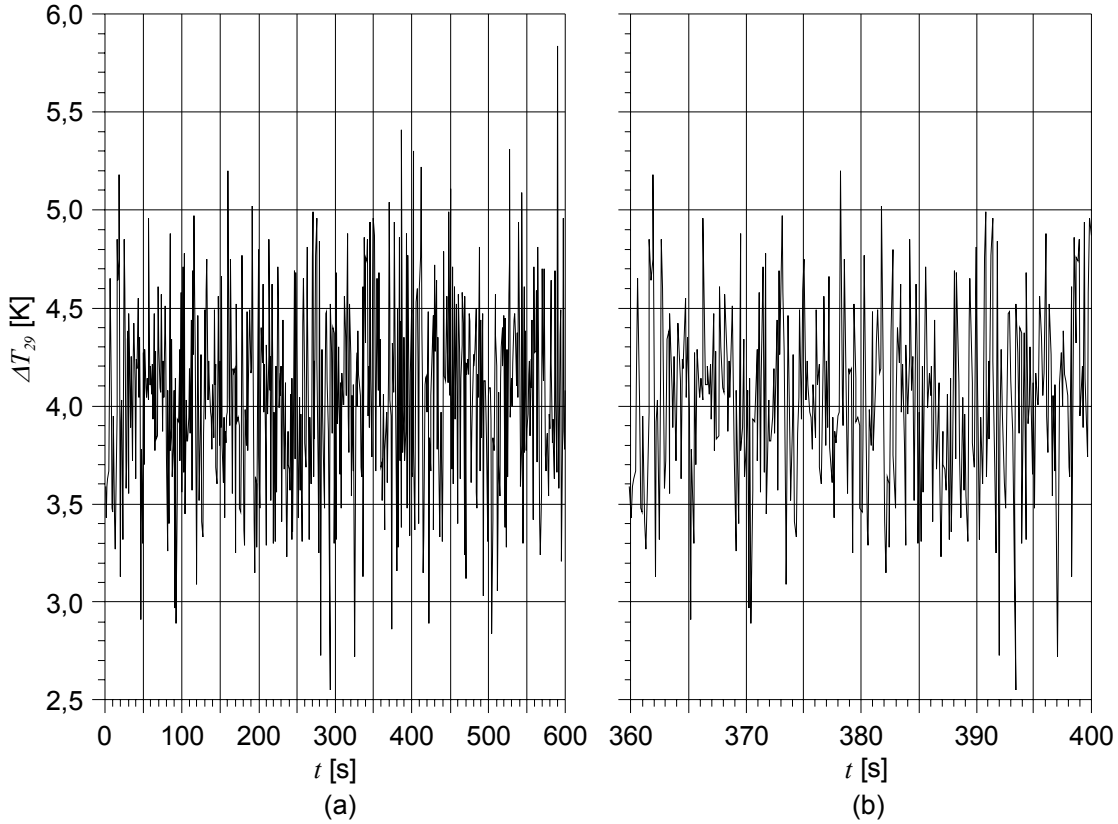

Figure 7.9: Time signal of the temperature at the thermocouple T_{29} (z=43.7mm, r=59.5mm and ϕ=180°) for the conditions Q_{main}=15m^3/h, Q_{jet}=1.2m^3/h, T_{in}=300°C and $T_{in,jet}$=360°C in two temporal resolutions.

The figures 7.10 illustrate the radial RMS distribution in the nozzle plane (ϕ=0°-180°; fig. 7.10a-c) and in the plane perpendicular to it (ϕ=90°-270°;fig 7.10d-f) in the height z=105.7mm in a dimensional and non-dimensional way.

The main flow in the annular gap is almost free of temperature fluctuations at any main flow rate either in the nozzle plane and perpendicular to it. Also the temperature fluctuations near both riser walls in the nozzle plane are low. The absolute value of the normalized RMS-data near the riser walls slightly increase with increasing main flow rate.

The normalized fluctuation level of the lowest flow rate ratio Q_{main}/Q_{jet}=7.5 (Q_{main}=9m^3/h) is nearly constant at a value of approximately 0.1 across the radius in the nozzle plane. All other main flow rates show a local peak at the position r=22.5mm in the sector ϕ=0°. This peak continuously grows for increasing flow rate ratios and finally for Q_{main}/Q_{jet}=20 the fluctuation intensity nearly reaches the order of the adiabatic mixing temperature. Responsible for the high fluctuation level is the interaction of the jet with the main flow. An increasing flow rate ratio confine the jet to a narrow domain in the sector ϕ=0° due to the large momentum of the main flow. As shown in the mean temperature profiles in figure 7.5 for a flow rate ratio Q_{main}/Q_{jet}=17.5 two vortices travel are located at this z-height in the nozzle plane (ϕ=0°-180°). This explains why two peaks of the temperature fluctuations are visible for this flow rate. As the flow rate ratio exceeds Q_{main}/Q_{jet}>17.5 only one vortex remains, which is generated by the flow separation of the jet at the lower edge of the riser tube. This confined jet interacts with the main flow and wiggles in the plane ϕ=0°-180° around the centerline at $r\geq$0mm leading to fluctuation intensities of 56%.

In the plane normal to the nozzle (ϕ=90°-270°) the *RMS*-distribution of the temperature oscillations is far from being symmetric.

Except for the highest flow rate ratios (Q_{main}/Q_{jet}≥17.5; Q_{main}=21 and 24m^3/h) the fluctuation level in the sector ϕ=270° is of the same magnitude as that in the nozzle plane. Here, the fluctuation level is nearly constant over the cross-section for all flow rates, c.f. see the non-dimensional graph 7.10f.

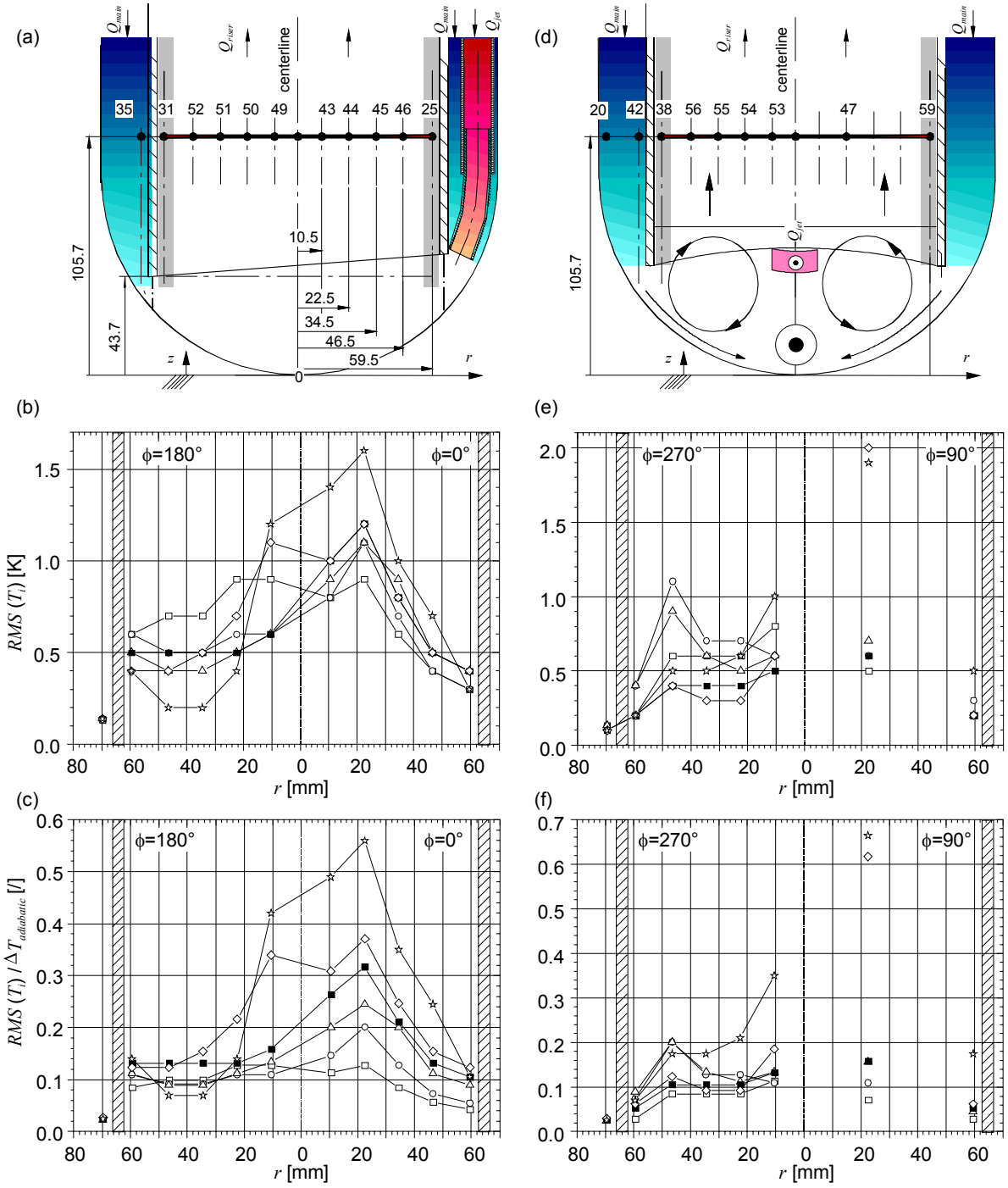

Figure 7.10: Measured dimensional (b, e) and non-dimensional (c, f) temperature fluctuation intensity (*RMS*-values) as a function of the radius r at a height z=105.7mm in the plane ϕ=0°-180°(a-c) and ϕ=90°-270° (d-f) for different main flow rates Q_{main} and reference conditions. (□) Q_{main}=9m^3/h, (O) Q_{main}=12m^3/h, (Δ) Q_{main}=15m^3/h, (■) Q_{main}=18m^3/h, (◊) Q_{main}=21m^3/h and (ζ) Q_{main}=24m^3/h.

As the main flow rate exceeds 21m^3/h ($Q_{main}/Q_{jet}\geq$17.5) the symmetry gets completely lost and strong temperature fluctuations appear in the middle between the centerline and the riser tube wall in the sector ϕ=90°. Especially the fluctuation intensity at the thermocouple T_{47} (r=22.5mm) increases by a factor of 10 for $Q_{main}\geq$21m^3/h compared to the smaller flow rate ratios. The fluctuation growth with increasing flow rate ratio, suggests a significant overall swirl flow arising supposedly from flow asymmetries at the riser tube rim. For Q_{main}/Q_{jet}=20 also a relatively high fluctuation level is even found near the wall.

7.1.3 Summary of the results for the variations of the main flow rate

The summary of this subchapter refers to the variation of the flow rate ratio in a range from 7.5$\leq Q_{main}/Q_{jet}\leq$20 corresponding to main flow rates of Q_{main}=9m^3/h to Q_{main}=24m^3/h at a fixed jet flow rate of Q_{jet}=1.2m^3/h and for constant inlet temperatures T_{in}=300°C and $T_{in,jet}$=360°C.
From the temperature readings and the spatio-temporal analysis mainly three-different flow patterns could be identified, which are sketched in figure 7.11.

Domain $Q_{main}/Q_{jet}\leq$12.5:

- Here, the jet flow covers the whole lower shell in the nozzle plane and sideways from it.
- Moreover, the jet flow is even able to enter the annular gap opposite the nozzle exit.
- Although this flow pattern is the most unsteady configuration, in which close to the shell fluctuation intensities of 80% and more appear, most of the fluctuations are located in a frequency range larger than 1Hz.
- The thermal mixing occurs on large scales within the lower part of the hemispherical shell in all directions.
- The thermal mixing of the jet with the main flow is mostly finished already in a height of z=105.7mm above the lower bottom of the shell. The temperature fluctuations recorded there are about 10-15%.

Domain 12.5<Q_{main}/Q_{jet}<17.5:

- For this configuration the pattern corresponds to the one of the nominal case, in which the jet impinges the lower shell and splits off in several streams.
- One of them enters the sector ϕ=180° and interacts with the main flow. Directly at the centerline the jet does not cover the lower bottom of the shell. Here, which is more severe for the application also the temperature fluctuation intensity is rather small.
- Another one forms a recirculation area in the sector ϕ=0°.
- A complex flow pattern evolves in the plane ϕ=90°-270°, which is characterized by the interaction of main and jet flow. Nevertheless the impact of the jet flow is significantly reduced in this plane.
- Downstream in the riser tube the main features observed correspond to ones found in chapter 6.
- The thermal mixing is weaker than in the previous flow rate ratio domain and it is not only concentrated to the shell region. Even for z>236mm measurable tempera-

ture differences are found. Especially at the line f=0° close to the riser tube lumps of fluid with high temperature are observed. They show a high fluctuation intensity.

Domain Q_{main}/Q_{jet}>17.5:

- For this flow rate ratios the flow pattern evolving in the shell domain and in the riser differ from that found in the nominal case. Here, the jet is mainly confined to the nozzle plane ϕ=0°-180°. The temperature fluctuation intensity close to the shell is considerably lower than for the lower flow rate ratios.
- The jet hardly reaches the lower bottom of the shell at the centerline of the geometry.
- Before the jet reaches the plane ϕ=90°-270° at the centerline it is displaced sideways. Thus the highest measured temperatures and temperature fluctuation intensities are not found on the centerline. They are displaced by about 30mm from the centerline.
- Moreover, most of the temperature rise occurs in the nozzle adjacent domain in the sector ϕ=0°.
- The thermal mixing is compared to the other two cases the worst, because a significant portion of the jet is involved in the flow separation at the lower edge of the riser tube generating there a large scale recirculation area confined to the sector ϕ=0°. The thermal energy from this sector to the adjacent fluid domains is rather poor.

General conclusion:

The application in the MEGAPIE target requires that the jet covers the centerline at the lower bottom of the shell in both planes ϕ=0°-180° and ϕ=90°-270°. This constraint is only fulfilled for flow rate ratios $Q_{main}/Q_{jet}\leq$12.5. Also the fluctuation intensities are largest for this configuration, the fluctuations are located in a frequency range larger than 1Hz, which does not yield to significant temperature oscillations of the lower shells material. For these flow rate ratios the fluctuations occur on large geometrical scales mainly in the lower part of the shell. This, however, leads to an efficient thermal mixing of both fluid flows, so that the temperatures are mostly equalized to the adiabatic mixing temperature even in a distance of less than 150mm away from the lower bottom of the target shell. An efficient mixing is desired in MEGAPIE to keep the thermal stresses of the riser tube within acceptable limits.

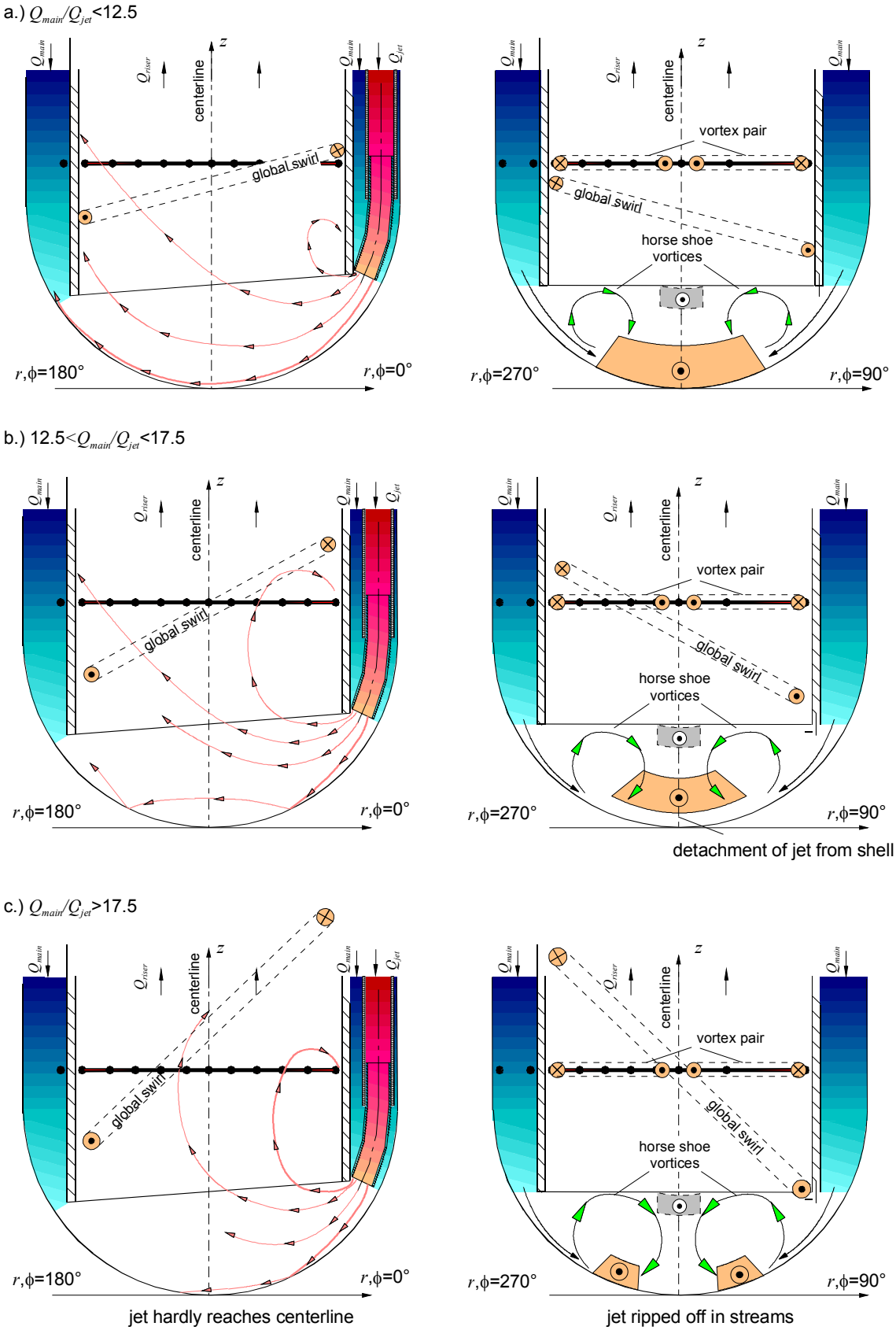

Figure 7.11: Sketch of the flow patterns detected by the spatio-temporal analysis of the experimental data for the flow rate ratio ranges $Q_{main}/Q_{jet}\leq 12.5$ (a), $12.5<Q_{main}/Q_{jet}<17.5$ (b) and $Q_{main}/Q_{jet}>17.5$ in the nozzle plane ϕ=0°-180° and transverse to it ϕ=90°-270°.

7.2 Variation of the jet flow rate

A sudden beam focusing or a higher beam power may require an increased flow rate of the jet flow in order to keep the temperatures within the structural material at the shell in an acceptable range. Changes of the jet flow rate may also be caused by the temperature dependent wetting of the working fluid within the gap of the pump. Here, higher temperatures or a reducing atmosphere could lead to a better wetting in the electrical sense in such a way that the specific electric resistance at the fluid-wall interface decreases, see Knebel et al. (2003). As a consequence the flow rate of the pump is increased although the supplied electric power remains unchanged. All these events may lead to critical stages of operation in terms of a possibly exceeding the sustainable material temperatures at the beam window. Similarly as in the previous case the parameter variation performed was aimed to give an indication of the threshold for reliable thermal-hydraulic operation of the MEGAPIE design. Therefore, the jet flow has been varied in the experiment in five steps from 0.8m^3/h to 1.62m^3/h at a constant main flow rate of Q_{main}=18m^3/h and constant inlet temperatures of the main flow of T_{in}=300°C and the jet flow of $T_{in,jet}$=345°C with an accuracy of ±0.1°C.

The mean velocities of the jet $u_{mean,jet}$, in the riser tube $u_{mean,riser}$, the adiabatic mixing temperature ($T_{adiabatic}$-T_{in}) and the kinetic and densimetric Froude numbers Fr_{kin}, Fr_{dens} related to these investigations are listed in table 7.3. The densimetric Foude number is considerably larger than the order O(10^2) and consequently the jet can be considered as an inertial jet, which allows to conclude from the temperature readings on the local velocities.

Q_{jet} [m^3/h]	$u_{mean,jet}$ [m/s]	Re_{jet} [/]	$u_{mean,riser}$ [m/s]	Q_{main}/Q_{jet} [/]	$T_{adiabatic}$-T_{in} [K]	Fr_{kin} [/]	Fr_{dens} [/]
0.8	1.111	90.395	0.4255	22.5	1.76	7.36	2714
1.0	1.389	112.993	0.4301	18.0	2.17	12.67	4088
1.2	1.667	135.592	0.4346	15.0	2.58	19.20	5664
1.4	1.944	158.191	0.4391	12.0	2.98	26.82	7287
1.62	2.25	183.050	0.4441	11.1	3.41	36.63	9952

Table 7.3: Calculated mean velocities in the annular gap and riser flow, hydraulic Reynolds number of the jet, adiabatic mixing temperature difference, kinetic and densimetric Froude numbers for varying jet flow in the heated jet experiment at a constant main flow rate of Q_{main}=18m^3/h ($Re_{mean,gap}$≈10^5) and T_{in}=300°C and $T_{in,jet}$=345°C. The nominal operation mode with Q_{main}/Q_{jet}=15 is highlighted in gray.

7.2.1 Mean temperature distribution for the jet flow variation

First the temperature rise distribution close to the lower shell is analyzed. The figures 7.12 and 7.13 show the temperature elevation as a function of the geometry adapted coordinate s for the individual jet flow rates.

In case of the lowest jet exit velocity with Q_{jet}=0.8m^3/h (Q_{main}/Q_{jet}=22.5), the jet flow looses most of its thermal energy from the inlet into the experimental mock-up down to the

nozzle exit. The temperature difference ΔT measured between T_{79} (at z=1683mm) and the nozzle exit T_{78} (at z=46.3mm) is 23.1°K although the mean fluid residence time of a fluid particle within the jet duct is rather short with only 1.47s. This temperature drop corresponds to more than half of the jets thermal energy.
With decreasing flow rate ratio Q_{main}/Q_{jet} the measured nozzle exit temperatures (T_{78}) continuously increase. But even at the highest investigated jet flow rate (Q_{main}/Q_{jet}=11.1) the nozzle exit temperature difference reaches only a value of 28.1K, which corresponds to a loss of 38% of the jets initial thermal energy.
For the largest flow rate ratio investigated Q_{main}/Q_{jet}=22.5 (Q_{jet}=0.8m^3/h) the temperature along the lower shell continuously decreases and at s=73.3mm hardly any temperature rise can be measured. Here the momentum of the main flow is so strong that the jet is pressed towards the shell. On both sides of the centerline only a marginal temperature rise is recorded indicating that only a negligible part of the jet is able to cross the centerline. A similar observation, but no so strongly pronounced, was observed for the flow rate ratio Q_{main}/Q_{jet}=20 discussed in chapter 7.1, see c.f. figures 7.1 and 7.2.
As the flow rate ratio drops to Q_{main}/Q_{jet}=18 (Q_{jet}=1m^3/h) the temperature difference at T_4 first falls and then grows to a local maximum at T_3, which can be explained by the jet impingement onto the shell. From there the temperature monotonically decreases to T_7. As the path proceeds to T_8 the temperature increases to a small peak and finally falls off to zero at T_9 and stays at this level. This kind of double peak temperature structure is even more expressed for the nominal case Q_{main}/Q_{jet}=15 (Q_{jet}=1.2m^3/h) and the reason is similar to the explanation given in chapter 6. The jet impinges on shell, detaches from it and reattaches at the opposite side of the symmetry line in the sector ϕ=180°. The double peak structure persists up to flow rate ratios Q_{main}/Q_{jet}=12.85 (Q_{jet}=1.4m^3/h) with a continuous increase of the temperature elevation along the shell. While decreasing the flow rate ratio only the second temperature peak is shifted towards the sector ϕ=180° opposite of the nozzle exit.
Only for the smallest flow rate ratio Q_{main}/Q_{jet}=11.1 (Q_{jet}=1.62m^3/h) the double peak structure of the temperature distribution diminishes and one large peak close to the centerline appears at T_2. Beyond this peak the temperature continuously drops down to T_{12}, where the inlet temperature of the main flow is obtained. Only for this flow rate ratio the momentum of the jet is strong enough to enter the annular gap of the downcomer.

The figure 7.13 shows the measured temperature distribution near the shell in the plane perpendicular to the nozzle ϕ=90°-270° as a function of the geometry adapted coordinate s.

The temperature profiles found here behave similar to the ones for the main flow variation at the same flow rate ratio Q_{main}/Q_{jet}. For large values of the flow rate ratio $Q_{main}/Q_{Jet}\geq$17.5 the jet is confined only to a narrow domain in the nozzle plane in the sector ϕ=0° and a marginal part of the jet is able to cross the centerline. Only close to the walls near the riser tube the temperature increases, which indicates the interaction of main and jet flow.

In the intermediate flow rate ratio between $12.5\leq Q_{main}/Q_{Jet}\leq 17.5$ the temperature distributions corresponds qualitatively to that of the nominal case discussed in chapter 6. For this combination the jet is able to cross the centerline and to interact with the main flow also in the region in the sector ϕ=180°. The temperature rise at the centerline covers the shell in both planes ϕ=0°-180° and ϕ=90°-270°.

Although for Q_{main}/Q_{Jet}=11.1 the jet is able to enter the annular gap opposite the nozzle the temperature profile in the plane ϕ=90°-270° corresponds qualitatively to that of the nominal case.

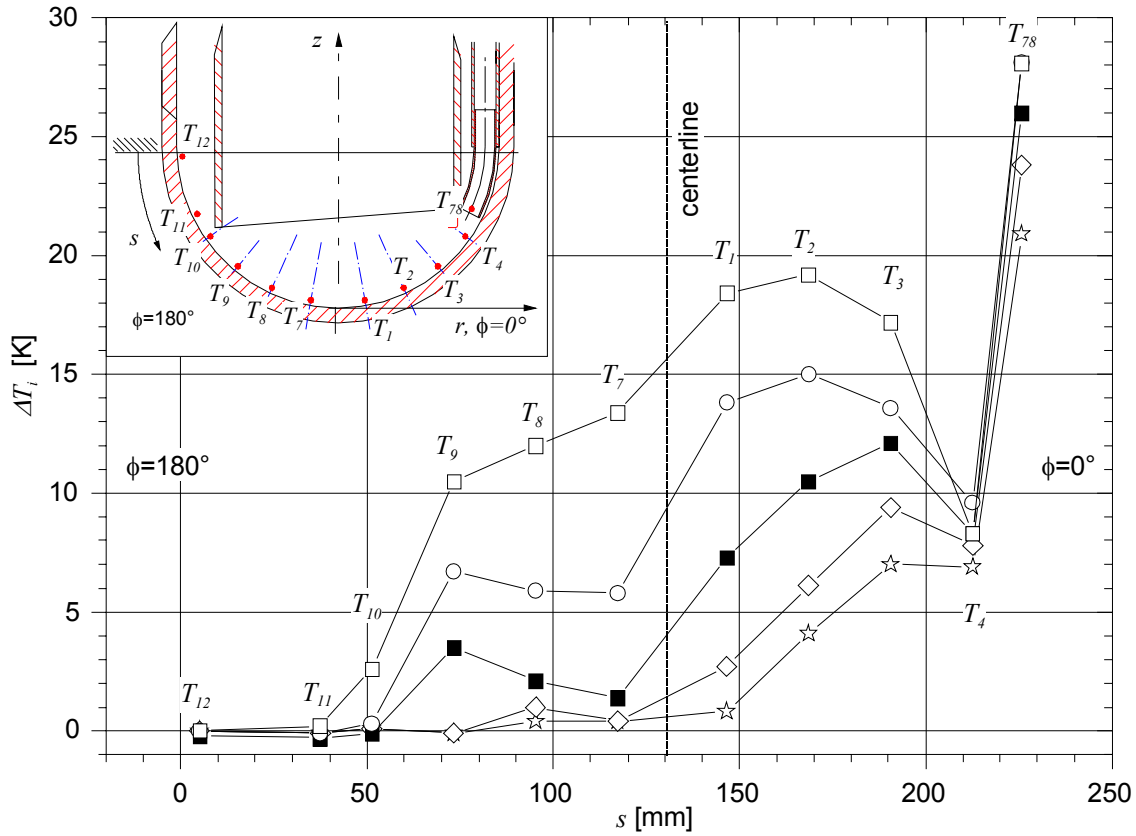

Figure 7.12: Measured temperature distribution as a function of the geometry adapted coordinate s in the plane ϕ=0°-180° for different jet flow rates Q_{jet} and the conditions Q_{main}=18m³/h, T_{in}=300°C and $T_{in,jet}$=345°C. (□) Q_{jet}=1.62m³/h, (O) Q_{jet}=1.4m³/h, (■) Q_{jet}=1.2m³/h, (◊) Q_{jet}=1m³/h and (ζ) Q_{jet}=0.8m³/h.

According to this experimental observation the leading parameter for the window cooling/heating is the flow rate ratio. The dependence of temperature distribution on the flow rate ratio in the current geometrical configuration holds as long as the flow is highly turbulent, which is ensured for main flow rates Q_{main}≥5m³/h and jet flow rates Q_{jet}≥0.33m³/h.

Unfortunately, for the small jet flows below (Q_{jet}≤0.5m³/h) a long term stable experiment could not be conducted, because the temperature differences in the lower part of the shell were extremely small and almost all thermal energy of the jet was transferred to the main flow in the annular gap before reaching the nozzle exit. Also the temperature regulation of the jet flow heater exhibited larger fluctuations, so that these results are not presented here.

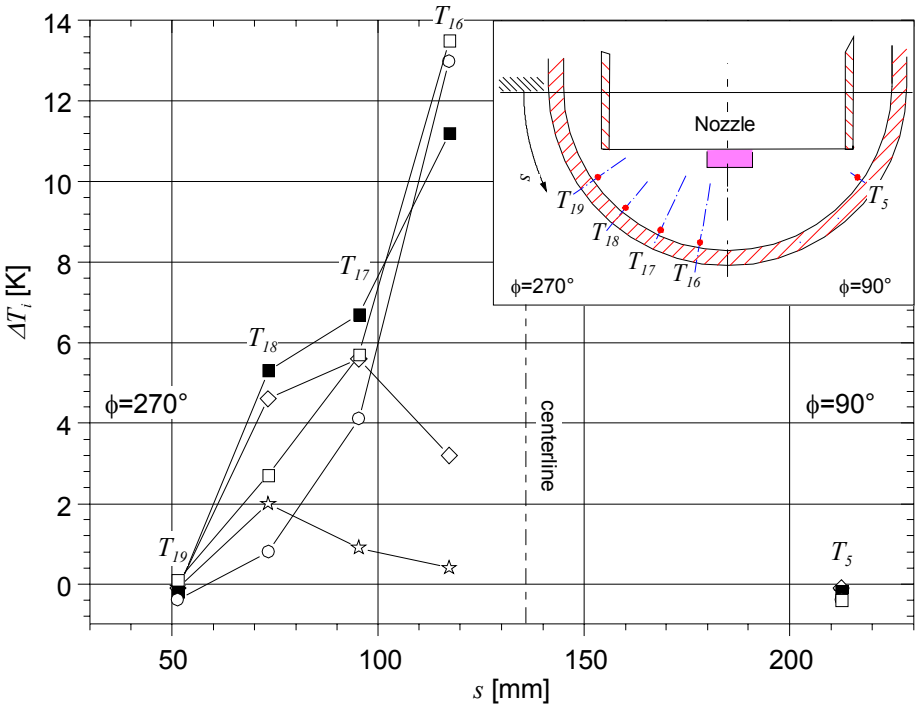

Figure 7.13: Measured temperature distribution as a function of the geometry adapted co-ordinate s in the plane ϕ=90° for different jet flow rates Q_{jet} and the conditions Q_{main}=18m^3/h, T_{in}=300°C and $T_{in,jet}$=345°C. (□) Q_{jet}=1.62m^3/h, (O) Q_{jet}=1.4m^3/h, (■) Q_{jet}=1.2m^3/h, (◊) Q_{jet}=1m^3/h and (ζ) Q_{jet}=0.8m^3/h.

The figures 7.14a-f show the temperature distribution near the riser wall along the axial coordinate z for several angular positions, ϕ=0°, ϕ=180° and ϕ=270°.

The figures 7.15 illustrate the temperature distribution at the thermocouple rake in the height z=105.7mm in the nozzle plane (ϕ=0°-180°) and normal to it (ϕ=90°-270°). Both figures are displayed in a dimensional and a non-dimensional way.

Especially the comparison of the non-dimensional values in both graphs exhibits clearly that the temperature distribution depends only on the chosen flow rate ratio Q_{main}/Q_{jet} and not on the chosen temperature level or the absolute value of the flow rate in the jet or main flow as long as both are highly turbulent.

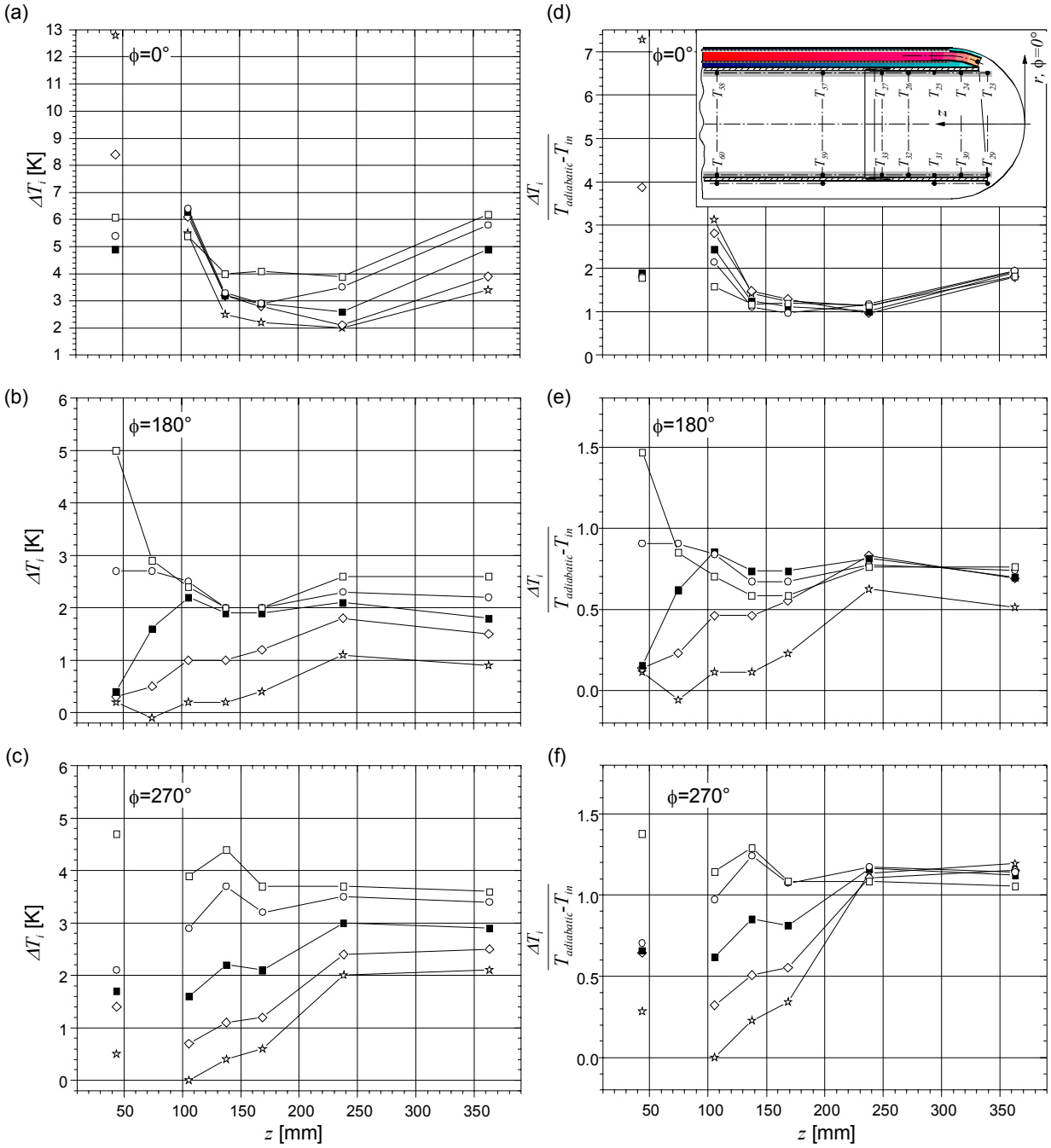

Figure 7.14: Measured dimensional and non-dimensional temperature distribution as a function of the axial length z at r=59.5mm for different jet flow rates Q_{jet} and the conditions Q_{main}=18m^3/h, T_{in}=300°C and $T_{in,jet}$=345°C. (a) and (d) ϕ=0°, (b) and (e) ϕ=180° and (c) and (f) ϕ=270°. (□) Q_{jet}=1.62m^3/h, (O) Q_{jet}=1.4m^3/h, (■) Q_{jet}=1.2m^3/h, (◊) Q_{jet}=1m^3/h and (ζ) Q_{jet}=0.8m^3/h.

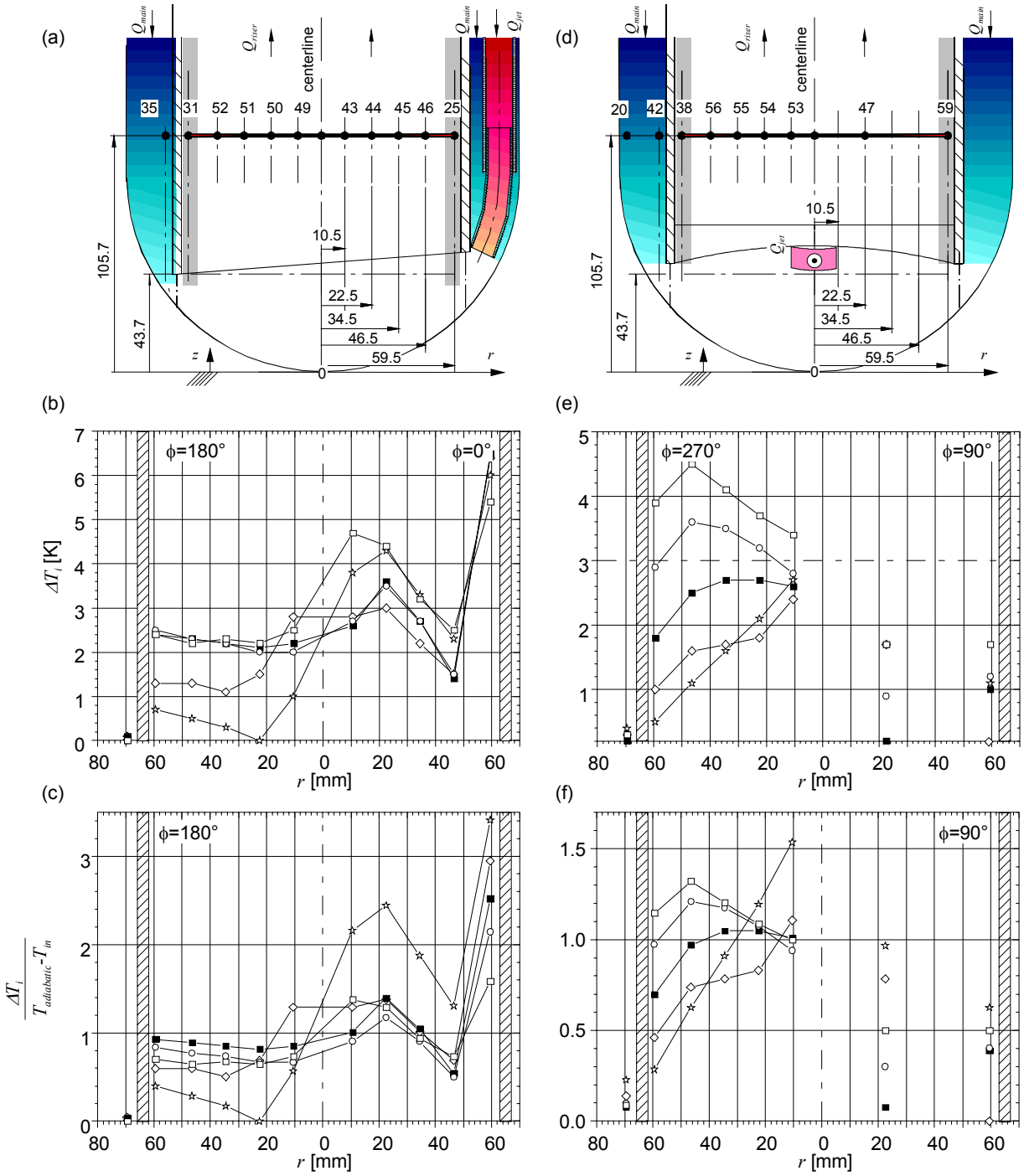

Figure 7.15: Measurement locations in the nozzle plane (a) on ϕ=0°-180° and normal to it (d) ϕ=90°-270°. Measured dimensional and non-dimensional temperature distribution as a function of the radius r at a height z=105.7mm for Q_{main}=18m^3/h, T_{in}=300°C and $T_{in,jet}$=345°C. (□) Q_{jet}=1.62m^3/h, (O) Q_{jet}=1.4m^3/h, (■) Q_{jet}=1.2m^3/h, (◊) Q_{jet}=1m^3/h and (ζ) Q_{jet}=0.8m^3/h.

7.2.2 Influence of the jet flow variation on the turbulent temperature fluctuations

Similar to the main flow variation also for the variation of the jet flow rate a non-steady behavior of the flow is found throughout the whole investigated parameter range. Again the spatial distribution of the normalized temperature fluctuations depends only on the adjusted flow rate ratio Q_{main}/Q_{jet} . This can be seen from the figure 7.16a-d, which show the tempera-

ture fluctuations close to the shell in both planes ϕ=0°-180° and ϕ=90°-270°. A comparison of the normalized values of the figures 7.16 with the data displayed in figures 7.6 and figures 7.7 confirms, that the fluctuation intensity is independent of the chosen temperature level.

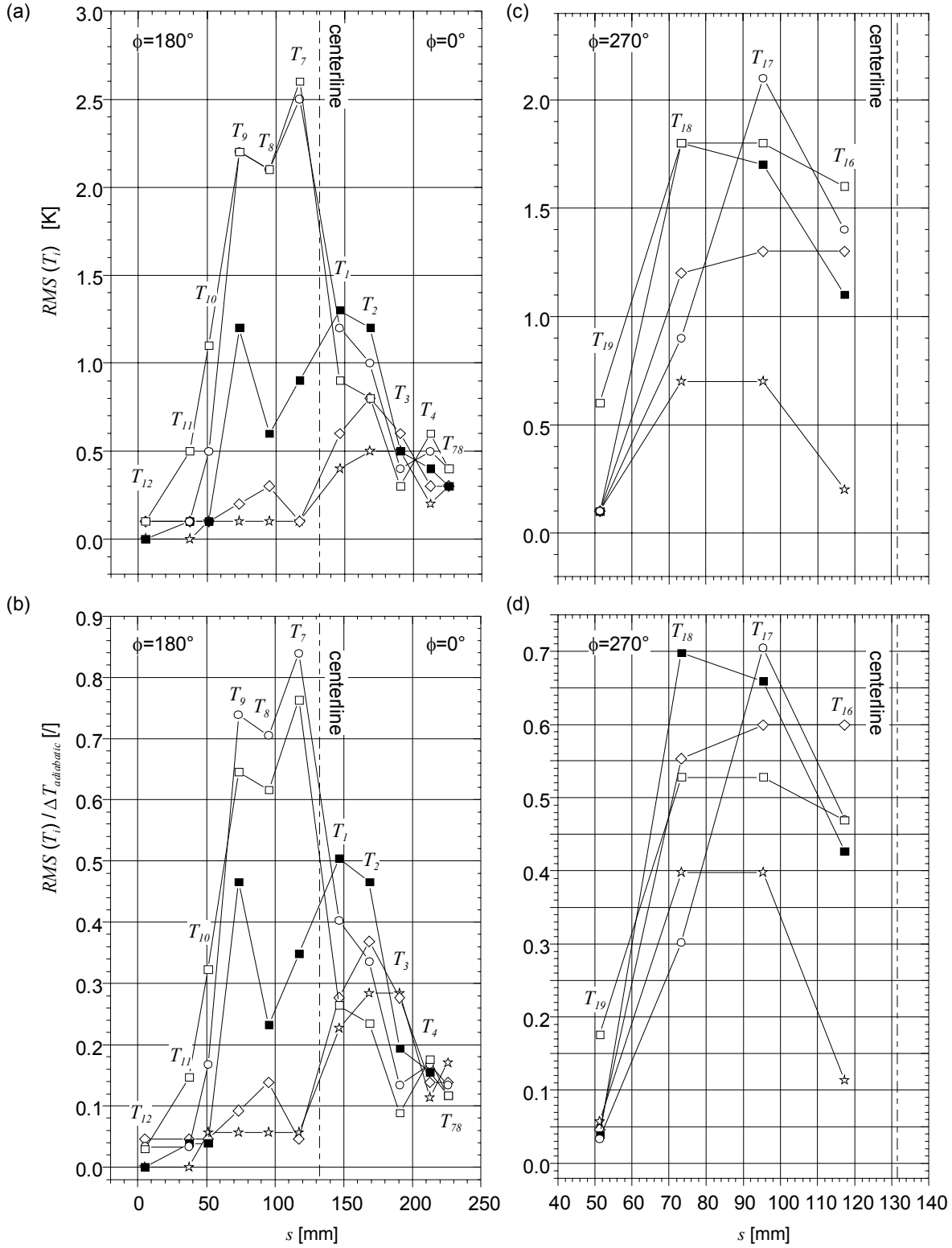

Figure 7.16: Measured dimensional and non-dimensional temperature fluctuation distributions (*RMS*-values) as a function of the geometry adapted coordinate s in the plane ϕ=0°-180° (a, b) and ϕ=90°-270° (c,d) for different jet flow rates Q_{jet} and the conditions Q_{main}=18m^3/h, T_{in}=300°C and $T_{in,jet}$=345°C. (□) Q_{jet}=1.62m^3/h, (O) Q_{jet}=1.4m^3/h, (■) Q_{jet}=1.2m^3/h, (◊) Q_{jet}=1m^3/h and (ζ) Q_{jet}=0.8m^3/h.

For completeness the figures 7.17 and 7.18 show the normalized *RMS*-Values of the temperature fluctuations in case of varying jet flow rates in a dimensional and non-dimensional way. But, again here no further insight and gain in understanding is obtained.

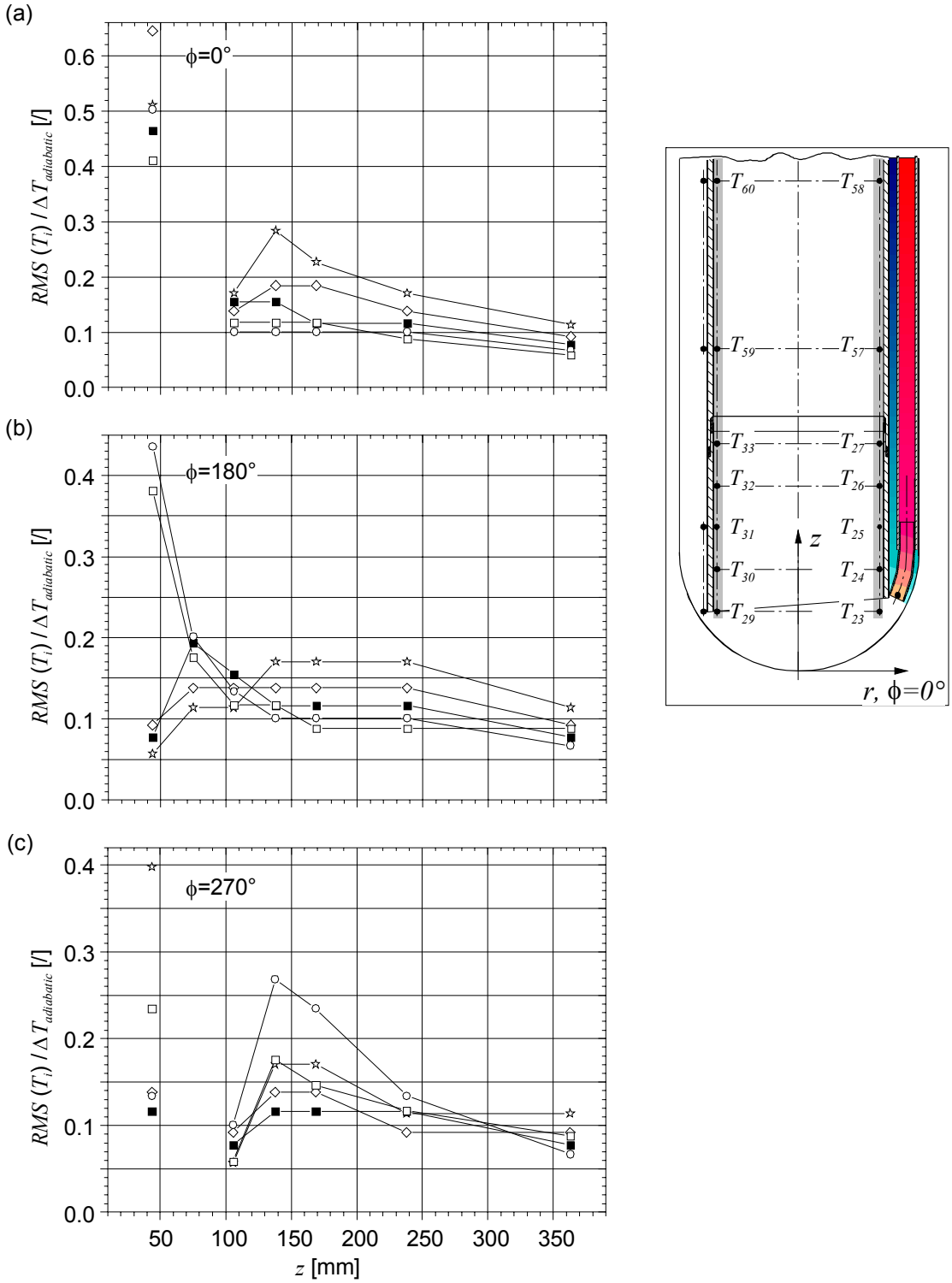

Figure 7.17: Measured non-dimensional temperature fluctuation distribution (*RMS*-values) as a function of the axial coordinate z on the lines ϕ=0°(a), ϕ=180°(b) and ϕ=270°(c) at r=59.5mm for different jet flow rates and the conditions Q_{main}=18m^3/h, T_{in}=300°C and $T_{in,jet}$=345°C. (□) Q_{jet}=1.62m^3/h, (O) Q_{jet}=1.4m^3/h, (■) Q_{jet}=1.2m^3/h, (◊) Q_{jet}=1m^3/h and (ζ) Q_{jet}=0.8m^3/h.

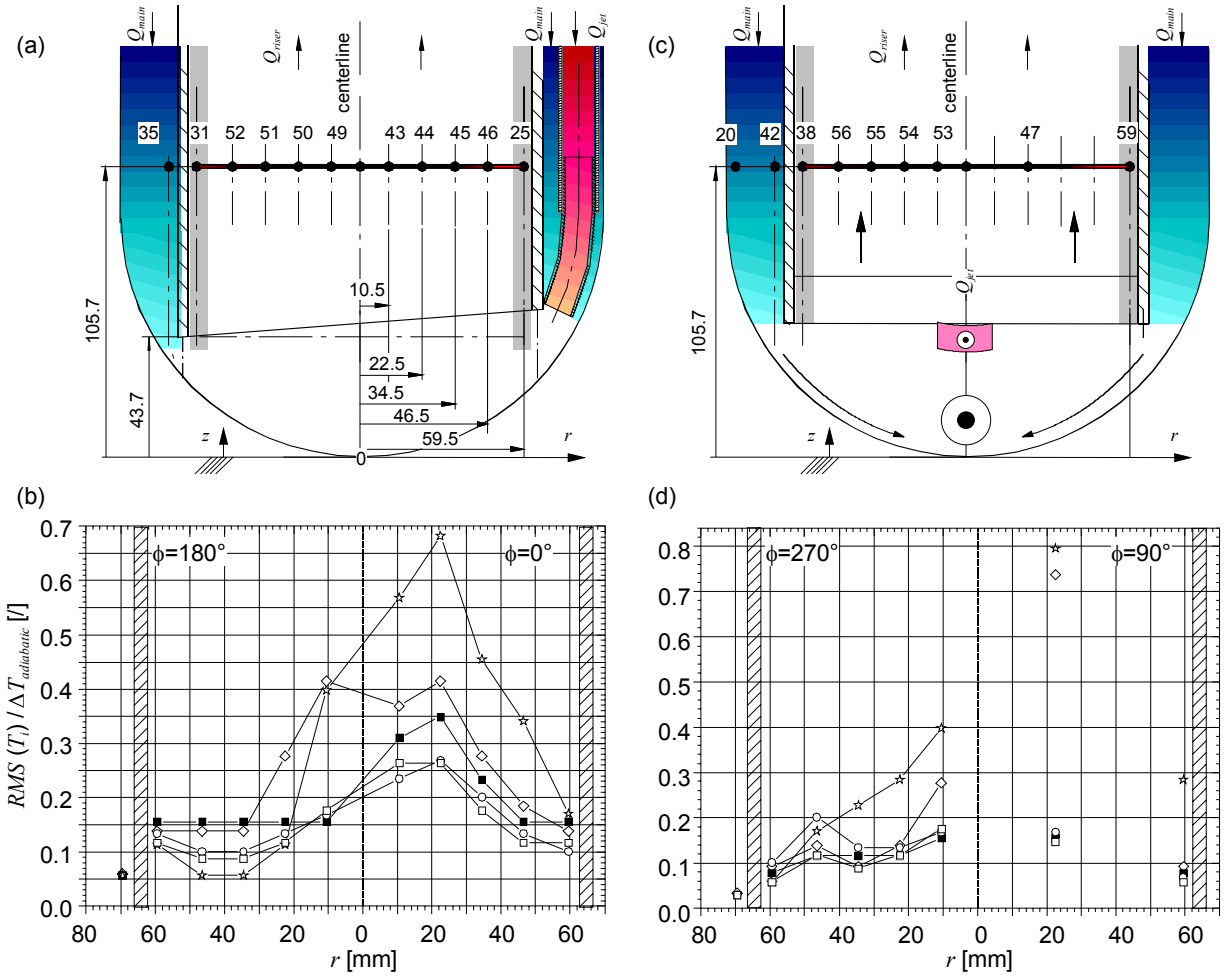

Figure 7.18: Measured non-dimensional (b, d) temperature fluctuation distribution (*RMS*-values) as a function of the radius r in a height z=105.7mm in the plane ϕ=0°-180° (a,b) and ϕ=90°-270° (c, d) for different jet flow rates Q_{jet} and the conditions Q_{main}=18m³/h, T_{in}=300°C and $T_{in,jet}$=345°C. (□) Q_{jet}=1.62m³/h, (O) Q_{jet}=1.4m³/h, (■) Q_{jet}=1.2m³/h, (◊) Q_{jet}=1m³/h and (ζ) Q_{jet}=0.8m³/h.

7.2.3 Summary of the jet flow rate variation

The jet flow rate variation was performed for jet flow rates from Q_{jet}=0.8m³/h to 1.62m³/h at a fixed main flow rate (Q_{main}=18m³/h) and constant inlet temperatures. The ratio Q_{main}/Q_{jet} covered in this investigation ranges from $11.1 \leq Q_{main}/Q_{jet} \leq 22.5$. Moreover, a lower jet inlet temperature has been chosen to investigate the influence of the thermal effects. The main results of this parameter variation are:

- In the investigated flow rate ratio range mainly three different flow types exist. The first one ranges appears $Q_{main}/Q_{jet} \leq 12.5$. The features of the mean temperature distribution and the fluctuations detected in this range correspond to the findings in chapter 7.1.3. Already at the flow rate ratio $Q_{main}/Q_{jet} \leq 12.85$ a double peak in the temperature distribution in the nozzle plane ϕ=0°-180° is recorded. This structure last up to flow rate ratios up to $Q_{main}/Q_{jet} \leq 18$. Thus, the limiting borders of the flow pattern in the lower shell which is similar to the nominal one discussed in chapter 6 ranges from $12.5 < Q_{main}/Q_{jet} \leq 18$. The third flow pattern for which the jet is mainly confined to the sector ϕ=0° starts to establish for the conditions $Q_{main}/Q_{jet} > 18$.

- The non-dimensional results of the mean temperature distributions and the corresponding temperature fluctuations for the variations of the jet and the main flow almost coincide for the same values of the ratio Q_{main}/Q_{jet}. This means that in the investigated parameter range only the chosen flow rate ratio determines the flow pattern and not the absolute values of the individual flow rates and also not the temperature difference between the main flow and the jet flow. Moreover, in all experiments the jet behaves as an inertial jet.
- For all jet and main flow variations investigated the flow close to the shell and also in the riser tube is time dependent. The local fluctuation intensities measured are of the order of several Kelvin. The fluctuation frequencies are larger than 1Hz.

General conclusion

One of the aims of the experimental series of the jet flow variation was to determine the borders of the different flow regimes occurring at different flow rate ratios Q_{main}/Q_{jet}. The most efficient mode to cool the lower bottom of the target shell in MEGAPIE is a flow rate ratio $Q_{main}/Q_{jet}\leq$12.5. Only below this limiting flow rate ratio border the jet covers the whole shell. Already at flow rate ratio of Q_{main}/Q_{jet}=12.85 the jet can detach from the shell before reaching the centerline. This would be associated with an increase of the window material temperatures. Although for $Q_{main}/Q_{jet}\leq$12.5 the temperature fluctuations are most pronounced they occur in a frequency range of larger than 1Hz. These rather high frequencies do not lead to large temperature pulsations for the MEGAPIE design. A shift of the temperature difference between main and jet flow at a constant flow rate ratio Q_{main}/Q_{jet} does not alter the evolving flow pattern. In all cases investigated and envisaged for MEGAPIE the jet behaves as an inertial jet.

8 Conclusions and recommendations

The liquid metal experiment named heated jet, which is presented in this report is a nearly 1:1 geometric representation of the lower part of the MEGAPIE target. In the context of the liquid metal experiment a heated jet is injected into a cold main flow in order to investigate the temperature distribution and the turbulent mixing of thermal energy within the lower part of the target geometry. One of the aims of the liquid metal experiment is to elaborate based on the temperature readings the borders between the different flow regimes in the MEGAPIE geometry, which occur in dependence on the flow rate ratio of main to jet flow (Q_{main}/Q_{jet}) and match these results with the velocity field data and observations gained in a water experiment with almost the same dimensions. This is of crucial importance since direct velocity measurements in the geometry were not possible. The experimental analysis is accompanied by a numerical simulation of the three-dimensional turbulent flow in the test geometry. Variations of the main flow rate and the jet flow rate which may occur due to incidents or chosen by the operator are investigated within the operational limits of the MEGAPIE target. Additionally, a temporal analysis of the data is performed in order to quantify their impact on the operational limits of the target and to determine the flow pattern evolving in the lower shell.

Although a considerable effort has been spent to simulate the turbulent flow in the geometry for the nominal flow rate ratio Q_{main}/Q_{jet}=15, a comparison of the numerical and ex-

perimental data revealed, that the geometry is highly sensitive to asymmetries and events far upstream. Although pre- and post test measurements of the test module show a symmetric experimental set-up with respect to the nozzle plane (ϕ=0°-180°), the experimental temperature data revealed a non-symmetric behavior especially in the riser tube. This asymmetry is independent of the history, the chosen temperature levels and the adjusted flow rate ratio and hence indicates the sensitivity of this flow geometry to marginal deviations. Due to the assumed symmetry in the nozzle plane ϕ=0°-180° the numerical simulation produced only steady results, while in the liquid metal experiment for all investigated flow rate ratio combinations a highly time-dependent flow was recorded.

The temperature oscillations found experimentally are considerably high. At the shell and in the lower part of the riser tube the dimensionless temperature fluctuations almost reach values of the order of one. However, most of the energy is stored in frequencies larger than 1Hz. Thus, the fluctuations are so fast, that they do not lead to large temperature oscillations within the structural material of the MEGAPIE target shell, which may lead to fatigue. The highest fluctuation intensities are recorded for low flow rate ratios $Q_{main}/Q_{jet}\leq$12.5 and appear close to the lower part of the shell. With increasing flow rate ratios the turbulence intensity decreases in the whole geometry.

A detailed temporal analysis of thermocouple readings in the geometry was performed for the nominal case with a flow rate ratio Q_{main}/Q_{jet}=15.

It exhibits a rather complex flow pattern in the lower shell. The main part of the jet flow hits the shell before reaching the centerline, detaches from it and a part of the jet reattaches the shell again beyond the centerline on the opposite side of the nozzle. While the jet detaches from the shell it interacts with the main flow forming a secondary flow at the bottom of the hemispherical shell. Additionally, the interaction of the jet with the shell and the main flow generates a pair of counter-rotating vortices, which rotate in the planes z=constant and are separated by the plane ϕ=0°-180°. A minor part of the jet flow separates at the lower edge of the riser tube in form of a separation vortex. Finally, an asymmetric detachment of the main flow at the lower rim of the riser tube generates a global helically upwards directed motion. Close to the shell the temperatures fluctuate considerably and RMS values of up to 50% of the adiabatic mixing temperature are obtained. As the flow proceeds downstream in the riser tube the fluctuation intensities continuously decrease. A power-spectral density analysis (PSD) for different temperature time series shows, that the turbulent temperature field in the riser tube is quasi-isotropic. Hence, the measured intensity of the detected vortices does not lead to a quasi two-dimensional turbulence structure.

The flow pattern established in the MEGAPIE design essentially depends on the chosen flow rate ratio (Q_{main}/Q_{jet}) between main flow and bypass flow. A dimensionless analysis of the experimental results yields that the flow pattern and the turbulence intensities are independent of the absolute values of the temperature and the flow rates as long as the main and bypass flow are highly turbulent. A change of the flow rate ratio leads to completely different flow patterns in the lower part of the hemispherical shell. In the scope of this experimental study we identified three different flow patterns.

- Q_{main}/Q_{jet}>18

  - Here, the jet is mainly confined to the nozzle plane in the sector ϕ=0°. Most of the temperature rise occurs in the nozzle adjacent domain in the sector ϕ=0°
  - The jet does not cover the whole lower part of the shell, because of the strong momentum of the main flow. It hardly reaches the lower bottom of the shell at the centerline of the geometry.
  - The temperature rise close to the centerline of the shell in the nozzle plane ϕ=0°-180° and transverse to it ϕ=90°-270° is rather low.
  - Before the jet reaches the plane ϕ=90°-270° at the centerline it is displaced sideways. Thus the highest measured temperatures and temperature fluctuation intensities are not found on the centerline. They are displaced by about 30mm from the centerline.
  - Most of the jet flow is separating at the lower rim of the riser tube and is transported downstream.
  - The thermal mixing is compared to lower flow rate ratios the worst, because a significant portion of the jet is involved in the flow separation at the lower edge of the riser tube generating there a large scale recirculation area confined to the sector ϕ=0°. The thermal energy from this sector to the adjacent fluid domains is rather poor.

- $12.5<Q_{main}/Q_{jet}\leq 18$
  - For this configuration the pattern corresponds to the one of the nominal case, in which the jet impinges the lower shell and splits off in several streams. One of them enters the sector ϕ=180° and interacts with the main flow.
  - Directly at the centerline the jet does not cover the lower bottom of the shell. Here, which is more severe for the application also the temperature fluctuation intensity is rather small.
  - Another one forms a recirculation area in the sector ϕ=0° arising from the separation at the lower edge of the riser tube.
  - A complex flow pattern evolves in the plane ϕ=90°-270°, which is characterized by the interaction of main and jet flow. Nevertheless the impact of the jet flow is significantly reduced in this plane.
  - Downstream in the riser tube the main features observed correspond to ones found in nominal case.
  - The thermal mixing is weaker than for flow rate ratios $Q_{main}/Q_{jet}\leq 12.5$ and it is not only concentrated to the shell region. Even for z>236mm measurable temperature differences are found. Especially at the line ϕ=0° close to the riser tube lumps of fluid with high temperature are observed. They show a high fluctuation intensity.

- $Q_{main}/Q_{jet}\leq 12.5$
  - Here, the jet flow covers the whole lower shell in the nozzle plane and sideways from it.
  - Moreover, the jet flow is even able to enter the annular gap opposite the nozzle exit.
  - Although this flow pattern is the most unsteady configuration, in which close to the shell fluctuation intensities of 80% and more appear, most of the fluctuations are located in a frequency range larger than 1Hz.

- The thermal mixing occurs on large scales within the lower part of the hemispherical shell in all directions.
- The thermal mixing of the jet with the main flow is mostly finished already in a height of z=105.7mm above the lower bottom of the shell. The temperature fluctuations recorded there are about 10-15%.

The observations and conclusions drawn from the temperature readings and the spatio-temporal analysis coincide with the experimental findings of the water experiment, see Stieglitz et al. (2005). There, also mainly three different flow patterns were detected appearing at the same flow rate ratio combinations.

Regarding the operational threshold of the MEGAPIE target flow rate ratios of Q_{main}/Q_{jet} >18 must be avoided in any case, because here the jet flow can not reach the lower bottom of the target shell and thus cool the window, where it experiences the highest heat load.

But also the flow rate ratio range from 12.5< Q_{main}/Q_{jet} <18 should be avoided. Although a strong interaction of the jet flow with the main flow and the shell was observed the temperature close to the centerline in the nozzle plane ϕ=0°-180° exhibited a local minimum and also the temperature fluctuation intensity there is not sufficiently large. Especially at this position the highest surface heat fluxes occur in the MEGAPIE target.

The MEGAPIE target requires that the jet covers the centerline at the lower bottom of the shell in both planes ϕ=0°-180° and ϕ=90°-270°. This constraint is only fulfilled for flow rate ratios $Q_{main}/Q_{jet}\leq$12.5. Also the fluctuation intensities are largest for this configuration, the fluctuations are located in a frequency range larger than 1Hz, which does not yield to significant temperature oscillations of the lower shells material. For these flow rate ratios the fluctuations occur on large geometrical scales mainly in the lower part of the shell. This, however, leads to an efficient thermal mixing of both fluid flows, so that the temperatures are mostly equalized to the adiabatic mixing temperature even in a distance of less than 150mm away from the lower bottom of the target shell. Consequently, these flow rate ratios ensure an efficient mixing desired in MEGAPIE to keep the thermal stresses of the riser tube within acceptable limits.

Acknowledgements
This work bas been performed within the context of the EU-programs TECLA (FIKW-CT2000-00092) and MEGAPIE-TEST (FIS5-2001-00090) and is supported by the HGF Strategy Fund Project (01SF9926/3). The authors thank to the fruitful discussion with Dr. G. Grötzbach (IKET), Prof. Dr. U. Müller, Dr. B. Smith (Paul-Scherrer Institute, Switzerland) and Dr. B. Sigg (ETH Zürich, Switzerland). A large scale experiment like the heated jet is impossible without the help of numerous unnamed technicians of the Institute for Nuclear and Energy Technologies, whom we thank here, too.

9 References

ADTF Design Team, 2002, *Private Communication, Argonne National Laboratory, May 2001 – January 2002.*

Arien, 2004, Assessment of Computational Fluid Dynamic codes for Heavy Liquid Metals-ASCHLIM, EC-Contract FIKW-CT-2001-80121-Final Report.

Batchelor, G.K., 1959, The theory of homogeneous turbulence. Cambridge University Press.

Batta, A., Daubner, M., Cheng, X., 2004, Investigation on turbulent mixing process in MEGAPIE target configuration, Jahrestagung Kerntechnik 2004, Düsseldorf 25th-27th May 2004. Berlin, INFORUM GbmH, 2004, CD-ROM, S. 88 - 91

Beitz, W, Küttner, K.-H., 1986, Dubbel-Taschenbuch des Maschinenbaus, Springer-Verlag, 15th edition; *ISBN 3-540-12418-7*, p. 1211 ff.

Bendat, J, Piersol, A., 1971, Random Data : Analysis and measurement procedures. Wiley and Sons, Inc.. ISBN 0-471-06470-X.

Bremhorst, K., Krebs, L., 1992, Experimentally determined turbulent Prandtl numbers in liquid sodium at low Reynolds numbers. Int. J. Heat and Mass Transfer, 35, p. 351-359.

Burr, U., 1998, Turbulent transport phenomena in magnetohydrodynamic channel flows. Forschungszentrum Karlsruhe, Wissenschaftliche Berichte, FZKA-6038.

Carteciano L.N., 1996, Entwicklung eines Turbulenzmodells für Auftriebsströmungen. Dissertation. Forschungszentrum Karlsruhe, Wissenschaftliche Berichte, FZKA 5775.

Carteciano, L. N., Wörner, M., Grötzbach, G., 1999, Erweiterte Turbulenzmodelle für technische Anwendungen von FLUTAN auf Naturkonvektion. Jahrestagung Kerntechnik 1999, Karlsruhe, 18. - 20.5.1999, Kerntechn. Ges. e.V., INFORUM Bonn (1999) S. 129 - 133

Chen, C.J., Rhodi, W., 1975, A review of experimental data of vertical buoyant jets. Rep. SFB 80/T/69. University Karlsruhe.

Chen, C.J., Rhodi, W., 1980, Turbulent buoyant Jets. A review of experimental data. Heat and Mass Transfer, Vol. 4., Pergamon Press.

Daubner, M, Batta, A., Fellmoser, F., Lefhalm, C.-H., Mack, K.-J., Stieglitz, R., 2004, Turbulent heat mixing of a heavy liquid metal flow within the MEGAPIE window geometry-the heated jet experiments. Journal Nuclear Materials, 335, p. 286-292.

Dementjev, S., Gröschel, F., Ivanov, S., Platacis, E., Von Holzen, G., Zik, A., 2003, EMPS for MEGAPIE target. Testing of the Prototype. PSI-Report MPR-11-DS34-005/0.

Donaldson, D., Snedekker, R., Margolis, D., 1971, A study of free jet impingement: Part 2-Free jet turbulent structure and impingement heat transfer. J. Fluid Mech., 45, p. 477-512.

Dury,T.V. 2002, Megapie – Design Using CFD of a Liquid-Metal Target to be Installed in SINQ, PSI Scientific Report 2001/ Vol. IV, Nuclear Energy and Safety, pp 95-105, March 2002.

Eiselt, C., 2003, Experimentelle Messung des Geschwindigkeitfeldes und der Druckverluste am MEGAPIE-Target, Studienarbeit der Universität Karlsruhe, Fakultät für Maschinenbau. *Gröschel, F.,* 2003, Status of PSI activities within WP1/Task 1.2, MEGAPIE-Test, 2nd Semi-Annual Meeting 10.-11.3.2003, PSI, Villigen.

Grötzbach, G., Batta, A., Lefhalm, C.H., Otic, I., 2004, Challenges in thermal and hydraulic analyses of ADS target systems, 6th Int. Conf. on Nuclear Thermal-Hydraulics Operations and Safety, NUTHOS-6, Nara, Japan, 4th –8th Oct. 2004, p. 2-18.

Hussein, H.J., Capp, S. P., George, W. P., 1994, Velocity measurements in a high Reynolds number, momentum-conserving, axissymmetric, turbulent jet. J. Fluid Mech., 258, 31-75.

Ichimiya, K., Yamada, Y., 2003, Three-dimensional heat transfer of a confined circular impinging jet with buoyancy effects, Transactions of the ASME- Journal Heat Transfer, 125, p. 250-256, April 2003.

Imbeni, V. Martini, C., Masini, S., Palombarini, G., 1999, The properties of the eutectic alloys Pb55.5Bi and Pb17Li. ENEA-Report DT-EUB-00001, Part 2.

ISO 3966-1977, 1999, Measurement of fluid flow in closed conduits -- Velocity area method using Pitot static tubes, Edition 1999.

Kader, B.A: 1981, „Temperature and concentration profiles in fully turbulent boundary layers". Int. J. Heat and Mass Transfer, 24(9), p. 1541-1544.

Kirillov, P., Subbotin, V., Suvorov, M, Troyanov, 1959, Heat transfer in a tube to sodium potassium alloy and mercury. Soviet Journal of atomic energy, Vol 6., p. 253-260.

Knebel, J.-U., Krebs, L., Müller, U., Axcell, B.P., 1998, A confined sodium jet in a co-flow. J. Fluid Mech., 368, p. 51-80.

Knebel,J.U., Cheng, X., Tak, N. 2001, Thermal-hydraulic Design of the MEGAPIE Spallation Target, 5th Topical Meeting on Nuclear Applications of Accelerator Technology, Reno, November 11-16.

Knebel, J.U.; Müller, G.; Konys, J.; KALLA-Team, 2002, HGF strategy fund project 99/16: thermalhydraulic and material specific investigations into the realization of an accelerator driven system (ADS) to transmute minor actinides. Programm Nukleare Sicherheitsforschung. Jahresbericht 2001. Teil 1 Forschungszentrum Karlsruhe, Wissenschaftliche Berichte, FZKA-6741 (Juni 2002) S.417-55.

Knebel, J.U., Cheng, X., Grötzbach, G., Stieglitz, R., Müller, G., Konys, J., 2003, Thermalhydraulic and Material Specific Investigations into the Realization of an Accelerator Driven System (ADS) to Transmute Minor Actinides- Final Report. Forschungszentrum Karlsruhe, Wissenschaftliche Berichte, FZKA 6868.

Krebs, L., Bremhorst, K. , 1983, Verification of the extended gradient diffusion model by measurement of the mean and fluctuating part of the temperature fields in sodium flow downstream of a multi-bore jet block. Proc. 4th Symp. Turbulent Shear Flows, Karlsruhe, Sept. 12 – 14, 1983, p. 17.1-17.5.

Kulite, 2003, Product Specification XTME-190, Kulite Semiconductor Product Inc., http://www.kulite.com.

Lefhalm, C.H., Tak, N.I., Grötzbach, G., Piecha, H., Stieglitz, R., 2003, *Turbulent Heat Transfer along a Heated Rod in Heavy Liquid Metal Flow.* Proceedings of the Tenth International Topical Meeting on Nuclear Reactor Thermal Hydraulics NURETH-10, Seoul, Oct. 5-11, 2003, Seoul: Korean Nuclear Society, 2003

Lefhalm, C.H., Tak, Piecha, H., Stieglitz, R., 2004, *Turbulent heavy liquid metal heat transfer along a heated rod in an annular cavity.* Journal Nuclear materials, 335, p.280-285.

Lefhalm, C.H., Gnieser, S., Stieglitz, R., 2005, Velocity Measurements within a beam window geometry. Jahrestagung Kerntechnik 2005, Inforum Verlag, p. 132-135.

Lefhalm, C.H., Daubner, M., Stieglitz, R., 2005, Validation of flow rate measurement techniques for liquid lead bismuth. Jahrestagung Kerntechnik 2005, Inforum Verlag, p. 566-570.

Lefhalm, C.H, 2005, Qualifizierung von Messtechniken zur Erfassung von Strömungsgrößen in flüssigen Schwermetallen. Forschungszentrum Karlsruhe, Wissenschaftliche Berichte, FZKA-7111.

Lesieur, M., Herring, J., 1985, Diffusion of a passive scalar in two-dimensional turbulence. J. Fluid Mech., 161, p. 77-95.

Lowery, G.W., Vachon, I., 1975, The effect of turbulence on heat transfer from heated cylinders. Int. J. Heat Mass Transfer, 18, p.1229-1242.

Lugt, H.J., 1996, Introduction to vortex theory, Vortex Flow Press, Inc., ISBN 0-9657689-0-2.

Lyon, R.N., 1952, Liquid metals handbook; Navexos P-733; Second edition.

Martinelli, 1947, Heat transfer to molten metals, Trans. of the American Society of Mechanical Engineers. Vol. 69, p. 947- 959.

Naguib, A.M, Koochesfani, M.M., 2004, On wall-pressure sources associated with the unsteady separation in a vortex-ring/wall interaction. Physics of Fluids, 16(7), p. 2613-2622.

Ogino, F., Takeuchi, H., Kudo, I., Mizushina, T., 1980, Heated Jet discharged vertically into ambient of uniform and linear temperature profile. Int. J. Heat and Mass Transfer, 23, p. 1581-1588.

Oh, C. , Lienhard, J., Hesham, F., Dahbura, R., Michels, D., 1998, Liquid jet array cooling modules for high heat fluxes. AIChE Journal , 44(4), p. 769-779.

Panametrics, 2000, http://www.panametrics.com, info 6/2000.

Patorski, J., Bauer, G., Platnieks, I., Takeda,Y., 2000, Experimental estimation of optimum Bypass-jet-flow conditions for the cooling of the window of the SINQ liquid metal target", *PSI Report 2000, ISSN 1423-7350*, Vol. VI, pp.42-44, PSI, CH-5232 Villigen, Switzerland.

Ricoud, F.P., Spalding, D. B., 1961, Measurement of entrainment by axisymmetric turbulent jets. J. Fluid Mech., 11, p.21-32.

Rimpault,G., et al., 2003, XADS technical Objectives and Justification of the Experimental Programme for ADS Transmutation Applications, DER/SPRC/LEDC-03/402, CEA, January 2003.

Rosemount, 2003, Model 3051T Gage and Absolute Pressure Transmitter. http://www.rosemount.com/products/pressure/m3051.html .

Roubin, P., 2001, MEGAPIE steady state simulation of the lower target thermalhydraulics. Preliminary cases without heat source in the structures. CEA-NT DEN/DTP/STH/LTA/2001-12.

Roubin, P., 2002, MEGAPIE steady state simulation of the lower target thermalhydraulics. Cases without Bypass (Benchmark M1). CEA-NT DEN/DTP/STH/LTA/2002-17.

Roubin, P., 2003, MEGAPIE steady state simulation of the lower target thermalhydraulics. Cases with Bypass and reference nozzle geometry. CEA-NT DEN/DTP/STH/LTA/2003-3.

Roubin, P., 2003, MEGAPIE steady state simulation of the lower target thermalhydraulics. Optimization of the nozzle geometry. CEA-NT DEN/DTP/STH/LTA/2003-25.

Ruffin, E, Schiestal, R, Anselmet, F., Ahmiel, H., Fulachier, 1994, Investigation of characteristic scales in variable density jets using a second order model. Physics of Fluids, 6, p.2785-2799.

Salvatores, M., Bauer, G., Heusener,G., 1999, The MEGAPIE Initiative – Executive Outline and Status as per November 1999, *Paul Scherrer Institut.*

Schneider, W., 1985, Decay of momentum flux in submerged jets. J. Fluid Mech., 154, p.91-110.

Shercliff, J. A. , 1962, The theory of electro-magnetic flow measurement; Cambridge University Press, 1962.

Shercliff, J. A. , 1987, The theory of electro-magnetic flow measurement-Induction devices; Cambridge University Press, 1987, ISBN 0521 335 54X.

Smith, B. 2002, Summary of the First MEGAPIE- CFD Benchmark Study PSI-Internal Report *MPBE-4-BR-1/0*, 2002.*E.*

Stieglitz, R., 2003, MHD-features of the Main service and Bypass pump in the MEGAPIE Design. Forschungszentrum Karlsruhe, Wissenschaftliche Berichte, FZKA-6826.

Tak, N.-I., Cheng, X., 2001, Numerical design of the active part of the MEGAPIE target, Forschungszentrum Karlsruhe, Wissenschaftliche Berichte, FZKA-6611, May 2001.

Vieser, W., Esch, Th., Menter, F., 2002, "CFX –5 Solver Theory"; CFX Ltd. Didcot Oxfordshire OX11 OQR, United Kingdom.

VDI-Wissensforum, 2001, Durchfluss und Mengenmessungen in Rohrleitungen, VDI-Seminar 361624, Universität Stuttgart.

Wilcox, D.C.,1986 , "Multiscale model for turbulent flows; 24th Aerospace Science Meetings; American Institute of Aeronautics and Astronautics.

Wolf, D., 1999, Signal theory. Springer-Verlag, ISBN 3-540—65793-2.

Yefimov, E.I., 1996, Preconceptional design of a 1MW flow Lead-bismuth target. State Scientific Centre of Russian Federation- Institute of Physics and Power Engineering. Report *No. 35-06/64-1996.*

Yefimov, *E.I.,* 1998, The main results of feasibility study of liquid metal targets and the working plan on the project 559, *Kick-off meeting on the ISTC project #559, February 1998, Obninsk, Russia.*

Zauner, E., 1985, Visualization of the viscous flow induced by a round jet. J. Fluid Mech., 154, p.111-119.

Appendix A Instrumentation positions in the experiment

No.	Sensor	∅ [mm]	L [mm]	Meas. range	r [mm]	ϕ [°]	z [mm]	local description
1	NiCrNi-TE	0,5	600	0 - 500°C	14,6	0	4,3	Shell
2	NiCrNi-TE	0,5	600	0 - 500°C	35,5	0	10,9	Shell
3	NiCrNi-TE	0,5	600	0 - 500°C	54,0	0	22,7	Shell
4	NiCrNi-TE	0,5	600	0 - 500°C	68,8	0	38,8	Shell
5	NiCrNi-TE	0,5	600	0 - 500°C	68,8	90	38,8	Shell
6	NiCrNi-TE	0,5	600	0 - 500°C	84,0	90	113,0	Shell
7	NiCrNi-TE	0,5	600	0 - 500°C	14,6	180	4,3	Shell
8	NiCrNi-TE	0,5	600	0 - 500°C	35,5	180	10,9	Shell
9	NiCrNi-TE	0,5	600	0 - 500°C	54,0	180	22,7	Shell
10	NiCrNi-TE	0,5	600	0 - 500°C	68,8	180	38,8	Shell
11	NiCrNi-TE	0,5	600	0 - 500°C	75,8	180	51,0	Shell
12	NiCrNi-TE	0,5	600	0 - 500°C	83,8	180	82,0	Shell
13	NiCrNi-TE	0,5	600	0 - 500°C	84,0	180	113,0	Shell
14	NiCrNi-TE	0,5	600	0 - 500°C	84,0	180	176,0	Shell
15	NiCrNi-TE	0,5	600	0 - 500°C	84,0	180	238,0	Shell
16	NiCrNi-TE	0,5	600	0 - 500°C	14,6	270	4,3	Shell
17	NiCrNi-TE	0,5	600	0 - 500°C	35,5	270	10,9	Shell
18	NiCrNi-TE	0,5	600	0 - 500°C	54,0	270	22,7	Shell
19	NiCrNi-TE	0,5	600	0 - 500°C	68,8	270	38,8	Shell
20	NiCrNi-TE	0,5	600	0 - 500°C	84,0	270	113,0	Shell
21	NiCrNi-TE	0,5	600	0 - 500°C	84,0	270	176,0	Shell
22	NiCrNi-TE	0,5	600	0 - 500°C	84,0	270	238,0	Shell
23	NiCrNi-TE	0,5	3500	0 - 500°C	59,5	0	43,7	End riser tube
24	NiCrNi-TE	0,5	3500	0 - 500°C	59,5	0	74,7	End riser tube
25	NiCrNi-TE	0,5	3500	0 - 500°C	59,5	0	105,7	End riser tube
26	NiCrNi-TE	0,5	3500	0 - 500°C	59,5	0	137,7	End riser tube
27	NiCrNi-TE	0,5	3500	0 - 500°C	59,5	0	168,7	End riser tube
28	NiCrNi-TE	0,5	3500	0 - 500°C	59,5	90	43,7	End riser tube
29	NiCrNi-TE	0,5	3500	0 - 500°C	59,5	180	43,7	End riser tube
30	NiCrNi-TE	0,5	3500	0 - 500°C	59,5	180	74,7	End riser tube
31	NiCrNi-TE	0,5	3500	0 - 500°C	59,5	180	105,7	End riser tube

No.	Sensor	∅ [mm]	L [mm]	Meas. range	r [mm]	ϕ [°]	z [mm]	local description
32	NiCrNi-TE	0,5	3500	0 - 500°C	59,5	180	137,7	End riser tube
33	NiCrNi-TE	0,5	3500	0 - 500°C	59,5	180	168,7	End riser tube
34	NiCrNi-TE	0,5	3500	0 - 500°C	69,5	180	43,7	End riser tube
35	NiCrNi-TE	0,5	3500	0 - 500°C	69,5	180	105,7	End riser tube
36	NiCrNi-TE	0,5	3500	0 - 500°C	59,5	270	43,7	End riser tube
37	NiCrNi-TE	0,5	3500	0 - 500°C	59,5	270	74,7	End riser tube
38	NiCrNi-TE	0,5	3500	0 - 500°C	59,5	270	105,7	End riser tube
39	NiCrNi-TE	0,5	3500	0 - 500°C	59,5	270	137,7	End riser tube
40	NiCrNi-TE	0,5	3500	0 - 500°C	59,5	270	168,7	End riser tube
41	NiCrNi-TE	0,5	3500	0 - 500°C	69,5	270	43,7	End riser tube
42	NiCrNi-TE	0,5	3500	0 - 500°C	69,5	270	105,7	End riser tube
43	NiCrNi-TE	0,5	3500	0 - 500°C	10,5	0	105,7	End riser tube
44	NiCrNi-TE	0,5	3500	0 - 500°C	22,5	0	105,7	End riser tube
45	NiCrNi-TE	0,5	3500	0 - 500°C	34,5	0	105,7	End riser tube
46	NiCrNi-TE	0,5	3500	0 - 500°C	46,5	0	105,7	End riser tube
47	NiCrNi-TE	0,5	3500	0 - 500°C	22,5	90	105,7	End riser tube
48	NiCrNi-TE	0,5	3500	0 - 500°C	59,5	90	105,7	End riser tube
49	NiCrNi-TE	0,5	3500	0 - 500°C	10,5	180	105,7	End riser tube
50	NiCrNi-TE	0,5	3500	0 - 500°C	22,5	180	105,7	End riser tube
51	NiCrNi-TE	0,5	3500	0 - 500°C	34,5	180	105,7	End riser tube
52	NiCrNi-TE	0,5	3500	0 - 500°C	46,5	180	105,7	End riser tube
53	NiCrNi-TE	0,5	3500	0 - 500°C	10,5	270	105,7	End riser tube
54	NiCrNi-TE	0,5	3500	0 - 500°C	22,5	270	105,7	End riser tube
55	NiCrNi-TE	0,5	3500	0 - 500°C	34,5	270	105,7	End riser tube
56	NiCrNi-TE	0,5	3500	0 - 500°C	46,5	270	105,7	End riser tube
57	NiCrNi-TE	1,0	3500	0 - 500°C	59,5	0	238,0	Innenrohr (Riser)
58	NiCrNi-TE	1,0	3500	0 - 500°C	59,5	0	363,0	Inner tube (riser)
59	NiCrNi-TE	1,0	3500	0 - 500°C	59,5	180	238,0	Inner tube (riser)
60	NiCrNi-TE	1,0	3500	0 - 500°C	59,5	180	363,0	Inner tube (riser)
61	NiCrNi-TE	1,0	3500	0 - 500°C	59,5	270	238,0	Inner tube (riser)
62	NiCrNi-TE	1,0	3500	0 - 500°C	59,5	270	363,0	Inner tube (riser)
63	NiCrNi-TE	1,0	3500	0 - 500°C	69,5	180	238,0	Inner tube (riser)
64	NiCrNi-TE	1,0	3500	0 - 500°C	69,5	180	363,0	Inner tube (riser)

No.	Sensor	∅ [mm]	L [mm]	Meas. range	r [mm]	ϕ [°]	z [mm]	local description
65	NiCrNi-TE	1,0	3500	0 - 500°C	69,5	270	238,0	Inner tube (riser)
66	NiCrNi-TE	1,0	3500	0 - 500°C	69,5	270	363,0	Inner tube (riser)
67	NiCrNi-TE.	0,5	3000	0 - 500°C	7,5		420,5	(ehemals mpp)
68	NiCrNi-TE	0,5	3000	0 - 500°C	7,5		420,5	(")
69	NiCrNi-TE	0,5	3000	0 - 500°C	7,5		427,5	(")
70	NiCrNi-TE	0,5	3000	0 - 500°C	7,0	270	427,5	Instr.-rod(Prandtl)
71	NiCrNi-TE	1,0	3000	0 - 500°C	15,5	0	485,0	Instr.-rod
72	NiCrNi-TE	1,0	3000	0 - 500°C	31,5	0	1542,0	Instr.-rod
73	NiCrNi-TE	1,0	3000	0 - 500°C	31,5	0	2000,0	Instr.-rod
74	NiCrNi-TE	1,0	1800	0 - 500°C	76,5	0	1730,0	above flow straight-ener
75	NiCrNi-TE	1,0	1800	0 - 500°C	76,5	90	1730,0	above flow straight-ener
76	NiCrNi-TE	1,0	1800	0 - 500°C	76,5	180	1730,0	above flow straight-ener
77	NiCrNi-TE	1,0	1800	0 - 500°C	76,5	270	1730,0	above flow straight-ener
78	NiCrNi-TE	1,0	2200	0 - 500°C	72,1	0	53,5	Jet duct nozzle
79	NiCrNi-TE	3,0	300	0 - 500°C	76,8	45	1542,0	Outer tube
80	NiCrNi-TE	3,0	300	0 - 500°C	76,8	45	892,0	Outer tube
81	TE + 8° ?	3,0	300	0 - 500°C	76,8	225	892,0	Outer tube
82	NiCrNi-TE	3,0	300	0 - 500°C	76,8	315	892,0	Outer tube
83	NiCrNi-TE	3,0	300	0 - 500°C	76,8	135	1542,0	Outer tube
84	NiCrNi-TE	3,0	300	0 - 500°C	76,8	225	1542,0	Outer tube
85	NiCrNi-TE	3,0	300	0 - 500°C	-	-	1637,0	jet duct -inflow
90	p_{abs} (KS)	10x1	-	0 - 3.5 bar	87,0	135	892,0	outer tube
91	p_{abs} (KS)	10x1	-	0 - 3.5 bar	-	0	1637,0	jet duct inflow
92	p_{abs} (KS)	10x1	(2400)	0 - 3.5 bar	10,5	180	700,0	instrumentation rod
93	p_{abs} (KS)	10x1	(905)	0 - 3.5 bar	31,5	180	1900,0	instrumentation rod
94	p_{diff} (Rsm)	6x1	(3000)	0 - 62 mbar	0,0	Z	350,0	instrumentation rod
	p_{diff} (Rsm)	6x1	(3000)		4,0	0/180	385,0	(Prandtl-probe)
95	p_{diff} (Rsm)	6x1		0 - 62 mbar				jet duct -inflow
	p_{diff} (Rsm)	6x1						(Pitot+stat. pressure)
96	p_{diff} (Rsm)	10x1		0 - 620 mbar				Annubar probe
	p_{diff} (Rsm)	10x1						

Appendix B Heat losses of the experiment to the ambient

Of crucial importance are the heat losses along the whole flow path to the ambient in order to calculate the adiabatic mixing temperature $T_{adiabatic}$. The adiabatic mixing temperature is obtained from an energy balance in the following way:

$$\rho(T_{in})\cdot Q_{main}\cdot c_p(T_{in})\cdot T_{in}+\rho(T_{jet,in})\cdot Q_{jet}\cdot c_p(T_{jet,in})\cdot T_{jet,in}=P_{loss}+\rho(T_{adibatic})\cdot Q_{total}\cdot c_p(T_{adibatic})\cdot T_{adibatic} \quad \text{with } T \text{ in } [K] \tag{C1}$$

The losses can be determined analytically over the whole length assuming heat conduction from the liquid/solid interface of the downcomer towards the outside of the thermal insulation in a cylinder of a length of 2.5m. The temperatures measured at the outside of the insulation were 26°C during the experimental runs and almost constant over the whole height. As the experimental runs in chapter 5-7 have shown, the temperature at the outside of the gap was almost that of the main flow inlet, which was 300°C. The thermal insulation consists of a multi-layer structure, in which beyond the steel walls confining the liquid an air gap exists necessary for the supplementary heaters. The air gap is bordered by a 0.2mm thick steel foil around which rock wool is wrapped. The final insulation layer is a 1mm thick aluminium foil. The detailed arrangement and the dimensions are shown in the figures C1.

The heat loss can be calculated by

$$Q=P_{loss}=(k\cdot A)\cdot(T_{main,in}-T_{ambient}) \quad , \tag{C2}$$

where k is the heat transfer coefficient and A an equivalent area [m^2]. The total heat transfer coefficient is calculated as a sum of the individual heat resistances $(k_i A_i)^{-1}$ of each layer,

$$\frac{1}{(k\cdot A)_{total}}=\sum_{i=1}^{n}\frac{1}{k_i\cdot A_i}, \tag{C3}$$

The heat transfer-coefficient of each individual layer k_i is defined by:

$$k_i=\frac{\lambda_i}{\Delta R_i}, \tag{C5}$$

with λ_i as the specific heat conductivity of the layer i and ΔR its thickness. The equivalent area A_i is given by relation C5

$$A_i=2\,\pi\;R_{\log}L \text{ with } R_{\log}=\frac{R_{a,i}-R_{i,i}}{\ln\left(\frac{R_{a,i}}{R_{i,i}}\right)}. \tag{C5}$$

Herein, $R_{a,i}$ and $R_{i,i}$ are the outer and inner radii of each layer. The calculation yields a total heat loss of the cylindrical part of 184Watt. A similar procedure for the lower part yields 32Watt. Thus, the total heat losses in the considered geometry amount to 216Watt, which is less than 1% of the thermal energy to be transferred in the module.

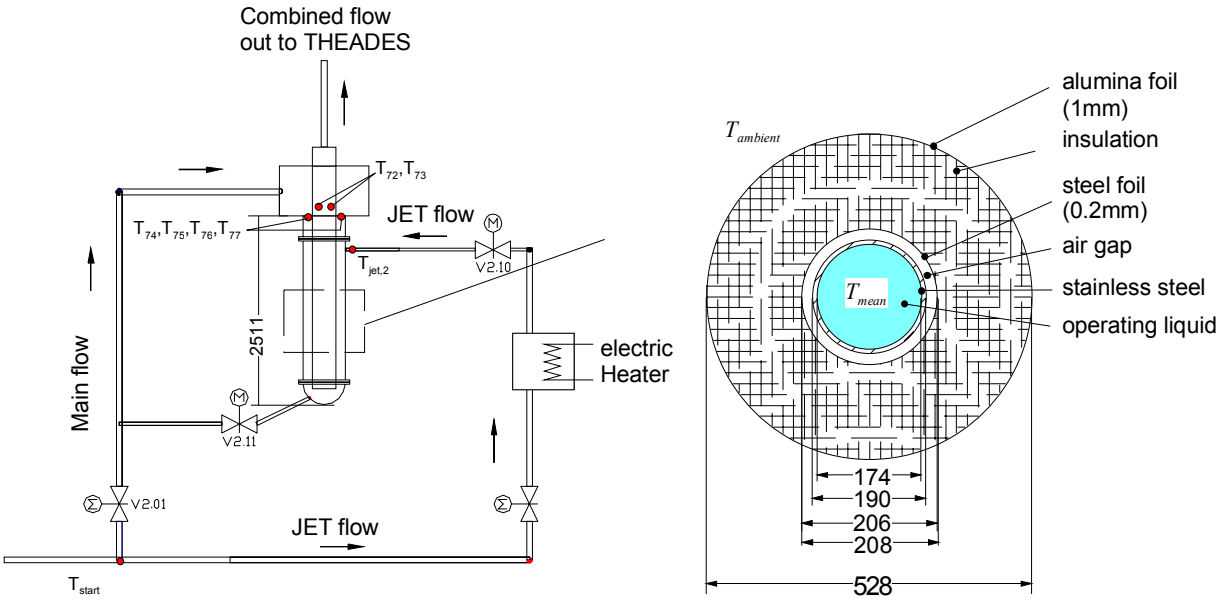

Figure 1: Geometric configuration of the thermal insulation used in the heated jet experiment.

Appendix C Thermo-physical properties of lead bismuth

T [°C]	ρ [kg/m^3]	λ [W/(mK)]	$\nu\,10^{-7}$ [m^2/s]	$\sigma\,10^5$ [A/Vm)]	c_p [J/(kgK)]
130	10559	8.9	3.006	9.004	150.4
150	10531	9.1	2.719	8.943	149.9
200	10462	9.7	2.275	8.771	148.7
250	10393	10.3	1.971	8.600	147.5
275	10359	10.6	1.854	8.565	146.9
300	10325	10.9	1.754	8.428	146.3
325	10290	11.3	1.700	8.386	145.7
350	10256	11.6	1.592	8.257	145.1
375	10221	11.9	1.525	8.211	144.5
400	10187	12.2	1.467	8.085	143.9

The values for the specific thermal-hydraulic properties have been calculated using the following correlations for the:

a.) density ρ [kg/m^3] :

$$\rho(T) = 10^3 \cdot \left(11.113 - 1.375 \cdot 10^{-3} \cdot T\right) \text{ with } T \text{ in [K]} \text{ valid for } 125°C<T<1222°C \quad \text{(C1)}$$

b.) specific heat conductivity λ [$W/(mK)$]

$$\lambda(T) = 6.851 + 1.0174 \cdot 10^{-2} \cdot T \text{ with } T \text{ in [K]} \text{ valid for } 130C°<T<700°C \quad \text{(C2)}$$

c.) kinematic viscosity $\nu\,10^{-6}$ [m^2/s] :

$$\nu(T) = \frac{0.497 \cdot \exp\left(\frac{741}{T}\right)}{\left(11.113 - 1.375 \cdot 10^{-3} \cdot T\right)} \text{ with } T \text{ in [K]} \text{ valid for } 300°C<T<637°C \quad \text{(C3)}$$

d.) specific electric conductivity $\sigma\,10^6$ [$A/(Vm)$] :

$$\sigma(T) = \frac{1}{89.343 + 5 \cdot 10^{-2} \cdot T} \text{ with } T \text{ in [K]} \text{ valid for } 200°C<T<500°C \quad \text{(C4)}$$

e.) heat capacity c_p [$J/(kg\,K)$] :

$$c_p(T) = 10^3 \cdot \left(0.160 - 2.385 \cdot 10^{-5} \cdot T\right) \text{ with } T \text{ in [K]} \text{ valid for } 125°C<T<827°C \quad \text{(C5)}$$

The thermo-physical values are taken from Imbeni et al. (1999) [28], Lyon [55] and Yefimov [56].

Appendix D Repeatability of the measurements

In order prove the quality of the experimental results the reference case has been measured at different days. Additionally, the adjustment of the flow rate ratio between main flow and bypass flow has been realized in different ways. This methodology has been chosen to exclude a flow pattern establishment, which might depend on the history caused by flow induced asymmetric inlet flow or other reasons. The figures D1- D4 show the mean temperatures and the RMS values of the temperature fluctuations measured at three different days for the reference case in the nozzle plane ϕ=0°.

Regarding the mean values the maximum deviation between the individual data sets reached has been a little less than 0.4K. This occurred immediately at the shell, while in the rest of the measurement positions the deviations are considerably smaller. Normalized with the driving temperature difference ΔT this represents a spread-width of the measurements of 0.12%, which is less than the accuracy of the thermocouples.

At the same position also the maximum bandwidth of the RMS-values has been detected. In absolute values the differences between the data sets reached a ΔRMS of 0.2K, which is normalized with the adiabatic mixing temperature a deviation of at maximum 5%. At all other positions in the flow domain the temperature fluctuation differences are significantly smaller.

Based on this results the measurements can be considered as time and history independent with a considerable large confidence.

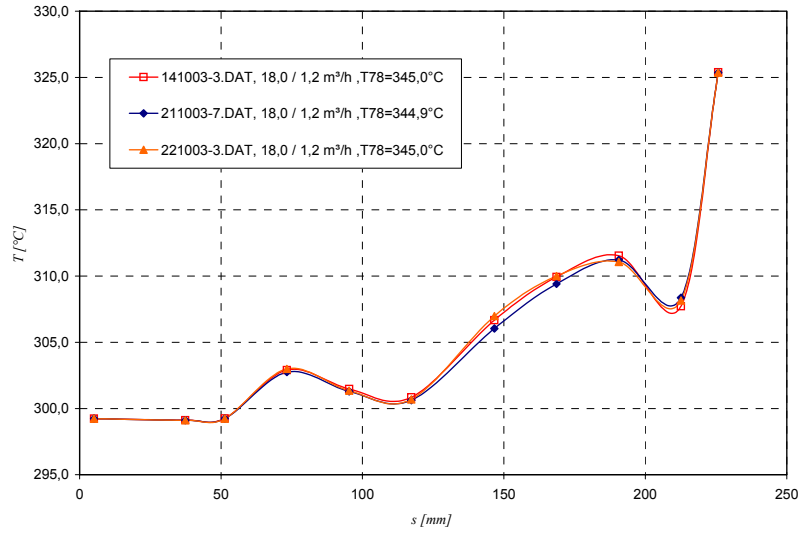

Figure D.1: Temperature distribution measured at three different days as a function of the geometry adapted coordinate s in the plane ϕ=0° and the reference conditions Q_{main}=18m^3/h, Q_{jet}=1.2m^3/h.

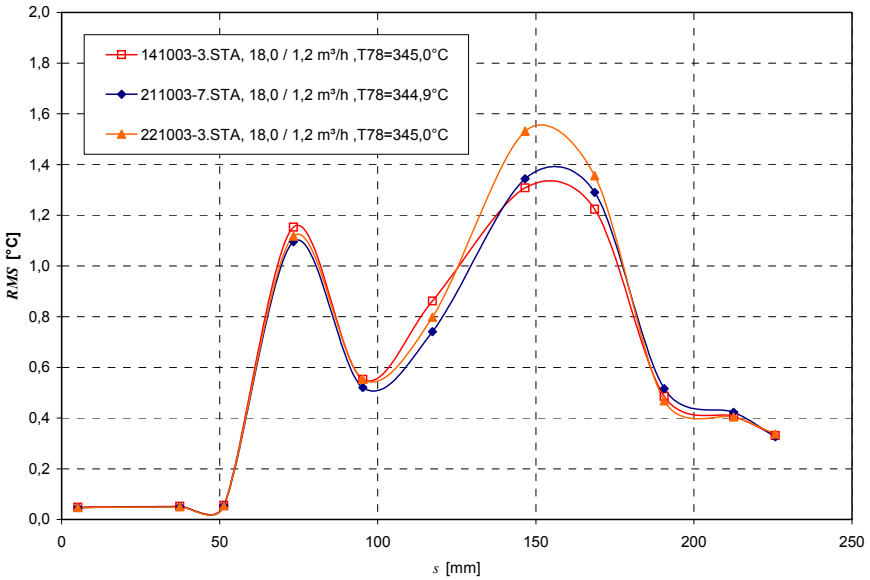

Figure D.2: Temperature fluctuation distribution (RMS-values) recorded at three different days as a function of the geometry adapted coordinate s for ϕ=0° and the reference conditions Q_{main}=18m^3/h, Q_{jet}=1.2m^3/h, T_{in}=300°C and $T_{in,jet}$=360°C.

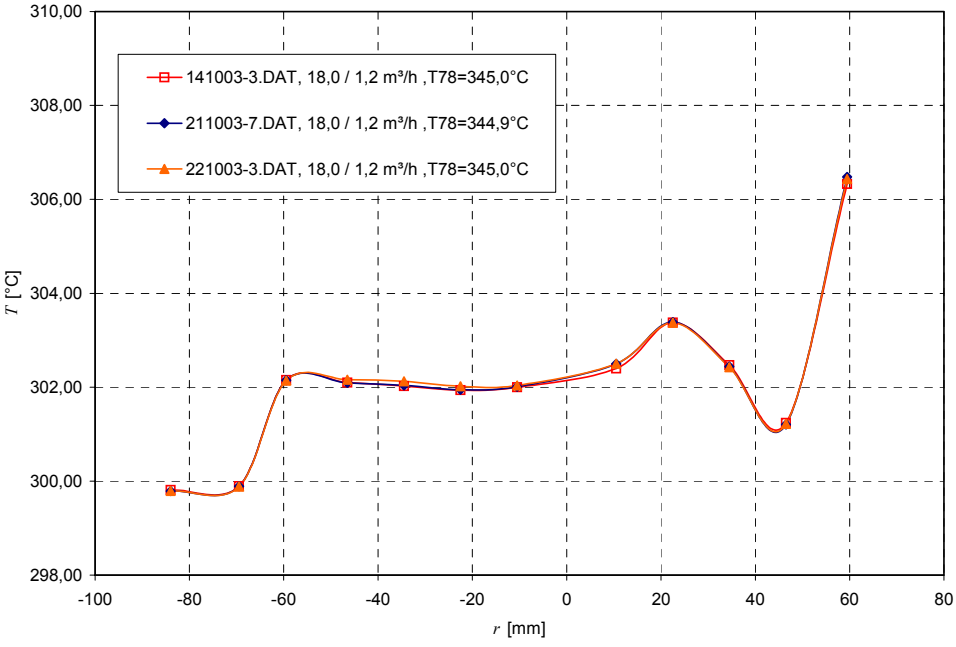

Figure D.3: Temperature distribution in the plane z=105.7mm measured at three different days as a function of the radius r for ϕ=0° and the reference conditions Q_{main}=18m^3/h, Q_{jet}=1.2m^3/h, T_{in}=300°C and $T_{in,jet}$=360°C.

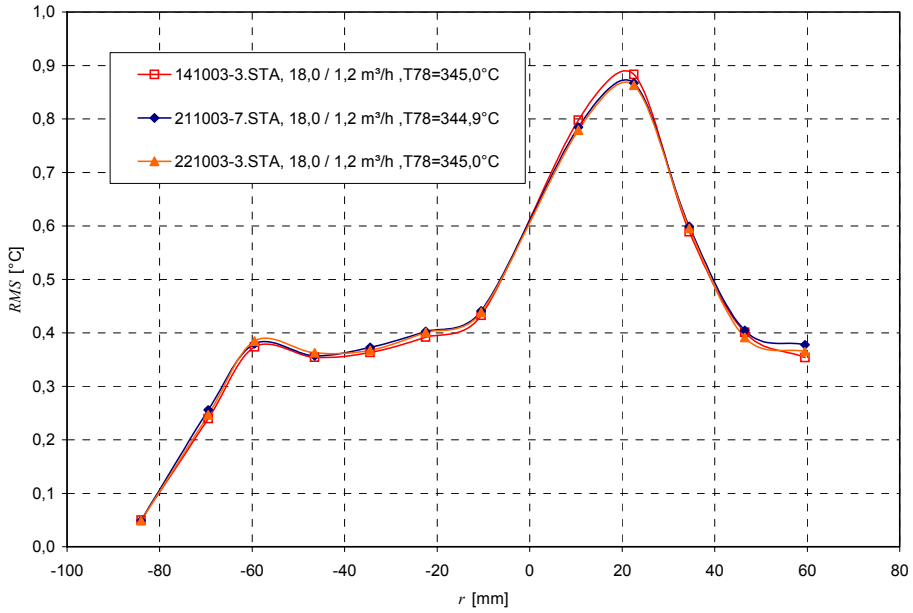

Figure D.4. Temperature fluctuations recorded at a height z=105.7mm as a function of the radius r at three different days for ϕ=0° and the reference conditions Q_{main}=18m^3/h, Q_{jet}=1.2m^3/h, T_{in}=300°C and $T_{in,jet}$=360°C.